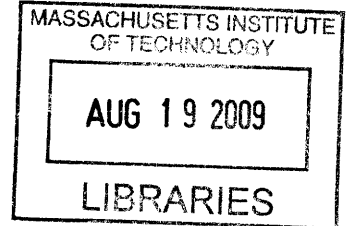# Current Profile Measurements Using MSE on Alcator C-Mod

by

Jin-Seok Ko

B.E. Nuclear and Energy Engineering (1999)
Jeju National University, Korea

M.S. Nuclear Engineering (2001)
Seoul National University, Korea

Submitted to the Department of Nuclear Science and Engineering
in partial fulfillment of the requirements for the degree of
Doctor of Philosophy in Nuclear Science and Engineering
at the
MASSACHUSETTS INSTITUTE OF TECHNOLOGY
June 2009

ARCHIVES

Author ..
Department of Nuclear Science and Engineering
May 22, 2009

Certified by.....
Steven D. Scott
Principal Research Scientist, Princeton Plasma Physics Laboratory
Thesis Supervisor

Read by ....
Ian H. Hutchinson
Professor and Head of Nuclear Science and Engineering
Thesis Reader

Accepted by ....
Jacquelyn C. Yanch
Chairman, Department Committee on Graduate Students

Current Profile Measurements Using MSE on Alcator C-Mod

by

Jin-Seok Ko

Abstract

A Motional Stark Effect (MSE) diagnostic system has been installed on the Alcator C-Mod tokamak to measure the plasma internal magnetic pitch angle profile. The diagnostic utilizes polarization patterns from Doppler-shifted Balmer-alpha decay emission from an energetic neutral beam injected into a magnetically confined plasma. This dissertation consists of three parts: (1) the current status of the C-Mod MSE diagnostic which includes major upgrades in the hardware and calibration techniques; (2) the elimination of the spurious drift in the polarization measurements due to thermal-stress induced birefringence; and (3) the measurement of current density profiles in Lower Hybrid Current Drive (LHCD) experiments.

The major hardware upgrades include replacement of photomultiplier tubes (PMT's) with avalanche photodiodes (APD's) which enhanced the quantum efficiency; installation of a wire-grid polarizer to verify small Faraday rotation in the diagnostic; installation of steep edge filters to minimize pollution by the thermal Balmer-alpha signals; rotation of the Diagnostic Neutral Beam (DNB) which significantly reduced the anomalous effect from the secondary beam neutrals during the beam-into-gas calibrations. The new calibration techniques include two plasma calibrations: plasma current sweeping and the plasma size sweeping whose feasibility was experimentally proven; and an absolute intensity calibration which measured the real optical throughput of the system. A large database study indicates the signal-to-background ratio larger than 100 is required to have the measurement uncertainty under 0.1 degrees.

The spurious drift in the measurement has been identified as the thermal-stress induced birefringence imposed on the in-vessel lenses. By modeling this effect as a single wave plate, an in-situ calibration method has been proposed and its feasibility was experimentally verified. Based on the experiments that characterized the thermal response of the system, a single-layer heat shield with gold plating and a lens holder which reduces the thermal conduction path to the lens have been designed and fabricated. A more rigorous model that includes an intrinsic phase shift by mirrors reveals the thermal phase shift can be greatly magnified by the intrinsic phase shift.

The current density profiles from LHCD experiments have been obtained from

the MSE data corrected by a baseline magnetic equilibrium whose internal profile is constrained by the sawtooth inversion radius. The resultant profiles successfully demonstrate several standard predictions of LHCD theory such as the dependence of efficiency on the parallel refractive index and the off-axis current drive.

Thesis Supervisor: Steven D. Scott
Title: Principal Research Scientist, Princeton Plasma Physics Laboratory

Acknowledgments

parents in Korea, which I could not do here. The cheers from their two daughters, Eunbin and Eunsu, have always been pleasant and delighting. Finally, I express my heartfelt thank and love to my wife Hyunju. Her love, support, understanding, and sacrifice made all these accomplishments possible, combined with the endless source of joy, happiness, and energy - my daughter Yerin.

Contents

List of Figures

14

16

23

25

26

31

33

34

37

List of Tables

Chapter 1

Introduction

1.1 Significance of measurements of internal magnetic field structures in tokamaks

In magnetically confined fusion devices such as a tokamak, many global properties including plasma current, loop voltage, plasma position and shape can be obtained by simple external magnetic probes, loops and coils [1, 2]. However, many of the present-day tokamak experiments pursue advanced tokamak regimes to achieve steady state operations, which involve optimizing the plasma shape, current density, and pressure profiles for stability to magnetohydrodynamic (MHD) modes with real-time active feedback controls [3, 4, 5] and reducing cross field transport by changing the properties of microinstabilities [6, 7]. Information on the internal profiles of local current density and safety factor are among the most important quantities for these studies [8, 9, 10].

The MHD safety factor, q, is defined by the change in toroidal angle during one poloidal turn of a magnetic field line in an axisymmetric equilibrium of a tokamak and an important parameter in determining plasma stability. Using the equation of the field line

$$\frac{R d\phi}{ds} = \frac{B_\phi}{B_p},$$ (1.1)

41

where ds is the distance moved in the poloidal direction while moving through a toroidal angle $d\phi$, and B_p and B_ϕ are the poloidal and toroidal magnetic fields, one can derive an expression for q as [2]

$$q = \frac{1}{2\pi} \oint \frac{1}{R} \frac{B_\phi}{B_p} ds, \tag{1.2}$$

where the integral is carried out over a single poloidal circuit around the flux surface. Applying Ampere's law to the toroidal current density in cylindrical coordinates (R, ϕ, z) gives

$$J_\phi = \frac{1}{\mu_0} \left(\frac{\partial B_R}{\partial z} - \frac{\partial B_z}{\partial R} \right), \tag{1.3}$$

where μ_0 is the permeability of free space, B_R is the radial magnetic field strength, and B_z is the vertical magnetic field strength and equal to B_p when measured along the midplane. Evaluating Eqns 1.2 and 1.3 requires the knowledge of the internal magnetic field structure, especially the poloidal magnetic field, B_p. Therefore, any direct measurements of the local magnetic field direction and/or magnitude can, in principle, provide this information. However, since the plasma cross sections in present-day tokamaks are non-circular and/or strongly shaped, it is not straightforward to directly calculate the q or J_ϕ from the measurements. Instead, these measurements serve as 'internal constraints' for full magnetic topology reconstruction procedures such as EFIT [11, 12, 13] along with some basic external magnetic measurements including magnetic probes, flux loops, Rogowski coils, and diamagnetic loops which serve as the boundary conditions. The internal constraint is essential for the full equilibrium reconstruction since otherwise, the reconstruction procedure produces large uncertainties as it approaches the central region of the plasma unless it is constrained by some internal information. Some efforts for direct usage of the internal magnetic field structures have been made for the safety factor [14] and the current density [15, 16] with appropriate assumptions and approximations in the plasma shape, some of which have been used in this thesis (Chapter 4).

A number of diagnostic techniques have been developed to measure the magnetic

field line topology, and thereby q and/or J_ϕ [1, 2, 17, 18]. The most successful and reliable is the method using the motional Stark effect (MSE) [19, 20, 21, 22, 23, 24, 25, 26, 27] which will be introduced in the next section.

1.2 Principle of MSE diagnostics

The Stark effect is the shifting and splitting of spectral lines of atoms and molecules due to the presence of an external static electric field. The amount of spectral shift is called the Stark shift. When the Stark effect is linear, that is, the shift is linear in the applied electric field, which is the regime that most fusion plasmas reside, the shifts in wavelength for H_α line in a hydrogen atom can be expressed as [28]

$$\Delta\lambda_S = 2.757 \times 10^{-8} nkE \ [nm] \tag{1.4}$$

where E is the applied electric field in V/m and $k = 0, \pm 1, \pm 2, ..., \pm(n-1)$ where n is the principal quantum number. Since $n = 3$ and 2 in this transition, there are 5 upper states and 3 lower states and only 9 out of 15 possible transitions have significant line strength. The prominent feature in the Stark effect is that each transition is linearly polarized either parallel or perpendicular to the external electric field when appropriately viewed. When viewed transversely to the electric field, the $\Delta m = 0$ (π lines) and the $\Delta m = \pm 1$ (σ lines) transitions are linearly polarized parallel and perpendicular to the electric field, respectively. The π radiation has a zero intensity and the σ radiation is circular polarized when viewed parallel to the field. Fig 1-1 illustrates the H_α transition with the Stark effect and its spectrum when viewed transversely to the electric field.

When an energetic neutral beam propagates through a plasma, collisional excitations of the beam atoms by the background plasma ions and electrons take place. These beam particles also experience a strong Lorentz electric field $\mathbf{E} = \mathbf{v} \times \mathbf{B}$ in their rest frame, where $\mathbf{v}$ is the beam particle velocity and $\mathbf{B}$ is the external magnetic field in the plasma, and the Stark effect comes in play by this 'motional' electric
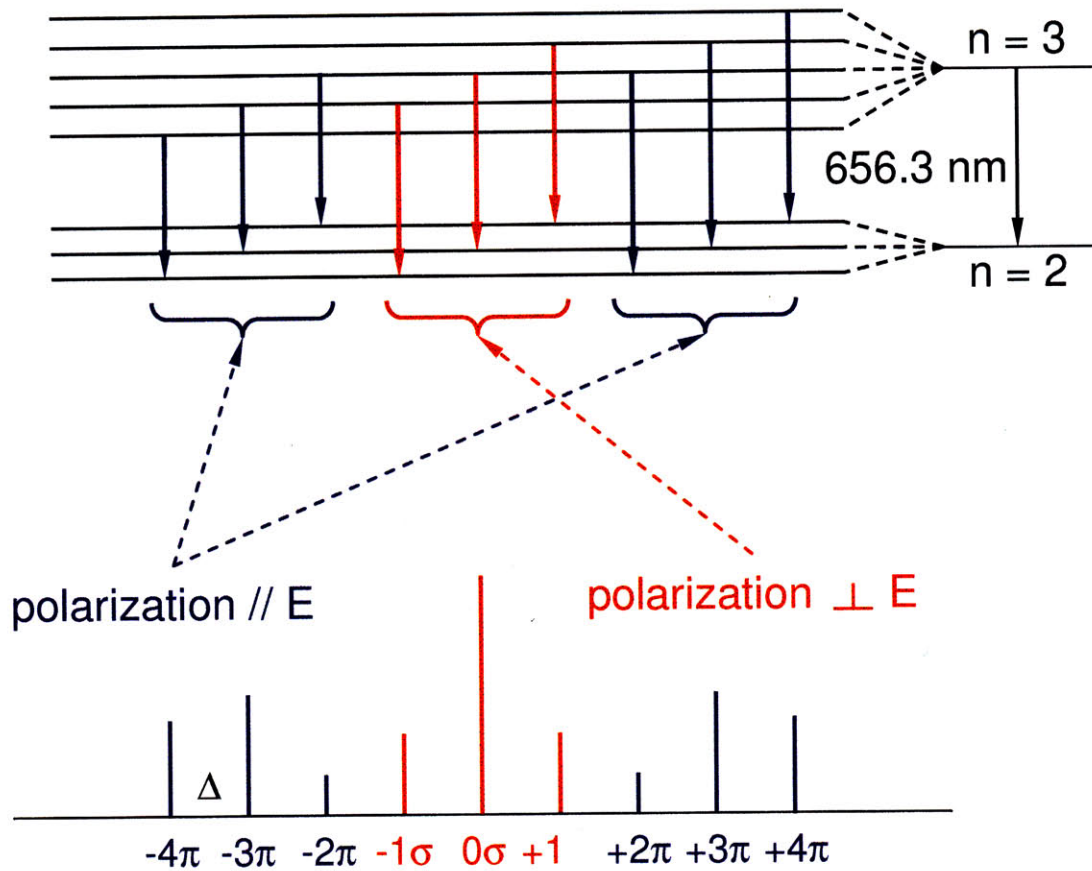
Figure 1-1: Illustration of Stark effect for hydrogen Balmer-α transition. Stark splittings of the $n = 3$ and 2 principal quantum energy levels and their transitions are shown in the top and the position of each line on the spectrum when viewed transversely to the applied electric field shown in the bottom with π and σ lines distinguished. Δ corresponds to $2.757 \times 10^{-8} E$ nm from Eqn 1.4.

field. The motional Stark effect under usual experimental conditions in a tokamak ($E_b \approx 50 \sim 150$ keV and $B \approx 4$ Teslas) dominates strongly over the Zeeman effect. From Eqn 1.4, the Stark splitting, Δ_S, (Δ in Fig 1-1) can be conveniently written in terms of E_b in keV and B in Tesla as

$$\Delta_S = 0.452\sqrt{E_b/50 keV}\,(B/5.3T)\ [nm] \qquad (1.5)$$

and also the Zeeman splitting in wavelength can be written equivalently as [29]

$$\Delta_Z = 0.106(B/5.3T) \ [nm] \tag{1.6}$$

for a hydrogen atom experiencing Balmer-α transition. Eqns 1.5 and 1.6 then gives

$$\frac{\Delta_S}{\Delta_Z} = 4.264\sqrt{E_b/50keV}. \tag{1.7}$$

For $E_b = 50 \sim 150$ keV, this factor ranges $4.2 \sim 7.4$

Hydrogen Balmer-α (H_α) lines, whose intensity is relatively strong and whose wavelength falls into the visible range, are typically used in MSE diagnostics. Having the signals in the visible range enables one to use conventional optics. The MSE-induced emissions are Doppler-shifted in wavelength by the velocity component projected onto the sight line, i.e.

$$\frac{\Delta\lambda}{\lambda} = \frac{\mathbf{v} \cdot \hat{\mathbf{s}}}{c} \tag{1.8}$$

where $\hat{\mathbf{s}}$ is the unit vector along the sightline and c is the speed of light. This helps one obtain an MSE spectrum distinguished from the thermal H_α line whose intensity is much (orders of magnitude) larger than the MSE emission due to the beam. In addition, the use of hydrogen has the unique characteristic that the Stark effect is in the linear regime with a large spectral shift. Therefore, the underlying principle of the diagnostic is to deduce the direction of the local external magnetic field ($\mathbf{B}$), or magnetic pitch angle, by measuring the linear polarization either parallel or perpendicular to the Lorentz electric field ($\mathbf{E}$) with the known direction and magnitude of the neutral beam ($\mathbf{v}$). The detailed derivations of these relations and how to infer the pitch angle in the tokamak frame from the measured polarization direction are given in App A. If the spectral shift is large enough to be accurately resolved, it is also possible to deduce the magnitude of B by measuring the line intensity and shift and therefore, the magnitude of E [30, 31].

The measurement of the linear polarization is in general made by the dual PEM (Photo-Elastic Modulator) polarimetry technique [32, 33, 34]. A PEM is a solid-

crystal waveplate whose retardance varies with a frequency imposed by a piezo-electric transducer using the principle of stress-induced birefringence. The key components of the dual PEM Stokes polarimeter are two PEMs, an analyzer (linear polarizer), a photo detector, and signal processing electronics. The two PEM's are oriented 45° from each other and the analyzer bisects the optical axes of the two PEMs. Using this optical configuration, no crossed terms between the two PEMs are required for measuring the Stokes parameters of input polarized light [35]

$$
S_{in} = \begin{bmatrix} I \\ Q \\ U \\ V \end{bmatrix} = \begin{bmatrix} I_u \\ 0 \\ 0 \\ I_c \end{bmatrix} + \begin{bmatrix} I_p \\ I_p \cos(2\gamma) \\ I_p \sin(2\gamma) \\ 0 \end{bmatrix}, \tag{1.9}
$$

where I_u is the intensity of unpolarized light, I_p is the intensity of polarized light with an angle γ to the horizontal, I_c is the intensity of circularly polarized light. By combining Eqn 1.9 with the two Müller matrices for the PEMs with their fast axes oriented horizontally and 45°, that is,

$$
M_{PEM1} = \begin{bmatrix} 1 & 0 & 0 & 0 \\ 0 & \cos(A_1 \cos(\omega_1 t)) & 0 & -\sin(A_1 \cos(\omega_1 t)) \\ 0 & 0 & 1 & 0 \\ 0 & \sin(A_1 \cos(\omega_1 t)) & 0 & \cos(A_1 \cos(\omega_1 t)) \end{bmatrix} \tag{1.10}
$$

and

$$
M_{PEM2} = \begin{bmatrix} 1 & 0 & 0 & 0 \\ 0 & 1 & 0 & 0 \\ 0 & 0 & \cos(A_2 \cos(\omega_2 t)) & \sin(A_2 \cos(\omega_2 t)) \\ 0 & 0 & -\sin(A_2 \cos(\omega_2 t)) & \cos(A_2 \cos(\omega_2 t)) \end{bmatrix}, \tag{1.11}
$$

respectively, where A_1 and A_2 are the amplitudes of the retardances imposed by the PEMs with the frequencies of ω_1 and ω_2, and the Müeller matrix for an analyzer at

46

an angle 22.5° with respect to horizontal

$$M_p = \frac{1}{2} \begin{bmatrix} 1 & \sqrt{2}/2 & \sqrt{2}/2 & 0 \\ \sqrt{2}/2 & 1/2 & 1/2 & 0 \\ \sqrt{2}/2 & 1/2 & 1/2 & 0 \\ 0 & 0 & 0 & 0 \end{bmatrix}, \tag{1.12}$$

one can write down the following expression for the output Stokes vector

$$S_{out} = M_p \cdot M_{PEM2} \cdot M_{PEM1} \cdot S_{in}. \tag{1.13}$$

Note that constructing the Müeller calculus as in Eqn 1.13 assumes the constituent optics elements behave ideally and therefore should be considered only as a conceptual guideline to the principle of the diagnostic. A previous dissertation on the C-Mod MSE evaluates the effect of various non-ideal optical factors [36]. The evaluation of Eqn 1.13 allows one to obtain an expression of the measured net intensity I_{net} by taking the first element of S_{out} which is

$$I_{net} = \frac{I_p + I_u}{2} + \frac{I_p \cos(2\gamma)\cos(B)}{2\sqrt{2}} \quad + \quad I_p \left[\frac{\cos(A)}{2\sqrt{2}} + \frac{\sin(A)\sin(B)}{2\sqrt{2}} \right] \sin(2\gamma)$$
$$- \quad I_c \left[\frac{\sin(A)}{2\sqrt{2}} - \frac{\cos(A)\sin(B)}{2\sqrt{2}} \right] \tag{1.14}$$

where $A \equiv A_1 \cos(\omega_1 t)$ and $B \equiv A_2 \cos(\omega_2 t)$. Using Jacobi-Anger expansion [37]

$$\cos(A_i \cos \omega_i t) = 2\sum_{n=1}^{\infty}(-1)^n J_{2n}(A_i)\cos(2n\omega_i t) + J_0(A_i), \tag{1.15}$$

$$\sin(A_i \cos \omega_i t) = 2\sum_{n=1}^{\infty}(-1)^{n-1} J_{2n-1}(A_i)\cos((2n-1)\omega_i t), \tag{1.16}$$

the $\sin(A)$, $\sin(B)$, $\cos(A)$, and $\cos(B)$ in Eqn 1.14 can be written as

$$\sin(A) = 2J_1(A_1)\cos(\omega_1 t) - 2J_3(A_1)\cos(3\omega_1 t) + 2J_5(A_1)\cos(5\omega_1 t) - \cdots \tag{1.17}$$

$$\sin(B) = 2J_1(A_2)\cos(\omega_2 t) - 2J_3(A_2)\cos(3\omega_2 t) + 2J_5(A_2)\cos(5\omega_2 t) - \cdots \tag{1.18}$$

$$\cos(A) \;=\; -2J_2(A_1)\cos(2\omega_1 t) + 2J_4(A_1)\cos(4\omega_1 t) - \cdots + J_0(A_1) \tag{1.19}$$

$$\cos(B) \;=\; -2J_2(A_2)\cos(2\omega_2 t) + 2J_4(A_2)\cos(4\omega_2 t) - \cdots + J_0(A_2) \tag{1.20}$$

Therefore, I_{net} consists of various combinations of the harmonics of the two PEM frequencies. It is noted that the input polarization angle γ is contained in even harmonics and the intensity of circular polarization in odd harmonics. The simplest among them are

$$I_{\omega_1} \;=\; -I_c \frac{J_1(A_1)}{\sqrt{2}} \tag{1.21}$$

$$I_{\omega_2} \;=\; I_c \frac{J_0(A_1)J_1(A_2)}{\sqrt{2}} \tag{1.22}$$

$$I_{2\omega_1} \;=\; -I_p \frac{\sin(2\gamma)J_2(A_1)}{\sqrt{2}} \tag{1.23}$$

$$I_{2\omega_2} \;=\; -I_p \frac{\cos(2\gamma)J_2(A_2)}{\sqrt{2}} \tag{1.24}$$

where I_ω is the harmonic of the frequency ω and J_n is the nth order Bessel function of the first kind. These expressions indicate that the Stokes parameters Q and U can be measured at the second harmonics of both PEMs ($2\omega_1$ and $2\omega_2$) and V can be measured from the fundamental harmonics of the PEMs (ω_1 and ω_2). The input linear polarization angle can be obtained by taking the ratio of 1.23 and 1.24, which yields

$$\gamma = \frac{1}{2}\arctan\left(\frac{I_{2\omega_1}}{I_{2\omega_2}}\frac{J_2(A_2)}{J_2(A_1)}\right). \tag{1.25}$$

It should be noted that γ obtained from Eqn 1.25 is not the real magnetic pitch angle of the tokamak. Two more considerations must be evaluated to infer the final field line pitch in the tokamak frame. The first consideration actually involves two factors: one from the fact that the polarimeter frame, where the PEMs and the analyzer share an axis in the direction of the light propagation, can be different from the frame of the object lens which accepts the Stark-induced polarization from the plasma and the other from the non-ideal characteristics of the constituent optics elements. For example, imperfectly coated mirrors can cause an additional phase

48

shift and non-unity reflectiviy ratio between the S- and P-polarizations. The second consideration is to convert the measured polarization (electric field) into the local magnetic field.

The first consideration can be treated by the 'invessel calibration' where the response of the polarimeter system including all the optical elements to absolutely known polarization angles is characterized. This is further discussed in 2.2 along with some other important functions of the invessel calibration. The second consideration involves the vector algebra in 3D and some coordinate transforms to derive the field line pitch angle (γ_m) as a function of the measured polarization angle (γ) in the frame of the object lens and some geometrical factors. The derivation of this relation and its application to the Alcator C-Mod geometry are given in App A. This relation is particularly important since the uncertainty in the final field line pitch angles tend to be larger than that in the polarization angle in the MSE frame due to unfavorable geometry (See Figs A-5). Therefore, when an attempt is made to modify the geometry of the MSE system such as the diagnostic beam direction or the line of sight, the resultant error multiplication should be taken into account.

In addition to the invessel calibration which is usually done in an atmospheric pressure without any magnetic field, the MSE diagnostic requires some other calibration procedures since the invessel calibration cannot address the effects such as the Faraday rotation through the optical elements and the stress-induced birefringence on the vacuum window. In principle, these effects can be inferrred from beam-into-gas calibrations where the torus is filled with a neutral gas in vacuum and the magnetic field configurations are pre-defined by the external field coils only. However, recent studies in C-Mod demonstrate a critical limitation of this approach depending on the torus operation gas pressure and the diagnostic neutral beam orientation [38, 39, 40, 41], which is introduced in more detail in Section 2.1.4. Therefore, the effects of the Faraday rotation and the vacuum window birefringence should be treated in a way different from beam-into-gas calibrations in reality. These alternative approaches are also discussed in Sec 2.1.2.

1.3 Brief introduction to MSE diagnostic in Alcator C-Mod

Alcator C-Mod is a compact high-performance divertor tokamak with a typical toroidal field of 5.4 T (maximum $\sim$ 8 T) and a plasma current of $\leqslant$ 2 MA with a major radius $R \sim 0.67$ m and a minor radius $a \sim 0.21$ m [42, 43]. Particle and momentum source-free heating and current drive are main features of C-Mod. This requires a separate neutral beam system specific for various active diagnostics: a low-power (250 kW) Diagnostic Neutral Beam (DNB) [44] provides a neutral particle source for MSE, BES (Beam Emission Spectroscopy) [45], and CXRS (Charge Exchange Recombination Spectroscopy) [46, 47] diagnostics.

Fig 1-2 shows a plan view of the Alcator C-Mod tokamak with the sightlines of the MSE diagnostic. The red 'bar' in the figure denotes the trajectory of the DNB system which injects 50-keV hydrogen neutral atoms. Originally, the DNB injection was purely radially inward until it was pivoted by 7° prior to the FY07 Campaign to reduce the effect of secondary beam neutral emission which is discussed in Sec 2.1.4. There are 10 spatial channels that collect polarized emission along the DNB, covering $r/a = 0.1 \sim 0.9$ at the low field side of the plasma. The green structure on the figure indicates the Ion Cyclotron Radio Frequency (ICRF) heating antennas installed in the vessel, which form the viewing 'dump' of the MSE lines of sight. The possible effect of having these shiny ICRF antennas as a viewing dump is discussed in Sec 2.3. The geometry of viewing sightlines and the DNB systems yields only modest spatial resolution, the normalized spatial resolution being $\Delta r/a \approx 0.09$ at the edge and 0.41 at the core with the beam 13 cm in cross sectional diameter. As shown in Fig 1-2, there is no direct line of sight through the existing ports to the DNB trajectory, making the structure of the in-vessel periscope complicated. Fig 1-3 shows (a) 3D view of the MSE periscope with a portion of the vacuum vessel and (b) 3D view of the optical train. The orange cylinder in Fig 1-3 (a) denotes the DNB and the rays from three MSE spatial channels are traced through the optical train for demonstration. As shown in Fig 1-3 (b), there are 3 in-vessel mirrors (M1, M2, and
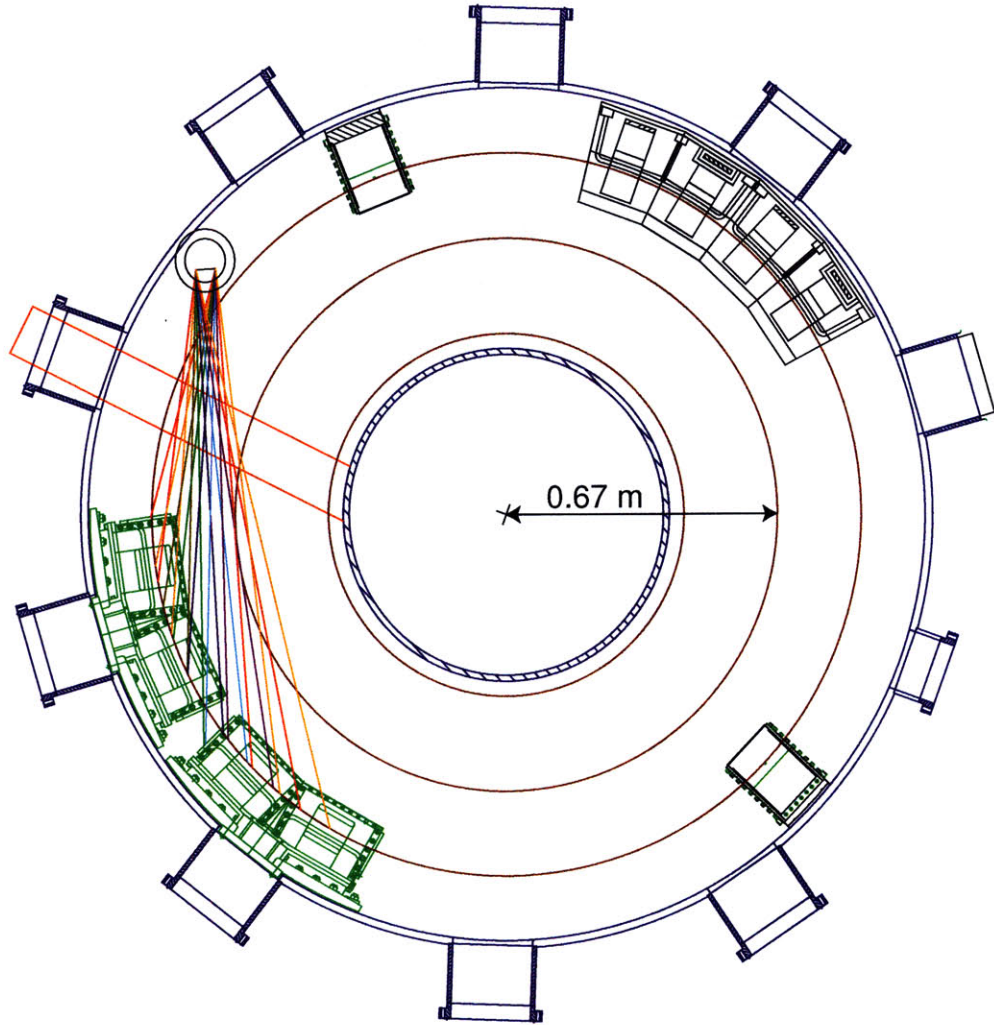
Figure 1-2: Plan view of the C-Mod torus, the MSE lines of sight, and the DNB trajectory (red rectangle). The green structures are the ICRF antennas.

M3) and 5 in-vessel lenses (L1, L2 (doublet), and L3 (doublet)). A dual PEM-based polarimeter with 5 more lenses are located after the vacuum window. The two PEMs are driven by the resonant frequencies of 20 and 22 kHz, which correspond to ω_1 and ω_2 in Eqns 1.10 and 1.11, respectively. All the lenses and the vacuum window are made of SFL6 glass material which has a low Verdet constant to minimize the Faraday rotation (which will be discussed in Sec 2.1.2. The exception is the PEM windows, which are made of fused silica.

After the fiber dissector (FD), which positions and holds the fiber bundles (2×8
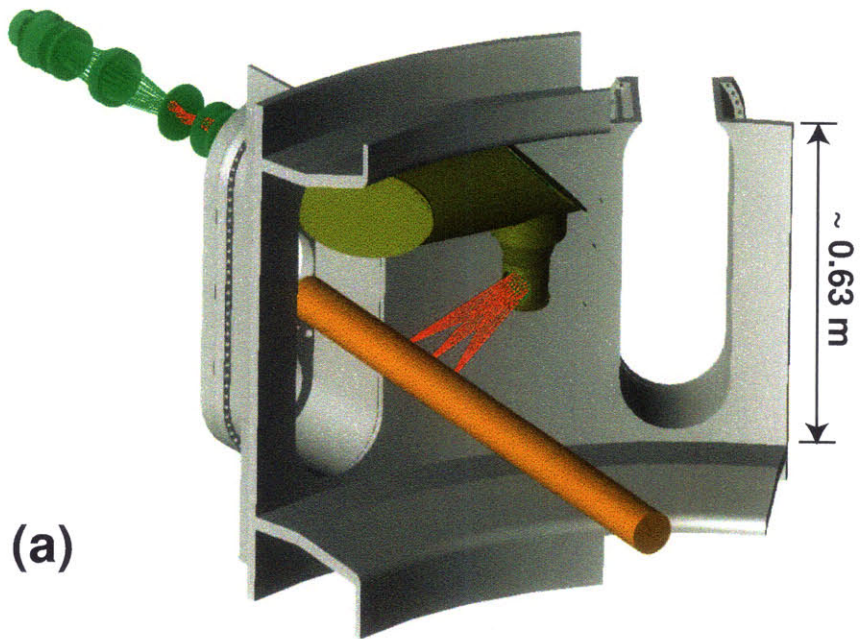
(a)
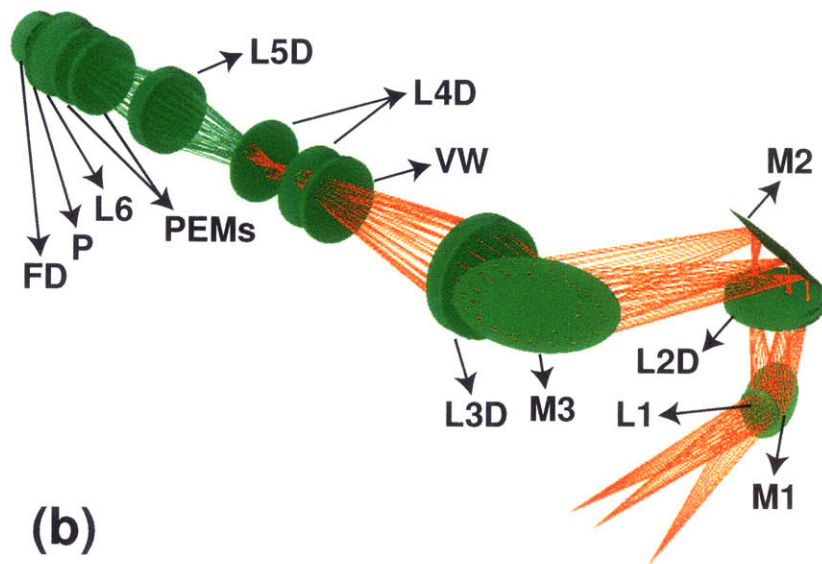
(b)

Figure 1-3: (a) 3D view of the MSE periscope with a portion of the vacuum vessel of C-Mod. The orange cylinder denotes the DNB trajectory. (b) 3D view of the MSE optical train inside the periscope with the following notations; L: lens, LD: lens doublet, M: mirror, VW: vacuum window, P: linear polarizer, and FD: fiber dissector. In both figures, the rays from three MSE spatial channels are traced for demonstration.

fiber array) from each channel such that they correctly collect the focused rays from each footprint on the DNB trajectory, the fiber bundles run about 30 m from the test cell to the diagnostic lab where there are temperature-tuning narrow bandpass filters with FWHM of $\sim$ 0.9 nm which allow to pass only a part of the red end of the Doppler shifted Stark Balmer-α components (usually 3π and 4π). Avalanche photo diodes, which have recently replaced the photo multiplier tubes, and other digitizing electronics are located after the filter assemblies.

1.4   Thesis goals and outline

The goals of this work are

- to identify the spurious thermal drift problems in the MSE diagnostic in Alcator C-Mod
- to upgrade the diagnostic to overcome the problems; and
- to measure the current density profile modifications in the Lower Hybrid Current Drive (LHCD) experiments using the MSE diagnostic.

The major upgrades on the hardware, the various calibration activities and analysis methods are introduced in Chapter 2 along with some challenges faced by the diagnostic. The discovery that thermal stress-induced birefringence causes a spurious drift in the polarization measurements is discussed in Chapter 3. In this chapter, a between-shot calibration scheme is proposed based on a simple model and its feasibility is evaluated. Various tests to characterize the thermal response of the diagnostic system and various design approaches to overcome this problem are also presented in the chapter. Finally, the MSE measurements of the current density profile modifications in the LHCD experiments are presented in Chapter 4, followed by the summary and the discussion on possible future work in Chapter 5.

Chapter 2

Current status of MSE diagnostic on C-Mod

A previous dissertation on the Alcator C-Mod MSE diagnostic describes most aspects of the diagnostic system [36]. This includes the specifications on the invessel and air-side components, the introduction to the digital lock-in analysis scheme, the discussion on invessel and beam-into-gas calibrations. This chapter describes subsequent upgrades and changes in the hardware. Various calibration techniques and their results are presented along with some new understandings in the analysis method. Finally, the current challenges in the diagnostic are discussed.

2.1 Hardware upgrades summary

The most recent upgrades regarding thermal stress-induced birefringence effect on the invessel optics are discussed in a separate chapter (Chapter 3) which is dedicated exclusively to the thermal issue in the diagnostic system. These include a new lens holder that provides thermal conductive isolation from the invessel optical periscope; new heat shields that are installed over the entire invessel periscope and that reduce thermal radiative heat flux from the plasma; gold-plating the invessel periscope to reduce its absorption of infrared radiation; and procurement of new mirrors with smaller intrinsic phase shifts which can reduce the phase shift on the lenses resulted from the

	APD	PMT
QE	$\sim 90\%$	$10 \sim 25\%$
mechanical	rugged, compact, monolithic	bulky, fragile
linear range	$\sim 10^6$	$\sim 10^4$
settling time	0	long
internal gain	~ 350	$\sim 10^6$

Table 2.1: Comparison of general specifications between APD and PMT

thermal stress-induced birefringence. In this section, four other major hardware upgrades are described including the motivations for the upgrades and the results on the diagnostic performance.

2.1.1 Avalanche photodiodes

The original photomultiplier tubes (PMT) were replaced by avalanche photodiodes (APD) during the FY06 campaign. APD is a semiconductor photo detector with internal gain [48, 49]. Absorption of an incoming photon creates an electron-hole pair as in conventional photodiodes. Higher reverse bias (up to 2 kV) allows this electron-hole pair to be multiplied by avalanche breakdown (impact ionization), resulting in the internal gain of several hundreds as in PMTs. Table 2.1 summarizes a comparison of some general features between APD and PMT and implies APD is preferred to PMT in overall performance.

Sensitivity on the intensity of the ratio of 40 and 44 kHz signals

The raw angle that MSE measures in its frame of reference is given in Eqn 1.25. Assuming $A_1 = A_2$, which is typical in practice, the equation is simplified as $\gamma = 0.5\ tan^{-1}(A40/A44)$, where $A40 = I_{2\omega_1}$ and $A44 = I_{2\omega_2}$, the amplitudes of the 40 and 44 kHz components in the signal, respectively. The uncertainty in the raw angle (y) that can arise from the uncertainty in the value $x = A40/A44$ is, therefore,

$$\Delta y = \sqrt{\left(\frac{\partial y}{\partial x}\Delta x\right)^2} = 0.5\ \cos^2(\tan^{-1}(x))|\Delta x|, \qquad (2.1)$$

where Δx is the uncertainty in x. At a typically measured angle ($y \sim 22.5^o$) and a 1 % error in x ($x = 1$ and $\Delta x = 0.01$), the uncertainty in the raw angle is about 0.14^o. When converted into the tokamak frame of reference to infer the real pitch angle, this angle is multiplied by an appropriate geometrical factor (~ 3 for the edge channel; See the bottom plot on Fig A-5), resulting in a **0.42^o** error for this channel. The sensitivity of the APD response to the ratio of A40/A44 with respect to the light intensity was investigated. Two different frequency signals (40 and 44 kHz) were generated by TENMA 5MHz 72-5016 and TENMA 2MHz 72-5015 function generators, respectively, and summed to generate a two-frequency light source from an LED. The input light intensity was smoothly changed by two linear polarizers positioned in front of the LED with one of them being rotated every shot, maintaining the APD bias voltage to be 1896 V. The voltage across the resistor which is connected to the LED in series is measured simultaneously to measure any possible drift in the light intensity in the circuit. The experimental setup is shown in Fig 2-1.

Fig 2-2 shows the ratio of $A40$ and $A44$ as a function of the input light intensity ($A44$) measured by the APD (black). This ratio is the value corrected by a small drift in the function generator (therefore, noted as 'corrected APD' on the plot). Each point represents a 0.5 sec-long shot, each shot having a different input light intensity. The error bar is the statistical uncertainty (standard deviation of the mean) from multiple (~ 16) 30-msec 'micro' time bins per shot, indicating the larger uncertainties at lower light intensities. The input light changes by about a factor of $16 \sim 17$, which reasonably covers the typical MSE input signal range. Also shown in the picture are the $A40$ and $A44$ ratios calculated from the summing amplifier (red) and resistor (orange) signals. Any possible drift in the function generators was monitored by directly measuring the signal from the circuit through the DTACQ channels 5 in Fig 2-1). The raw ratio measured by APD was corrected against this drift by normalizing the raw ratio with that from the circuit (which was also normaized prior to this process). However, this correction is very small since the drift in the actual LED light intensity during the measurement is tiny, indicated by the linear slope of -0.00006 ± 0.00009. The same measurement was done 10 times for statistical purposes. Fig
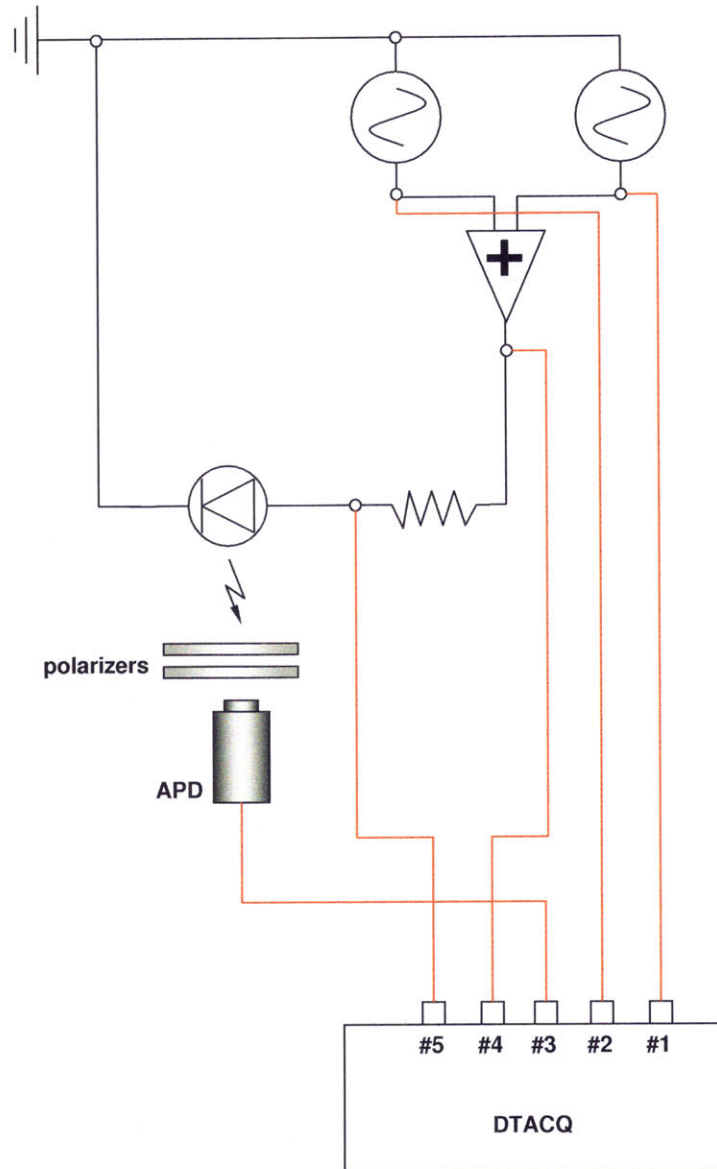
Figure 2-1: Experimental setup for the measurement of APD A40/A44 gain with different light intensity. The input light to the APD varies as one of the polarizers in front of it rotates. The light intensity *in the circuit* is monitored by measuring the voltage across the resistor.
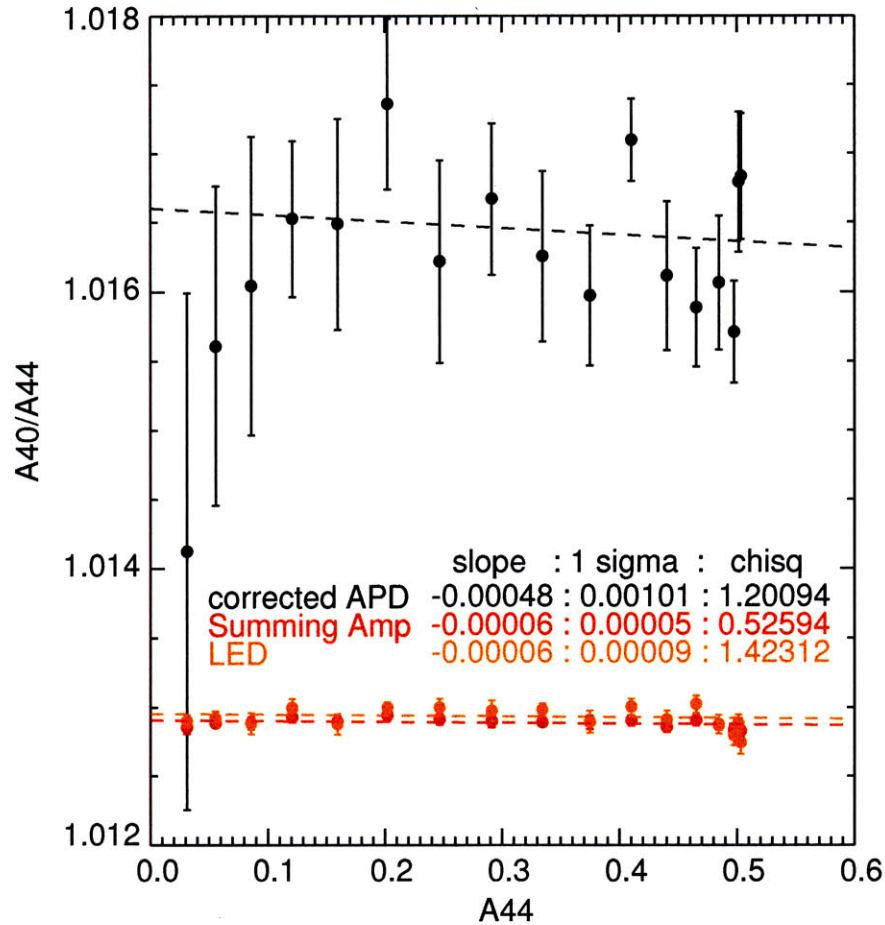
Figure 2-2: A40/A44 vs A44 measured from the APD (black), the summing amplifier (red), and the resistor (orange). The ratio measured at the resistor is considered equivalent to that at the LED. The slope in the linear fit, the 1 sigma in the slope, and the χ^2 are given for each output.

2-3 summarizes these 10 series of measurements, showing the slopes along with their 1-σ uncertainties, like the ones calculated from Fig 2-2, as a function of the series number. Notice that the case shown in Fig 2-2 corresponds to the series 3 in this figure. The average slope for these 10 measurements and its standard deviation is also shown in Fig 2-3. For the APD, the upper bound of this average slope is 0.00032 + 0.00134. Therefore, $|\Delta x|$ in Eqn 2.1 is $|0.00032 + 0.00134| \times 0.47 = 0.00078$ ($\sim$ 0.08 %), where 0.47 is the change in the x axis ($A44$ amplitude). Then, Eqn 2.1 gives $\Delta y = 0.011^o$ in the MSE frame and for the edge channel, the error in the pitch angle
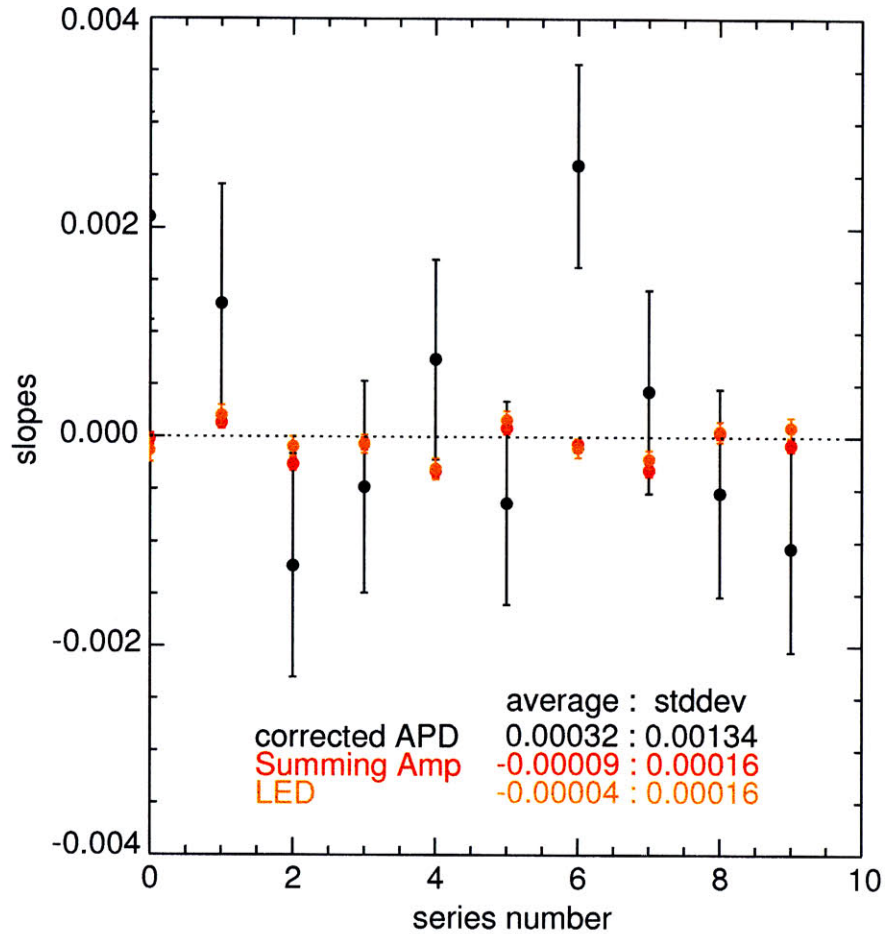
Figure 2-3: Linear slopes and their 1 sigmas from the linear fit of A40/A44 vs A44 measured from the APD (black), the summing amplifier (red), and the resistor (orange) for all 10 series of measurements. The result in Fig 2-2 corresponds to the series 3 in this plot. The average and its standard deviation are also given.

is $0.011^o \times 3 = \mathbf{0.033^o}$. Also, note that the average slope of 0.00032 is smaller than its standard deviation 0.00134 by a factor fo 4, indicating the slope is effectively zero within experimental uncertainty.

Observation of improved quantum efficiency based on the photon statistics

The MSE raw signal, which is in the form of voltage read by a digitizer, can be expressed as

$$S = N \times Q \times \langle G \rangle, \tag{2.2}$$

60

where

- N is the number of photons that hit detector in one time interval, typically 1 μsec. During a plasma shot, N varies with time and with channel number,

- Q is the quantum efficiency of the detector. It can vary with detector type (PMT vs APD); and

- $\langle G \rangle$ is the *mean* internal gain of the detector. There is a finite distribution in the internal gain arising the statistical nature of the avalanche process. This varies with HV applied to the detector.

The variance of S over a chosen time period can be expressed

$$
\begin{aligned}
\sigma_S^2 &= \langle G \rangle^2 \sigma_{NQ}^2 + (NQ)^2 \sigma_{\langle G \rangle}^2 \\
&= \langle G \rangle^2 NQ + NQ\sigma_G^2 \\
&= NQ(\langle G \rangle^2 + \sigma_G^2) = NQ\langle G^2 \rangle
\end{aligned}
\tag{2.3}
$$

where σ_{NQ}^2 is the variance in the number of *counted* photons and $\sigma_{\langle G \rangle}^2$ is the variance in $\langle G \rangle$ and Poission statistics is assumed in $\sigma_{NQ}^2 = NQ$. Using the definition of the excess noise factor $F \equiv \langle G^2 \rangle / \langle G \rangle^2$ [50, 51, 52, 53, 54], Eqn 2.3 can be written as

$$
\sigma_S^2 = NQ\langle G \rangle^2 F
\tag{2.4}
$$

The final expression in Eqn 2.4 comes from the assumption that the MSE signals are dominated by photon statistics, an assumption that needs to be verified. Combining Eqns 2.2 and 2.4 gives

$$
\frac{\sigma_S}{\sqrt{S}} = \frac{\langle G \rangle \sqrt{NQF}}{\sqrt{NQ\langle G \rangle}} = \sqrt{\langle G \rangle F}.
\tag{2.5}
$$

It is noted that this quantity is independent of N and Q. Fig 2-4 (a) shows the measured standard deviation in signal intensity, normalized to square-root of signal intensity, i.e., the LHS of Eqn 2.5 from a shot where the signals from MSE channel 0 are measured with the APD and the signals from the rest of the channels by the PMT.

To compensate for zero offset of digitizer and dark current, the signals with no plasma (first 0.1 msec of shot) are subtracted from the measured signals. As shown in the figure, this quantity, as expected from Eqn 2.5, is nearly an invariant for each channel even though the actual intensity varies considerably during the shot and among the various MSE channels as shown in Fig 2-4 (b).

Another combination of Eqns 2.2 and 2.4 is

$$\frac{S}{\sigma_S} = \frac{NQ\langle G \rangle}{\sqrt{NQF}\langle G \rangle} = \sqrt{\frac{NQ}{F}}, \tag{2.6}$$

which enables one to compare the quantum efficiencies (divided by the excess noise facotr which is in order of unity) among detectors, assuming N, the number of photons incident upon each MSE detector, is a weak function of channel number. So if one observes large differences in this quantity between two adjacent channels, it can be inferred that this is caused by differences in the quantum efficiency. Fig 2-5 (a) plots the quantity $(S/\sigma_S)^2 = NQ/F$ for each channel and shows this quantity is $10 \sim 30$ times larger in Channel 0 which uses the APD detector. Fig 2-5 (b) shows the shot-averaged NQ/F as a function of channel number, implying that the quantum efficiency of the APD detector is an order of magnitude higher than that of the PMTs. This result is also consistent with what is given in Table 2.1.

2.1.2 Possible Faraday rotation in MSE lenses

The plane-of-vibration of linear light incident on a material medium rotates when a strong magnetic field is applied in the propagation direction. The amount of rotation, β, in degree is given by the empiricaly determined expression $\beta = VBd$ where B is the static magnetic field and d is the length of medium. Both quantities are along the direction of the light propagation. V is a factor of proportionality known as the Verdet constant. As mentioned briefly in Sec 1.3, all the transmissive media in the MSE system except the PEM windows are made of SFL6 with a very low Verdet constant of < 0.05 radian/mT ($2.86\ ^o$/mT). For example, the radial magnetic field generated by two equilibrium field coils with EF3 = 5 kA and EF4 = 6 kA in
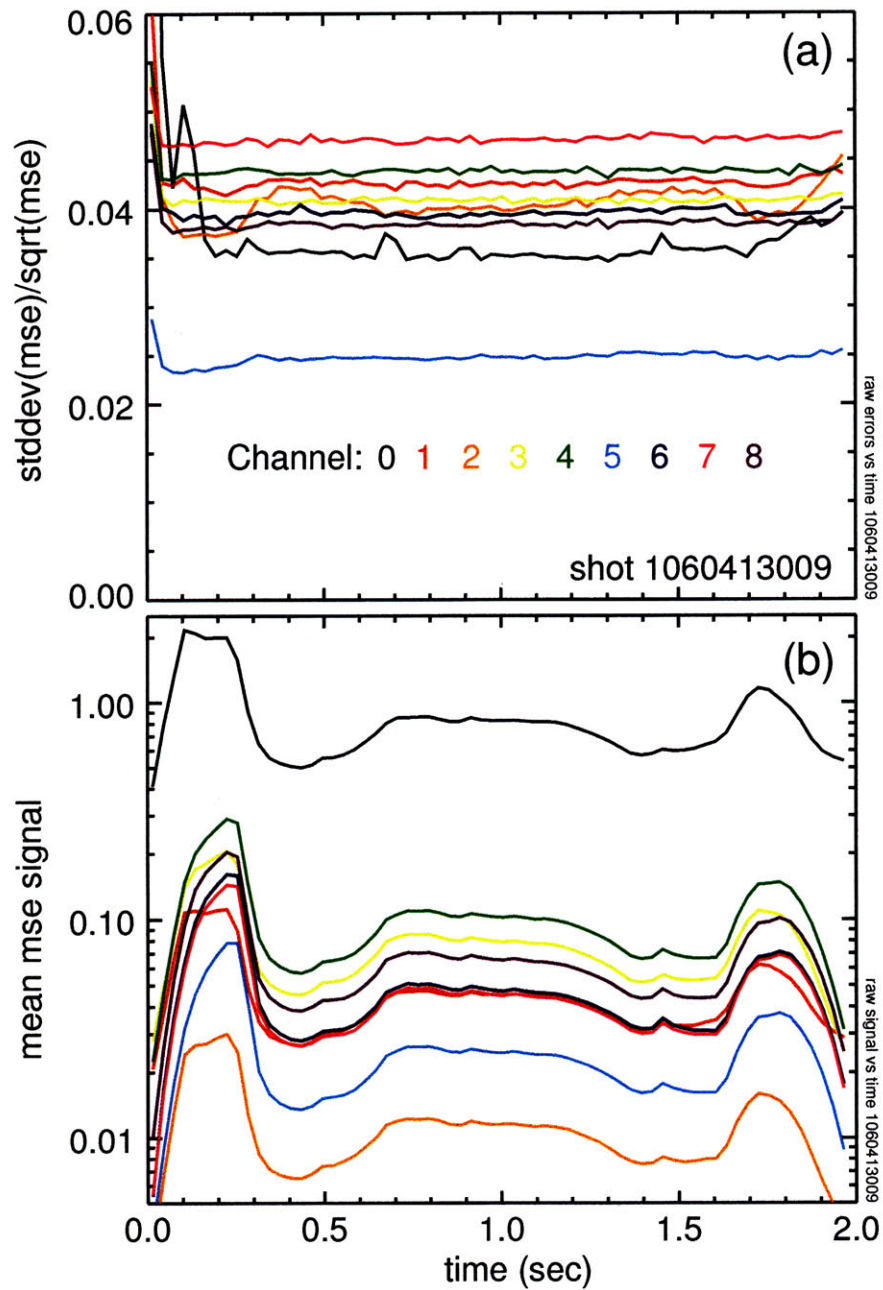
Figure 2-4: (a) The measured standard deviation in signal intensity, normalized to square-root of signal intensity ($\sigma_S/\sqrt{S}$), and (b) the measured intensity. Channel 0 signal is from APD and the rest of the channels from PMT. Binning time is 30 msec and PEM is off for this shot.
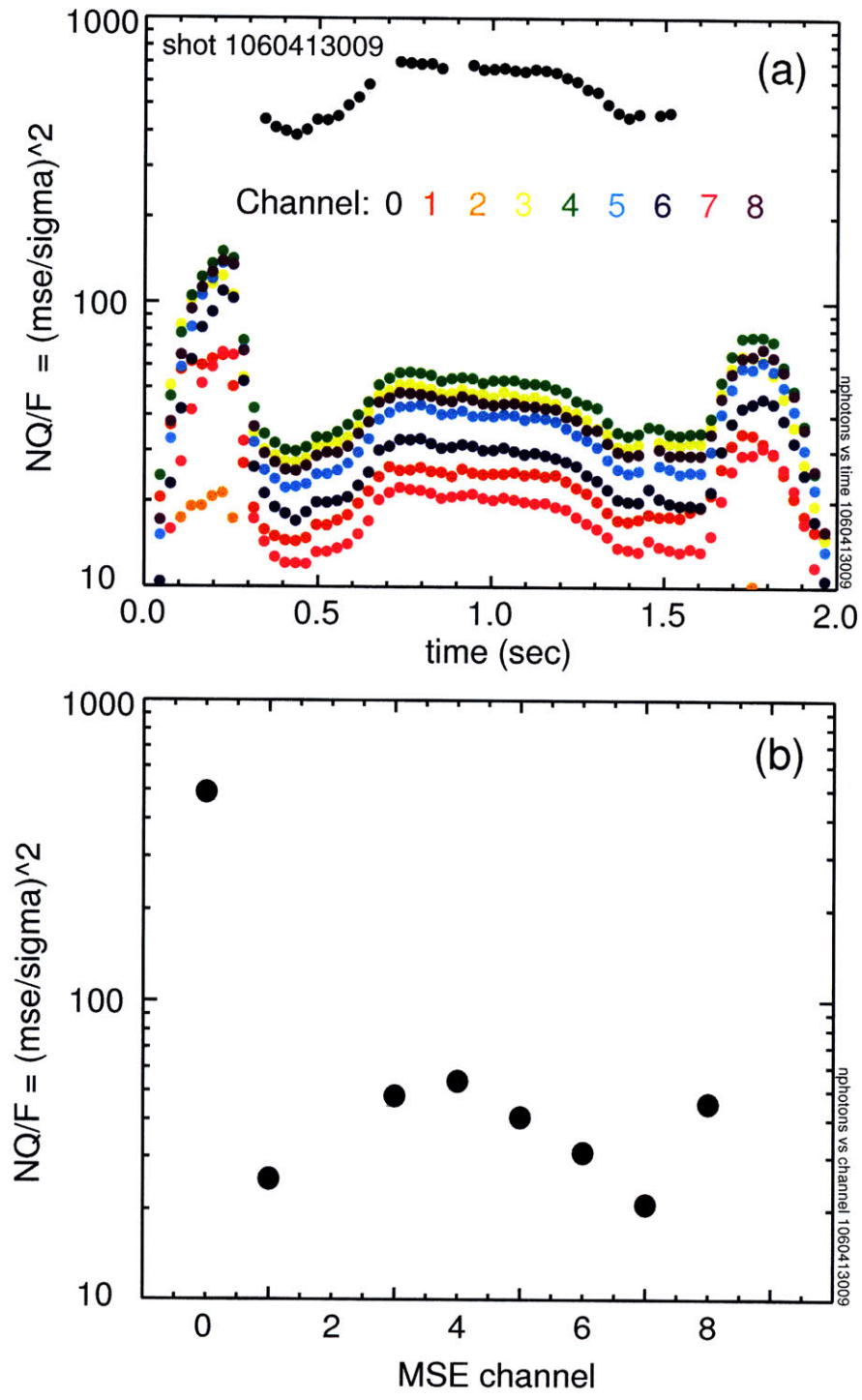
Figure 2-5: (a) Square of the measured intensity normalized by its standard deviation (S^2/σ_S^2) which corresponds to the quantity NQ/F, and (b) the same quantity (shot-averaged) as a function of MSE channel number. Channel 0 signal is from APD and the rest of the channels from PTM. Binning time is 30 msec and PEM is off for this shot.

a typical beam-into-gas calibration (1030521009) is estimated about 0.27 T at the major radius of 1.39 m where the vacuum window is located. The Faraday rotation by this field through the vacuum window (thickness = 9.5 mm)) is 0.007 $^{\circ}$. If the vacuum window were made of normal BK7 glass material whose Verdet constant is about 220 $^{\circ}$/mT, the resultant Faraday rotation would be 0.56° which cannot be negligible. Table 2.2 summarizes the estimates of the typical Faraday rotation for major optics components in MSE. According to Table 2.2, the accumulated Faraday

Element	Material	Thickness mm	Dominant field	Field T	β_{SFL6}	β_{BK7}
L1	SFL6	5.0	B_t	5.4	0.077	5.94
L2D	SFL6	2 $\times$ 13	B_z	0.5	0.037	2.86
L3D	SFL6	2 $\times$ 15	B_r	0.3	0.026	1.98
VW	SFL6	9.5	B_r	0.3	0.008	0.63
PEM	BK7	2 $\times$ 10	B_r	0.03		0.13

Table 2.2: Expected Faraday rotation (β_{SFL6} and β_{BK7}) of major MSE optics components. B_r is from 1030521009 beam-into-gas shot with EF3 = 5 kA at the location of the element. β_{SFL6} is the Faraday rotation for SFL6 material and β_{BK7} is the Faraday rotation *if* the material of the element is BK7. The Verdet constants are 2.86 $^{\circ}$/mT for SFL6 and 220 $^{\circ}$/mT for BK7.

rotation seems to be marginally acceptable only if the elements made of SFL6 have a correct Verdet constant. Also, note that these angles are in the MSE frame, so the rotation in the real pitch angle would be 2 $\sim$ 3 times larger, making any possible Faraday rotation worrisome.

Wire grid polarizer

A Wire Grid Polarizer in general is constructed of a thin layer of aluminum wires on a glass substrate and has its application that requires extremely high durability, contrast and a wide field of view from visible through IR including the telecom wavelengths. In particular, the WGP offers the performance quality of dichroic sheet polarizers without the problems of thermal meltdown commonly associated with sheet-type polarizers. A VersaLight WGP from Meadowlark Optics with an extinction ratio of 99.8% at around 650 nm has been installed onto the cylindrical shutter mechanism
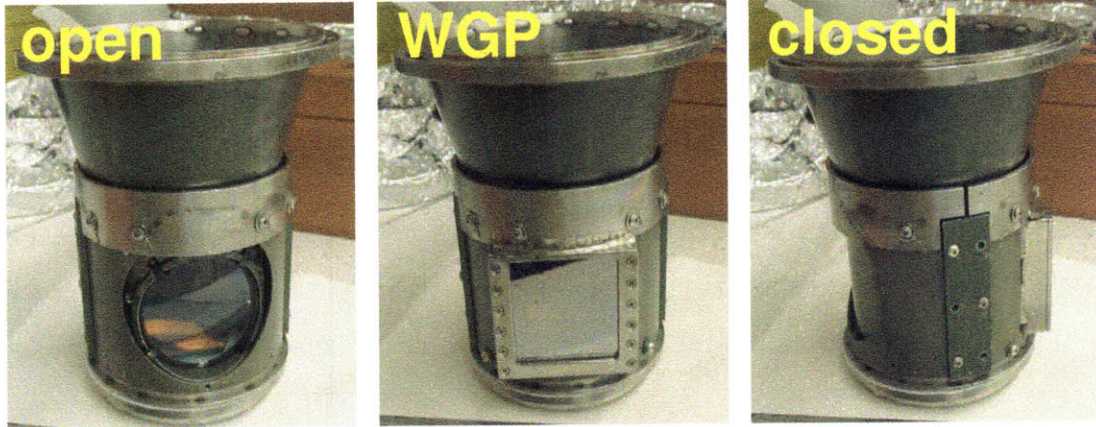
Figure 2-6: Three possible rotational positions of the upgraded MSE shutter. The WGP allows the MSE system to respond to non-motional-Stark-effect-induced polarized light. The shutter is controlled by the push-pull mechanism.

that protects the object lens in the vessel. The main purpose of the WGP is to measure the effects of Faraday rotation in the lenses and birefringence in the vacuum window. The shutter now has three configurations: open, closed, and WGP, which are shown in Fig 2-6.

A care should be taken when it is installed in the vessel. During the Faraday rotation test, the polarized light is generated as the light from the plasma passes the wire side of the WGP. If the wire side faces the plasma light source and then the generated polarized light passes through the glass substrate, it experiences the Faraday rotation though the glass substrate (normally, fused silica; Verdet constant ~ 4 rad/mT) which would make hard the Faraday rotation measurement on the real MSE optics. Figuring out which side is which for a WGP is rather fun and simple. Since the grid reflects the rejected polarization state, it looks like a front surface mirror all the way to the edge of the polarizer. Therefore, if one is unable to see the edges of the glass inside the substrate, she/he is facing the wire side, vise versa.

Polarization angle for arbitrary angles of incidence

Since the angle of incidence of light from individual MSE channels is not perpendicular to the WGP, the expected polarization angle through the polarizer with an arbitrary

angle of incidence has been studied. Indeed, the effect on oblique incidence at WGPs has been an area of intensive studies for decades [55, 56, 57, 58, 59], some also including the effect of anti-reflection coatings on the WGP [60] and finite conductivity of the wires [61]. The relation between the transmitted and incident electric fields vectors, E_t and E_i, respectively, can be expressed as

$$E_t = M_c^{-1} \cdot M_p^{-1} \cdot M_{ta} \cdot M_p \cdot M_c \cdot E_i, \qquad (2.7)$$

where M_c is a matrix that transforms the lab frame (x, y, z) into the polarizer frame (y', z'), M_p is a transform matrix from the polarizer frame to a frame composed of the transmission and extinction axes (effectively, a rotational transform matrix by angle θ, the transmission axis of the polarizer with respect to horizontal), i.e.,

$$M_p = \begin{bmatrix} \cos\theta & \sin\theta \\ -\sin\theta & \cos\theta \end{bmatrix}. \qquad (2.8)$$

M_{ta} is a 'matrix' that selects the field component parallel to the transmission axis only and if the coordinate system is rotated such that the transmission axis is aligned to vertical in the polarizer frame after the matrix M_p, M_{ta} would simply be

$$M_{ta} = \begin{bmatrix} 1 & 0 \\ 0 & 0 \end{bmatrix}. \qquad (2.9)$$

A 3D vector analysis in a spherical coordinate system which is similar to one given in App A.1 can be used to derive the matrix M_c. From Fig 2-7 (which is also very similar to Fig A-1 (b)), it is inferred that the unit vectors that represent the horizontal and the vertical directions on the polarizer plane ($\mathbf{e}_{y'}$ and $\mathbf{e}_{z'}$, respectively) are such that

$$\begin{aligned} \mathbf{e}_{y'} = \mathbf{e}_\epsilon &= (\mathbf{e_x} \cdot \mathbf{e}_\epsilon)\mathbf{e_x} + (\mathbf{e_y} \cdot \mathbf{e}_\epsilon)\mathbf{e_y} + (\mathbf{e_z} \cdot \mathbf{e}_\epsilon)\mathbf{e_z} \\ &= -\sin\epsilon\,\mathbf{e_x} + \cos\epsilon\,\mathbf{e_y}, \end{aligned} \qquad (2.10)$$
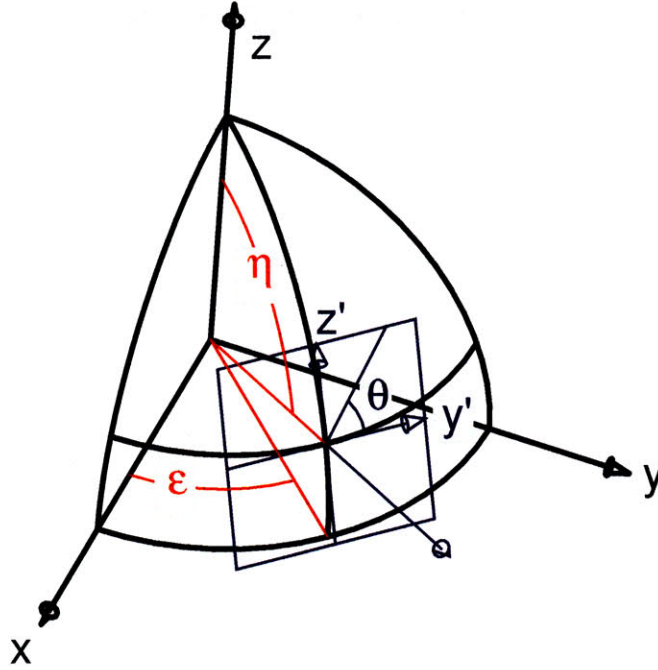
Figure 2-7: The coordinate system. The blue square is the polarizer plane arbitrarily mounted, which has y' and z' as the coordinate system to define θ, the transmission axis. ϵ defines the angle of incidence and η defines the tilting angle. For example, $\eta = 90^o$ when there is no tilting.

$$
\begin{aligned}
\mathbf{e_{z'}} = -\mathbf{e_\eta} &= -(\mathbf{e_x} \cdot \mathbf{e_\eta})\mathbf{e_x} - (\mathbf{e_y} \cdot \mathbf{e_\eta})\mathbf{e_y} - (\mathbf{e_z} \cdot \mathbf{e_\eta})\mathbf{e_z} \\
&= -\cos\eta\cos\epsilon\,\mathbf{e_x} - \cos\eta\sin\epsilon\,\mathbf{e_y} + \sin\eta\,\mathbf{e_z},
\end{aligned}
\tag{2.11}
$$

where $\mathbf{e_x}$, $\mathbf{e_y}$, and $\mathbf{e_z}$ are the unit vectors in x, y, and z directions, respectively, and ϵ and η are the azimuthal and zenithal angles, respectively, in the lab spherical coordinate system. In addition, the unit vector that represents the normal to the polarizer plane, $\mathbf{e_{x'}}$, is simply the radial unit vector in this coordinate system:

$$
\begin{aligned}
\mathbf{e_{x'}} = \mathbf{e_r} &= (\mathbf{e_x} \cdot \mathbf{e_r})\mathbf{e_x} + (\mathbf{e_y} \cdot \mathbf{e_r})\mathbf{e_y} + (\mathbf{e_z} \cdot \mathbf{e_r})\mathbf{e_z} \\
&= \sin\eta\cos\epsilon\,\mathbf{e_x} + \sin\eta\sin\epsilon\,\mathbf{e_y} + \cos\eta\,\mathbf{e_z},
\end{aligned}
\tag{2.12}
$$

Since the dot products between the unit vectors $(\mathbf{e_{x'}}, \mathbf{e_{y'}}, \mathbf{e_{z'}})$ and the incident electric field vector in the lab frame (E_{xi}, E_{yi}, E_{zi}) give the field components along the x', y',

and z' directions, we can construct the matrix M_c such that

$$M_c \cdot E_i = \begin{bmatrix} \sin\eta\cos\epsilon & \sin\eta\sin\epsilon & \cos\eta \\ -\sin\epsilon & \cos\epsilon & 0 \\ -\cos\eta\cos\epsilon & -\cos\eta\sin\epsilon & \sin\eta \end{bmatrix} \begin{bmatrix} E_{xi} \\ E_{yi} \\ E_{zi} \end{bmatrix}. \tag{2.13}$$

Furthermore, if we fix the light propagation direction as the x direction, which is equivalent to have $E_{xi} = 0$, we can greatly simplify the above 3×3 matrix to a 2×2 matrix. Therefore, we can rewrite equation (2.13) as

$$M_c \cdot E_i = \begin{bmatrix} \cos\epsilon & 0 \\ -\cos\eta\sin\epsilon & \sin\eta \end{bmatrix} \begin{bmatrix} E_{yi} \\ E_{zi} \end{bmatrix}. \tag{2.14}$$

Using Eqn 2.14 for M_c and Eqns 2.8 and 2.9 for M_p and $M_t a$, respectively, evaluates Eqn (2.7) as

$$\begin{aligned} E_{yt} &= \cos\theta \left[E_{yi}\cos\theta + \sin\theta(E_{zi}\sec\epsilon\sin\eta - E_{yi}\cos\eta\tan\epsilon) \right], \\ E_{zt} &= E_{yi}\cos^2\theta\cot\eta\sin\epsilon + (E_{zi} - E_{yi}\cot\eta\sin\epsilon)\sin^2\theta \\ &\quad + \cos\theta\sin\theta \left[E_{yi}\cos\epsilon\csc\eta + \cos\eta(E_{zi} - E_{yi}\cot\eta\sin\epsilon)\tan\epsilon \right], \tag{2.15} \end{aligned}$$

where E_{yt} and E_{zt} are the electric field components for the transmitted polarized light. Finally, the polarization angle for the transmitted light is

$$\tan\theta_p = \frac{E_{zt}}{E_{yt}} = \cot\eta\sin\epsilon + \cos\epsilon\csc\eta\tan\theta. \tag{2.16}$$

Note that the final polarization angle θ_p is independent of the polarization state of the incident light, which should be so.

An alternative, but more rigorous, way to derive this result involves a derivation of M_{ta} in a 3×3 form. Let $\mathbf{k'}$ and $\mathbf{E'}$ represent the k-vector and electric-field vector of the incident light expressed in the rotated coordinate system (x', y', z'). Recall that

in the lab frame, the incident light is $\mathbf{E_i} = [0, E_{yi}, E_{zi}]$ and $\mathbf{k} = [k_{xi}, 0, 0]$. Then,

$$
\begin{bmatrix} k_{x'} \\ k_{y'} \\ k_{z'} \end{bmatrix} = M_p \cdot M_c \cdot \begin{bmatrix} k_{xi} \\ 0 \\ 0 \end{bmatrix}, \tag{2.17}
$$

$$
\begin{bmatrix} E_{x'} \\ E_{y'} \\ E_{z'} \end{bmatrix} = M_p \cdot M_c \cdot \begin{bmatrix} 0 \\ E_{yi} \\ E_{zi} \end{bmatrix}.
$$

It is straightforward to perform the matrix multiplications in Eqn 2.18 to verify that $\mathbf{k'} \cdot \mathbf{E'} = 0$, insuring that the electric field vector must always be exactly perpendicular to the direction of propagation). The heart of this alternative derivation involves the proper treatment of the matrix M_{ta}, which imposes the effect of the linear polarizer. Effectively, the polarizer eliminates light intensity along its extinction axis (which in this analysis lies in the z' direction) and an ideal polarizer has no effect on light intensity along its transmission axis (which in this analysis lies in the y' direction). However, it is not so obvious what effect the polarizer has on the intensity in the x' direction, i.e. in the direction normal to its surface. What is obvious, however, is that the light that emerges from the polarizer must continue to satisfy $\mathbf{k'} \cdot \mathbf{E'} = 0$. Since the polarizer eliminates the electric field in the z' direction, $\mathbf{k'} \cdot \mathbf{E'} = 0$ implies that $E_{x'} = -k_{y'} E_{y'}/k_{x'}$, so M_{ta} can be expressed as a matrix that first forces $E_{z'} = 0$ multiplied by another matrix that forces $E_{x'}$ to have a value that satisfies $\mathbf{k'} \cdot \mathbf{E'} = 0$, which is

$$
M_{ta} = \begin{bmatrix} 0 & -k_{y'}/k_{x'} & 0 \\ 0 & 1 & 0 \\ 0 & 0 & 1 \end{bmatrix} \cdot \begin{bmatrix} 1 & 0 & 0 \\ 0 & 1 & 0 \\ 0 & 0 & 0 \end{bmatrix} \tag{2.18}
$$

$$
= \begin{bmatrix} 0 & -k_{y'}/k_{x'} & 0 \\ 0 & 1 & 0 \\ 0 & 0 & 0 \end{bmatrix}.
$$

$$(2.19)$$

Using this expression for M_{ta} and Eqn 2.13 for M_c (instead of Eqn 2.14) produces

$$\tan \theta_p = \frac{\cos \theta \cos \eta \sin \epsilon + \sin \theta \cos \epsilon}{\cos \theta \sin \eta}, \qquad (2.20)$$

which is identical to Eqn 2.16. Note that in this derivation, the polarizer is assumed to be ideal, i.e., the 100% of extinction ratio. This assumption seems to be valid from the fact that the WGP used in the MSE system has the extinction ratio of 99.8%.

The derived expressions (Eqns 2.16 and 2.20) have been compared with the data from the laboratory test where unpolarized collimated LED light is incident on a WGP positioned with various vertical tilting (η) and horizontal rotation (ϵ) angles. The polarization direction after the WGP is measured by another polarizer using Malus's law [35]. Fig 2-8 shows the measured polarization angles as a function of incident angles (ϵ) for the transmission axis of the WGP oriented with 45° and (b) 135°. The vertical tilting angle ($90^o - \eta$) in both cases is 5.1^o. In order to estimate the vertical tilting effect, the expected polarization direction calculated by Eqn 2.16 with $\eta = 90^o$ ('zero' tilting assumption) is overplotted along with that from the full Eqn 2.16. The measured data show a better agreement with the analytic predictions when the tilting effect is included. This analysis can explain the channel-to-channel variation that is observed with the fixed WGP in front of the L1 and the usage of the WGP for testing the Faraday effect is justified because only *changss* in the polarization angle is of interest in this test.

Faraday rotation tests

A series of laboratory measurements using high field permanent magnets (0.25 T at maximum) confirm most of the invessel lenses are within the specified Verdet constant for SFL6 but some are 2 to 3 times the specified value. In an invessel Faraday rotation measurement using one of the equilibrium field coils (EF4) with $B_{radial} \sim 0.005$ T, the total change in the polarization angle is only 0.01^o with large uncertainty due to
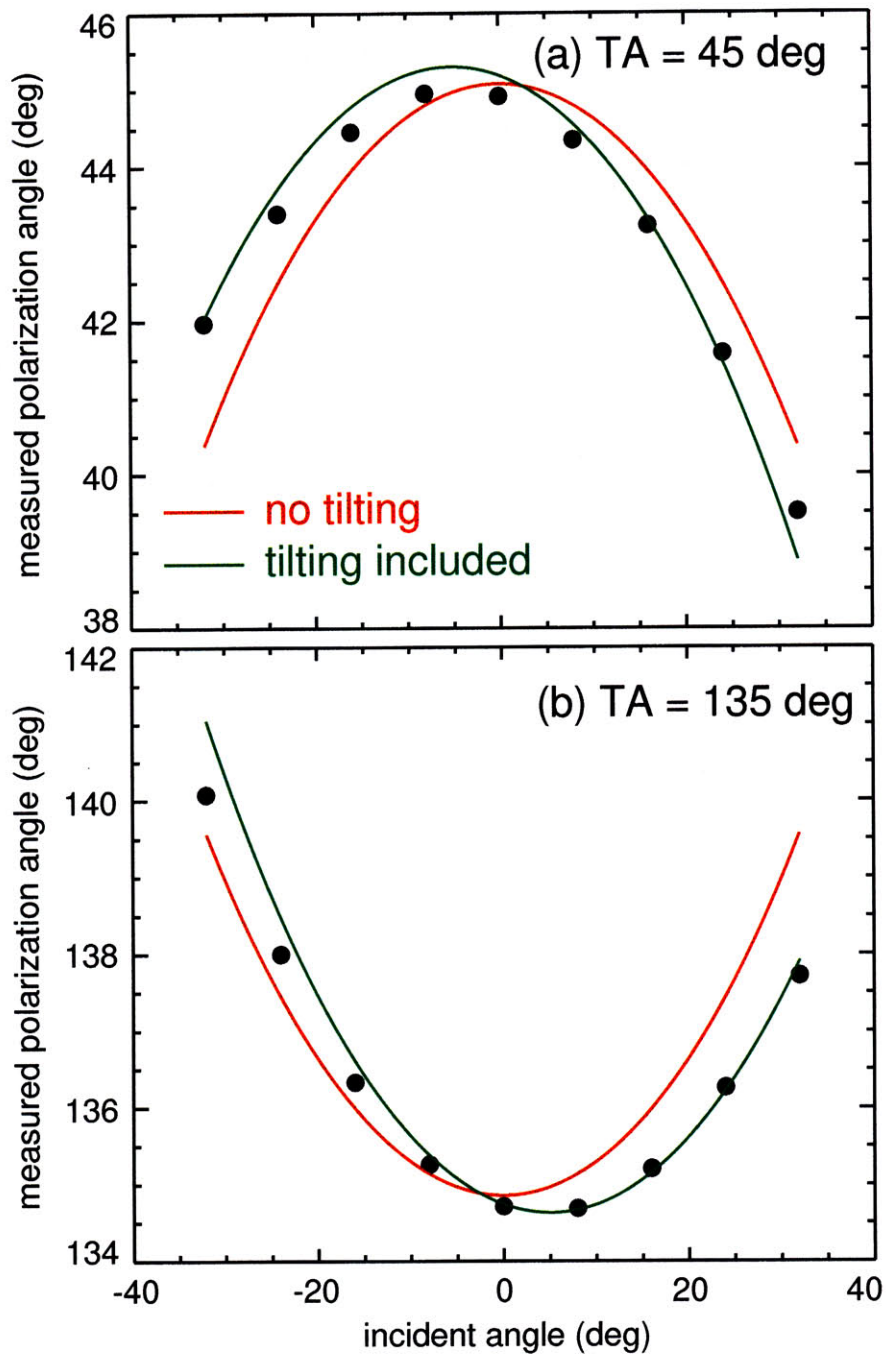
Figure 2-8: The measured polarization angle of the transmitted light as a function of angle of incidence (ϵ) with a fixed vertical tilting angle ($\eta = 5.1°$) for the reference transmission axes of (a) $45°$ and (b) $135°$. The data are compared with Eqn 2.16 without (red) and with (green) tilting effect into consideration.

the weak magnetic field [62].

With the newly installed WGP, the more straightforward and exact tests have been possible, where plasmas are used as light source and the polarized light is generated by the WGP positioned in front of the MSE object lens. This of course dispenses with the DNB. Fig 2-9 shows the waveforms of the plasma current (I_p), toroidal field (B_T), and density (nl_{04}) for the test. To eliminate possible shot-to-shot changes in the polarization angles due to, for example, small variations of the shutter (WGP) orientation etc., a reasonably wide range of B_T and I_p ramps in a single shot. In addition, the ramping parameters are alternated shot by shot in order to separate the effects from the toroidal and poloidal magnetic fields. Fig 2-10 shows the measured
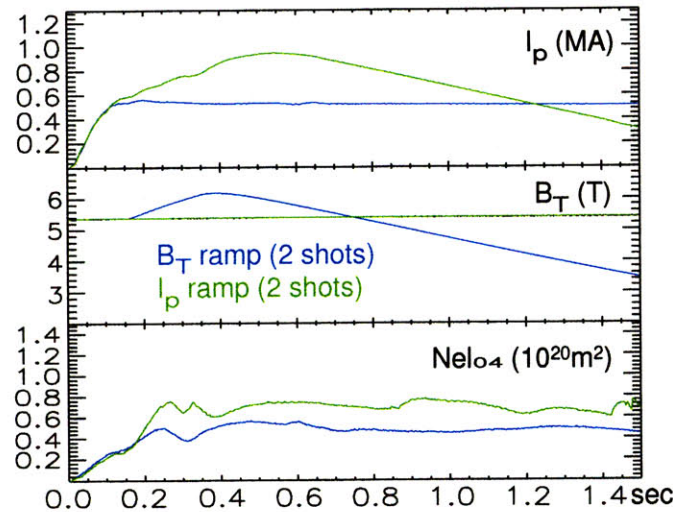
Figure 2-9: The waveforms of I_p, B_T, and nl_{04} for the Faraday rotation test using the invessel WGP. Two I_p-constant and B_T-ramping shots (1051108020, 1051108024) and Two B_T-constant and I_p ramping shots (1051108027, 1051108029) are used.

polarization angle in the MSE frame as a function of (a) B_T (with constant I_p) and (b) I_p (with constant B_T) from the shots shown in Fig 2-9 for two MSE spatial channels (Channels 2 and 7). At a glance, it is hard to find a correlation between the measured polarization angle and either ramping parameter, implying there is no noticeable Faraday rotation. To be quantitative, a linear fit on this data is done and the 1-sigma error in its linear coefficient is calculated for each case. The linear fit coefficients and its error are averaged over all the MSE channels for each ramping case
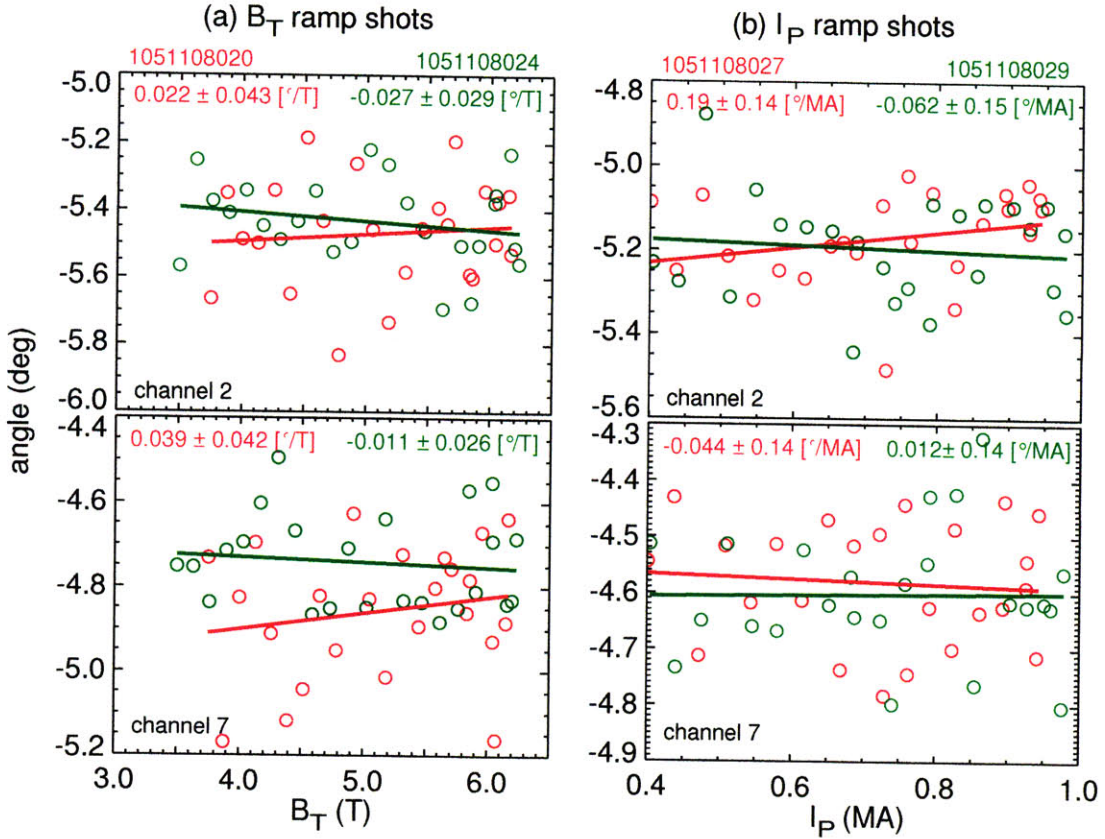
Figure 2-10: The measured polarization angle in the MSE frame as a function of (a) B_T (with constant I_p) and (b) I_p (with constant B_T) from the shots shown in Fig 2-9 for two MSE spatial channels (Channels 2 and 7). A linear fit coefficient and its 1-sigma error is written for each shot.

and the result is shown in Fig 2-11, estimating the channel-averaged Faraday rotation to be $-0.002 \pm 0.021°/B_T$ (in Tesla) and $-0.047 \pm 0.104°/I_P$ (in MA; poloidal field). Both values are less than the measurement uncertainty, implying the correlation with the magnetic fields are not different from zero statistically. From this test, it can be concluded that Faraday rotation in not an important issue for the C-Mod MSE system.

2.1.3 Steep edge filters

During the 2007 campaign, it was found that thermal emission H_α was well correlated with the MSE 'background' signal, implying that H_α light somehow becomes linearly
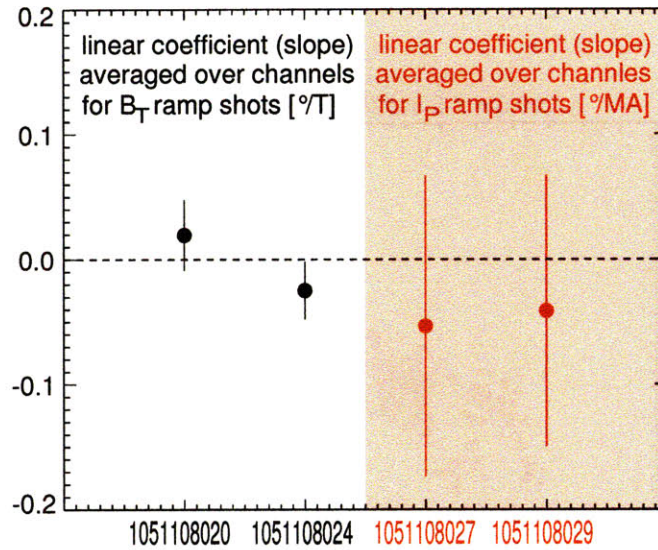
Figure 2-11: The linear fit coefficient with its 1 sigma error averaged over the MSE channels from four shots given in Fig 2-9 and 2-10.

polarized and passes through the MSE narrow bandpass filters, thereby polluting the MSE signal. Some details are discussed here. Based on this observation, 'steep edge' filters that can exclude residual thermal H_α 'wings' near the pass band of the MSE spectrum have been installed in the existing bandpass filter assemblies.

Motivation: MSE background signal *vs* H_α

A database was built for MSE background signals along with several plasma parameters from the 1070516 run where $1 \sim 2.5$ MW ICRF was applied for about 0.7 sec in a shot and where quite a large range of plasma density was available (nl_{04} ranging 0.8 $\sim 1.9 \times 10^{20}$ m^2). The integration time is about 10 msec. This database study reveals that the magnitude of the MSE signals taken without the beam pulse (i.e. background) is well correlated with the H_α signals. Fig 2-12 shows (a) the Z brightness and (b) H_α as a function of the second harmonics amplitudes of the PEM frequencies, A40 and A44 (40 and 44 kHz components, respectively) from the MSE edge channel (Ch0) during the flattop ($I_p \approx 0.8MA$ and $B_T \approx 5.3$ T) phases where the MSE measures the background plasma signals without the beam. The lack of correlation in
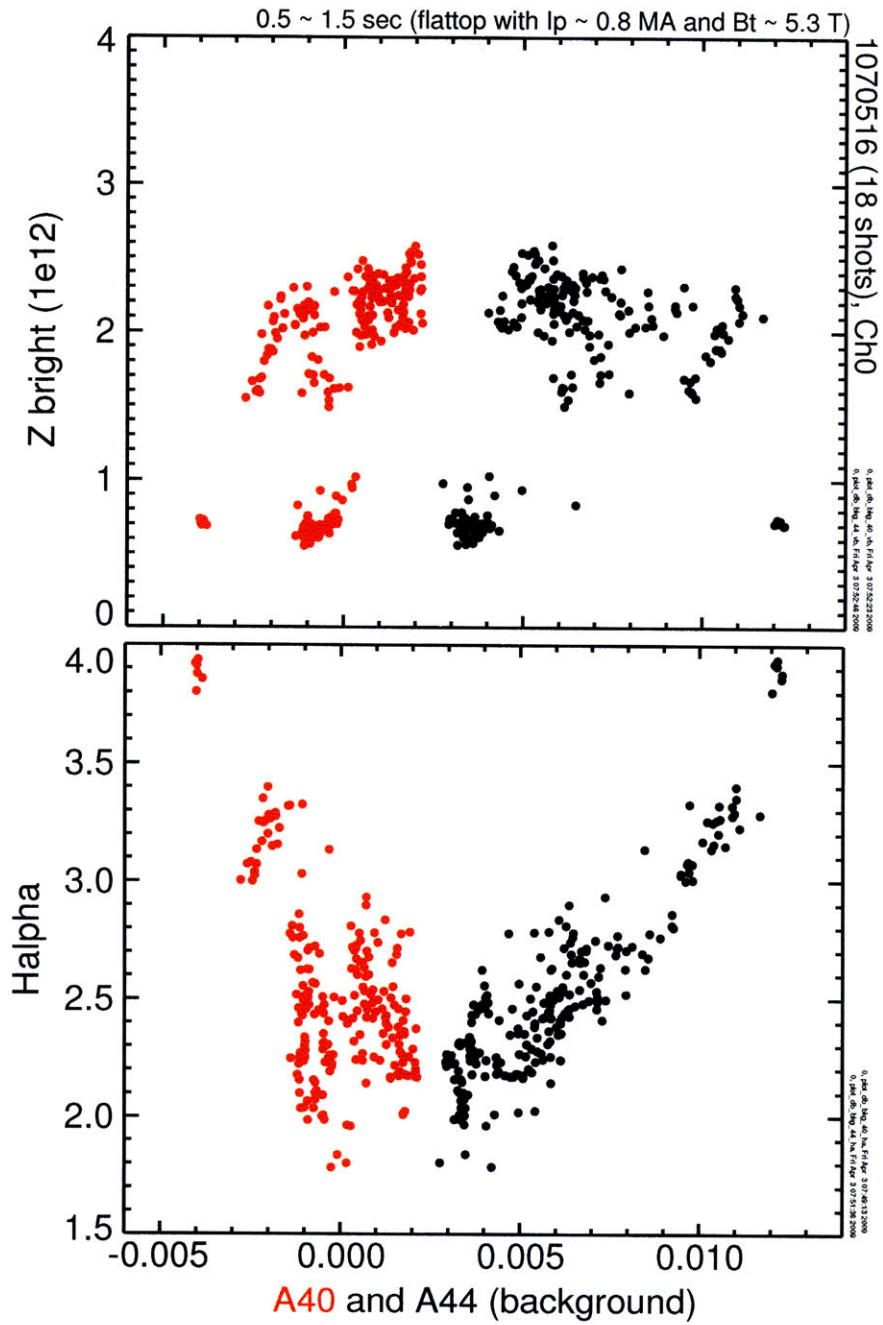
Figure 2-12: 40 and 44 kHz ampltiudes in MSE background signals from Channel 0 (edgemost channel; R = 85.7 cm) versus (a) Z brightness and (b) H_α during the flatop phases.

Fig 2-12 between A40 or A44 and the visible bremsstrahlung intensity suggests that visible Bremsstrahlung light within the MSE pass band is not a major contributor to the MSE background light. Instead, it is clearly indicated that some correlation between the MSE background signals and H_α, the 44 kHz amplitude having slightly stronger correlation with H_α than the 40 kHz amplitude. Recall the expressions for the FFT amplitudes of the second harmonics in the measured intensity (Eqns 1.23 and 1.24), which are rewritten here and scaled as

$$I_{2\omega_1} = A40 = -I_p \frac{\sin(2\gamma)J_2(A_1)}{\sqrt{2}} \sim I_p\gamma \qquad (2.21)$$

$$I_{2\omega_2} = A44 = -I_p \frac{\cos(2\gamma)J_2(A_2)}{\sqrt{2}} \sim I_p \qquad (2.22)$$

when γ, which in this case is the polarization angle of the background light, is small. The measured polarization angles of the background light are indeed small in these shots, ranging $0^o \sim 10^o$. According to the above equations, 40 and 44 kHz do not have the same scaling with I_p, where I_p is the background intensity that is polarized (not a plasma current). In order to avoid any confusion that can arise from this effect, it is more appropriate to deal with the total background intensity, $\sqrt{A_{40}^2 + A_{44}^2}$, rather than $A40$ and $A44$ individually. Fig 2-13 shows this, plotting H_α and visible Bramstrahlung as a function of the total background intensity without losing the general observation on the stronger H_α correlation.

The H_α correlation is further observed during the H-mode transition driven by Lower Hybrid Resonance Frequency (LHRF) heating. Fig 2-14 shows the waveforms of some plasma parameters for Shot 1070523013 where the L-H transition takes place in the middle of the LHRF pulse at about 1.05 sec (red vertical line). This discharge is particularly good opportunity to distinguish the effects of the visible Bremsstrahlung and those of H_α on the MSE background signals since the usual correlations between the visible Bremsstrahlung and the H_α breaks in the H-modes driven by LH heating without Ion Cyclotron Resonance Frequency (ICRF) heating. Shown in Fig 2-15 is the time evolution magnified during the H-mode including the L-H transition in this shot for the Z brightness and H_α along with the total MSE background intensity from
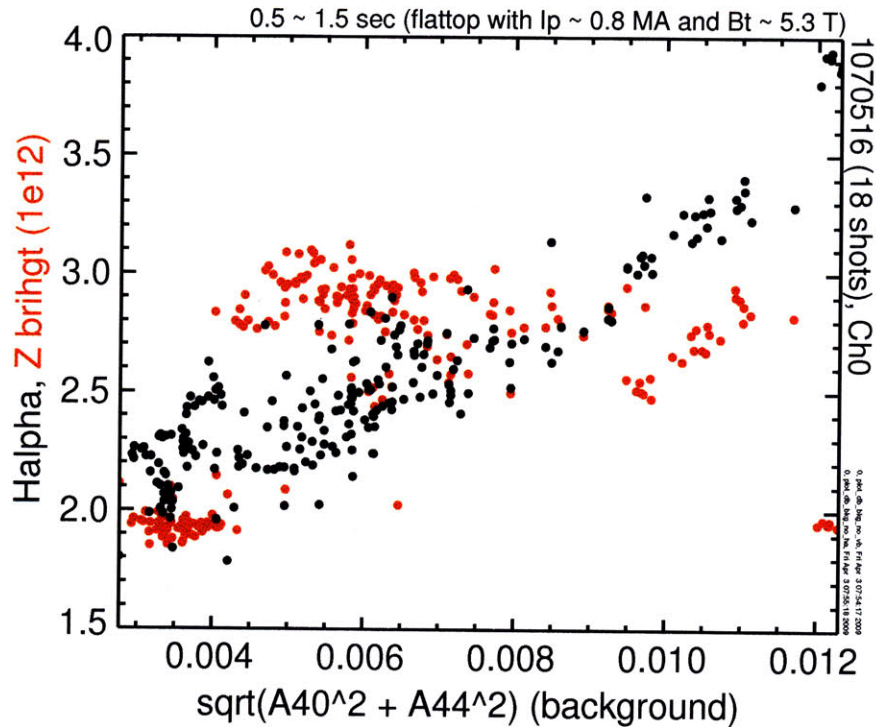
Figure 2-13: Total MSE background signals from Channel 0 (edgemost channel; R = 85.7 cm) versus (a) Z brightness and (b) H_α during the flatop phases.

several MSE channels. All values are normalized at a time near the L-H transition (vertical dashed line). The correlation between the MSE background and H_α through the H-mode is stunning. These strong correlations between H_α and the MSE background signals motivated the installation of the edge filter which would reject the H_α wing that may extend and smear into the MSE pass band.

Installation and results

The steep edge filters have been fabricated by Barr Associates, Inc. with the specifications of rejection > OD2 from 652 ~ 656.9 nm and transmission > 80% from 659.2 ~ 665 nm. This can reduce the unshifted thermal H_α intensity by more than a factor of $10^2 \times 10 = 10^3$ at 656.9 nm where the relative intensity of H_α wing is already less than 0.1 when the ion temperature is about 500 eV. The blocking threshold and the high pass region are chosen to guarantee that the pass bands of the existing bandpass
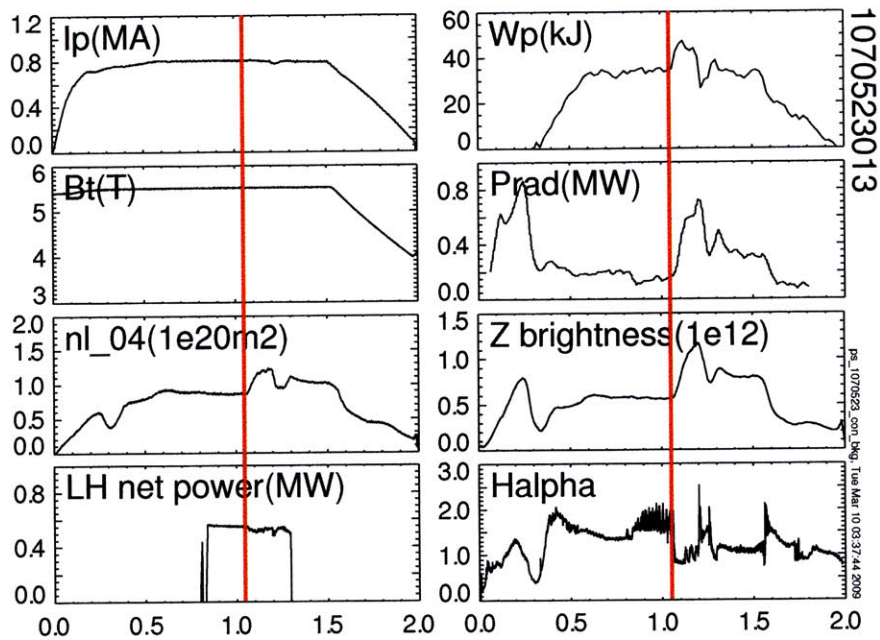
Figure 2-14: The waveforms of some plasma parameters from Shot 1070523013 for the MSE background study. The H-mode is induced by LH heating only (no ICRF). L-H transition is marked with a vertical red line.

filters from all ten MSE spatial channels are under the high pass band of the edge filters.

Another important factor in the edge filter specification is its temperature coefficient. The pass band of the bandpass filter is tuned by the temperature according to the applied toroidal magnetic field since the Stark splitting depends on the toroidal field. Currently, the central wavelength of the bandpass filter is controlled such that it stays at either the $1\sigma + 0.98$ nm or the 3π, whatever is larger. The temperature coefficient of the bandpass filter is 0.017 nm/°C and the range of the temperature is room (23°) to 60°, providing a one-way (red) tunable range of 0.63 nm. The temperature coefficient of the new edge filter is 0.02 nm/°C which would cause 'unwanted' tuning of 0.74 nm in the edge filter when the bandpass filter is tuned. This effect should be taken into account when specifying the high-pass characteristics.

Figs 2-16, 2-17, and 2-18 show the new edge filter functions along with the existing MSE bandpass filter functions in several MSE channels covering the innermost and
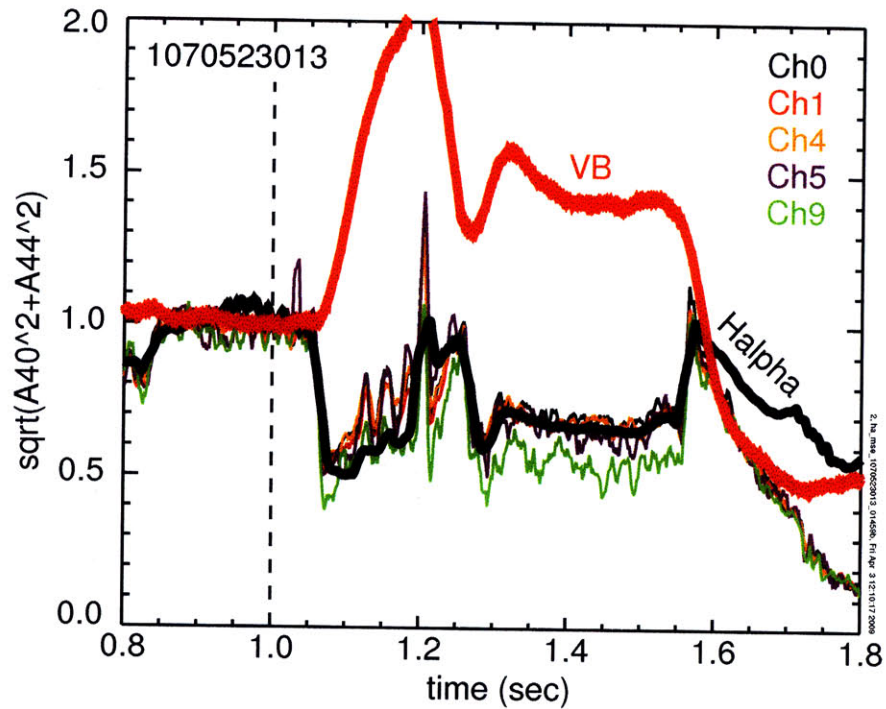
Figure 2-15: Time evolution of the Z brightness and H_α along with the MSE background from several MSE channels during the H-mode from Shot 1070523013 shown in Fig 2-14. The signals are normalized at a time near the L-H transition, which is marked with a vertical dashed line.

edgemost ones, for $B_T = 2.8$, 5.4, and 6.2 T, respectively. Also shown in the figures are the expected Stark lines from Doppler-shifted full, half, and a third beam energy components for a given magnetic filed. The ratio of 0.25:0.50:0.25 is used for the intensity of the three different beam energy components and the relative intensities of the various σ (no-filled bars) and π (filled bars) lines are from Ref [63] (Table 20b, p.277). These plots assure that the OD greater than 2 is achieved at 656.9 nm and pass bands for all MSE channels at various toroidal fields are always in the high pass region of the edge filter. Table 2.3 shows the current allocation of the Barr steep-edge filters on the MSE system. For further reference, the current inventory and allocation of the Andover bandpass filters are given here in Table 2.4.

After installation, the performance of the edge filters was tested. Unfortunately, the measurements indicate the edge filters have absolutely no effect on the magnitude
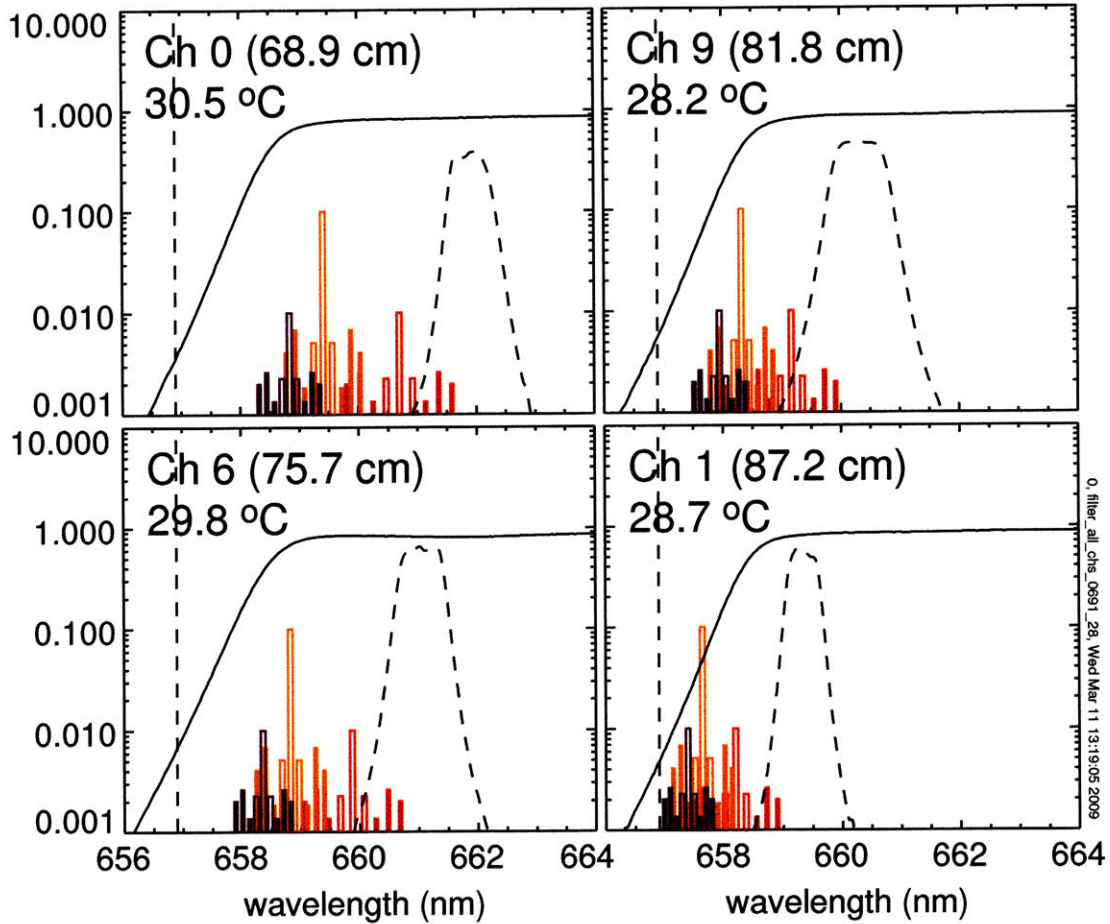
Figure 2-16: Edge (solid) and bandpass (dashed) filter functions in several MSE channels for $B_T = 2.8$ T along with the expected Stark lines (σ in unfilled bar and π in filled bar) from Doppler-shifted full (red), half (orange), and a third (blue) beam energy components. The vertical line is at 656.9 nm where the blocking OD should be greater than 2 according to the spec. The oven temperature of the filter assembly is also given.
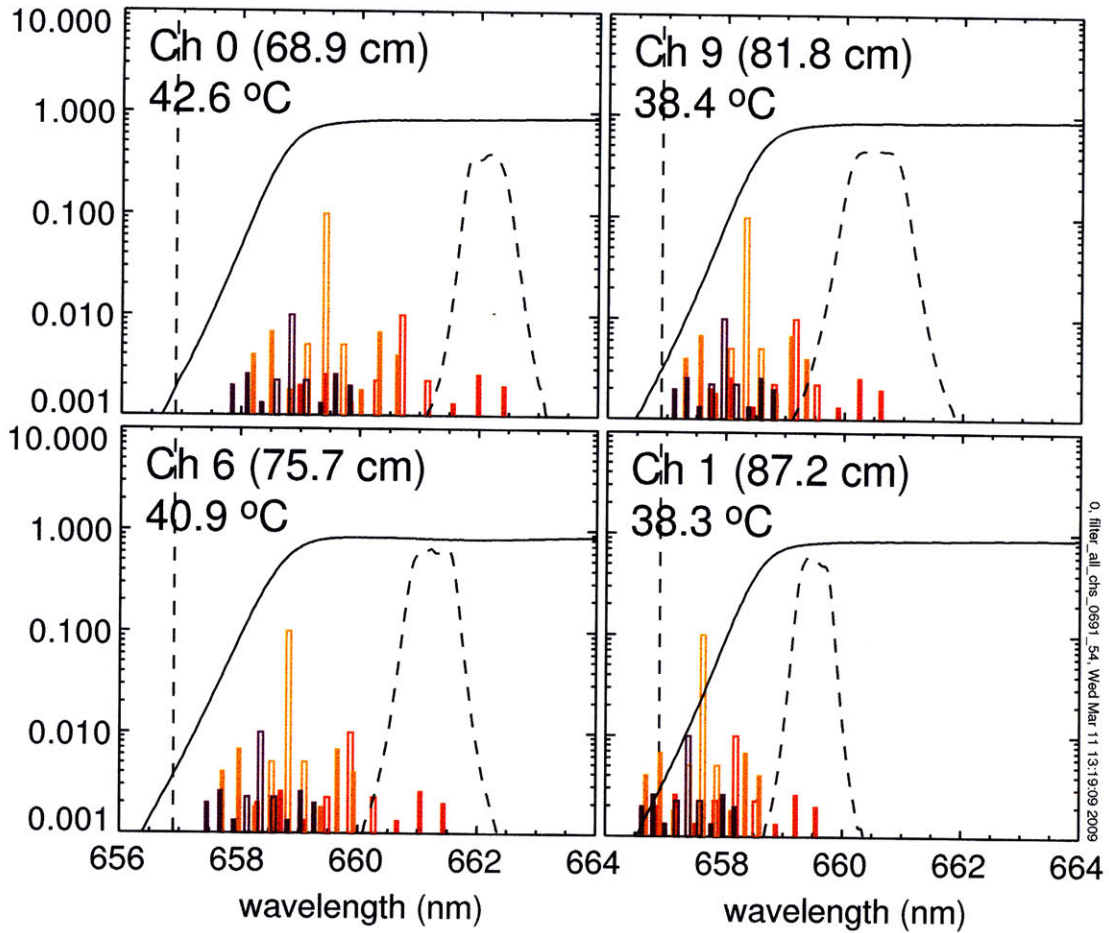
Figure 2-17: Edge (solid) and bandpass (dashed) filter functions in several MSE channels for $B_T = 5.4$ T along with the expected Stark lines (σ in unfilled bar and π in filled bar) from Doppler-shifted full (red), half (orange), and a third (blue) beam energy components. The vertical line is at 656.9 nm where the blocking OD should be greater than 2 according to the spec. The oven temperature of the filter assembly is also given.
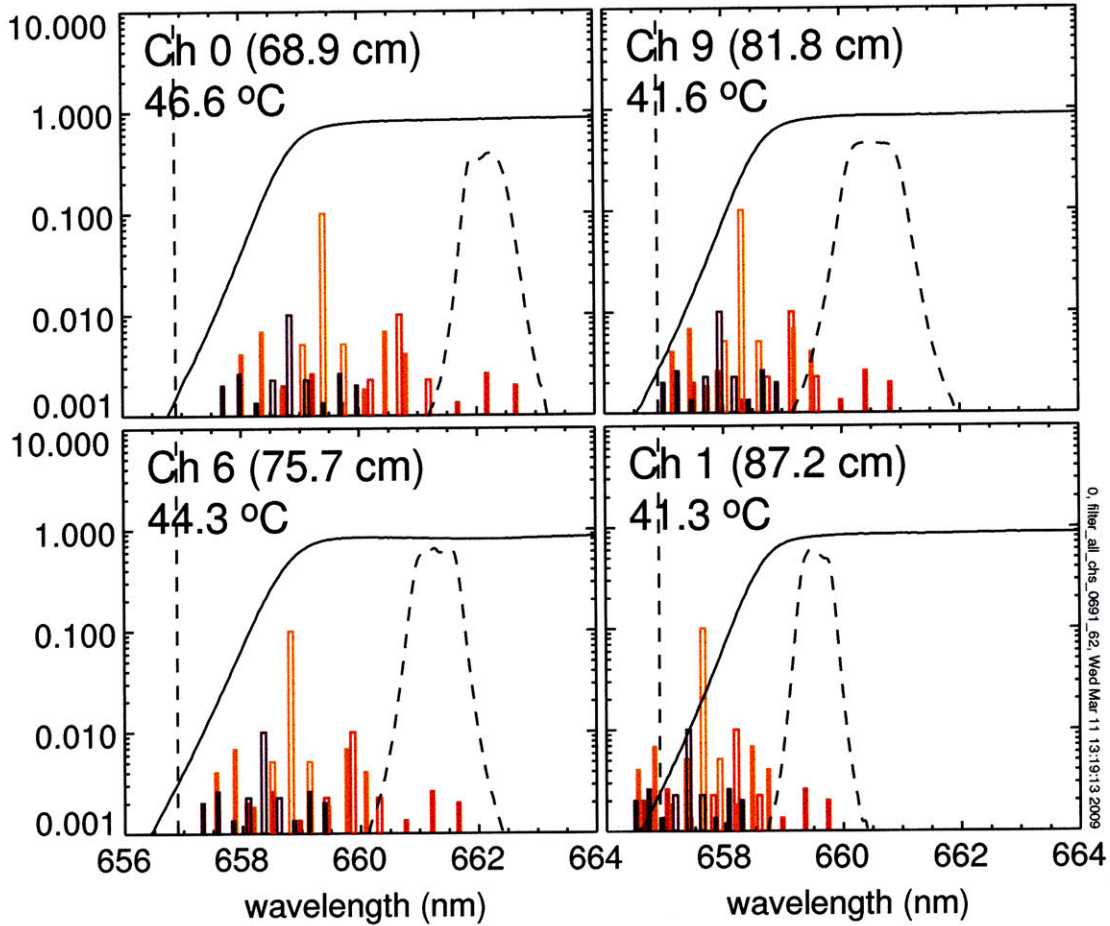
Figure 2-18: Edge (solid) and bandpass (dashed) filter functions in several MSE channels for $B_T = 6.2$ T along with the expected Stark lines (σ in unfilled bar and π in filled bar) from Doppler-shifted full (red), half (orange), and a third (blue) beam energy components. The vertical line is at 656.9 nm where the blocking OD should be greater than 2 according to the spec. The oven temperature of the filter assembly is also given.

LOT #	PC #	RW (nm)	OD @ RW	TW (nm)	T @ TW (%)	MSE Ch
4007	1	656.9	2.0416	659.2	80.53	4
4007	2	656.9	2.0121	659.2	80.88	7
4007	3	656.9	2.0314	659.2	81.58	5
4007	4	656.9	2.0158	659.2	82.10	6
4007	5	656.9	2.0546	659.2	81.64	9
4007	7	656.9	2.1684	659.2	80.32	1
4007	9	656.9	2.1235	659.2	80.35	3
4407	3	656.9	2.1531	659.2	75.66	2
4407	4	656.9	2.2007	659.2	75.93	0
4407	5	656.9	1.6729	659.2	79.31	8

Table 2.3: Steep-edge filter allocation on the MSE system (November 20 2007)

of the MSE noise nor on its correlation with the H_α intensity at L-H transition. Fig 2-19 shows the time evolution of the Z brightness and H_α along with the MSE background intensity from several MSE channels. All signals are normalized at a time during the shot. These plots can be directly compared with Fig 2-15 where the same quantities are plotted for a shot without the steep-edge filters. According to Fig 2-19, there is still a strong correlation between the MSE background and H_α. The magnitude of the MSE background signals has not been reduced with the edge filter either. Fig 2-20 shows the magnitude of the MSE background signal as a function of H_α intensity for two collections of shots before (red triangle) and after (green circle) the edge filter installation.

The tentative conclusion made from these observations is that the background source is not the H_α radiation itself but something that is correlated with the H_α signal. The possible background sources are

- Impurity line radiation from charge exchanges with neutrals,

- D_2 molecular line radiation; or

- H_α itself (assuming the steep-edge filters are not properly working).

In addition, two different mechanisms in terms of the background source locations can be considered:

- local, i.e., the sources are located within the MSE viewing sightlines; or

AM #	ANDV #	CWL (nm)	MSE Ch
16203	6608	660.88	
16203	6609	660.83	
26752	4237	661.40	8
26752	4238	661.77	0
26752	4244	662.36	
31927	5203	660.94	6
31927	5204	660.68	
31927	5205	660.69	5
31927	5208	659.61	2
31927	5211	659.21	1
39816	6604	658.00	
39816	6605	658.35	
39816	6606	658.58	
39816	6607	660.01	
39816	6608	660.25	
39816	6609	662.49	
39816	6610	662.77	
64780	10414	659.87	3
64780	10415	660.25	9
64780	10416	660.39	4
64780	10417	661.29	7

Table 2.4: Bandpass filter inventory and allocation on the MSE system (March 10 2008)

- global, i.e., the sources are outside the MSE viewing sightlines but are reflected onto the RF antennas which are effectively the MSE viewing dumps.

2.1.4 Pivoting DNB: Effect of secondary beam neutrals

As briefly introduced in Sec 1.2, beam-into-gas calibrations were typically performed to investigate the effects that in-vessel calibrations cannot deal with. The pitch angles are 'pre-defined' by the toroidal and the vertical field coils and computed by magnetic measurements using the vacuum field reconstruction code, MFLUX. Typically, the currents on two equilibrium field coils, EF3 and EF4, are scanned, or manipulated, to produce the pitch angle (range) that is desired in experiments. The engineering limits for these two coils typically ranges $0 \sim 12$ kA and $-5 \sim 5$ kA for EF3 and EF4,
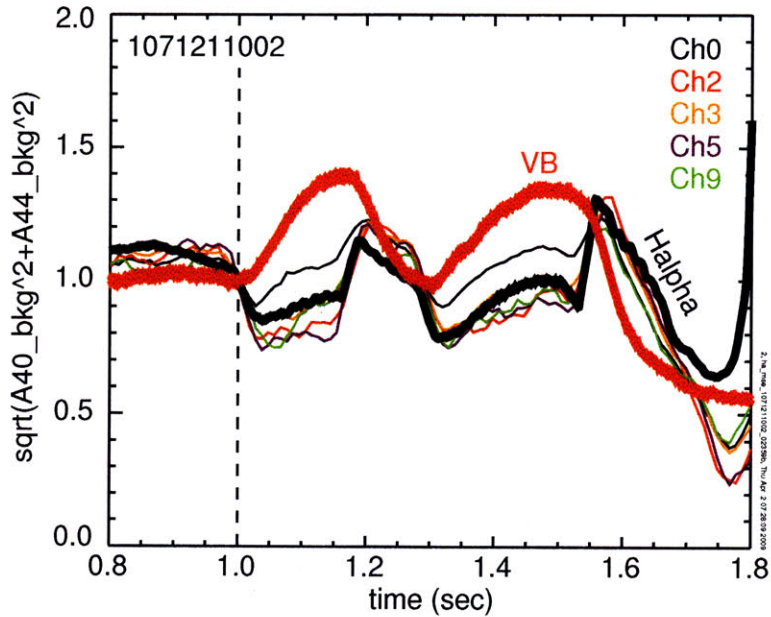
Figure 2-19: The time evolution of the Z brightness and H_α along with the MSE background from several MSE channels from Shot 1071211002 with the new steep-edge filters installed. The signals are normalized at 1 sec (dashed line). This is directly compared with Fig 2-15 which is the case without the steep-edge filters

respectively, making the pitch angle ranges about $-5^o \sim 12^o$ for $B_T = 5.4T$. This range is usually sufficient to cover the range of pitch angles expected in C-Mod plasmas ($0^o \sim 12^o$). The typical waveforms for the experimental conditions are shown in Fig 2-21. Note the high signal-to-noise ratio (100 to 1000) across the channels, which is one of the big advantages of beam-into-gas calibrations.

However, it turns out that conventional beam-into-gas calibrations have serious limitations depending on the background gas pressure and the orientation of the DNB. These limitations manifests themselves in what is shown in Fig 2-22 where the pitch angle measured by MSE is compared with the expected pitch angles for a typical beam-into-gas calibration shot taken before the beam pivoting. Strong anomalies are observed in this figure including: an 'offset' that exists for all channels at zero pitch angle; the slopes of the measured response are greater than unity; and strong channel dependence of theses anomalies, the edge channels being stronger.

A conjecture pertaining to these limitations and the anomalies is following; When
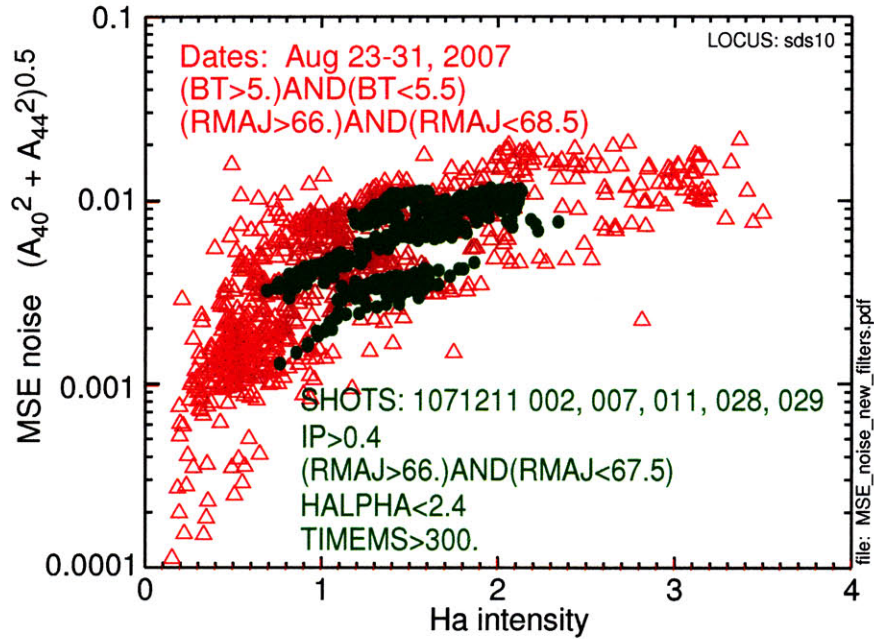
Figure 2-20: The magnitude of MSE noise as a function of H_α for the MSE channels with major radii between about $66 \sim 68$ cm from two groups of shots: before (red triangle) and after (green circle) the edge filter installation.

the beam is fired in a direction purely perpendicular to the magnetic field, the fast beam neutrals that become ionized through collisions with gas in the torus remain in the viewing footprint of the MSE channels for a long period of time, because they have zero velocity along the magnetic field. In this case, their residence time in the MSE viewing volume is limited only by the ∇B drift and it is long enough for these fast ions to experience another charge exchange and become 'secondary' neutrals. For a typical 2 mTorr-H_2 gas calibration case at room temperature, the density of H_2 is about $n_{H_2} = 6.6 \times 10^{19}$ m^{-3}. The charge exchange cross section for a 50 keV proton is $\sigma_{CX} \sim 1.0 \times 10^{-20}$ m^2. These give the mean free path for the charge exchange $\lambda_{CX} = 1/(n_{H_2}\sigma_{CX}) = 1.5$ m. If one compares the velocity of the 50-keV ion, $v_{ion} = 3.1 \times 10^6$ m/s, and the ∇B drift velocity, $v_{\nabla B} = 1.4 \times 10^4$ m/s, it is estimated that the ion moves the distance $v_{ion}/v_{\nabla B} = 221$ cm per vertical drift of 1 cm. This produces an effective mean free path of $\lambda_{CX}/221 = 0.007$ m, which can be compared with the MSE footprint vertical extension 0.035 m. Therefore, essentially
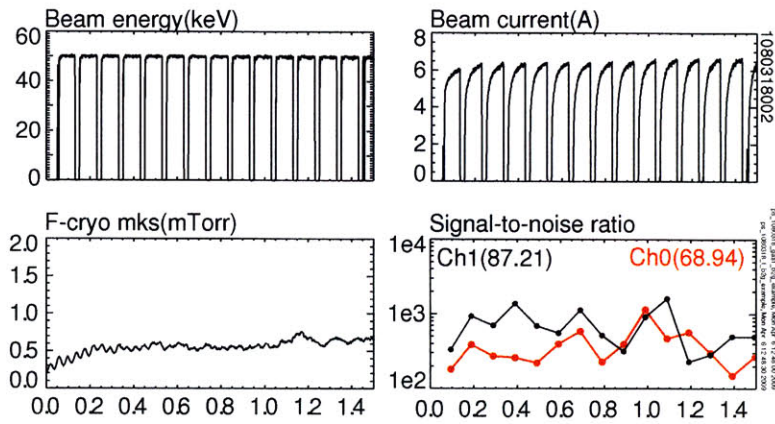
Figure 2-21: Typical beam-into-gas calibration conditions. The torus gas pressure ranges $0.3 \sim 3$ mTorr. Signal-to-noise ratio is shown for the innermost (Ch0) and the outermost (Ch1) channels.
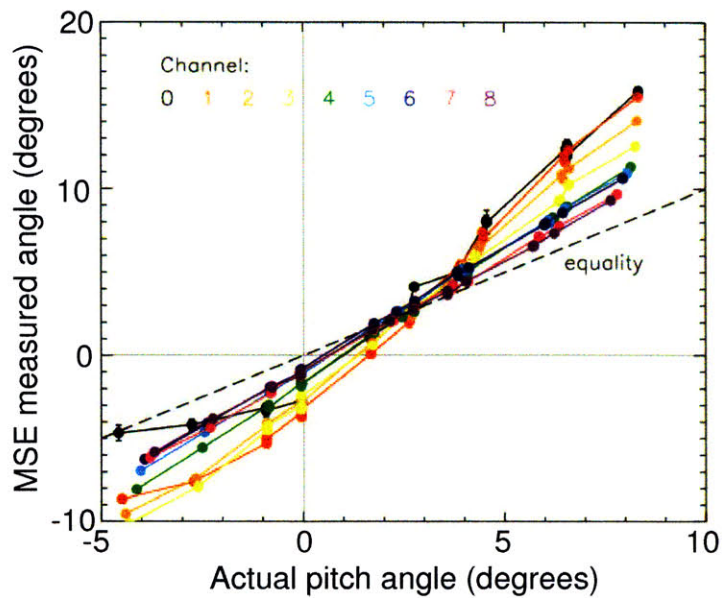
Figure 2-22: Pitch angle measured by MSE vs real pitch angle calculated by MFLUX from a typical beam-into-gas shot prior to the DNB pivoting.

100% of the fast ions experience charge exchange before they leave the MSE viewing area.

Both the primary and secondary beam neutrals become excited into a variety of excited states including the n = 3 state through subsequent collisions with the torus gas, and emit the usual n = 3 → 2 (motional) Stark polarization spectrum. However, since the secondary beam neutrals emit at a random gyrophase, the $E = v \times B$ polarization direction is also random and a fraction of the emission has the proper Doppler shift to pass through the MSE bandpass filters and will contribute to the signals from the primary emission. Therefore, the polarization angle measured by MSE will be influenced by the emission properties of the secondary emission as well as the primary emission, and therefore it will not track perfectly well the pitch angle of the local magnetic field. Based on some experimental and theoretical studies on this argument, which are given in the following subsections, the DNB was rotated by 7° toroidally, which was the maximum angle that could be tilted under the geometric constraints, prior to the FY07 campaign to reduce the population of the secondary.

Effect on pitch angle measurements

A significant improvement has been observed in the pitch angle measurements during beam-into-gas calibrations following pivoting the beam by 7°. Fig 2-23 compares the MSE pitch angle mapping to the real pitch angle from 1050830 (radial DNB) and 1070425 (tilted DNB) beam-into-gas shots for four different MSE channels. The plots show the anomalies mentioned in Fig 2-22 have basically disappeared although there are still small deviations from the equality line in the order of a few degree for certain pitch angles in the tilted-DNB mapping results.

It is also found that these a-few-degree order deviations vary depending on the torus pressure, which can be expected from the nature of the secondary neutral beam effect. Fig 2-24 shows the MSE pitch angle mapping for three different torus pressures from Channel 0, including one shown in Fig 2-23 for the same channel with some magnification in the vertical scale. It is observed from this figure that the deviation also depends on the pitch angle. The pressure effect is significant at negative pitch
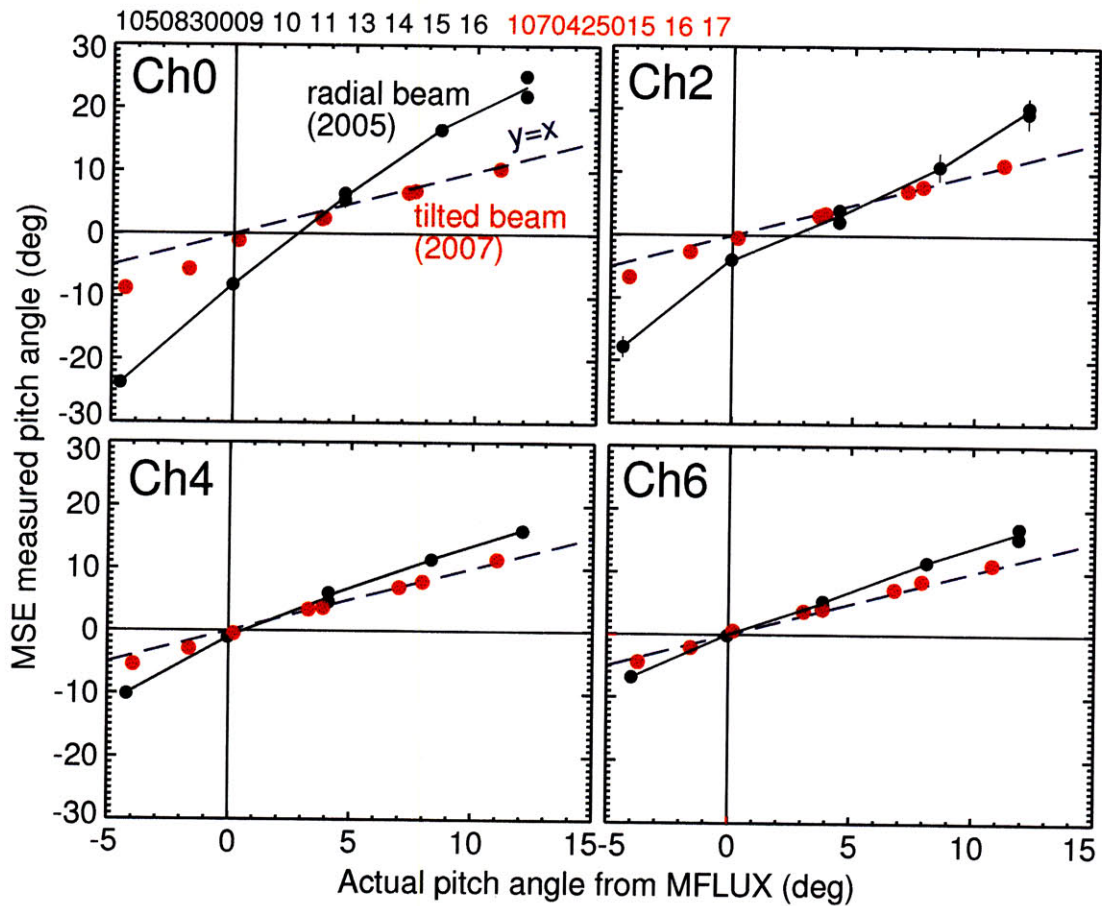
Figure 2-23: Comparison of MSE vs real (MFLUX) pitch angle mappings from 1050830 (with radial DNB) and 1070425 (with 7°-tilted DNB) beam-into-gas calibrations for four MSE channels.
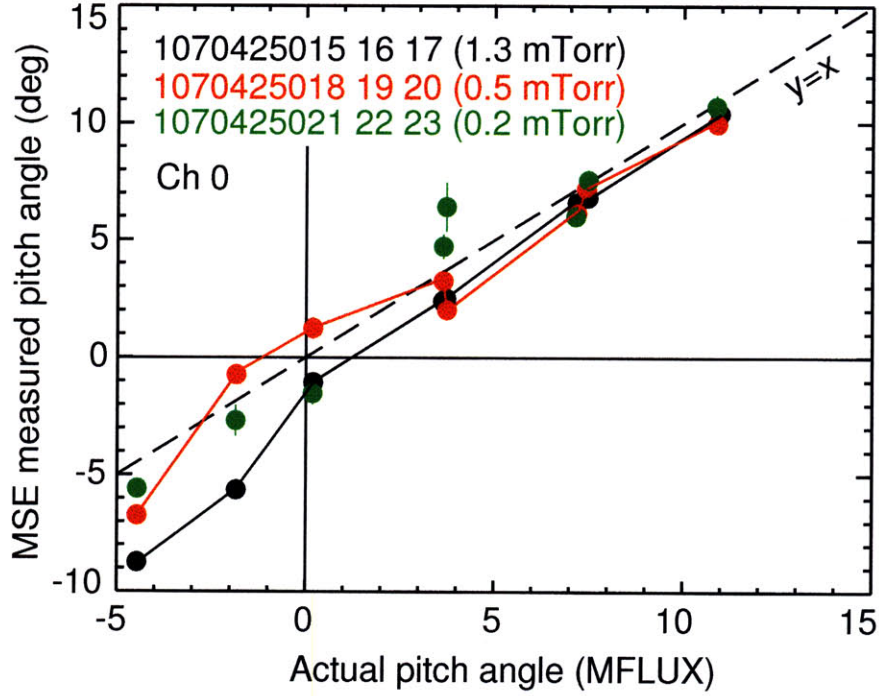
Figure 2-24: Comparison of MSE vs real (MFLUX) pitch angle mappings from 1070425 (with 7°-tilted DNB) beam-into-gas calibrations for three different torus pressures from MSE Channel 0. The results from Shots $1070425015 \sim 17$ (for 1.3 mTorr) are the same shown in Fig 2-23 for the same channel with the tilted beam but with a different vertical scale.

angles and there is little effect at large positive pitch angles.

An analytic expression has been derived for the ratio of secondary-to-primary H_α emission intensity, I_s/I_p, using the 'drift-tube' argument [39] which assumes the dominant process for the loss of beam fast ions is their simple parallel motion along the drift tube in the beam region in estimating their population. This assumption takes advantage of the fact that the mean free paths for all collisional processes are much larger than the length of the drift tube itself, which is of order of the DNB radius (~ 0.06 m). The final expression for I_s/I_p is written as

$$\frac{I_S}{I_p} = n_{He} \left(\frac{\sigma_{CX}(3)\sigma_{ion}(1)}{\sigma_{ex}(13)} \right) \left(\frac{cL_T}{2r_{DNB}} \right) \frac{MIN(L_w, h_{MSE}/\tan\theta_d)}{2\sin\theta_{inj}}, \qquad (2.23)$$

where n_{He} is He gas pressure, $\sigma_{CX}(3)$, $\sigma_{ion}(1)$, and $\sigma_{ex}(13)$ are the cross sections for

charge exchange into n = 3 state, ionization from the ground state, and collisional excitation from n = 1 to n = 3 state, respectively. c is a constant to include the following two comparable effects

$$H^+ + He \quad \rightarrow \quad H^0(3s + 3p + 3d) \tag{2.24}$$
$$H^+ + He \quad \rightarrow \quad H^0(1s) + He \rightarrow H^0(3s + 3p + 3d)$$
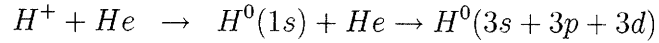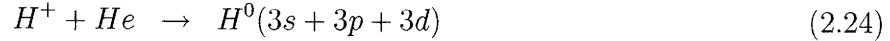
in one formula. L_T is the length of the drift tube of the secondary neutrals, r_{DNB} is the cross sectional beam radius, L_w is the length of the sightline from its beam intersection to the wall, h_{MSE} is the height of the MSE footprint, θ_d is the vertical angle of the drift orbit, and finally, θ_{inj} is the beam injection angle. Note that according to the drift-tube model, I_s/I_p is only a linear function of the gas pressure at fixed geometry. For a typical C-Mod geometry, the term $cL_T/(2r_{DNB})$ is approximately unity. With $L_w \approx 1.7$ m at $R = 0.8$ m, $h_{MSE} = 0.03$ m, and $\theta_d = 5^o$, the term $MIN(L_w, h_{MSE}/\tan\theta_d) \approx h_{MSE}/\tan\theta_d$. Therefore, for the 50 keV beam energy, Eqn 2.23 reduces to

$$\frac{I_s}{I_p} = \frac{0.013P}{\sin\theta_{inj}\tan\theta_d}, \tag{2.25}$$

where P is the Helium torus pressure in mTorr. For typical values ($P = 1.3$ and $\theta_{inj} = 10^o$), Eq 2.25 yields $I_s/I_p = 1.1$. This indicates the secondary emission intensity is comparable to the primary emission even after pivoting the beam, which may be the reason that the reduction in the 'blue feature' is so small with the tilted DNB discussed in the next subsection. On the other hand, pivoting the DNB still can reduce the beam-into-gas anomaly because the secondary beam emission along the downstream of the sightline may be Doppler-shifted beyond the passband of the MSE narrow bandpass filters, which may the reason we see a significant improvement in the beam-into-gas calibration shown in Fig 2-23.

The linear scaling with the torus pressure in the secondary neutral effect has been tested in another beam-into-gas calibration where a pressure is ramped up during a

shot and each shot has a fixed pitch angle configuration by having constant B_T, EF3, and EF4. Fig 2-25 plots the deviation between the true pitch angle and the measured pitch angle as a function of torus pressure for 3 different pre-defined constant pitch angles from 5 MSE channels. According to Fig 2-25, the error varies roughly linearly with the torus pressure, confirming the scaling given in Eqns 2.23 and 2.25. In addition, the absolute deviation varies smoothly with MSE channel number, decreasing from edge (Ch0) to core (Ch7) channels. Eqn 2.23 has been used to define the population of the secondary neutrals and their effect on the MSE calibration has been calculated by adding the Stokes vectors for all secondary-beam gyro angles whose Doppler shift lies within the MSE filter passband. Fig 2-26 shows the pitch angle deviation from the true pitch angle as a function of I_s/I_p from this calculation for several true pitch angles. The channels identical or close to the real MSE channels shown in Fig 2-25 have been used, so the scales can be directly compared with Fig 2-25. The results shown in 2-26 have many features in common with those from the experiments shown in 2-25. The computed calibration error increases linearly with torus pressure and has distinct dependencies on MSE viewing geometry (i.e., channel) and pitch angle. A more rigorous 3D modeling estimates the fill gas pressure must be reduced to 0.01 mTorr before secondary emission is reduced to a level to allow for pitch angle calibration with a 7° tilt angle [41]. The 3D model also indicates that with 14° tilting, C-Mod would be able to calibrate at 0.05 mTorr, however, this is not feasible given port restrictions in Alcator C-Mod.

Spectral evidence: Blue feature

In the absence of the secondary beam neutral effect, all of the individual H_α MSE spectral lines should be on the red (long wavelength) side of the unshifted H_α line, because the beam neutrals move away from the MSE sightline, and the Doppler shift is larger than the Stark shift. With the secondary neutral effect, however, there should be some emission on the blue side of the unshifted H_α line, because part of the emission is generated by fast particles that have gyrated by $\sim 180^o$ from their original direction, and so their velocity vector is pointed toward the MSE optics.
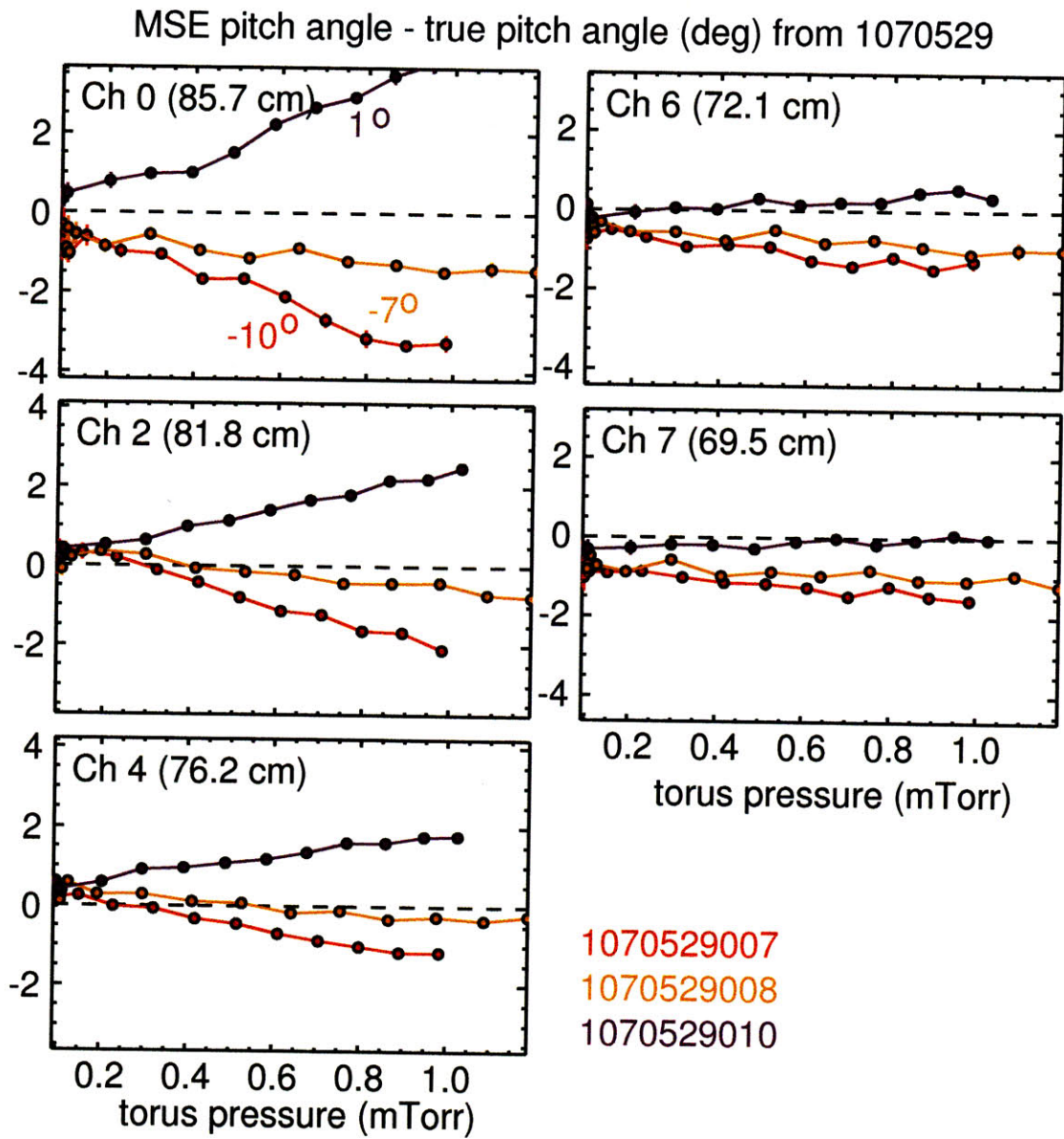
Figure 2-25: Error in the measured pitch angle (MSE pitch angle - true pitch angle) as a function of torus pressure for 3 different fixed pitch angles from 5 MSE channels.
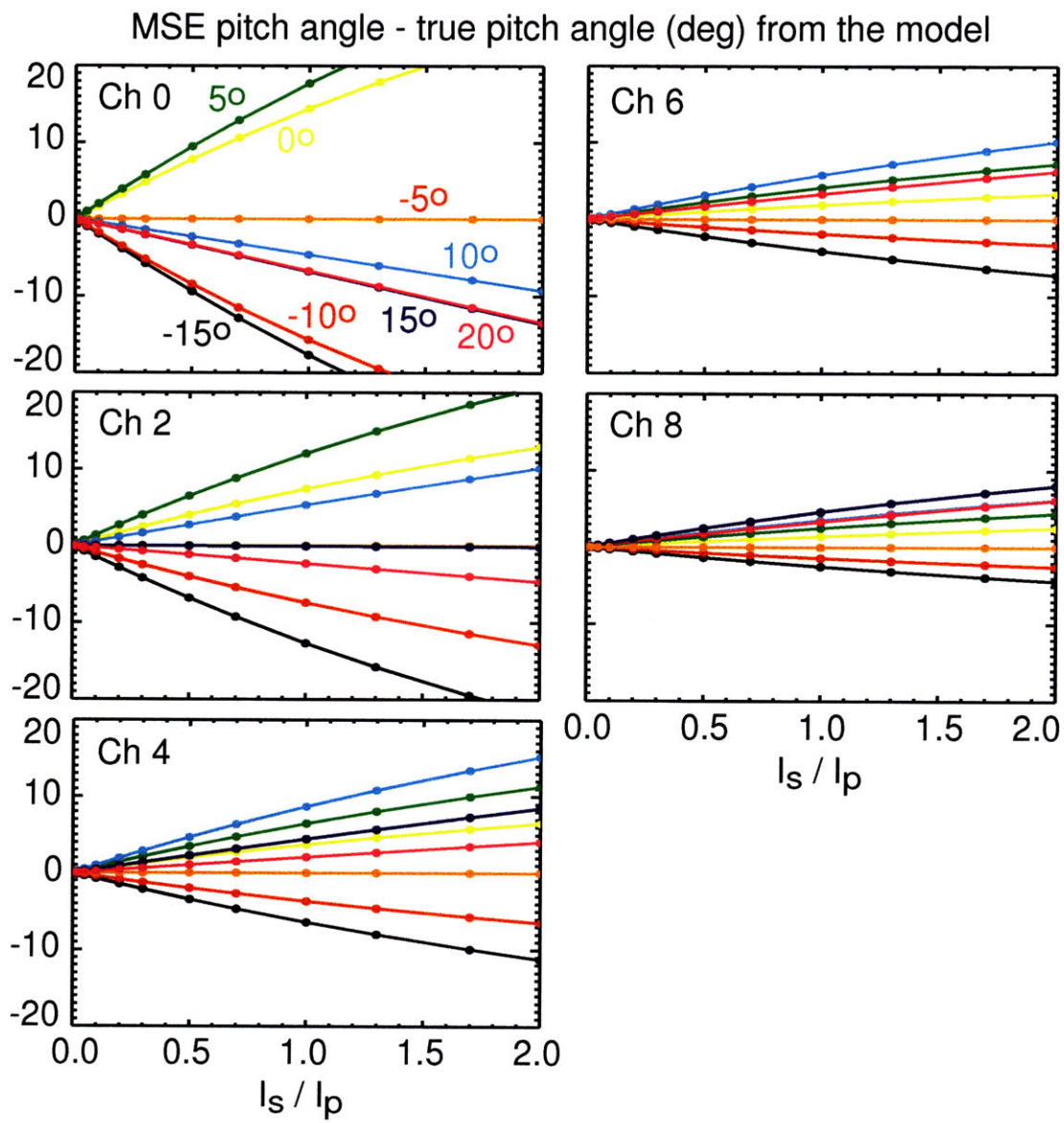
Figure 2-26: Error in the computed pitch angle (MSE pitch angle - true pitch angle) as a function of I_s/I_p for 8 different fixed pitch angles from 5 MSE channels.

Fig 2-27 shows the measured spectra on the blue side of the unshifted H_α line for two MSE channels from the beam-into-gas experiments with two pre-defined pitch angle configurations done prior to the DNB pivoting. Not only finite blue wings but also strong channel dependence is observed in this figure, which is consistent with the fact that the inner channels (Ch 7) have larger Doppler shifts projected onto the MSE sightline than the outer channels (Ch 0).

The blue feature was subsequently tested after the DNB was pivoted and the results are compared with the spectra measured before the beam tilting in Fig 2-28. Each plot contains the spectra with and without the magnetic fields. The spectrum with no field is used to locate 0σ lines for each beam energy components and the aperture broadening. Also shown in the plot are the Stark-split lines from the full, half, and a third, an eighteenth (water) beam energy components similar to those shown in Figs 2-16, 2-17, and 2-18. The expected aperture broadening based on the beam energy, the sightline and the size of the object lens is compared with that estimated from the FWHM of the Gaussian fit of the spectrum.[1] Here, we focus on the blue feature of the spectrum. It is rather hard to draw a firm conclusion from the comparison shown in Fig 2-28 because the DNB conditions are not identical between both years and the Doppler shifts in the Stark lines from FY07 shots are different from those from FY06 shots due to the change in the geometry. Also, there might be some thermal broadening effects from the residual unshifted H_α and D_α lines in the Helium-filled torus. To deal with these ambiguities, the unshifted H_α and D_α components are subtracted, whose components can be found from a Gaussian fit of the no-field spectra assuming the amounts of H and D do not depend on the 'main' torus gas (Helium). Then, the intensities are normalized to the 4π line in each spectrum which can be located from 0σ line in the 'no-field' shots and the knowledge of the magnetic field. Finally, the spectra from FY07 shots (tilted-beam shots) are shifted to match its 4π with that from FY06 shots (radial-beam shots).

Such processes have been done for the spectrum data with fields given in Fig 2-28

---

[1]Interestingly, the measured aperture broadening is *smaller* than that calculated. This has motivated another intensive series of studies on the aperture broadening of the system which is given as an appendix in App B.
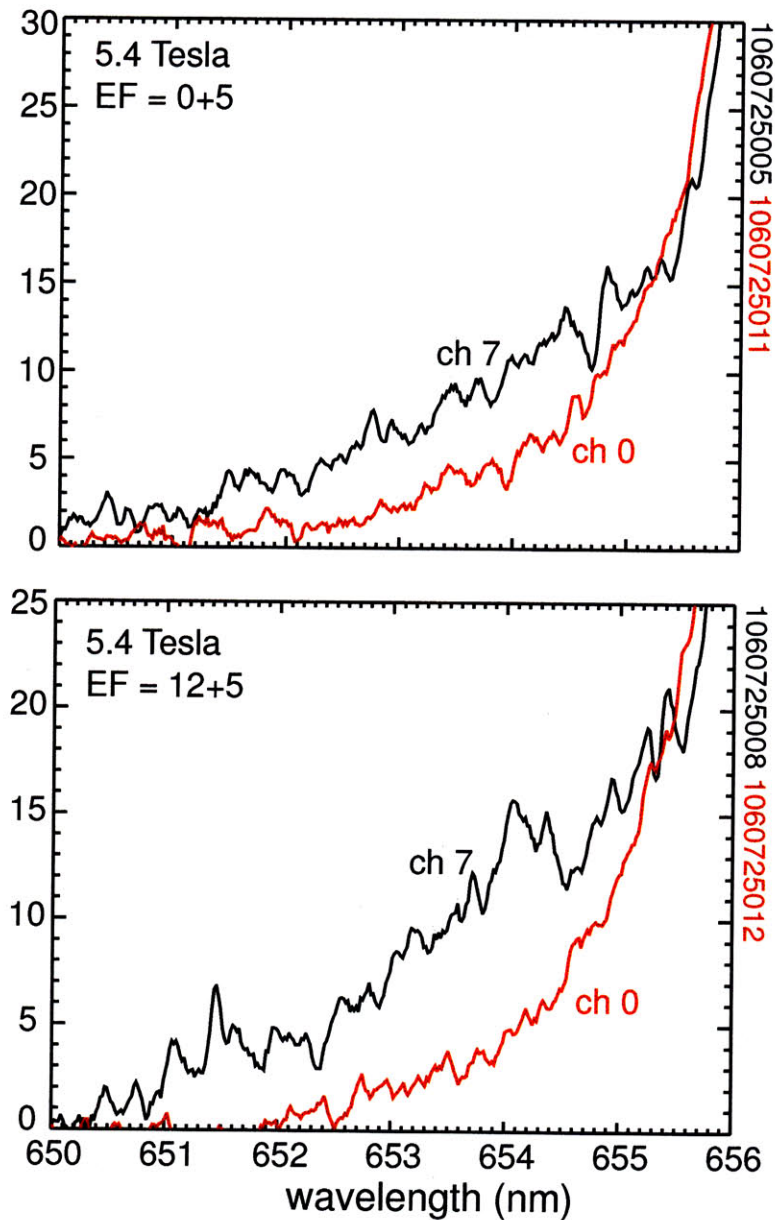
Figure 2-27: Measured spectra on the blue side of the unshifted H_α line for two MSE channels from the beam-into-gas (He) experiments performed prior to the DNB pivoting. Two (top and bottom) pre-defined pitch angle configurations are made by the equilibrium field coils EF3 and EF4 and the current applied to each coil is written in this order. The gas pressure for all the shots is 1 mTorr.
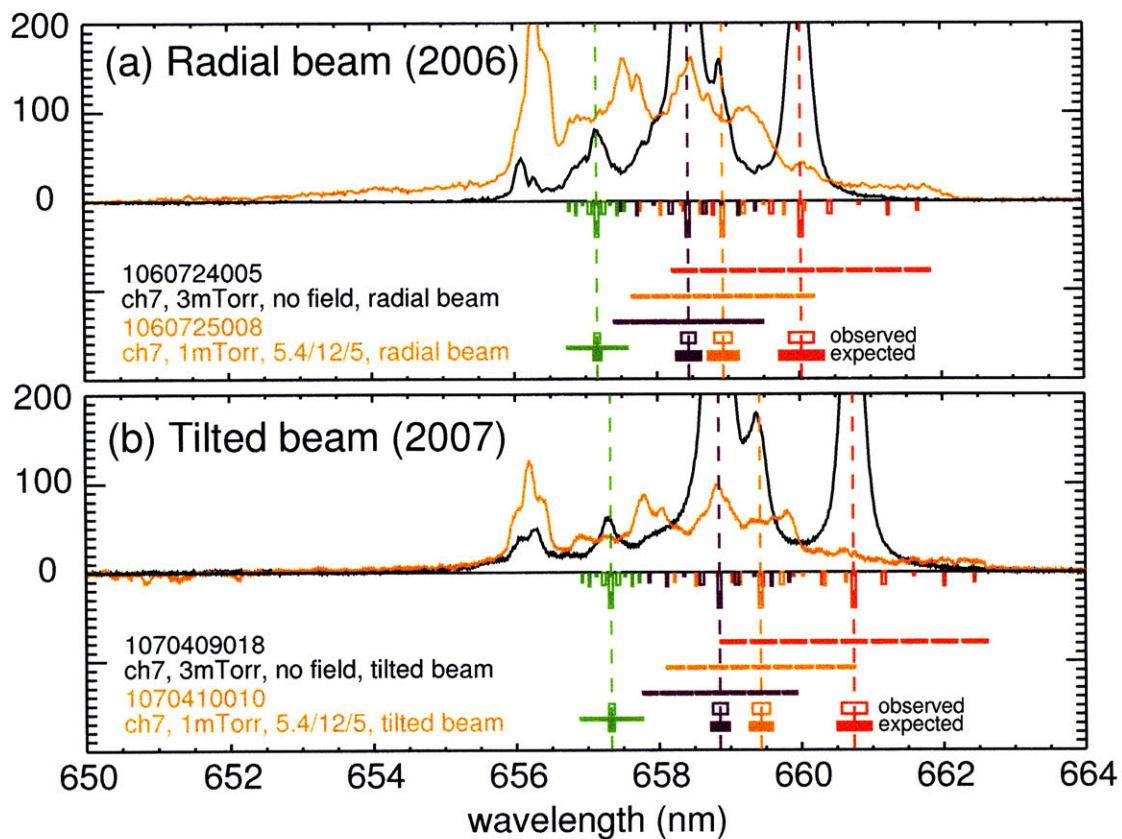
Figure 2-28: Measured spectra from the beam-into-Helium-gas calibrations done (a) before and (b) after the DNB rotation for MSE Channel 7. Each plot shows a pair of spectra, one without the field (black) and the other with the filed (orange). The expected Stark lines (σ in unfilled bar and π in filled bar) from Doppler-shifted full (red), half (orange), a third (blue), and an eighteenth (green) beam energy components are also shown in each plot along with its each 0σ marked with dashed vertical lines. The expected and observed aperture broadening sizes are given for each energy components as well.
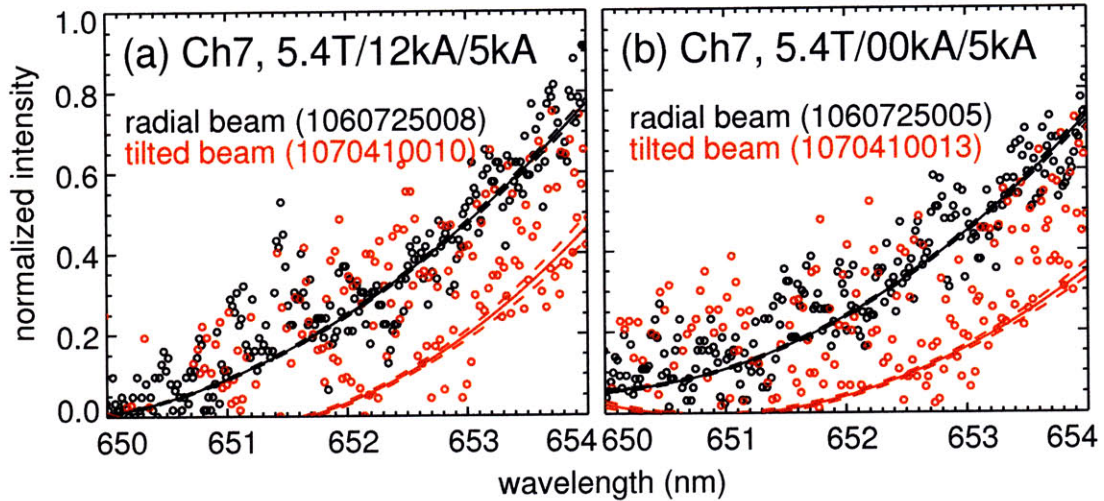
Figure 2-29: Comparison of blue features in the spectrum from the beam-into-Helium-gas calibration done before (black) and after (red) the DNB rotation from MSE Channel 7 for two pre-defined external magnetic field configurations which are marked as B_T/EF3/EF4 in (a) and (b). For a direct comparison, the residual unshifted H_α and D_α components have been subtracted first. Then the intensities have been normalized to their respective 4π lines and the tilted-beam spectra have been shifted such that their 4π lines match those of the radial-beam spectra.

and the results are shown in Fig 2-29 (a). Another pair of spectra before and after the pivoting with a different combination of EF3 and EF4 are compared in Fig 2-29 (b). The comparisons shown in this figure imply only a small reduction ($\lesssim$ a factor 2) in the secondary beam neutral effects after pivoting the beam by 7°. Overall, the signal to noise ratio is too low to make a strong argument from these data. The following subsection explains why the reduction in the blue feature, that is, the reduction in the contribution of the secondary beam neutrals, is small even after tilting the beam by 7°.

Implications of beam-into-gas calibration

Based on the discussions in the previous subsections, it is concluded that it is almost impossible to calibrate MSE using the beam-into-gas technique on C-Mod unless one of the followings is done:

- Significantly improve the photon-gathering power of the optical system, which

would enable one to gather sufficient photons even at lower torus pressure.

- Dedicate significant run time to the calibration to increase the number of photons, i.e. take one to several shots per calibrated pitch angle. In the economic point of view, this concept can be compared with the beam-into-gas calibrations that have typical been done for the past years where the vertical field is ramped during a single shot, calibrating $5 \sim 10$ pitch angles per shot.

- Calibrate the MSE diagnostic at a high torus pressure in a pressure scan, where the secondary beam neutrals are expected to have an effect on the calibration, then extrapolate these results to low torus pressure.

2.2 Calibrations and analyses

2.2.1 Calibrating edge channels in a plasma

One more common and basic calibration technique in addition to the beam-into-gas calibration is the invessel calibration, which is also briefly introduced in Section 1.2. In the invessel calibration, a linear polarizer is mounted on a precision rotating stage in the torus when it is up-to-air. The light source is positioned behind the polarizer, and the unit is pointed toward the MSE object lens. The MSE system then measures the polarization angle as the polarizer is rotated through 360°. This calibration procedure is important for characterizing the non-ideal properties of the three mirrors used in the system, which can shift the measured polarization direction by $1 \sim 2^\circ$, and for correctly relating the polarization angle measured in the 'PEM frame' with the polarization direction of the light incident on the object lens. However, the invessel calibration does not provide any information related to the performance of the MSE bandpass filters, Faraday rotation effects, or stress-induced birefringence at the vacuum window.

The beam-into-gas calibration, on the other hand, should deal with these effects in principle. This calibration uses the actual motional Stark effect and thus is subject to the actual performance of the bandpass filters. Also, the calibration is conducted

at full magnetic field and thus can provide some information about Faraday rotation. Since the calibration is conducted under vacuum, it includes effects due to stress-induced birefringence on the vacuum window as well. As discussed in Sec 2.1.4, however, the beam ions may be subject to the secondary charge exchange that can confuse the measurements considerably, particularly for perpendicular beam injection. For the MSE systems that use tangential beams under a sufficiently low torus pressure, the beam-into-gas calibration is still useful. For example, The NSTX (National Spherical Torus Experiments) device routinely uses this technique with a torus gas pressure of 0.05 mTorr [41]. The invessel calibration is routinely performed in DIII-D, with the Faraday rotation corrected from a separate in-vessel (atmospheric), but with magnetic fields, calibration [64]. Joint European Torus (JET) uses a technique similar to the invessel calibration but it is performed off the tokamak [65].

Besides two basic calibration methods - invessel and beam-into-gas, the MSE system can be calibrated in real plasmas in which case all the physics can be captured in the calibration. The plasma calibrations usually utilize the fact that the pitch angle information close to or on the edge of the plasma can be inferred quite accurately from numerical magnetic reconstruction procedures such as EFIT with the boundary conditions measured by external magnetic coils and probes. Therefore, this approach is limited to calibrating the MSE channels close to the plasma boundary.

A related calibration method with a plasma relies on the assumption that the safety factor, q, is equal to 1 at the sawtooth inversion radius [2]. This method also involves a magnetic reconstruction to produce the q value at a specific major radius. Since $q = 1$ flux surface is usually near the magnetic axis, this technique is, in principle, a single-point calibration.

The first two basic 'non-plasma' calibration schemes - invessel and beam-into-gas - are introduced and discussed in detail in the previous dissertation on the C-Mod MSE system [36] and have been conducted on a very routine basis for several years. Recently, two different plasma calibration techniques have been tried in C-Mod and their results and feasibilities are discussed in the following subsection.

Plasma current ramp calibration

In this calibration, MSE measures the pitch angle as the plasma current, I_p, is ramped (with the plasma size constant). This provides a considerably large range of pitch angles to be calibrated. At $B_T = 5.4$ Tesla, it should be possible to cover a range of $I_p = 0.25 \sim 1.2$ MA or about a factor of 5 in pitch angle. As discussed above, this technique basically calibrates MSE against EFIT and so is accurate only for the outer-edge channel.

Four shots from 1070615 (19, 20, 23, and 24) ramped the plasma current over a considerable range within a single pulse. Fig 2-30 shows the waveforms of several plasma parameters along with EFIT-calculated pitch angles from these shots. In the standard 2-second plasma pulses (shots 19, 20 and 24), I_p is ramped from 0.8 MA at 1 sec to 0.1 MA at 1.9 sec during the B_T flattop, providing the pitch angle range -10 to -1° for the edge channel. For these 3 shots, the pitch angles measured by MSE and calculated by EFIT during the quiesent I_p ramping phase (0.8 $\sim$ 1.8 sec) from two MSE channels (edgemost and near-optical-axis) are compared in Fig 2-31. Also shown in the figure is the linear fit of the data for each shot. First, for the edgemost channel (Ch0), there seems to be an almost constant offset between the MSE and EFIT pitch angles. This observation is more obvious if one takes a look at their fit coefficients shown in Table 2.5. From the table, the slope of the fit ('b') for Channel

channel	shot	a	δa	b	δb
0 (85.74 cm)	19 (black)	1.69	0.17	1.03	0.02
	20 (red)	1.81	0.22	1.02	0.02
	24 (purple)	2.56	0.22	1.05	0.03
9 (78.22 cm)	19 (black)	2.67	0.12	1.41	0.02
	20 (red)	2.76	0.12	1.43	0.02
	24 (purple)	3.52	0.14	1.45	0.02

Table 2.5: Coefficients of the linear fit $y = a + bx$ from Fig 2-31. The shot number is 10706150xx and the color name is the same as shown in Fig 2-31. δ denotes the 1-σ error of the fit coefficient.

0 is effectively unity within its uncertainty every shot. This indicates that the edge channel can be correctly calibrated simply by adding or subtracting the linear offset
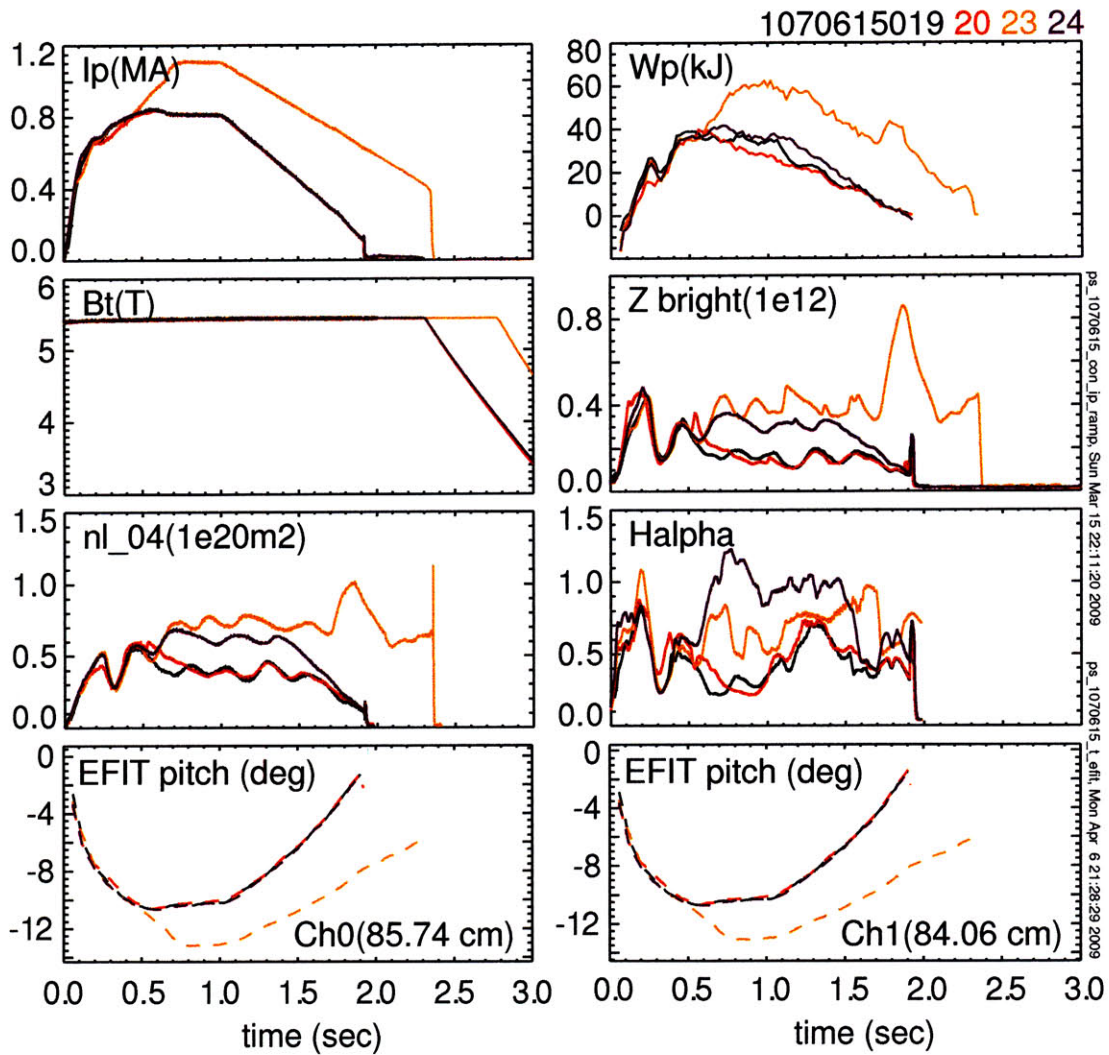
Figure 2-30: Waveforms of some plasma parameters from Shots 1070615019, 20, 23, and 24 for MSE I_p-ramp calibration feasibility study. The two bottom plots show the pitch angles calculated from EFIT for two outer MSE channels (Chs 0 and 1). Also note that Shot 23 has an extended pulse length (3 sec) and an Ohmic H-mode driven from 1.8 to 2.1 sec.
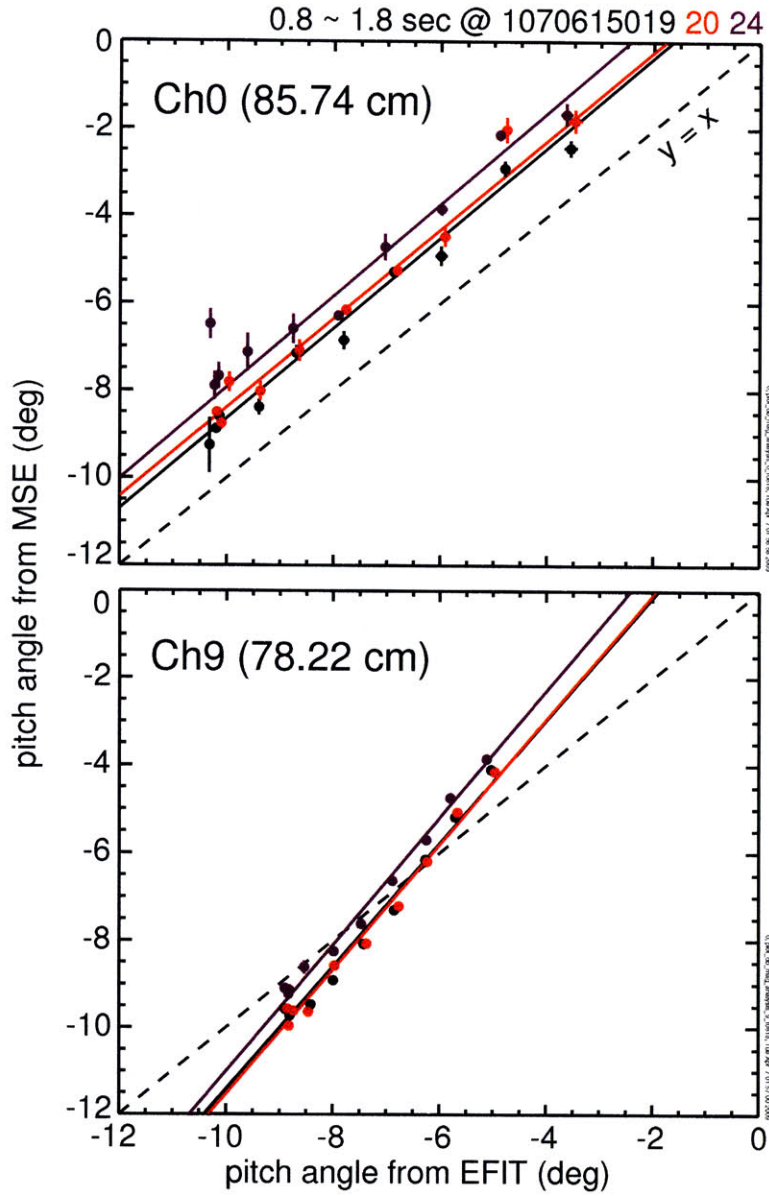
Figure 2-31: Comparison of pitch angles from MSE and EFIT during the quiescent I_p ramping phase in the 3 standard 2-sec shots shown in Fig 2-30. The edgemost (Ch0; Top) and the near-optical-axis (ch9: Bottom) results are shown. The solid lines are the linear ($y = a + bx$) fits and the fit coefficients are given in Table 2.5.

('a') which is different shot by shot. On the other hand, the slope for Channel 9 deviates from unity, which may be due to incorrect pitch angle calculations by EFIT inside the plasma. Nevertheless, it is encouraging that the slopes are still identical within their uncertainties for all three shots, implying that it might be possible to calibrate this inner channel only with a single piece of information (e.g. the linear offset, a). These observations strengthen the validity of the 'within-shot' calibration scheme which is discussed in Sec 4.2.1.

In shot 23, a 3-second long pulse plasma was attempted to obtain a larger pitch angle range. Although the discharge disrupts about at 2.3 sec, I_p ramping from 1 MA at 1 sec to 0.4 MA at 2.3 sec was obtained, resulting in the pitch angle range from -13 to -5°. In addition, an Ohmic-H mode phase from 1.8 to 2.1 sec has been obtained in this shot, which can be indicated the increase in plasma density, stored energy and Z brightness and the decrease in H_α intensity during this time frame shown in Fig 2-30. This is an important data set regarding the observation that MSE signals can be contaminated by the H_α FFT components mentioned in Sec 2.1.3. Normally, the MSE background signals during beam pulses are linearly interpolated based on the background measured before and after individual beam pulses and subtracted from the main signals. However, this non-ICRF-driven H mode can provide a real-time correlation between the H_α signals and the MSE background and therefore, one can try to interpolate the MSE background during the beam pulse based on the H_α intensity variation. This scheme has been tried for Shot 23 and the time evolution of pitch angles obtained from this H_α-based background subtraction scheme has been compared with that from the standard linear background scheme from several (edge) channels in Fig 2-32. Note that at the time of the H-mode onset, which is about 1.7 sec, there is some variability in the pitch-angle evolution in the standard analysis, but the H_α analysis is considerably smoother.

This calibration scheme may be combined with the inner-channel calibration method using the knowledge of the sawtooth inversion radius, which will provide 'internal' calibration points in addition to the calibration obtained by comparing to EFIT at the edge. In the I_p ramp shots, there will be a considerable change in the
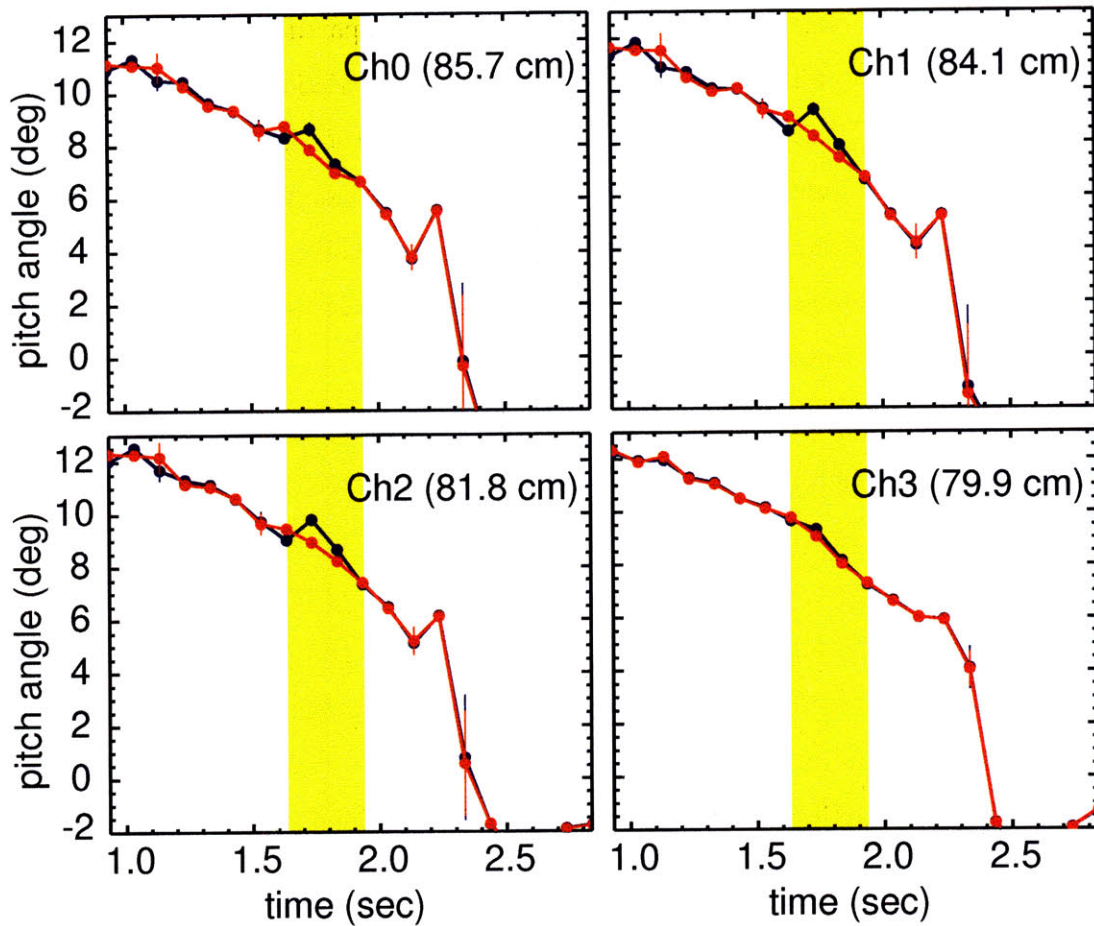
Figure 2-32: Comparison of pitch angle variability from the standard linear (blue) and the H_α interpolation (red) schemes in the background subtraction for the four outer MSES spatial channels from Shot 1070615023. The H-mode and its transition are marked in the yellow box.

sawtooth-inversion radius, so this can provide a calibration not just at a single MSE channel, but several internal channels, unlike mentioned in the earlier part of this section. When the I_p drops to sufficiently low values, q will rise to above unity on-axis and the sawteeth will go away entirely. On this particular run day, unfortunately, the ECE was not available, so this combined calibration was not tried.

Plasma sweep calibration

This calibration technique also relies on the fact that the pitch angle computed by EFIT at the plasma edge does not depend on EFIT's assumption of the radial profile

of current. Therefore, the MSE-measured angle is compared to that computed by EFIT only as the plasma edge is swept past a given MSE channel. This technique can be compared with the I_p-ramp calibration introduced in the previous subsection in that the former can calibrate multiple channels with a limited number of pitch angles whereas the latter can calibrate multiple pitch angles with a limited number of channels. The technique to sweep the plasma has also been used in TFTR [66] and DIII-D [67] and proposed in JET [68] to cross calibrate sightlines in their MSE systems.

Ideally one would like to carry out the calibration over as wide a range in pitch angle as possible, but there is one well-known constraint in this approach: the stability limit at low q_{edge}. The edge q is approximated by [69]

$$q_{edge} = \frac{5a_p^2 B_T}{R_p I_p} \left[\frac{1 + \kappa^2(1 + 2\delta^2 - 1.22\delta^3)}{2} \right] \left(\frac{1.17 - 0.65\epsilon}{(1 - \epsilon^2)^2} \right) \tag{2.26}$$

where a_p and R_p are the plasma minor and major radii, respectively, κ is the elongation at the edge of the plasma, δ the triangularity, and $\epsilon = a_p/R_p$. This implies that when the plasma minor radius shrinks, it is necessary to reduce I_p as well in order to keep q_{edge} greater than a certain safety margin (~ 3) with various other equilibrium parameters also involved.

In 1070629 run, plasma edge sweeping was attempted and three successful shots were obtained, the edge major radius ranging from 89 to 76 cm and minor radius from 22 to 16 cm. Fig 2-33 shows the time evolution of some plasma equilibrium parameters including the safety factor at 95 % flux surface, q_{95}, which is maintained above 3, by appropriately ramping down I_p along with the plasma size. As the edge of the plasma is swept at the line of sight of a certain MSE spatial channel, the measured pitch angle at that channel is compared with that from the EFIT. The top plots in Fig 2-34 show the edge radius time history from the shots from 2-33. The vertical line on the plots indicates the MSE channel number which corresponds to the location of the plasma edge at that time point. Assuming the EFIT always estimates the pitch angle at the plasma boundary accurately, this technique can calibrate any channel whose

107
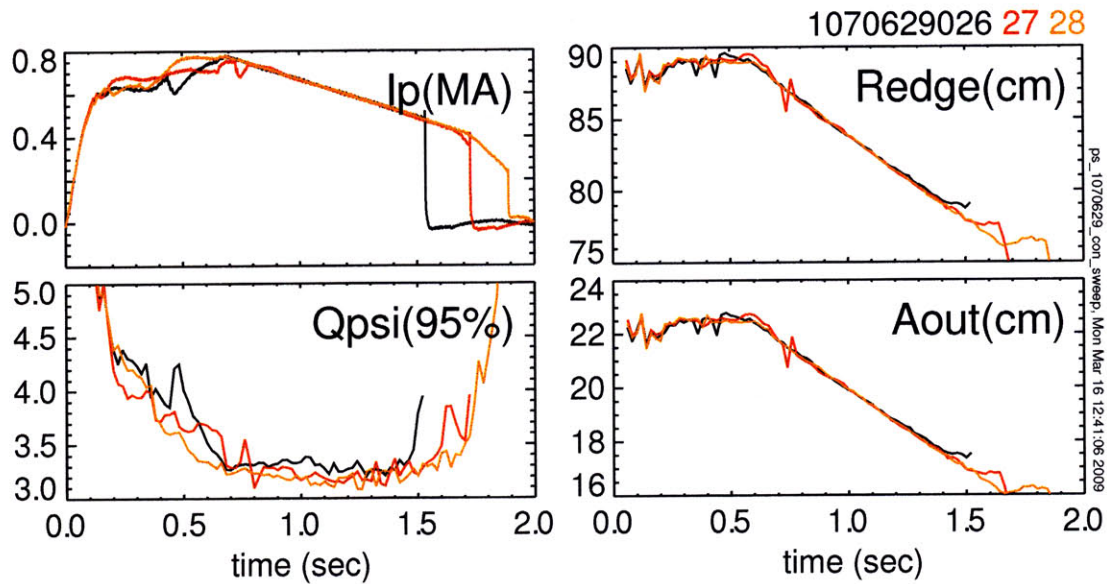
Figure 2-33: Waveforms of I_p, safety factor at 95 % flux surface ("Qpsi(95%)"), major radius of the edge ("Redge"), and minor radius of the plasma ("Aout") from Shots 1070615019, 20, and 23 for the plasma-sweep calibration feasibility study.

position is 'swept' by the plasma edge during the pulse. The example is shown on the middle plots in Fig 2-34 where the pitch angles from the MSE channels whose colors correspond to those on the top plots are traced. Also shown on the middle plots in Fig 2-34 are the pitch angle traces calculated by EFIT at R_{edge}. The vertical lines for Shot 1070629027 on the middle plot indicate the channels (or time points) that should be excluded in the analysis because the plasma is disrupted during the DNB pulse over which the MSE signals are time-averaged, therefore, possibly giving wrong pitch angles. The difference in the pitch angle between MSE and EFIT is plotted on the bottom.

As shown in Fig 2-34, up to 7 channels can be calibrated using the plasma-sweep approach and the difference in pitch angle between MSE and EFIT is fairly reproducible. This difference is large at the MSE edge channel and decreases as one moves into the plasma. This may be due to the channel-dependent feature in the thermal stress-induced birefringence in the MSE invessel optics, which is most unfavorable for outer channels. This issue is discussed in Chapter 3. Once the thermal drift
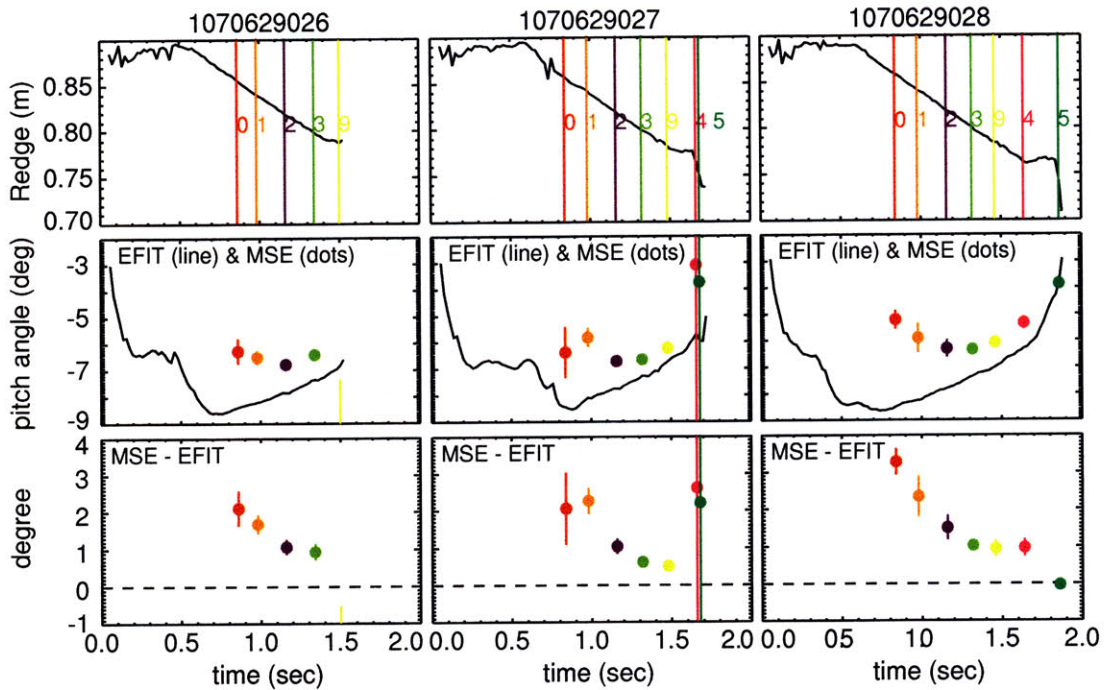
Figure 2-34: Plasma edge sweeping experiments from 1070629. The time evolution of plasma edge position (top) with the vertical lines indicating the MSE channel number whose position is swept by the plasma edge at that time point. The middle plots show the pitch angle measured by the channel marked with the same color shown on the top plot (point) with the pitch angle computed by EFIT (black line). The vertical lines for 1070629027 on the middle plot indicates those channels can be excluded in the analysis because the data from those channels are taken include some spurious signals at the moment of the plasma termination. The bottom plots show the difference in pitch angles between MSE and EFIT.

problem is resolved, this calibration technique can be re-visited and more aggressive sweeps can be tried to cover more inner channels at different plasma currents to get calibration at multiple pitch angles.

2.2.2 Intensity and position calibrations

In addition to the pitch angle calibrations discussed in the previous subsections, the absolute intensity and position calibration activities have been done for the first time and briefly introduced here.

109

Absolute intensity calibration

An absolute intensity calibration has been performed for the full MSE system using Labsphere URS-600, a light source with absolutely calibrated spectral radiance, in the sight line of each MSE channel. The output signal from the digitizer for each channel can be expressed as, in voltage,

$$
\begin{aligned}
v_{out}^{full} &= f_o f_p f_{fe} f_g E_{full} \int_0^\infty I_{full}(\lambda) f_e(\lambda) f_b(\lambda) f_r(\lambda, HV_{full}) Q \ d\lambda \\
&= f_o f_p f_{fe} f_g E_{full} J_{full}(HV_{full}),
\end{aligned}
\tag{2.27}
$$

where f_o is the efficiency of the optical elements which involves the transmission of individual lenses and windows (both vacuum and PEM windows) and the reflection of individual mirrors. f_p is the transmission of the linear polarizer installed after the PEMs and estimated to be about 0.5 for all the channels from a separate intensity calibration test. f_{fe} is an efficiency that combines the effect of the fiber bundle transmission and some small variability of the APD detector over channels, which turns out to be near unity. f_g is the APD preamplifier gain and known to be 2×10^7 V/A. E_{full} is the étendue of the entire optical system that includes the object lens and the fibers in cm^2.sR, $I_{full}(\lambda)$ is the spectral radiance of the light source in W/cm^2.sR.nm used in the full system calibration. $f_e(\lambda)$ and $f_b(\lambda)$ are the transmission coefficients of the steep-edge filter and the bandpass filter, respectively, as a function of wavelength (λ). $f_r(\lambda, HV)$ is the gain (responsivity) of the APD detector in A/W and depends on the wavelength of the incident light and the bias voltage (HV_{full}) applied to the detector. Finally, Q is the quantum efficiency of the APD which is taken as 80 % at 650 nm from the APD model SD 394-70-72-591 data sheet. The integral $J_{full}(HV_{full})$ is numerically evaluated with a given $I_{full}(\lambda)$ from the Labsphere calibration data over a wide range of wavelength, given $f_e(\lambda)$ and $f_b(\lambda)$ from the manufacturers, and $f_r(\lambda, HV)$ from a given gain curve of the APD. However, the factors $I_{full}(\lambda)$ and $f_r(\lambda, HV)$ are fairly constant over the pass band of the bandpass filter, so real dominant factors are $f_e(\lambda)$ and $f_b(\lambda)$. Note that Eqn 2.27 is the complete and full version of its (very) simplified form, Eqn 2.2. Fig 2-35 (a) shows the measured raw signal
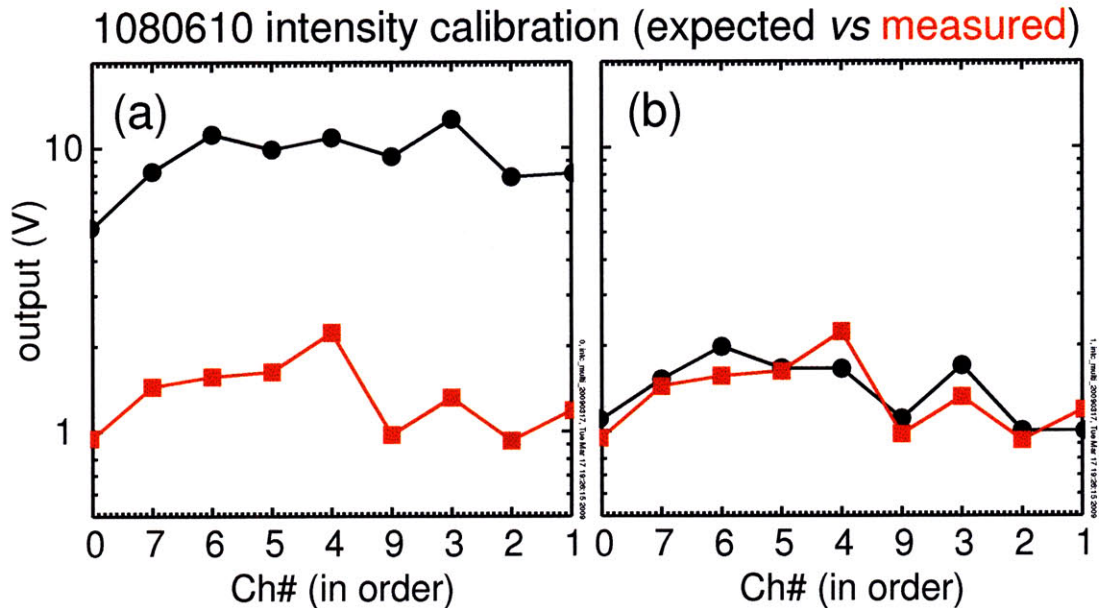
Figure 2-35: Comparison of measured (red) and calculated (black) MSE signals as a function of channel number in 1080610 absolute intensity calibration. The calculated signal uses Eqn 2.27 (a) with the assumption that $f_o = 1$ and that E_{full} is dominated by the 5-cm diameter object lens and (b) with the correction to the product of $f_o E_{full}$ using Eqn 2.30.

with the background subtracted (red) and the signal calculated from Eq 2.27 (black) as a function of channel number. Note that f_o cannot be measured separately, so it is assumed to be unity for the calculation. In addition, the étendue of the full system, E_{full}, is estimated on the basis of the object lens 5 cm in diameter, which may not represent the minimum étendue of the system. Additional uncertainties can reside in estimating f_{fe}, f_g, and f_r. An order of magnitude difference between the measured and calculated signals shown in Fig 2-35 (a) should be caused by one or more of these factors.

In order to separate some parameters from computing the expected intensity, another calibration (1080926) without any optical elements has been done where the optical periscope, PEMs, and the polarizer are detached from the system and a calibrated light source shines directly onto the fibers. This setup has an advantage in that (1) the étendue of the system is well defined with known f-number of the fibers

111
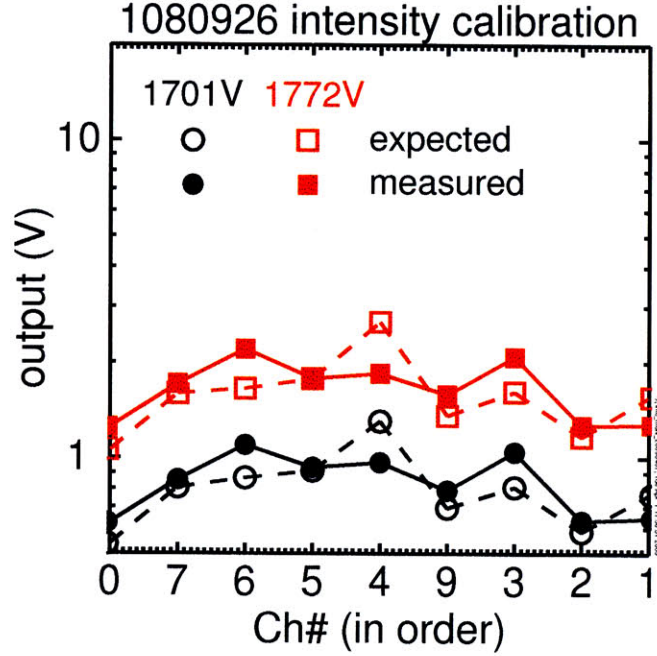
Figure 2-36: Comparison of measured (solid symbols) and calculated (empty symbols) MSE signals as a function of channel number in 1080926 absolute intensity calibration for two different bias voltages (1701 and 1772 V). The calculated signal uses Eqn 2.28 with the assumption that $f_{fe} = 1$.

and (2) the unknown transmission efficiency of the lenses and windows are excluded from the calculations. Then the output signal can be written as

$$
\begin{aligned}
v_{out}^{fiber} &= f_{fe}f_g E_{fiber}\int_0^\infty I_{fiber}(\lambda)f_e(\lambda)f_b(\lambda)f_r(\lambda, HV_{fiber})Q\ d\lambda \\
&= f_{fe}f_g E_{fiber}J_{fiber}(HV_{fiber}),
\end{aligned}
\tag{2.28}
$$

where $I_{fiber}(\lambda)$ is the spectral radiance of the light source used in this 'fiber-only' system calibration. Also note that the bias voltage applied to the detector differs calibration to calibration. Therefore, a distinguishing subscript is added to HV_{full} and HV_{fiber}. Fig 2-36 shows the measured raw signal with the background subtracted (solid symbols) and the signal calculated from Eqn 2.28 (empty symbols) as a function of channel number for two different HV_{fiber} values. Unlike the order-of-magnitude difference between the measured and calculated signal intensities observed for the full

system calibration (Fig 2-35 (a)), the measured intensity is almost identical to that calculated using Eqn 2.28. It is also noted that the agreement is consistent for two different bias volatages (HV_{fiber}). This result implies that the assumptions for f_{fe}, f_g, and f_r are not worrisome and their current values are valid enough not to cause any order-of-magnitude errors that are observed in the full-system calibration. Dividing Eqn 2.27 by Eqn 2.28 gives

$$\frac{v_{out}^{full}}{v_{out}^{fiber}} = f_o f_p \frac{E_{full}}{E_{fiber}} \frac{J_{full}(HV_{full})}{J_{fiber}(HV_{fiber})}. \tag{2.29}$$

This expression can give a useful piece of information which is

$$f_o E_{full} = \frac{v_{out}^{full}}{v_{out}^{fiber}} \frac{E_{fiber}}{f_p} \frac{J_{fiber}(HV_{fiber})}{J_{full}(HV_{full})}, \tag{2.30}$$

that is, the product of the transmission efficiency of the optics and the étendue of the full system, which is unknown. Since all the parameters on the RHS of Eqn 2.30 are either known or measured quantities, combining the results from full and fiber-only calibrations can provide the unknown quantity, $f_o E_{full}$. It is encouraging to see, in Fig 2-35, a significant reduction in the difference between the measured and calculated signals when the quantity $f_o E_{full}$ obtained from Eqn 2.30 is applied to Eqn 2.27.

The validity of the correction scheme using Eqn 2.30 can be checked by the observation that the expression of $f_o E_{full}$ in Eqn 2.30 should be invariant against the applied bias voltages, HV_{full} and HV_{fiber}. Since the fiber-only calibration has been done for two different HVs (1700 and 1770 V), this can be easily tested. Fig 2-37 (a) shows the parameter $f_o E_{full}$, as a function of channel number, calculated by Eqn 2.30 for two different bias voltages and supports this argument. Another HV-invariant feature should be present in estimating the parameter f_{fe}, which essentially contains the fiber bundle transmission and some variability in the APDs channel to channel, directly from Eqn 2.28 with the measured v_{out}^{fiber}. Fig 2-37 (b) has the f_{fe} profile obtained this way and confirms that this parameter is indeed HV-invariant.

The étendue of the full system can be calculated if one can estimate the optics efficiency, f_o, in an independent way. A measurement of the transmission and reflec-

113
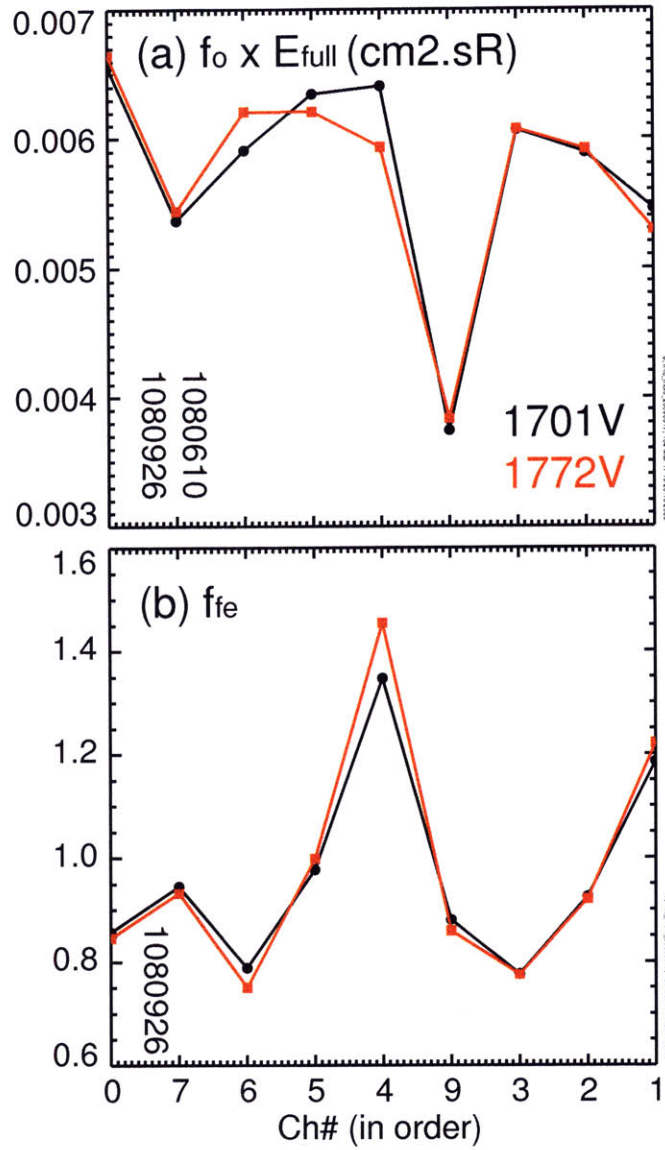
Figure 2-37: (a) The product of $f_o E_{full}$ calculated by Eqn 2.30 and (b) The parameter f_{fe} calculated by Eqn 2.28 for two different HV_{fiber}.

Element	Transmission or Reflection	Date
L1	0.863	Dec 18 2008
M1	0.990	
L2a	0.987	
L2b	0.987	
M2	0.990	
M3	0.990	
L3a	0.981	Jan 6 2009
L3b	0.981	
VW	0.910	
L4a	0.986	
L4b	0.986	
L5a	0.986	
L5b	0.986	
PEM1	0.962	
PEM2	0.962	
L6	0.988	
Total	0.617	

Table 2.6: Measured transmission and reflection of MSE optics elements

tion of the individual lenses and mirrors, respectively, has been performed wherein laser light is transmitted through a lens or reflected onto a mirror and its intensity is measured before and after the interaction. Different angles of incidence have been investigated and the effect is found to be negligible up to about $45°$. Table 2.6 summarizes the results from this measurement. It seems that the anti-reflection (AR) coatings on most of the lenses (L2, L3, L4, L5, and L6) do not perform properly, their transmissions being only 98 ~ 99 % The reflectivites in the range of 0.1 ~ 0.2 % for the nominal wavelength of 650 ~ 660 nm for AR coating were measured at time of fabrication and it is possible that the AR coating has deteriorated over time. The transmission of the vacuum window, known not to be AR coated, is consisitent with what would be obtained with the 4 % of reflectivity per non-AR coated glass surface. The fused-silica windows of PEMs also show a lower transmission of 96 %, which is also close to non-AR coated glass. The particularly low transmission of L1, the non-plasma-facing side of which is only AR-coated, may be due to some direct

Ch#	0	1	2	3	4	5	6	7	8	9
R (cm)	68.94	87.21	85.13	83.34	79.91	77.87	75.74	73.56	71.15	81.75
θ (deg)	-10.7	13.4	9.82	7.48	2.86	0.07	-2.10	-5.30	-8.17	4.62
d (cm)	44.27	35.65	36.27	36.88	38.27	39.18	40.27	41.48	42.91	37.47
n_f	16	15	16	16	16	15	14	13	16	11.5

Table 2.7: Major radius R, angle between the sightline and that of the optical axis θ, distance between the footprint center and L1 d, and the number of intact fibers n_f for each channel. $\theta > 0$ indicates that channel more inward than the optical axis, and *vice versa*. This table is consistent with the MSE channel configuration as of March 2009.

depositions over time and higher reflection on the plasma facing side. All the mirrors pose very low absorption coefficients, reflecting about 99 % of the incident light. The total throughput based on this measurement gives about 62 % of total optics transmission/reflection efficiency, which is equivalent to f_o in Eqn 2.30 and can be used to evaluate the étendue of the full MSE system, E_{full}. Fig 2-38 compares E_{full} calculated from Eqn 2.30 (also shown in Fig 2-37 (a)) with $f_o = 0.62$ ('star') with E_{full} estimated at L1 ('circle') and E_{fiber} estimated at the fiber entrance ('square') which are calculated from

$$E_{full} = A_{ff} \times n_f \times \pi r_{L1}^2 \cos(\theta)/d^2 \qquad (2.31)$$

$$E_{fiber} = A_{fe} \times n_f \times \pi(NA)^2, \qquad (2.32)$$

respectively, where A_{ff} is the area of a single fiber at the DNB footprint and equal to $\pi(0.25)^2 = 0.2$ cm^2, A_{fe} is the area of a single fiber and equal to $\pi(0.1)^2 = 0.03$ cm^2, r_{L1} is the radius of the L1 lens (2.5 cm), and NA is the numerical aperture of the fiber (0.3). θ is the angle between the sight line of a channel and that of the optical axis, d is the distance between the footprint of a channel and L1, and finally, n_f is the number of fibers available (i.e., not broken) for each channel. θ, d, and n_f are summarized in Table 2.7 along with the major radius, R. According to Fig 2-38, the étendue based on the intensity calibration and the measurement of optics efficiency is smaller by a factor of $3 \sim 4$ than the étendue either from L1 or from the fiber
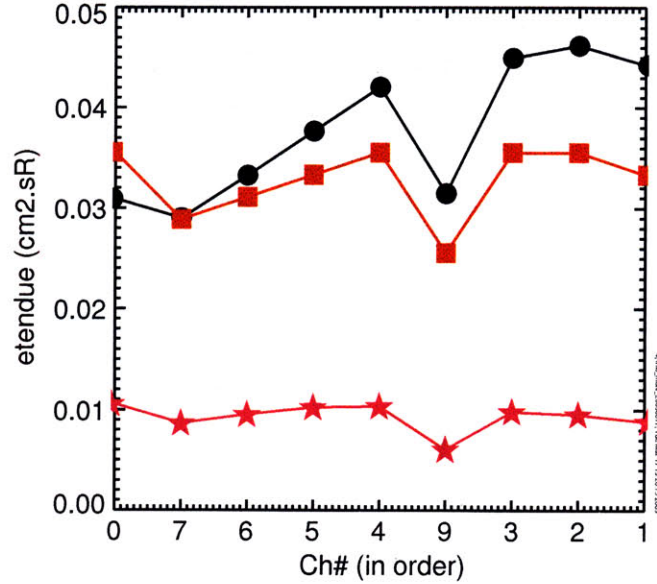
Figure 2-38: Comparison of étendue based on Eqn 2.30 and measured f_o ('star') with E_{full} ('circle') and E_{fiber} ('square') calculated at L1 using Eqn 2.31 and the fiber entrance using Eqn 2.32, respectively.

entrance.

This implies that the real minimum étendue that limits the system is not either L1 or the fiber, but somewhere else in the optical train. For example, the 3D ray tracing calculation indicates the solid angle of the rays incident on the fiber entrance from the beam trajectory is only about 77% of that inferred from the advertised NA of the fiber (27° vs 35°). Then, the effective NA becomes $\sin(27^o/2) = 0.23$. Since the étendue scales with $(NA)^2$, this results in the reduction in the étendue by 40%. It is interesting to see this reduction factor of $3 \sim 4$ in étendue can be converted into a possible reduction of $1.7 \sim 2$ in the radius of the L1 aperture from the scaling of $r_{L1} \sim \sqrt{E}$, which might explain why the measured aperture broadening is already smaller by about $50 \sim 60$ % than that estimated from the real L1 radius of 5 cm and the broadening does not change until 50 % of the L1 aperture is masked. The experimental evidence of this observation is introduced in App B.
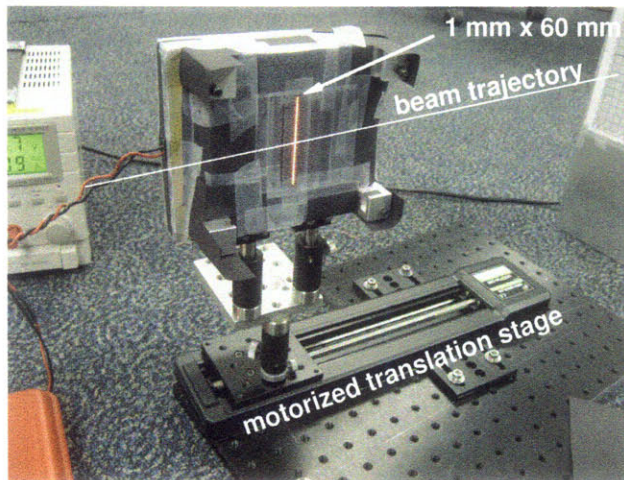
Figure 2-39: Setup for the radial intensity weighting calibration (Feb 13 2007)

Intensity weighting (position) calibration

Another instrumental calibration which was performed first time is an MSE footprint position calibration using the intensity weighting. An LED light source shrouded so as to have 1 mm × 60 mm slit is prepared and mounted on a precision motorized translation stage which is placed along the DNB trajectory so that the slit is vertically centered about the midplane and toroidally aligned along the beam trajectory. The translation stage translates the light source by a millimeter per step. Fig 2-39 shows this setup built prior to the invessel entry.

A total of 300 shots were taken to cover the major radius range of 61.22 ∼ 91.18 cm which includes the major radii of the MSE channels (See Table 2.7). Care must be taken in setting the operating bias voltage of the APD at the beginning of the scan so as not to saturate detectors in other MSE channels. There are indeed several shots saturated and for those shots (i.e., those major radii), a separate scan has been done with a reduced bias voltage and the magnitude has been corrected and included into the main scan. Fig 2-40 shows the result from this test. The intensity is measured for each channel while the light source travels along the DNB trajectory by 1 mm per shot, so the major radius in the horizontal axis on the plot is equivalent to the shot number. There are 10 large peaks from 10 MSE channels. By virtue of this fine-
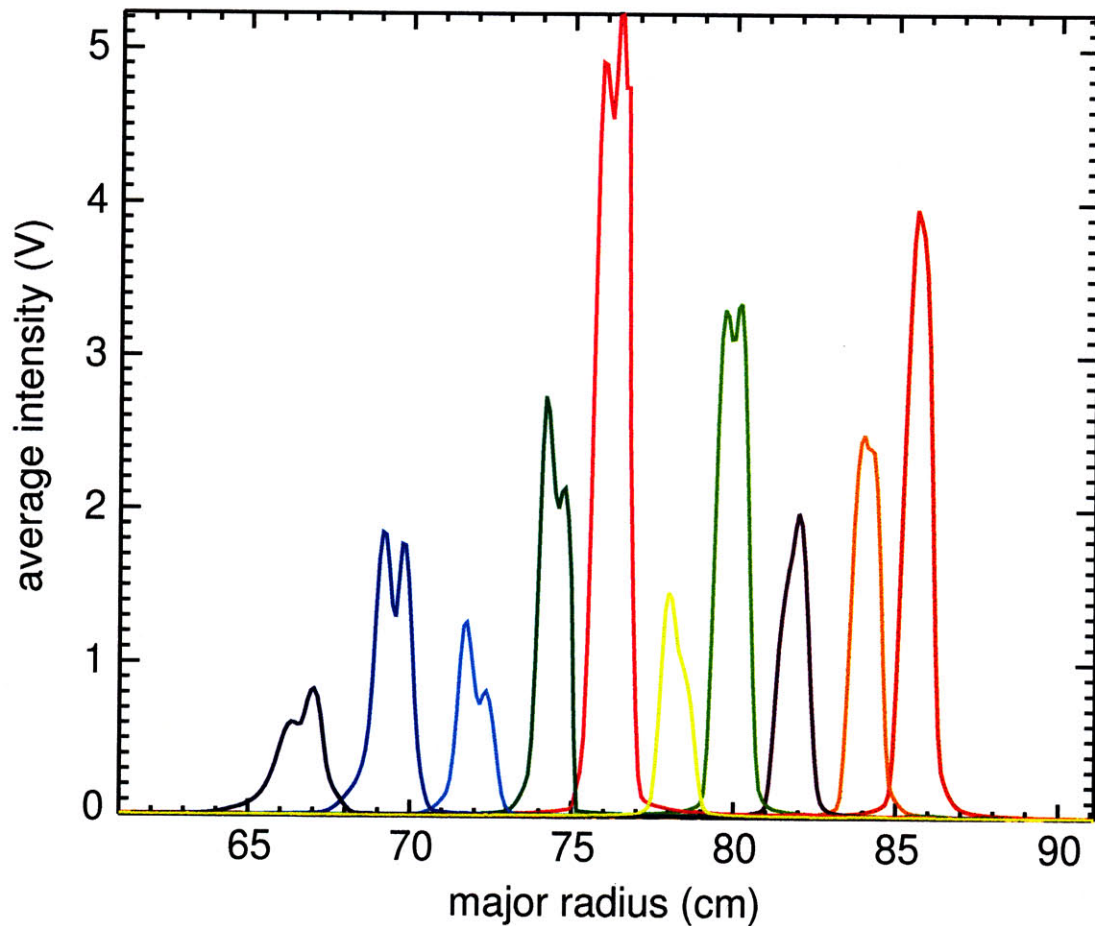
Figure 2-40: Result of intensity weighting calibration. The intensity is measured for each channel while the 1 mm × 60 mm-slit light source shown in Fig 2-39 is translated along the DNB trajectory on the midplane by 1 mm per shot. The signal from each channel, after the background subtraction, is plotted here as a function of major radius (that is, shot number) in a different color. The saturated shots have been taken care of by replacing them with the shots taken separately with a lower bias voltage and with a corrected magnitude. Note there are ten peaks from ten MSE channels.

distance scan, it is noted that the two columns of fibers that constitute one channel are clear reflected by two small peaks in each large peak.

The intensity profile from each channel shown in Fig 2-40 can be Gaussian-fit. It is fair to do a double-Gaussian fit since a channel has two small peaks from the two columns of fibers. Figs 2-41 and 2-42 show the single (cyan) and double (red) Gaussian fits overplotted on the measured profile (black dashed line) for four MSE channels. The coefficients and the FWHMs from each fit are written on the plot. It is apparent from Figs 2-41 and 2-42 that the double Gaussian fits the data much better than the single one. The FWHM from each Gaussian in the double Gaussian fit can be regarded as the effective diameter of the footprint for a single fiber in a channel and it ranges from $0.5 \sim 0.6$ cm. Therefore, the assumption of $A_{ff} = \pi(0.25)^2$ cm^2 made for Eqn 2.31 seems to be valid. From the fit, it is straightforward to take the useful information such as (1) relative optical throughput by observing the Gaussian peak, (2) the effective 'width' of the channel footprint by observing the Gaussian width and FWHM, and (3) the major radius of the channel by observing the Gaussian center.

For example, the major radius estimated from this intensity weighting calibration can be compared with those from the invessel 'backlighting' calibration where a sheet of graph paper is installed along the DNB trajectory and a light source shines through the other end of the fibers to make an image on the graph paper. The major radius is estimated by reading the position of the image on the paper. Fig 2-43 (a) plots three sets of the major radii as a function of channel order: one from the backlighting position calibration (black) and the other two from the single (red) and double (blue) Gaussian fit of the intensity weighting calibration.

For the double Gaussian fit, the centers of two constituent Gaussians have been averaged to produce a single center position. It is shown that for the purpose to define the major radii, both the single and the double Gaussian fits effectively give the same result. Fig 2-43 (b) shows this where the difference in the major radius between the backlighting and the intensity weighting calibrations is plotted. Although there is up to 6-mm difference between two calibrations, the difference between the two Gaussian fits from the intensity weighting calibration is small except for some outer channels
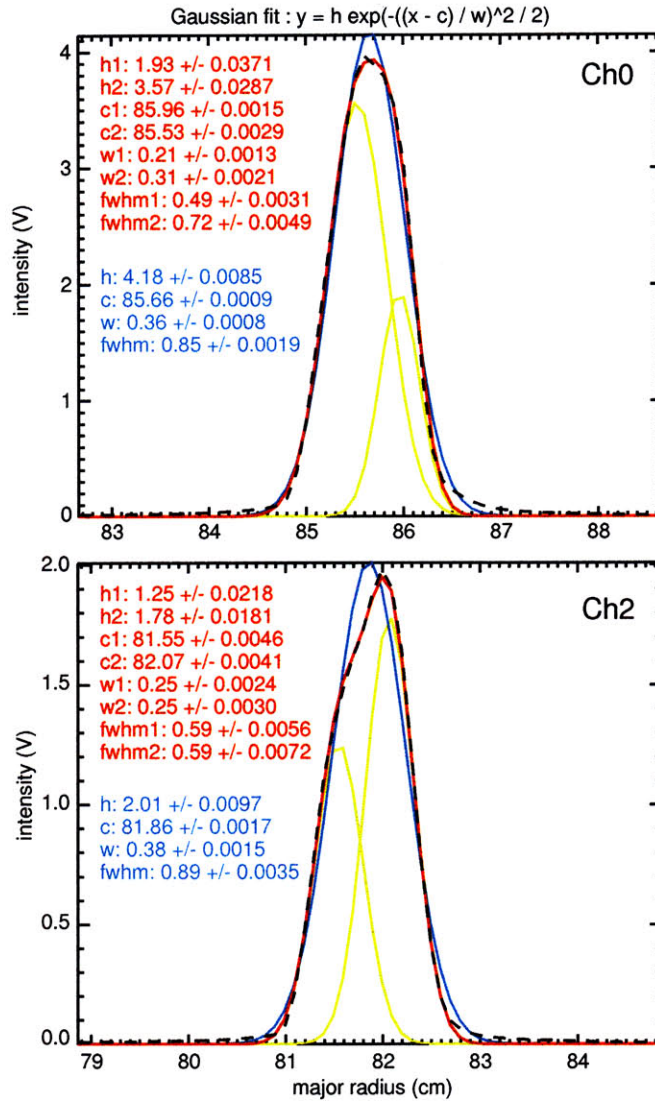
Figure 2-41: Double (red) and single (cyan) Gaussian fits for the intensity profile shown in Fig 2-40 (black dashed) for the MSE channels 0 and 2 (in major radius order). The fit coefficients and the FWHM's are given on each plot. The two yellow fits are the two 'small' Gaussian fits that constitute the double Gaussian by summing them (red).

Gaussian fit : y = h exp(-((x - c) / w)^2 / 2)

Ch9

h1: 0.89 +/- 0.0131
h2: 1.31 +/- 0.0110
c1: 78.49 +/- 0.0053
c2: 77.95 +/- 0.0035
w1: 0.27 +/- 0.0029
w2: 0.22 +/- 0.0028
fwhm1: 0.64 +/- 0.0069
fwhm2: 0.52 +/- 0.0065

h: 1.40 +/- 0.0077
c: 78.18 +/- 0.0020
w: 0.38 +/- 0.0017
fwhm: 0.90 +/- 0.0041

Ch6

h1: 1.22 +/- 0.0092
h2: 0.74 +/- 0.0092
c1: 71.73 +/- 0.0042
c2: 72.42 +/- 0.0062
w1: 0.27 +/- 0.0032
w2: 0.24 +/- 0.0045
fwhm1: 0.63 +/- 0.0076
fwhm2: 0.57 +/- 0.0106

h: 1.07 +/- 0.0060
c: 71.95 +/- 0.0026
w: 0.47 +/- 0.0023
fwhm: 1.11 +/- 0.0054
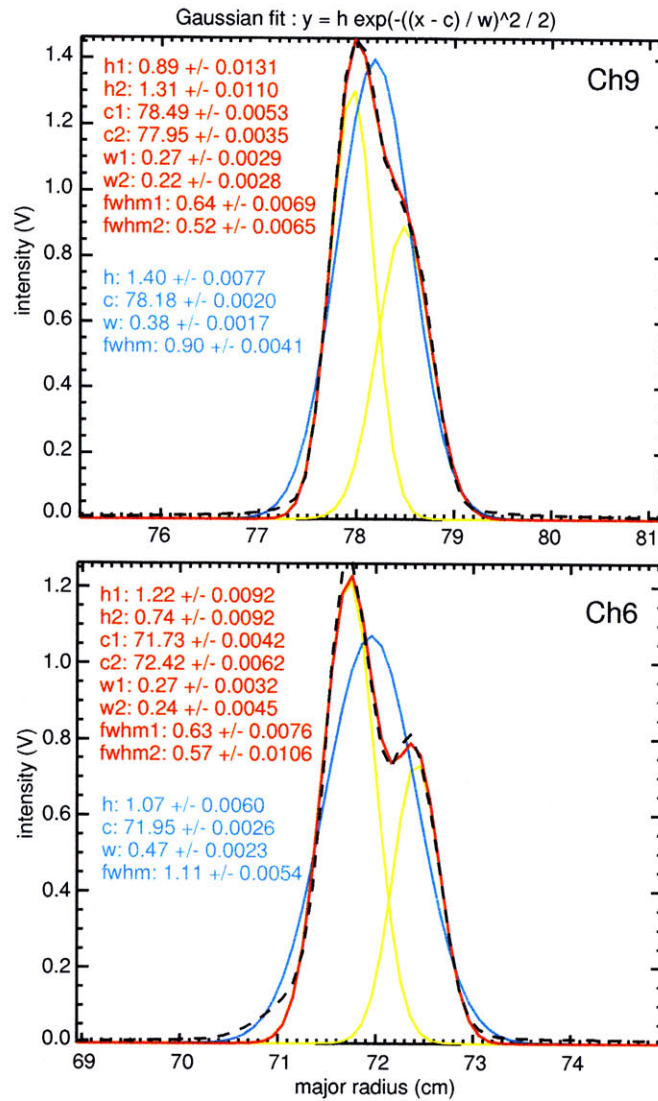
Figure 2-42: Double (red) and single (cyan) Gaussian fits for the intensity profile shown in Fig 2-40 (black dashed) for the MSE channels 9 and 6 (in major radius order). The fit coefficients and the FWHM's are given on each plot. The two yellow fits are the two 'small' Gaussian fits that constitute the double Gaussian by summing them (red).

(a) Major radii from Intensity weighting vs backlighting (cm)

Backlighting (Jan 8, 2007)
Intensity weighting with single Gaussian (Feb 14, 2007)
Intensity weighting with double Gaussian (Feb 14, 2007)

(b) Difference in major radius (backlighting - intensity weighting; cm)

Single Gaussian
Double Gaussian

channel order (core -> edge)
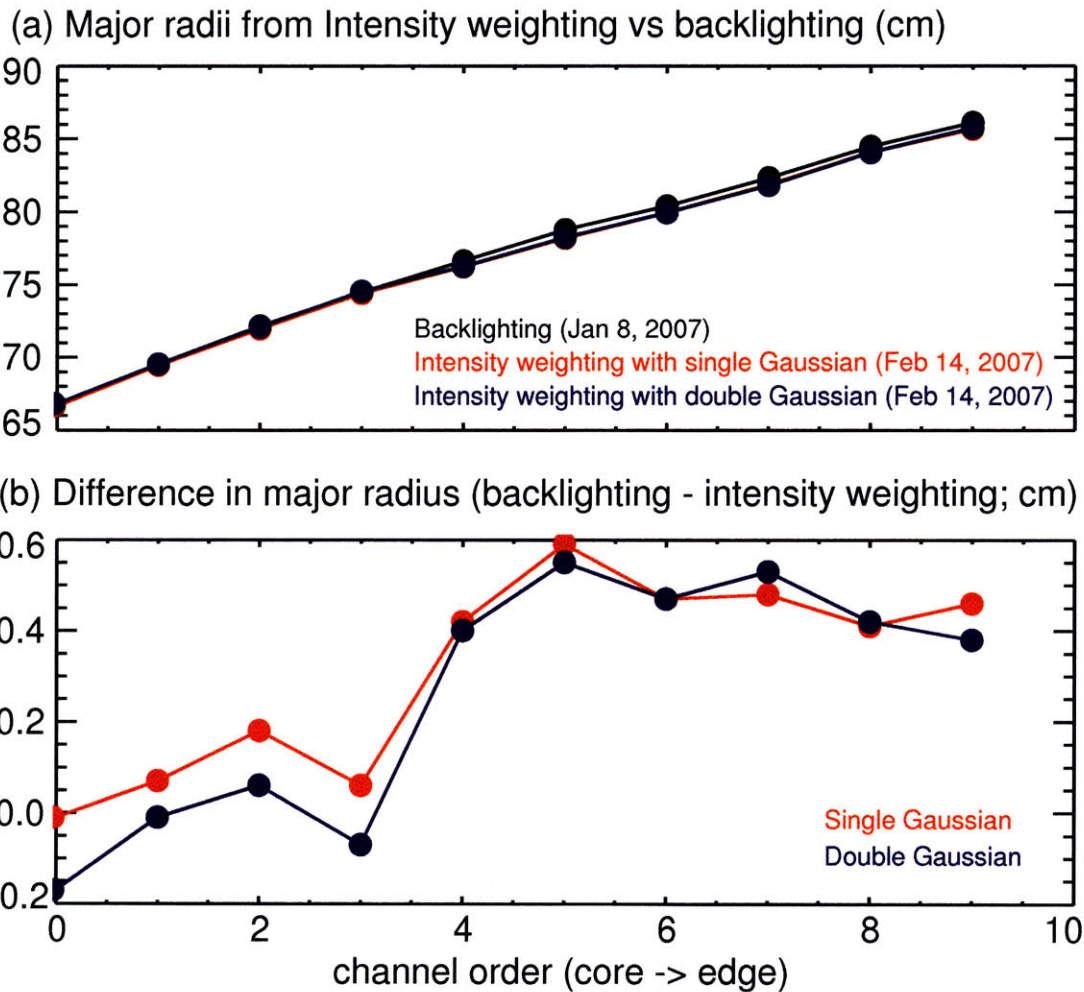
Figure 2-43: (a) Major radii as a function of channel order estimated from the invessel backlighting calibration (black) and the signle (red) and double (blue) Gaussian fits of the intensity weighting calibration. (b) The deviation in the major radius of the single (red) and the double (blue) Gaussian fits from the backlighting calibration.

where the differences are about < 2 mm.

2.2.3 Caveats in analyses

As the last part of Section 2.2, two issues are discussed related to analyzing the MSE raw intensity data, more specifically, to inferring the magnitudes of harmonics of interest from the modulated signal. One issue is a non-negligible error in the pitch angle in a long-pulse (e.g., 8-sec) shot when the fundamental frequency is estimated over the entire shot. The other issue relates to the advantage of using the 'numerical-lock-in' technique, which has been adopted in analyzing the MSE data in C-Mod, against nominal FFT techniques.

Effect of errors in reference frequency

During the invessel calibration activities performed in September to October in 2007, it was found that on some long-pulse (8-sec) shots, the measured polarization angle drifted by as much as $0.2°$ to $0.3°$ under conditions where the actual polarization angle was constant. This calibration activity was originally designed to evaluate the effect of instant heating onto the MSE object lens on the polarization measurement. In order to provide a time long enough to apply heat during a shot, the data acquisition time was increased from 2 to 8 sec. No correlation was found between instant heat and the measured polarization angle. Instead, an anomalous drift was found which did not exist nominal 2-sec-long shots. Fig 2-44 shows the time evolution of the measured polarization angle from 8-sec-long shots. This is a separate set of shots taken without any heat after the non-thermal drift effect became suspicious in the heated shots. As shown in the figure, up to $0.3°$ drift within a shot is observed in many of these shots.

It turns out that this drift is caused by a small error in the frequency of the reference sinusoidal waveform calculated in the process of so-called 'numerical lock-in' analysis. The PEM frequency can be determined quite accurately by digitizing and fitting the drive signal to the PEM optical heads. As shown in Table 2.8, over the course of an 8-sec integration period, the period of the drive signal changes by
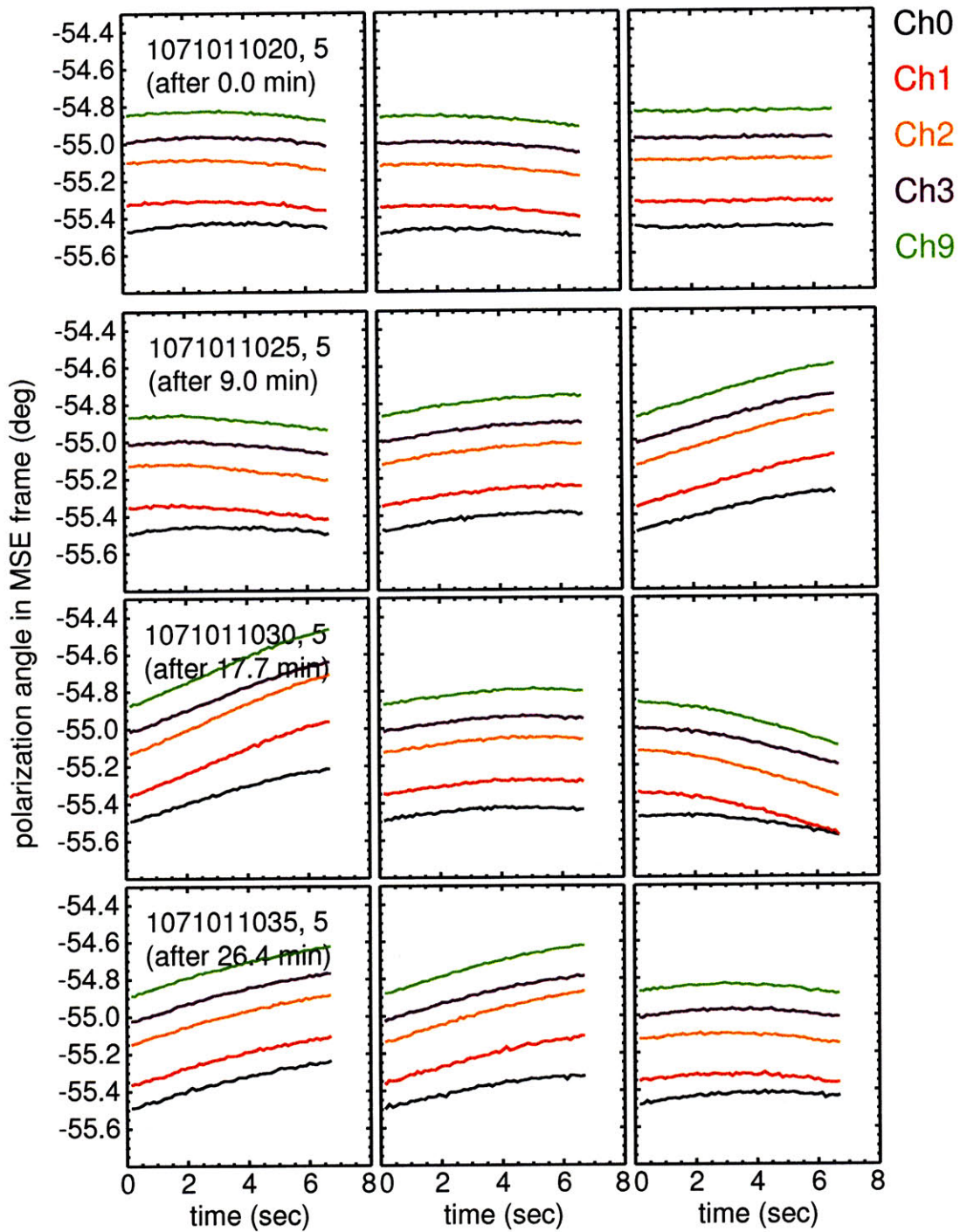
Figure 2-44: Measured polarization angle vs time for 5 MSE channels from 8-sec shots The shot number, mse 'analysis number', and the time elapsed after the first shot are given for the first shot on each row.

time	PEM-1	PEM-2
(sec)	(μ sec)	(μ sec)
0.1 - 0.6	49.589279	45.108196
1.1 - 1.6	49.589279	45.108196
2.1 - 2.6	49.589275	45.108196
3.1 - 3.6	49.589275	45.108192
4.1 - 4.6	49.589275	45.108192
5.1 - 5.6	49.589275	45.108192
6.1 - 6.6	49.589272	45.108192
0.1 - 6.9	49.589275	45.108192

Table 2.8: Period of photo elastic modulators on Shot 1071011022 as determined from their drive waveforms.

only a few parts in 10^{-8}. However, this small variation is multiplied by the length of the shot and becomes large enough to produce an error of a few tenth of degree in the polarization angle.

Consider a signal $S(t)$ that is the sum of many harmonics,

$$S(t) = \sum_j A_j \cos(2\pi f_j t), \qquad (2.33)$$

where f_j is a harmonic in Hz. In the usual numerical lock-in analysis, a reference waveform $R(t)$

$$R(t) = \cos(2\pi f' t) \qquad (2.34)$$

is constructed from the measured PEM frequency f' which may differ slightly from the actual PEM frequency f where $f' = f + \Delta f$ and $\Delta f / f \ll 1$. The amplitude at frequency f at a particular time $t = t_0$ is determined by numerically multiplying the measured $S(t)$ by $R(t)$ and integrating over one period, that is,

$$
\begin{aligned}
A_{cal} &= 2f \int_{t_0}^{t_0+1/f} S(t) R(t) \, dt \\
&= 2f \int_{t_0}^{t_0+1/f} A_{real} \cos(2\pi f t) \cos(2\pi (f + \Delta f)) \, dt
\end{aligned}
\qquad (2.35)
$$

$$= 2f \int_{t_0}^{t_0+1/f} A_{real} \cos(2\pi ft) \left[\cos(2\pi ft)\cos(2\pi t\Delta f) - \sin(2\pi ft)\sin(2\pi t\Delta f)\right] \, dt,$$

where A_{real} is true amplitude at frequency f in the input signal. If we take $\Delta f \sim 10^{-3}$ Hz based on Table 2.8, $2\pi t\Delta f \sim 10^{-2} \ll 1$, then using $\sin x \approx x$ and $\cos x \approx 1 - x^2/2$ with $x \ll 1$, Eqn 2.36 is approximated to

$$A_{cal} = 2f A_{real} \int_{t_0}^{t_0+1/f} \left[\cos^2(2\pi ft)\left(1 - \frac{(2\pi t\Delta f)^2}{2}\right) - \frac{1}{2}\sin(4\pi ft)(2\pi t\Delta f)\right] \, dt.$$

$$(2.36)$$

A handful of algebra simplifies this into

$$A_{cal} = A_{real}\left[1 - \frac{(2\pi t_0 \Delta f)^2}{2} + \frac{1}{2}\left(\frac{\Delta f}{f}\right)\cos(4\pi f t_0)\right].$$

$$(2.37)$$

Note that the error in the reference frequency, Δf, results in a finite deviation in the calculated magnitude of that harmonic in the form of the last two terms in Eqn 2.37. It is also noted that the magnitudes of the last two terms are compared as follows:

$$\frac{(2\pi t_0 \Delta f)^2}{2} = 19.74(t_0 \Delta f)^2 \sim 10^{-3}$$

$$(2.38)$$

$$\frac{1}{2}\left(\frac{\Delta f}{f}\right)\cos(4\pi f t_0) \sim 10^{-8}$$

$$(2.39)$$

with the assumptions of $\Delta f \sim 10^{-3}$ Hz, $f \sim 10^4$ Hz, and $t_0 = 6.5$ sec, making Eqn 2.37 further simplified to be

$$A_{cal} = A_{real}\left[1 - \frac{(2\pi t_0 \Delta f)^2}{2}\right].$$

$$(2.40)$$

It is tempting to ignore even the second term in Eqn 2.40 since it is still much smaller than unity. The question is how much error this small term ($\sim 10^{-3}$) can cause in the final polarization angle. Recalling the polarization angle $\gamma = 0.5\tan^{-1}(A_1/A_2)$, where A_1 and A_2 are the amplitudes of the second harmonics of the two PEMs, the error in the polarization angle, $\Delta\gamma$, caused by the errors in A_1 and A_2 (ΔA_1 and ΔA_2,

respectively) can be written as

$$
\begin{aligned}
\Delta\gamma &= \sqrt{\left(\frac{\partial\gamma}{\partial A_1}\Delta A_1\right)^2 + \left(\frac{\partial\gamma}{\partial A_2}\Delta A_2\right)^2} \\
&= \left|\frac{A_1}{A_2}\right| \cos^2\left(\tan^{-1}\left(\frac{A_1}{A_2}\right)\right) \sqrt{\frac{1}{4}\left(\frac{\Delta A_1}{A_1}\right)^2 + \left(\frac{\Delta A_2}{A_2}\right)^2} \\
&= \left|\frac{A_1}{A_2}\right| \cos^2\left(\tan^{-1}\left(\frac{A_1}{A_2}\right)\right) \sqrt{\frac{1}{4}(\delta A_1)^2 + (\delta A_2)^2},
\end{aligned}
\tag{2.41}
$$

where the relative errors in A_1 and A_2 are denoted as δA_1 and δA_2, respectively, and Eqn 2.40 indeed provides the general form of δA which is simply the second term in the equation. Using this general form of δA and the relation given in Eqn 2.38 yields

$$
\Delta\gamma = 19.74\, t_0^2 \left|\frac{A_1}{A_2}\right| \cos^2\left(\tan^{-1}\left(\frac{A_1}{A_2}\right)\right) \sqrt{\frac{1}{4}(\Delta f_1)^4 + (\Delta f_2)^4},
\tag{2.42}
$$

where Δf_1 and Δf_2 are the errors in the calculated frequency for the two PEMs. Taking $t_0 = 6.5$ sec, which is the actual analysis period in these 8-sec shots, $A_1/A_2 \approx 2$, which is typically true for these shots, and finally, $\Delta f_1 = a_1 \times 10^{-3}$ Hz and $\Delta f_2 = a_2 \times 10^{-3}$ Hz, where a_1 and a_2 are positive constants of order unity, approximiates Eqn 2.42 to be

$$
\Delta\gamma \approx 0.019\sqrt{\frac{a_1^4}{4} + a_2^4}
\tag{2.43}
$$

where $\Delta\gamma$ is in degree. For example, $a_1 \approx 2.4$ for 40 kHz and $a_2 \approx 3.9$ for 44 kHz in Shot 1071011030, one of the 8-sec-long shots. Then this gives the error in the polarization angle of 0.29^o from Eqn 2.43, which is very similar to what is observed for this shot shown in Fig 2-44.

To avoid this error in calculating the frequency, the existing analysis procedure has been modified such that the period of the PEM drive is evaluated in piece-wise steps of 200 ms, rather than the previous approach of evaluating it over the entire shot, and the shots given in Fig 2-44 have been re-analyzed with this new procedure. Fig 2-45 shows the re-analyzed results and it is clear that the within-shot drift has

128

been eliminated.

Iterative Fast Fourier Transform

During the initial APD performance test in 2007, an LED was connected to a function generator with a certain frequency (say, 44 kHz) and its intensity was measured via the APD with different bias voltages and the magnitude of 44 kHz component is calculated. At first, the 44 kHz component in the raw intensity was fast Fourier transformed using the IDL function *fft.pro*. For a time-varying signal on a uniform time grid of N time points with time interval Δt, the *fft.pro* returns the complex amplitudes of components along a fixed frequency grid f_j

$$f_j = 0, \ \frac{1}{N \Delta t}, \ \frac{1}{N \Delta t}, \ \cdots. \tag{2.44}$$

In the nominal approach, one looks for the FFT component which has the largest amplitude in the neighborhood of 44 kHz but it turns out that this approach is not reliable in calculating the real amplitude of the frequency. The underlying problem is that the actual frequency does not, in general, exactly equal any of the elements of the FFT fixed-frequency grid. This causes the calculated 44 kHz amplitude to slightly vary depending on both the time interval and the number of samples for the FFT as shown in Fig 2-46 where the normalized 44 kHz amplitude is plotted as a function of bias voltage (a) for four different time intervals with a fixed number of samples and (b) for four different numbers of samples with a fixed time interval. Although the amplitudes roughly follow the gain curve from its spec sheet (dashed line), the values fluctuate with different time intervals and samples. An alternative approach might be to (for example) fit a Gaussian or some other smooth function to the FFT amplitudes in the neighborhood of 44 kHz, and then numerically compute the maximum of the fitted curve.

To avoid this problem, the following iterative procedure has been added to the FFT process:

1. An estimate of the actual frequency and a range of frequencies to search near
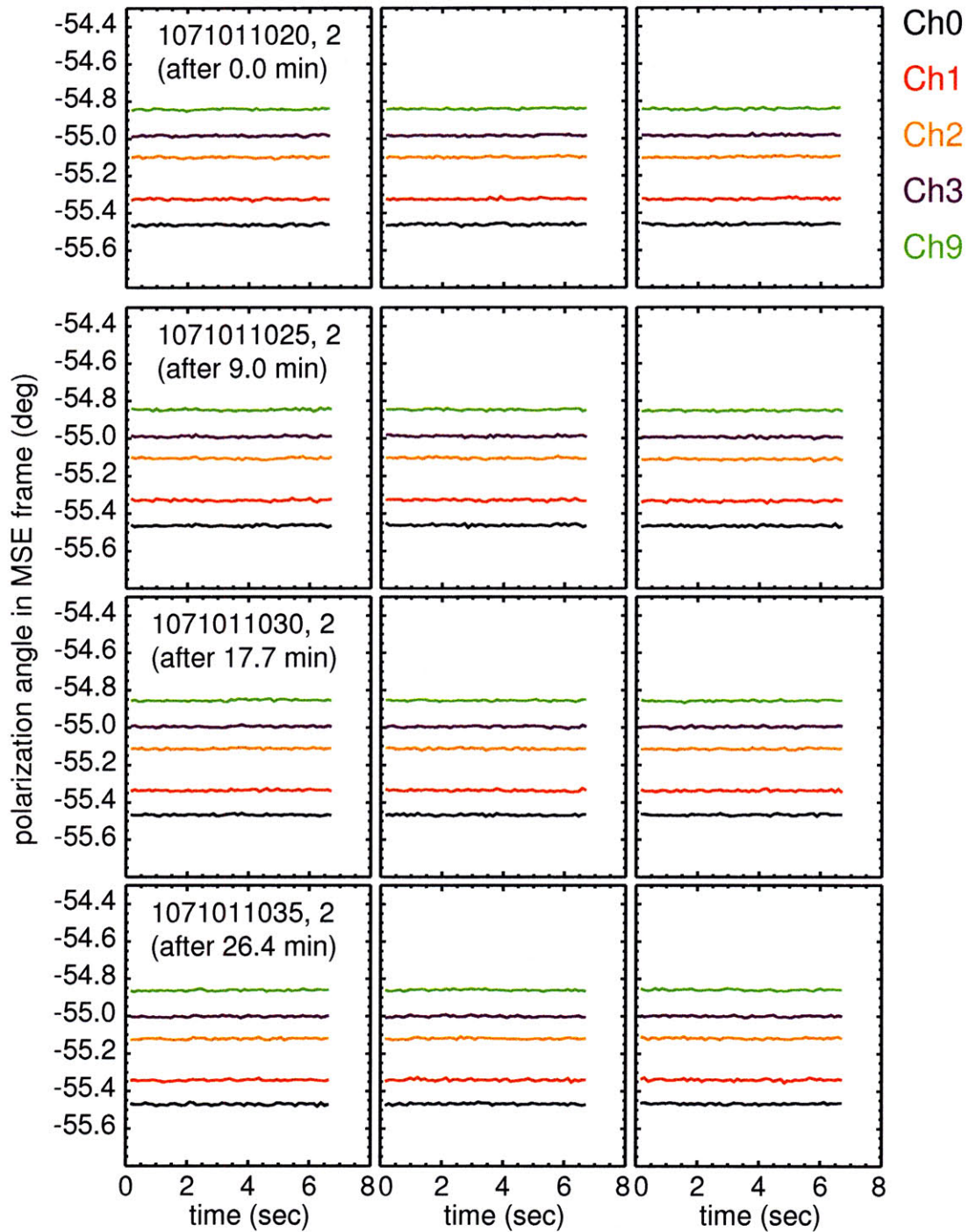
Figure 2-45: Measured polarization angle vs time for 5 MSE channels from 8-sec shots The shot number, mse 'analysis number', and the time elapsed after the first shot are given for the first shot on each row. These are the same shots shown in Fig 2-44 but with a new analysis.
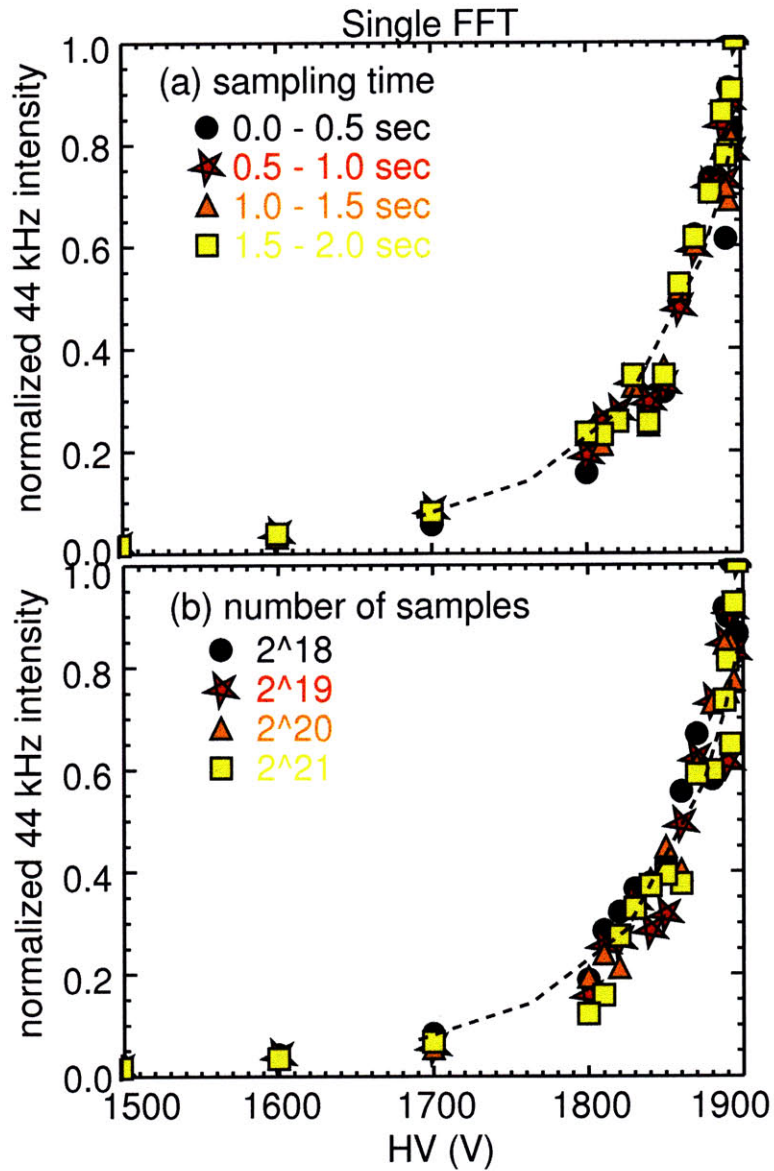
Figure 2-46: Normalized 44 kHz components calculated using the IDL function *fft.pro* as a function of bias voltage from an APD performance test using an LED (a) for 4 different time intervals with a fixed number of samples ($2^1 9$) and (b) for 4 different numbers of samples with a fixed time interval (2 sec). The dashed line is the APD gain curve on its spec sheet.

this estimate are provided by a user.

2. The procedure computes the FFT amplitude for a collection of frequencies in the specified range.

3. Over this range, it identifies the maximum FFT amplitude and the frequency at which the maximum occurs.

4. It then defines a narrower range of frequencies to search, near the maximum it just identified.

5. It computes another set of FFT amplitudes for this narrower range of frequencies.

6. It identifies the maximum FFT amplitude from this narrower set, and the frequency at which it occurs.

7. It repeats steps (4) $\sim$ (6) until the maximum amplitude changes by an amount less than a defined tolerance.

Fig 2-47 shows the 44 kHz amplitude calculated by this procedure, again (a) for four different time intervals with a fixed number of samples and (b) for four different numbers of samples with a fixed time interval. This is directly compared with Fig 2-46 and shows the amplitude calculated this way is independent of both the time interval and the number of samples. The APD performance tests introduced in Sec 2.1.1 indeed use this method to find 40 and 44 kHz amplitudes.

2.3   Low signal-to-background ratio

It is routinely observed that the MSE signal-to-noise level is often marginal, particularly in high density, ICRF-heated plasmas. The MSE raw signals are typically 'binned' over $8 \sim 10$ msec and the numerical lock-in procedure, introduced in Sec 2.2.3, is applied to this short individual bins to produce amplitudes of desirable harmonics. The length of this time bin is long enough to contain as many as 400 periods for, say, 44 kHz components

The MSE *raw* signal, i.e., the signal read by the digitizer and prior to the numerical lock-in procedure, typically increases less than a factor of 2 when the beam is on,
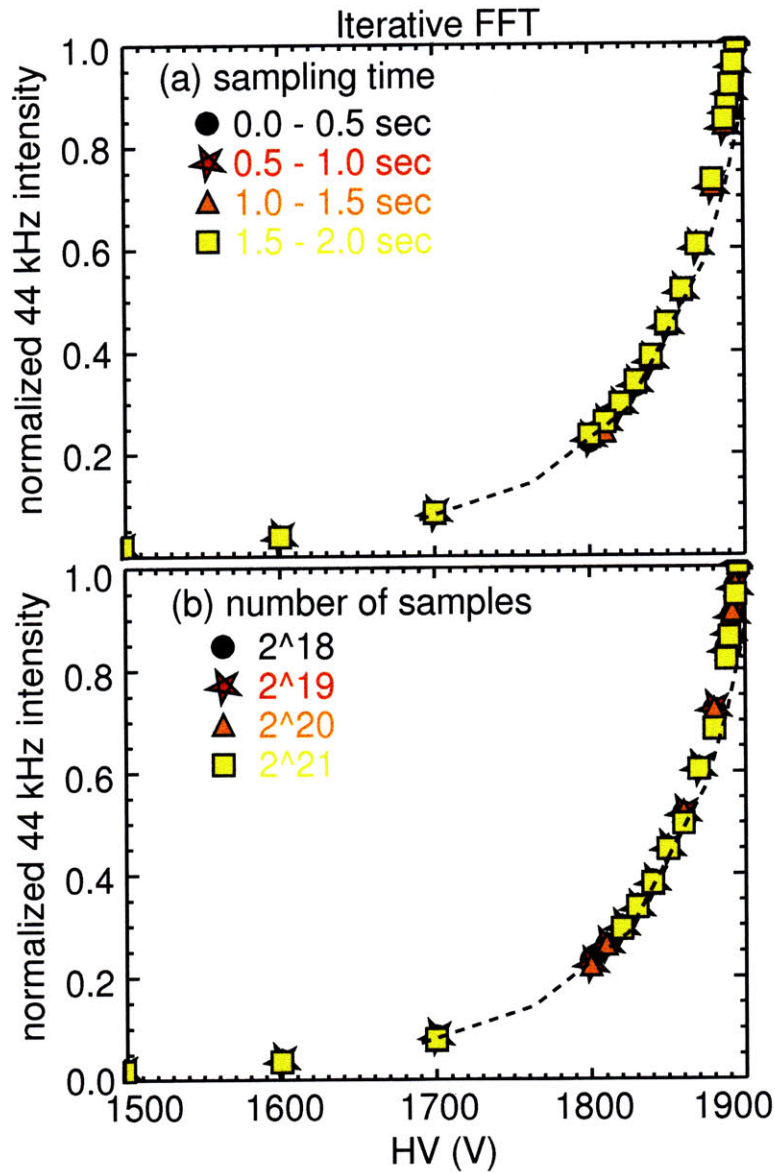
Figure 2-47: Normalized 44 kHz components, as a function of bias voltage, calculated using the IDL function *fft.pro* combined with an iterative procedure to locate the exact frequency of the incident signal from an APD performance test using an LED (a) for 4 different time intervals with a fixed number of samples (2^{19}) and (b) for 4 different numbers of samples with a fixed time interval (2 sec). The dashed line is the APD gain curve on its spec sheet.

compared with the level when the beam is off even at densities as low as $nl_{04} \approx 3 \times 10^{19}$ m^{-2}. To measure the background signal, the DNB is modulated normally for about 70 msec on and 25 msec off during a $\sim$ 1.7-sec-long beam, producing about $7 \sim 9$ 'micro-binned' measurements within one pulse of the beam. The average value of the measured pitch angles over one module (so called, 'macro bin') and its standard deviation of the mean are typically used in reporting the final pitch angle and its statistical uncertainty, respectively.

During injection of the diagnostic beam, the MSE diagnostic can be illuminated by the following incoherent sources of photons:

- The 'signal', i.e. polarized photons from the beam-plasma interactions (Doppler-shifted Stark-splitted Balmer-α emission from the beam atoms),
- Polarized background light, i.e. Bremsstrahlung radiation that becomes partially polarized upon reflection from the RF antenna,
- Unpolarized background light, i.e. Bremsstrahlung radiation that enters the diagnostic directly, without reflection from a metallic surface,
- Impurity line radiations from charge exchange with wall-recycled neutrals,
- D_2 molecular line radiation; and
- Thermal H_α.

Note that the last three items can also be polarized or unpolarized and are introduced in Sec 2.1.3 as a possible explanation of the observed correlation of the MSE background with H_α signal. Obviously, when the beam is off, only the first source of photons disappear, and the rest of the sources should remain. In order to eliminate these unwanted background components from the total signal measured during the beam pulse, the 40 and 44 kHz amplitudes of the background light before the start of and after the termination of the beam pulse are measured and then linearly interpolated to estimate the level of the 40 and 44 kHz amplitudes from background light during the beam pulse. This approach is based on the reasonable assumption that the beam does not affect the level of the background light, and thereby the measured pitch angle. For example, the effect of the impurity line radiations from

charge exchange with beam neutrals was tested on Run 1050830 where the comprison was made in the measured pitch angle with and without beam-excited Fluorine line radiations. No effect in the measurement was detected in this test.

An important limitation in this approach is that it assumes a simple linear variation in the background signal during a single beam pulse. This depends on not only the length of the beam pulse but also the condition of the plasma during that interval. For example, if the beam pulse is 100 msec long and the plasma density fluctuates rapidly somehow, the linear interpolation based on the measurement on both ends of the beam pulse may be different from the real variation of the background. This is especially true at the start of RF heating and at L-H transitions whose characteristic time scale over which the density changes is sometimes quite rapid. For this reason, following the observation that the MSE background signal correlates with H_α, an alternate interpolation scheme was developed based on the variation of the H_α signal. This gives a reasonable success as shown and discussed in Fig 2-32 in Sec 2.2.1.

The importance on accurately estimating the background level during the beam-on time can be appreciated from the database study performed for the shots from FY2008 with the DNB operating, where the sensitivity of the pitch angle error is scaled with the signal-to-background ratio. Out of 326 shots with the DNB have about 4000 macro time bins extracted, the typical sizes of the macro bins ranging 40 $\sim$ 80 msec. Figs 2-48 and 2-49 show the statistical macro-bin error in pitch angle for 4 MSE channels (2 channels per figure) as a function of signal-to-background ratio, $\sqrt{(A_{40}^{sig})^2 + (A_{44}^{sig})^2}/\sqrt{(A_{40}^{bkg})^2 + (A_{44}^{bkg})^2}$, where the superscripts sig and bkg indicate the background-subtracted signal and the background, respectively. The background amplitudes are from the linear interpolation based on the background signals before and after each beam module. The time points are from 0.5 to 1.7 sec in each pulse but include all the moments with ICRF heating and/or LH current drive. The minimum size of the macro bin is 50 msec. Plots (a) and (b) actually display the same data but (a) is sorted with 3 different density ranges, nl_{04} (10^{20} m^{-2}) = 0.2 $\sim$ 0.4 (white), 0.6 $\sim$ 0.8 (red), and 1.0 $\sim$ 1.2 (orange), and (b) is sorted with 5 different DNB current ranges, I_{DNB} (A) < 4 (white), 4 $\sim$ 5 (red), 5 $\sim$ 6 (orange), 6 $\sim$ 7 (violet), and >

7 (yellow green) (where no data happened to be available for $I_{DNB} > 7$ A). The solid line behind the data point is the linear fit *on* this log scale. Note that only three discrete density ranges have been chosen in these figures so as to avoid extreme denseness with points which may prevent easy observations. It has been verified that using these three density ranges only does not lose generality. The following points can be made by observing Figs 2-48 and 2-49:

1. The pitch angle error is a very sensitive function of signal-to-background ratio, requiring to have singal-to-background ratio $\gtrsim 100$ in order to have errors $\lesssim 0.1^{o}$ (dashed horizantal lines in each plot).

2. As seen from plots (a) in each figure, the signal-to-background ratio, as expected, is strongly correlated with the plasma density.

3. As seen from plots (b) in each figure, the signal-to-background ratio, as epxected, is strongly correlated with the beam current.

4. The above two comments (2 and 3) explain the variation of each other observed for the data points within the same range (of either density or beam current), i.e. the variation for the data points within $0.2 < nl_{04}$ (10^{20} m^{-2}) < 0.4 from plots (a), for example, is due to different beam current observed from the corresponding plots (b).

5. The quality of the current MSE data is limited by very low signal-to-background ratios for almost all the channels. Only when the plasma density is in the range of $nl_{04} = 0.2 \sim 0.4 \times 10^{20}$ m^{-2} **with** reasonably high beam current $\gtrsim 6$ A do several inner channels (channels 9, 6, and 0) have acceptable pitch angle errors.

6. For several channels (for example, Channel 0), it is observed that the pitch angle errors with high density ($nl_{04} > 1 \times 10^{20}$ m^{-2}) decrease rapidly when the signal-to-background dereases, which seems counter-intuitive. This may be due to the fact that the signal-to-background ratio becomes less than unity, which means the background signal is stronger than the signal from the beam, making these data points meaningless. The fits have indeed done after these data points are excluded.
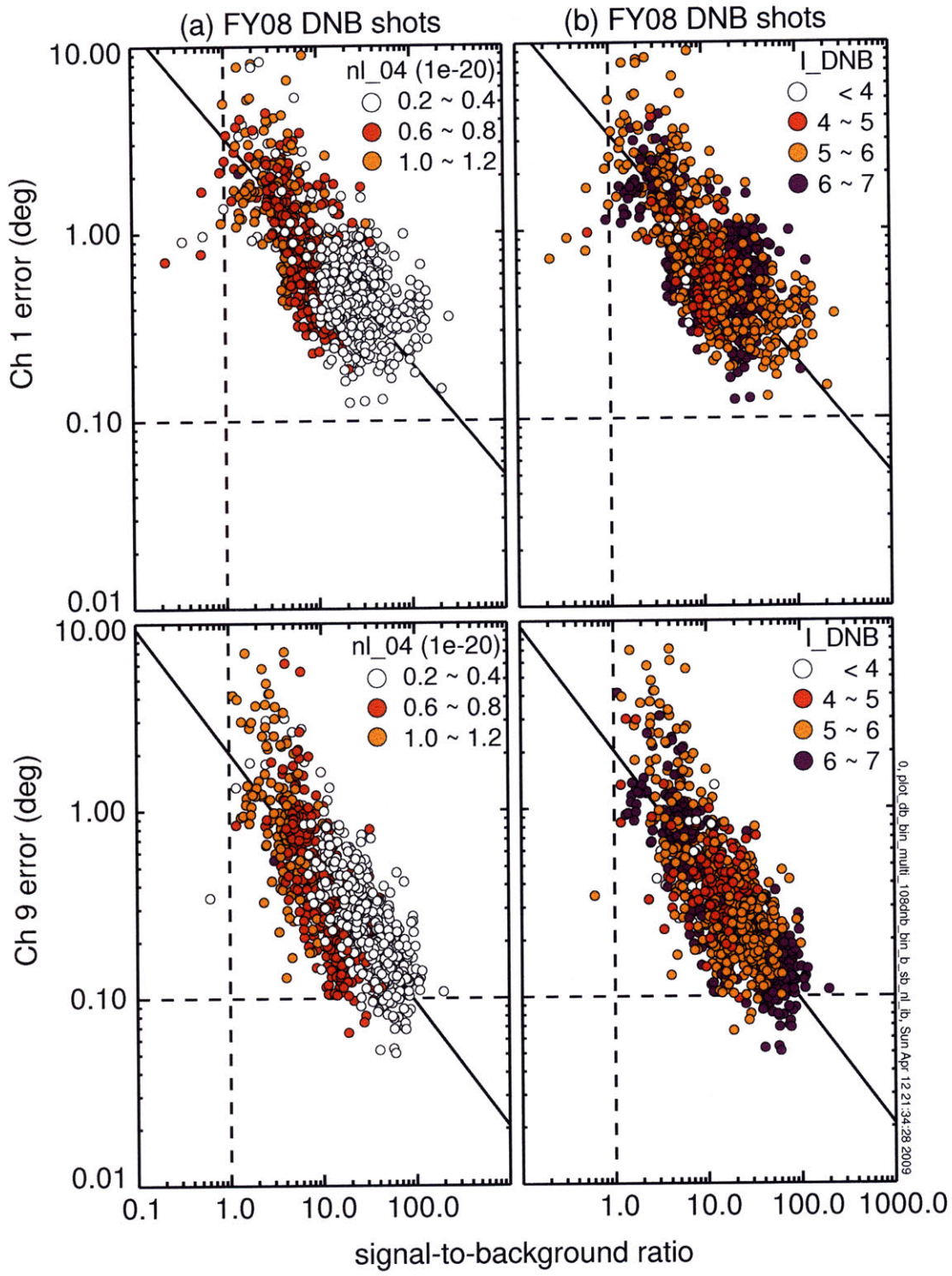
Figure 2-48: Macro-bin pitch angle error in degree vs signal-to-background ratio for the MSE channels 1 (Top: 87.21 cm) and 9 (Bottom: 81.75 cm) from FY2008 shots with DNB sorted by (a) 3 different density (nl_{04} in 10^{20} m^{-2}) ranges and (b) 4 different beam current (I_{DNB} in A) ranges. The solid line is the linear fit of the data *on* the log scale.
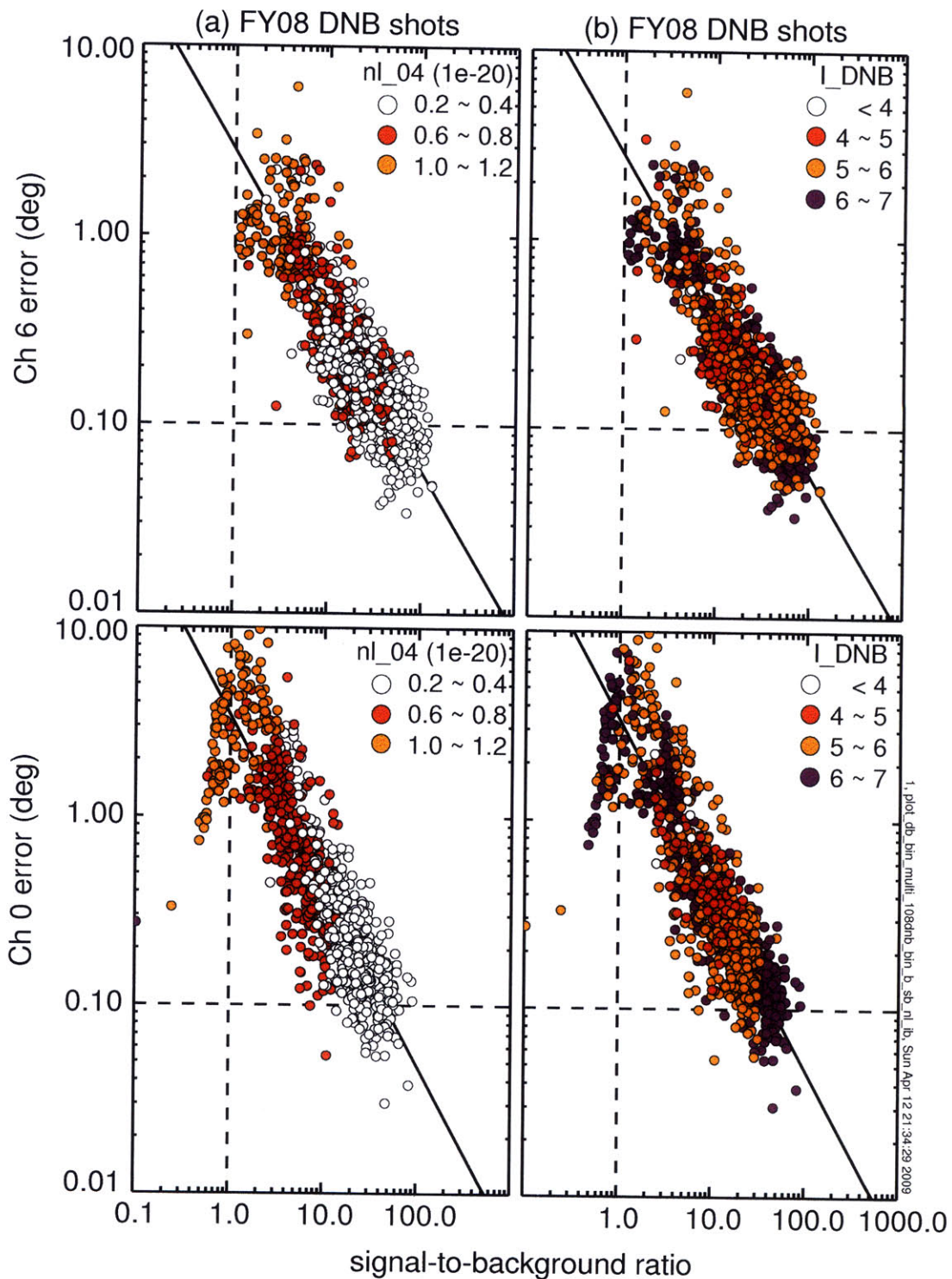
Figure 2-49: Macro-bin pitch angle error in degree vs signal-to-background ratio for the MSE channels 6 (Top: 75.74 cm) and 0 (Bottom: 68.94 cm) from FY2008 shots with DNB sorted by (a) 3 different density (nl_{04} in 10^{20} m^{-2}) ranges and (b) 4 different beam current (I_{DNB} in A) ranges. The solid line is the linear fit of the data *on* the log scale.

7. Note again these data do include those during H-mode with ICRF heating during which the density normally increases by a large factor. The data points within the highest range of nl_{04} (1.0 ~ 1.2; orange in plots (a)) are actually all from the shots with the ICRF heating and they still follow the overall scale except those with signal-to-background ratio < 1.

8. Finally, the linear slope in the fit slightly depends on channel, varying -0.59 at the edge (Channel 1) to -1.03 at the core (Channel 0). This implies that by the same amount of improvement in the signal-to-background ratio, the reduction in the error is larger at the core than at the edge. It is thought that this is due to the intrinsic channel dependence in the error multiplication factor in converting the polarization angle in the MSE frame into the pitch angle in the tokamak frame. This factor is the maximum at the edge and the minimum at the core as shown in Fig A-5.

In addition to the scaling of measurement error with the signal-to-background ratio, the errrors are plotted as a function of plasma density (nl_{04}) mainly for future experimental planning. Another elaborate mining of the same database was done to identify the plasma condition (L-mode, H-mode, or L-H transition) for each time bin based on the ratio of two soft x-ray channels looking near the plasma edge, edge electron and pressure gradients, and the time histories of nl_{04}, total radiated power ($Prad$), energy confinement time (τ_E), H_α intensity, ICRF, and LHCD powers.

Fig 2-50 shows the pitch angle error from 4 different MSE channels as a function of plasma density now with L-mode (white), H-mode (red), and L-H transition (orange) distinguished. Again, the minimum macro-bin timing is 50 msec and the data are taken between 0.5 and 1.7 sec in each pulse. Two more constraints have been applied in these plots: beam current > 6 A and the signal-to-background ratio greater than unity. As shown in the figure, the errors are roughly linearly scaled with the plasma density and larger during L-H transitions than either L or H-mode for the same plasma density. The effect of H-modes is a bit unclear.

A similar nl_{04}-scaling is given in Fig 2-51 to see the effect of the RF power. Since the L-H transitions generate larger errors for the same density, the data during the
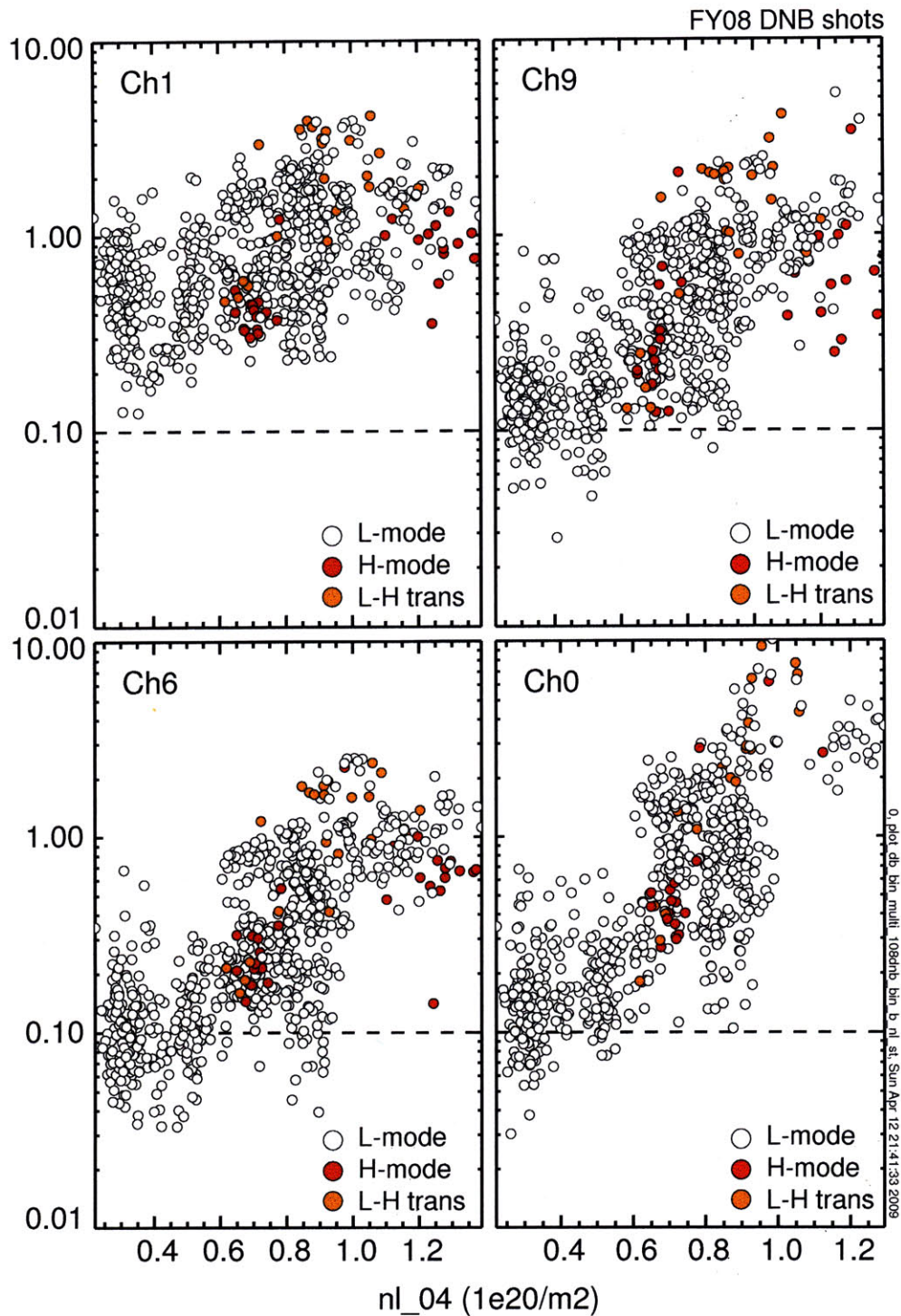
Figure 2-50: Macro-bin pitch angle error in degree vs plasma density, $nl_{04}(10^{20}$ m$^{-2})$ for the MSE channels 1 (87.21 cm), 9 (81.75 cm), 6 (75.74 cm) and 0 (68.94 cm) from FY2008 shots with DNB sorted by L-mode, H-mode, and L-H transition. Constraints are macro-bin timing > 50 ms, time between 0.5 ~ 1.7 sec, signal-to-background ratio > 1, and beam current > 6 A.

L-H transition have been excluded. Also excluded are the data during the H-mode although this may not affect the overall trend. The data now are distinguished by 4 different RF powers: < 0.1 MW (white), $1 \sim 2$ MW (red), and $2 \sim 4$ MW (orange). It is apparent from the figure, especially, around the region of $0.6 < nl_{04}(10^{20}$ m$^{-2})$ < 1.0, that the RF powers do generate larger error bars for the same density. An additional attempt has been made to distinguish the effect of ICRF antenna locations. Since none in the database has the ICRF power from the J antennas, the distinction has been made only between the other two, D and E, antennas. The ratio of the power from the E antenna to the total ICRF power, P_E/P_{ICRF}, has been used as a 'distinction parameter', denoting different ranges of this value with different symbols (< 0.5 with 'circle', $0.5 \sim 0.6$ 'square', $0.6 \sim 0.8$ with 'diamond', and > 0.8 with 'star'). No noticeable trend has been observed in the antenna dependence. It is thought that this data set is not adequate for this study mainly because of too small statistics available.

Finally, the pitch angle errors are scaled with the major radius and shown in Fig 2-52 for two different density ranges: $0.3 < nl_{04}(10^{20}$ m$^{-2}) < 0.6$ and $1.1 < nl_{04}(10^{20}$ m$^{-2}) < 1.3$. Shown in the figure are the data only from Ohmic L-mode plasmas since the L-H transitions and high ICRF powers tend to produce large errors. For both density ranges, the errors from the channels near the optical axis (~ 79 cm) are lower than those from inner and outer channels. It is conjectured that the beam attenuation and the local plasma density may be optimized to produce lower signal-to-background ratios around this region. Overall, however, it is somewhat surprising to see the errors are still large in most cases.
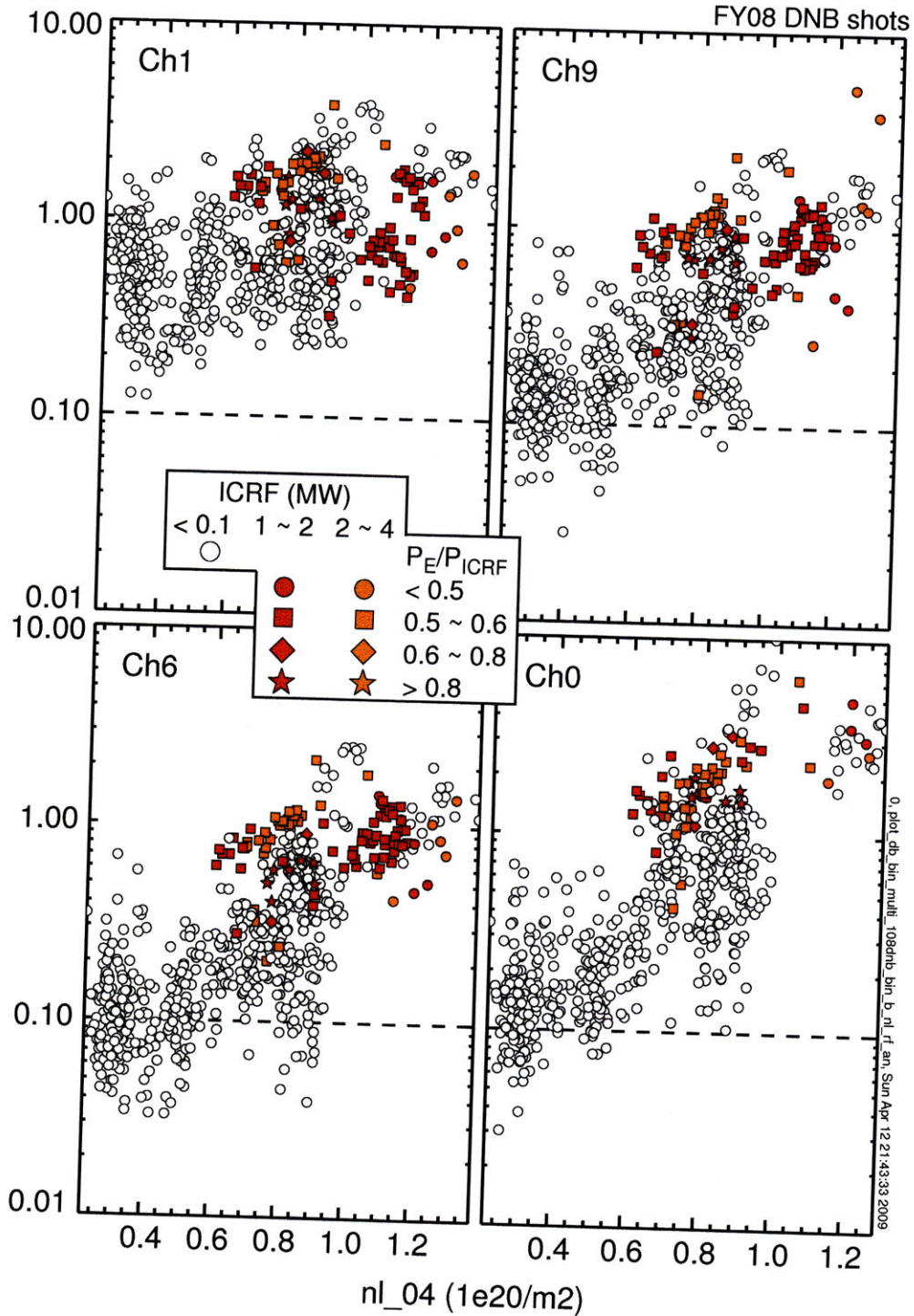
Figure 2-51: Macro-bin pitch angle error in degree vs plasma density, $nl_{04}(10^{20}$ m^{-2}) for the MSE channels 1 (87.21 cm), 9 (81.75 cm), 6 (75.74 cm) and 0 (68.94 cm) from FY2008 shots with DNB sorted by ICRF power with colors and by ICRF D and E antenna contribution with symbols. Constraints are macro-bin timing > 50 ms, time between 0.5 ~ 1.7 sec, signal-to-background ratio > 1, beam current > 6 A and only L-mode plasmas are shown.
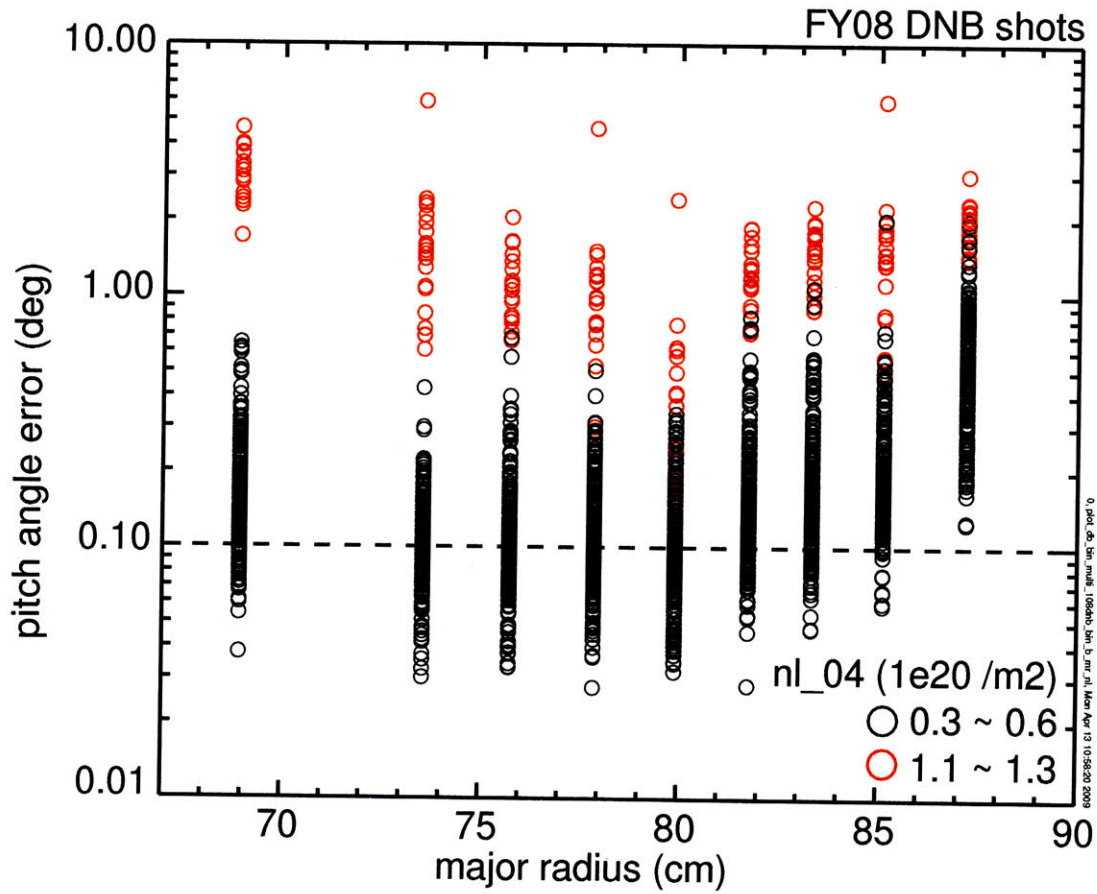
Figure 2-52: Macro-bin pitch angle error in degree vs major radius from FY2008 shots with DNB sorted by two different density ranges. Constraints are macro-bin timing > 50 ms, time between $0.5 \sim 1.7$ sec, signal-to-background ratio > 1, beam current > 6 A and only Ohmic L-mode plasmas are shown.

Chapter 3

Thermal drift issues on MSE diagnostic

As discussed in Sec 1.3, the MSE diagnostic on Alcator C-Mod uses an in-vessel optical system (5 lenses, 3 mirrors) to relay polarized light to an external polarimeter because port access limitations on Alcator C-mod preclude a direct view of the diagnostic beam. The system experiences unacceptable, spurious drifts of order several degrees in measured pitch angle over the course of a run day. Recent experiments illuminated the MSE diagnostic with polarized light of fixed orientation as heat was applied to various optical elements. A large change in measured angle was observed as two particular lenses were heated, indicating that thermal stress-induced birefringence is a likely cause of the spurious variability. Beginning with the experimental observations on the thermal shot-to-shot drifts, this chapter discusses possible solutions, including thermal isolation of the system, and an effort to model the effect more solidly with some implications for the system upgrade.

3.1 Experimental evidence

3.1.1 Observations on thermal effect

The shot-to-shot drift due to the temperature excursion on the in-vessel optics had been hard to identify because no dedicated runs for this effect had been designed. In usual runs, many plasma parameters such as plasma density, magnetic fields, impurity injection etc. change shot by shot, making the observation on the pitch angle variation shot by shot less consistent. In the past with a 50-msec short pulse beam, a random drift, or scattering, in the measured pitch angle was studied mainly by looking at the discrepancy with the pitch angles inferred from EFIT, which ranges $2^o \sim 5^o$ even in L-mode plasmas [36]. Not only were there such discrepancies but also were observed large variations in the discrepancy from this study, ranging $\pm 1.8^o$ for the edge and $\pm 1.0^o$. Several factors such as Faraday rotation and radial electric field were considered as the cause of this drift. However, the effects were not large enough to explain the observed scattering. No attempt was made to look for a long-time-scale drift over the course of a run day at that time.

The availability of the long-pulse ($\gtrsim 2$ sec) DNB has greatly improved the drift study. Not only does it give ~ 20 times more data per shot, thereby increasing the pool of data points, but it also allows one to look for the time scale of the drift, i.e. the spurious drift which will be introduced in this section does not occur on a time scale of seconds, but on a time scale of hours. The following subsections list the experimental evidence that the drift is mainly caused by the thermal drift on the system. Some additional evidence on the thermal effect is introduced in App C and some counter evidence is also discussed in App D.

Preliminary observation in Ohmic plasmas

The first observation on a long-time-scale drift in the pitch angle was made possible during LHCD experiments where the Lower Hybrid heating was applied from 0.8 to 1.3 sec with constant plasma current, magnetic field and density. The plasma conditions were almost identical in many aspects over the course of the run day except

146

this LH pulse in the middle of each shot, leaving a relatively 'clean' and quiescent Ohmic phase during the flattop of I_p and B_t at around 0.7 sec. Fig 3-1 shows the pitch angle measured by MSE as a function of shot number on the 1070613 LHCD run for 8 MSE channels. The macro-bin timing is from 0.71 to 0.76 sec, which is in the Ohmic phase with constant I_p and B_t. It is surprising to see the variation is clear, channel-dependent, and large, being about 8° in the edgemost channel. The variation becomes smaller for inner channels. Also note that there is a large and sudden drop in the pitch angle after Shot 12, after which the pitch angles are relatively constant along the shots.

A similar observation on another LHCD run day strengthens the consistency in this trend. Fig 3-2 shows the similar data set from the 1070828 LHCD run. Although the maximum pitch angle change for the edge channel is less than what is observed on the 1070613 run, the channel dependence is still clear and the shot-to-shot drifts themselves are substantial. These discrepancies are also comparable with what was observed in the previous study with a short pulse beam where there was clear channel dependence as well.

These observations lead to a notion that the cause of the shot-to-shot drift is thermal-relevant with a long time scale ($\sim$ several hours). It is noted, however, that there is a 'sudden drop' in the discrepancy between the MSE and EFIT pitch angles after some shots from both run days. Although such a drop observed in 1070828 run (Fig 3-2) might be explained by a long time elapsed between Shot 20 and the last shot (Shot 31) and in this sense, the drop is not actually 'sudden', it is hard to explain the drop that took place between Shots 12 and 13 observed in 1070613 run (Fig 3-1). Unfortunately, there is neither clear evidence nor indication that the thermal environment suddenly changed between these two shots.

After the FY07 campaign, where thermal-related issues were suspected to be a cause of the shot-to-shot drift, a variety of heating and stress tests were done on the MSE optics both for the entire optics system in the vessel and for the individual optics elements on the bench. These include heating and/or stressing the L2 doublet, the L3 doublet, and the mirrors. The following subsections summarize these activities

147
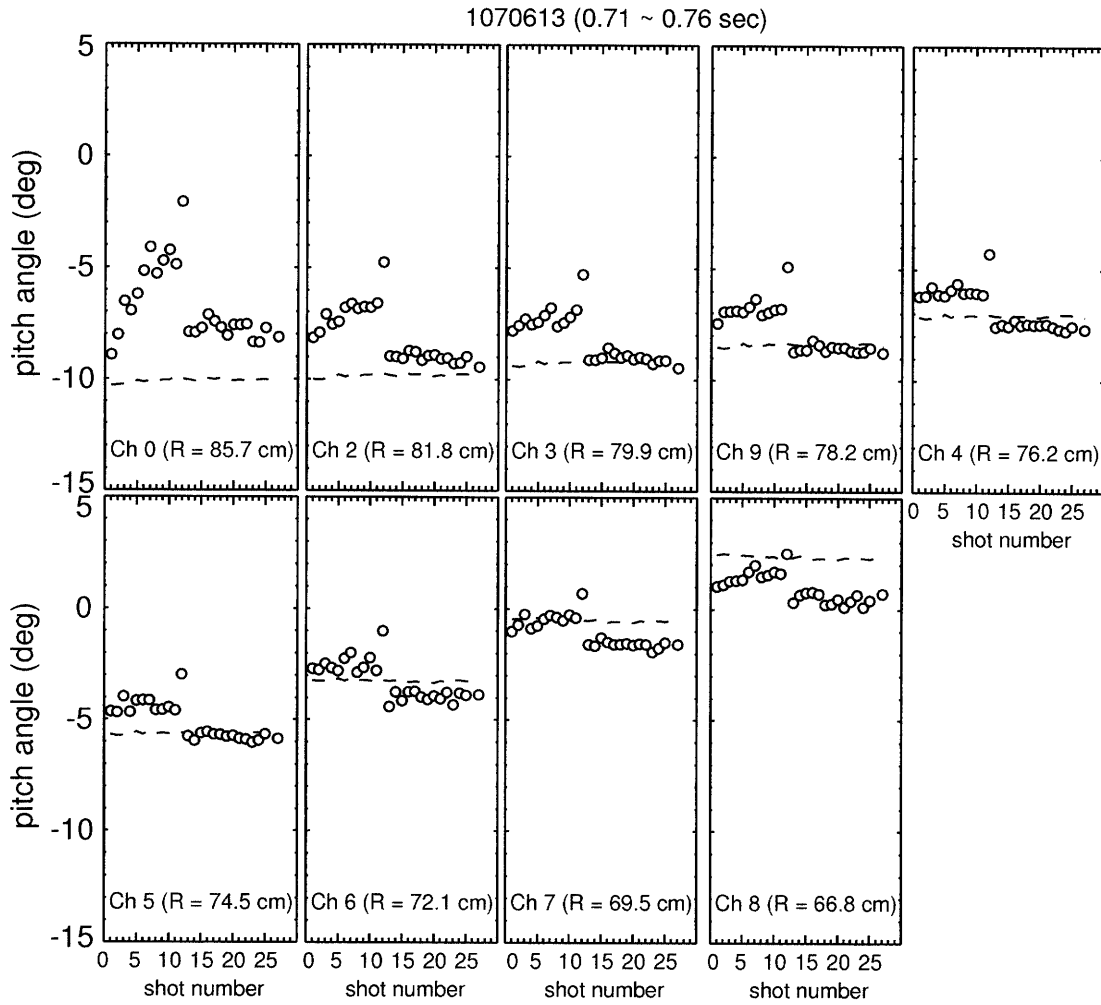
Figure 3-1: Pitch angle measured by MSE during a flattop Ohmic phase (averaged over 0.71 to 0.76 sec) as a function of shot number from 8 MSE channels on 1070613 LHCD run. $I_{DNB} \gtrsim 6$ A, $I_p = 0.8$ MA, $B_T = 5.4$ T, and $nl_{04} = 0.4 \sim 0.6 \times 10^{20}$ m^{-2} during this period of each shot. Error bars are included in the MSE data but smaller than the size of the symbols. The dashed lines are the pitch angles measured by EFIT.

1070828 (0.74 ~ 0.79 sec)
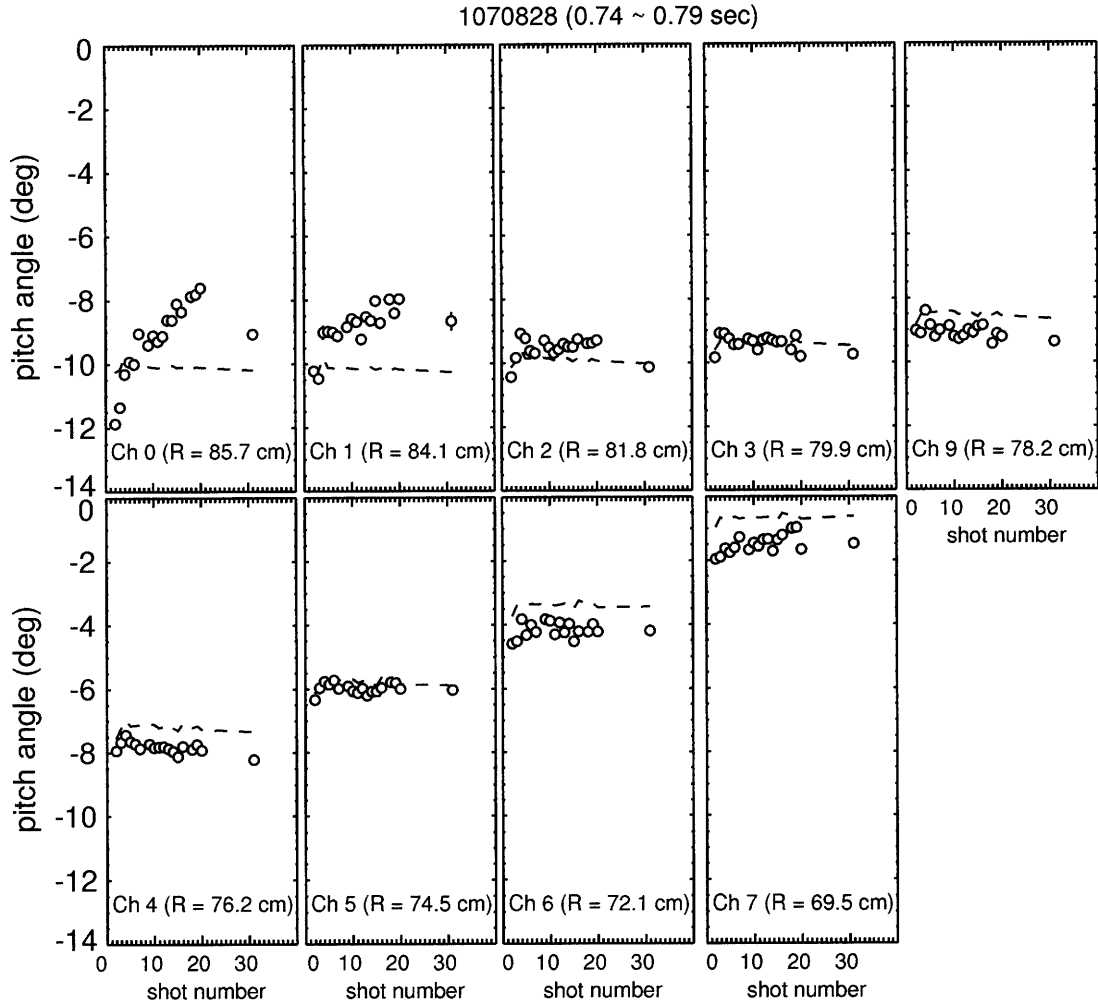
Figure 3-2: Pitch angle measured by MSE during a flattop Ohmic phase (averaged over 0.77 to 0.79 sec) as a function of shot number from 8 MSE channels on 1070828 LHCD run. $I_{DNB} \gtrsim 6$ A, $I_p = 0.8$ MA, $B_T = 5.4$ T, and $n l_{04} = 0.4 \sim 0.7 \times 10^{20}$ m^{-2} during this period of each shot. Error bars are included in the MSE data but smaller than the size of the symbols. The dashed lines are the pitch angles measured by EFIT.

149

and their results.

Lens heating: L2 vs L3

Two independent invessel heating tests were performed to evaluate the effect of thermal excursions on the MSE lenses: one for the L2 doublet and the other for the L3 doublet. The setup is similar to one in Fig C-1 except that the heating is applied to each doublet only by a narrow ($\sim$ 1 inch wide) heating tape surrounding it. The temperatures were measured at 5 locations, including at the polarizer to monitor any possible thermal distortion on it. In each scan, data was acquired for a total of 90 minutes and as before, the heating power was abruptly turned off mid-way through the experiment when the temperature reached 80 ^oC. Fig 3-3 shows (a) the L3 and (b) the L2 heating test results. The top plots show the temperature variation over the experimental time, the middle plots show the variation in the measured polarization angle and these plots are the magnified version of the bottom plots. Note that during the L3 heating test, the L2 remained at room temperature while the L3 went up to 80 ^{o} and vice versa. The temperature at the polarizer also remained unchanged from the room temperature in both tests. It is apparent from this figure that the L2 area is much more affected by the temperature change than the L3 region and that the effect is more localized (that is, more channel dependent), again the edge channels having larger variations. The maximum change in polarization from the edge channel with the L2 heating is about 11° whereas that with the L3 heating is only 0.15^o.

This fundamental difference in the thermal response between the L2 and L3 doublets can be explained by light pattern incident on them. Ray tracing indicates that light from the DNB is completely out of focus at the L3 position (nearly filling the lens), whereas it is nearly in focus at L2. Light from the outer spatial channels of MSE is focused onto spots near the periphery of the L2 doublet while light from spatial channels near the center of MSE's field of view is focused onto spots near the center of L2. This difference makes their respective responses to the thermal stress-induced birefringence considerably different: on L2, the edge channels are affected most strongly by heat penetration from the periphery, and on L3, the individual rays
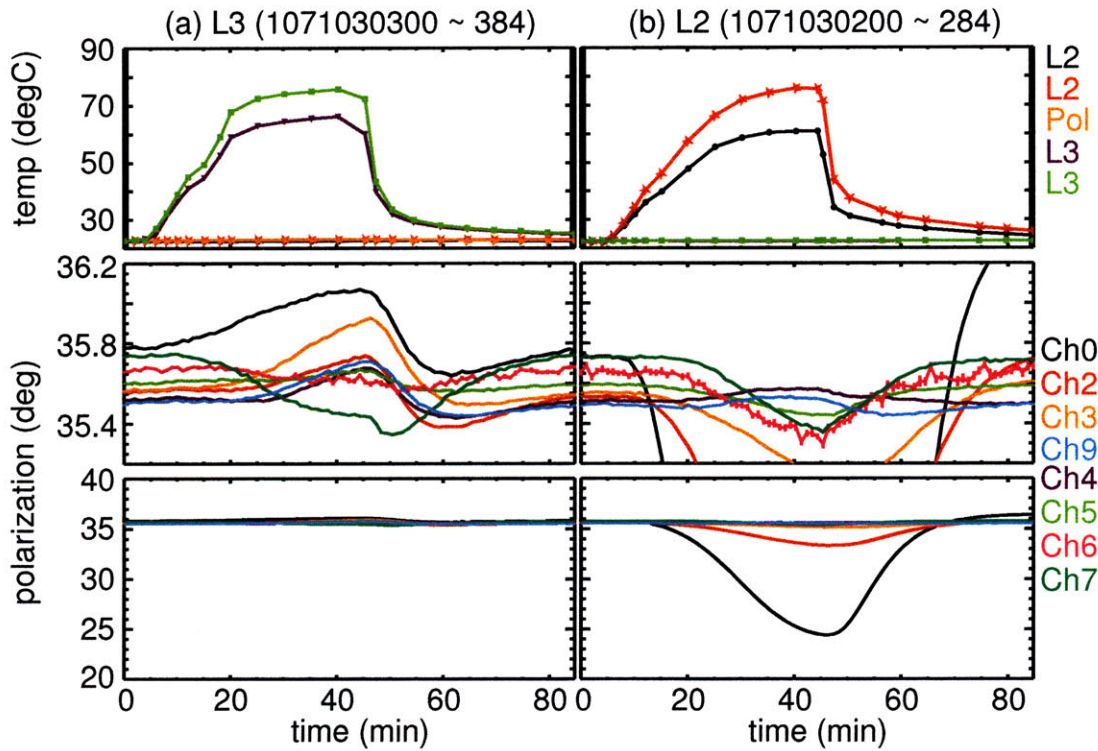
Figure 3-3: MSE invessel heating test result for (a) the L3 doublet and (b) the L2 doublet. Top plots show the temperature variations from 5 locations: 2 from L2, 2 from L3, and 1 from the polarizer surface. The middle plots are the variation in the measured polarization angle from 8 MSE channels and are magnified versions of the bottom plots. Channel numbers have been written in order of edge (Ch0) to core (Ch7).

151

from each channel experience all the temperature variations that exist on the L3 surface, averaging out the thermal effect in the zeroth order.

Another pair of two separate heating tests on the L2 and L3 doublets performed on the bench reconfirms this conjecture. Fig 3-4 compares the polarization angle change from the value prior to heating application between the L2 and L3 heating tests. Also shown in the figure are the illustrations on the ray focusing patterns on
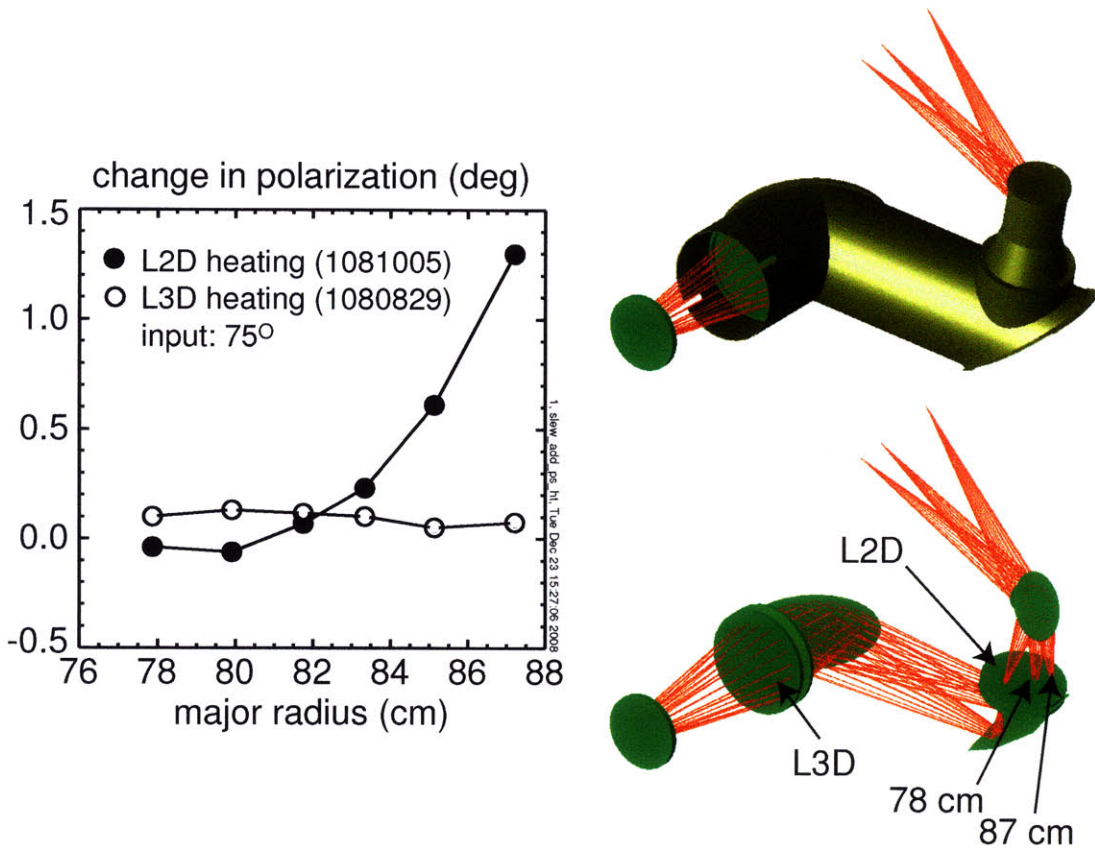
Figure 3-4: Comparison in the polarization angle change due to the heating on the L2 doublet (L2D) and L3 doublet (L3D) for 6 MSE channels. Each test has about 5 °C/hour slew rate and the maximum changes have been taken (about 40 minutes after the heat is applied). On the right, the ray focusing pattern is illustrated on L2D and L3D: the rays are locally focused on L2D and diffused on L3D.

the L2 and L3 doublets. As described above, the rays from different channels are focused at different portions on the L2 and completely illuminate the L3. The results given in Fig 3-4 imply the effect is an order of magnitude bigger at L2D than at L3D.

It should be noted, however, that in order to have a zero average value, the stress pattern, or the temperature non-uniformity, should be perfectly axially symmetric in addition to the symmetry of the incident light. This may be the reason that the polarization change observed on the L3D have non-zero, although small, values. In the test, there might have been a small finite asymmetry in the heating, mostly due to heat convection.

Correlation with fundamental harmonics in the signal

The intrinsic nature of the birefringence is that the birefringent medium imposes a certain amount of phase shift on the originally linearly polarized light (and of course, changes the polarization direction according to the amounts of phase shift given to the two perpendicular components of the incident polarization). This in general converts the purely linearly polarized light into the elliptically polarized light by adding a certain amount of circular polarization.

According to Eqns 1.21 and 1.22, the intensity of circularly polarized light, I_c, is proportional to the intensity of either fundamental harmonics, $I_{\omega 1}$ and $I_{\omega 2}$, which are the amplitudes of 20 and 22 kHz components for the C-Mod MSE. These scalings can provide a direct way to check whether the amount of thermal effect, or the deviation in the measured polarization angle from the true angle, is really proportional to, or scaled to, the amount of these fundamental frequency amplitudes. From a series of the L2-region heating tests on the bench with various temperature slew rates, the variations in 20 and 22 kHz amplitudes have been compared with those in the polarization drift and these comparisons are shown in Fig 3-5. These comparisons qualitatively agree with Eqns 1.21 and 1.22, implying the circular polarization components scale with the amount of the phase shifts induced by thermal stresses. One may think that this can actually open a way to calibrate the thermal stress effect in real time by measuring the intensity of I_c from the two fundamental frequency amplitudes. However, it should be noted that the expressions given in Sec 1.2, including Eqns 1.21 and 1.22 assume the system is ideal, that is, there is no additional phase shifts by the mirrors, no leakage of σ components, no rotational corrections on the mirrors,

153
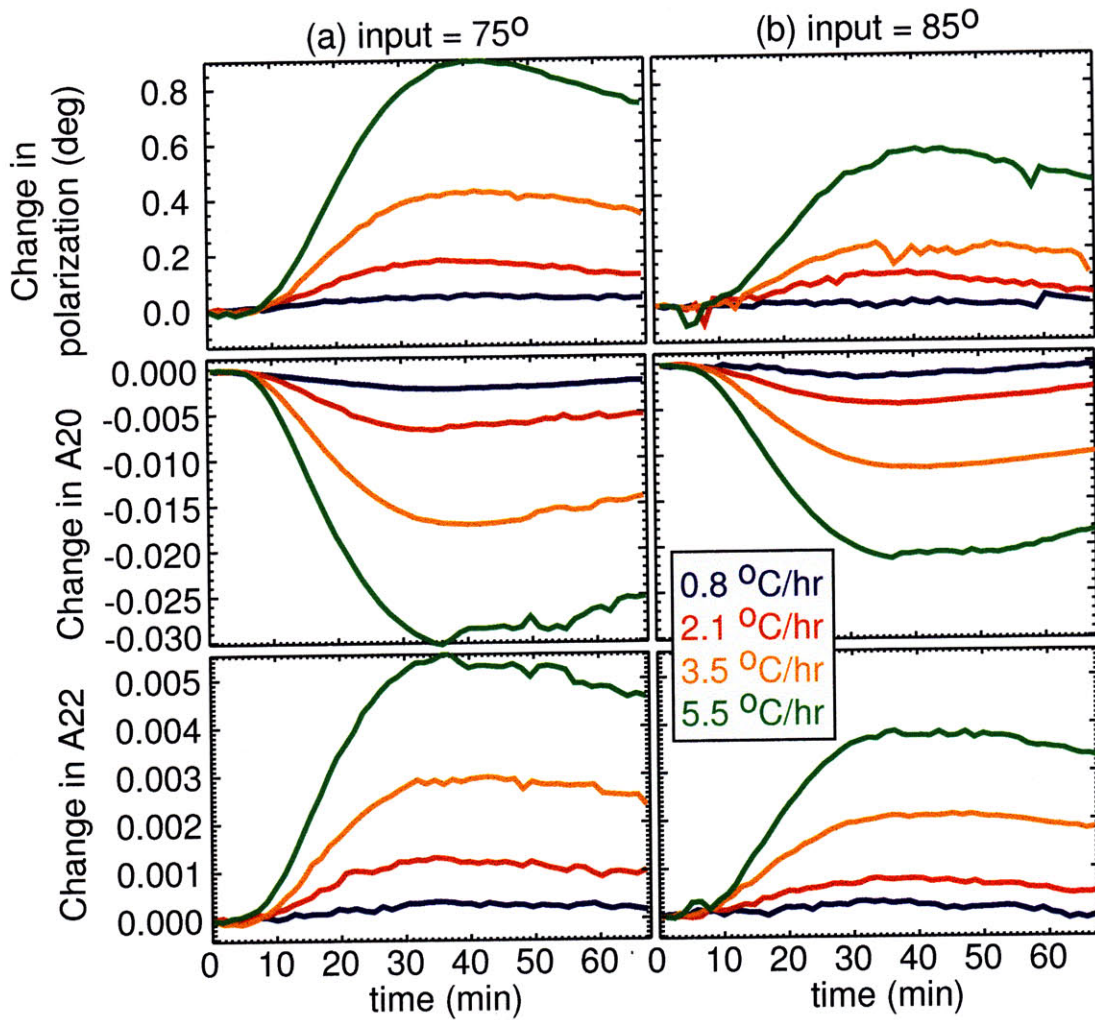
Figure 3-5: Change in the measured polarization angle (top) compared with the changes in the amplitudes of the 20 (middle) and 22 (bottom) kHz components from the L2-region heating tests on the bench with 4 different temperature slew rates which are given in the box on the plot. Two fixed input polarization angles are tried: (a) 75° and (b) 85°. These results are from the MSE channel 1, the edgemost channel, that tends to have the largest change when the L2 region is heated.

no background subtraction etc. When one or more of these effects are included, Eqns 1.21 $\sim$ 1.24 become extremely complicated. In fact, a more quantitative comparison was made between the change in polarization angle directly measured from some of the thermal bench tests and that inferred from $I_{\omega 1}$ in the same tests through a 'single-waveplate' model which will be discussed in Sec 3.1.3. There is a big discrepancy between these two quantities: the actual change in polarization is bigger, roughly be an order of magnitude, than that inferred from the magnitude of the fundamental harmonics through the simple model. Nevertheless, it is encouraging that the circular components scale reasonably with the change in the polarization by the thermal perturbation.

Estimate of birefringence due to temperature nonuniformity

In order to quantitatively estimate the effect of the temperature variability across the lens on the retardance, thereby the polarized light passing through it, a relation between the temperature profile and the stress-induced birefringence is derived using a simple flat disk model that mimics the L2 lens. The thermally-induced stress in a circular disk of uniform thickness b can be computed analytically if the temperature is a function only of radius. The normal stress component parallel to the radial direction, σ_{rr}, and the normal stress component parallel to the azimuthal direction, $\sigma_{\theta\theta}$, can be written as [70]

$$
\begin{aligned}
\sigma_{rr} &= \alpha E \left[\frac{1}{b^2} \int_0^b T\, r\, dr \; - \frac{1}{r^2} \int_0^r T\, r\, dr \right] \\
\sigma_{\theta\theta} &= \alpha E \left[\frac{1}{b^2} \int_0^b T\, r\, dr \; + \frac{1}{r^2} \int_0^r T\, r\, dr \; - T \right]
\end{aligned}
\tag{3.1}
$$

where α is the coefficient of thermal expansion and E is the modulus of elasticity of the disk material. Note that the stress at a given radius depends on the temperature distribution **everywhere** in the disk, so a temperature gradient *anywhere* in the disk will create stress throughout the disk. Note also that the stress at a given radius does not depend on the local temperature gradient there. This may explain why the time response to the thermal perturbation has little channel dependence, as discussed in

155

the previous subsections.

Assuming a simple power-law temperature profile,

$$T(r) \;=\; T_o + \Delta T \left(\frac{r}{b}\right)^m, \tag{3.2}$$

where b is the radius of the disk and m is any number. Eqn 3.1 becomes

$$\sigma_{rr} \;=\; \frac{\alpha E\,\Delta T}{m+2}\left[1 - \left(\frac{r}{b}\right)^m\right]$$
$$\sigma_{\theta\theta} \;=\; \frac{\alpha E\,\Delta T}{m+2}\left[1 - (m+1)\left(\frac{r}{b}\right)^m\right]. \tag{3.3}$$

The stress-induced birefringence Δs is related to the two principle stresses, σ_{rr} and $\sigma_{\theta\theta}$ by

$$\Delta s = \frac{\lambda}{360}\epsilon = Kd\left|\sigma_{rr} - \sigma_{\theta\theta}\right|, \tag{3.4}$$

where λ is the wavelength of the incident light, ϵ is the phase shift, in degree, imposed on the light by the birefringence, K is the stress-optical constant for the glass, in units of m^2/N, and d is the glass thickness. Combining Eqns 3.1 and 3.4 relates the phase shift to the temperature profile as

$$\epsilon \;=\; \frac{360Kd\alpha E}{\lambda}\left(\frac{m\Delta T}{m+2}\right)\left(\frac{r}{b}\right)^m = 22.673\left(\frac{m\Delta T}{m+2}\right)\left(\frac{r}{b}\right)^m, \tag{3.5}$$

where the last result comes out with $K = 2.79 \times 10^{-6}$ per MPa, $d = 1.78$ cm, which is the average of the thicknesses at the center (1.37 cm) and the edge (0.41 cm) of the L2 lens multiplied by 2, $\alpha = 9 \times 10^{-6}$ per Kelvin, $E = 93$ GPa, and $\lambda = 660$ nm. This relation implies that not only the magnitude of the temperature nonuniformity but also the shape of the temperature profile on the lens can directly affect the amount of phase shift. For example, the MSE edge channel ($r/b = 0.66$ on the L2 lens surface) can experience the phase shift as much as $4.94\Delta T$ for a parabolic ($m=2$) temperature distribution where ΔT can range $1 \sim 10$ °C. The relation between the change in the polarization and the thermal stress-induced birefringence will be discussed later on

156

in Sections 3.1.3 and 3.3.2.

An important constraint on this relation arises from the fact that generally, an unconstrained, linear isotropic material subject to a temperature field for which $\nabla^2 T = 0$ may deform but will remain unstressed [70, 71]. This means a temperature distribution which is linear produces no stresses. Although in reality, a condition such as being unconstrained or having a linear temperature distribution never occurs in the L2 area of the MSE periscope due to the compression from the lens holder and/or radiative heat transfer between the lens surface and the periscope inner wall, a caution should be taken in interpreting, for example, any temperature data taken around the L2 periphery through the thermocouples installed there. The experimental observation through these thermocouples is introduced in Sec 3.1.2

3.1.2   Direct tests during beam-into-gas runs

Thermocouple installation

Once the thermal stress-induced birefringence on the invessel lenses due to the non-uniform temperature distribution on them was identified to be the strongest candidate as the cause of shot-to-shot variability in the MSE diagnostic throughout the intensive thermal and stress tests during the manned access period in 2007, there was not much time remaining before the FY08 campaign began. Five thermocouples (TC's) were installed onto the invessel periscope to monitor the temperature variations in a routine manner and correlate them with the pitch angle variation. Fig 3-6 shows the locations of the TC's installed. PLC (Programmable Logic Controller) reads the thermocouple signals about every 2 minutes basically on a 24/7 basis and the signals are stored in the MDSPlus.

An example of the temperature monitoring over the course of a run day is given in Fig 3-7 where the temperatures from 3 thermocouples around the L2D are given as a function of time (or shot number written at the bottom of the plot box) from the 1071214 run. On this run day, the temperature at the plasma-facing side of the periscope (TC 1 and 3) is approximately $50 \sim 60°C$ at the beginning of the run due
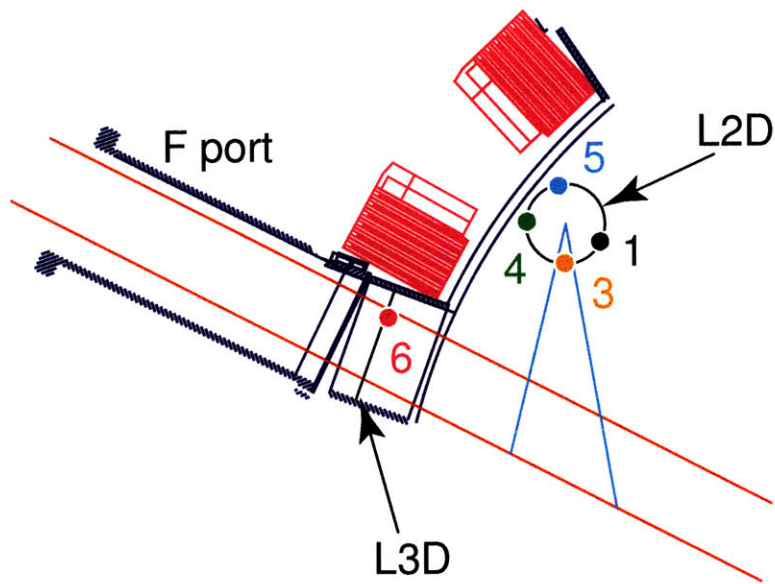
Figure 3-6: Five thermocouple (TC's) positions installed on the MSE invessel periscope seen from the top. TC 1, 3, 4, and 5 are around the L2D region and thermocouple 6 is beneath the L3D region. TC 2 was installed but broken during the installation.

to the overnight ECDC (Electron Cyclotron Discharge Cleaning) procedure. When the liquid nitrogen cooling system is turned on several hours before the first shot, the temperatures decrease. Note that each plasma pulse increases the temperature at the plasma-facing side by about $5 \sim 8$ °C and the temperature decreases gradually over the 15-minute between-shot interval. It should be noted, however, that due to the data acquisition cycle of the thermocouples (every 2 minutes, not correlated with the C-Mod shot cycle), the real post-shot maximum temperature may not be captured. Looking at the overall envelope, it is found that the outerwall-facing side of the periscope is cooled down gradually during the early stage of the run and is not affected much by individual shots while the plasma-facing side never reaches the temperature value comparable to that of the outerwall-facing side, implying a large temperature gradient across the L2 lenses.

It is interesting to track down what happened during the run based on the temperature history measured by these thermocouples. For example, between shot 4 and 5, there was a 'pause', that is, no plasma shots, and therefore, the temperatures
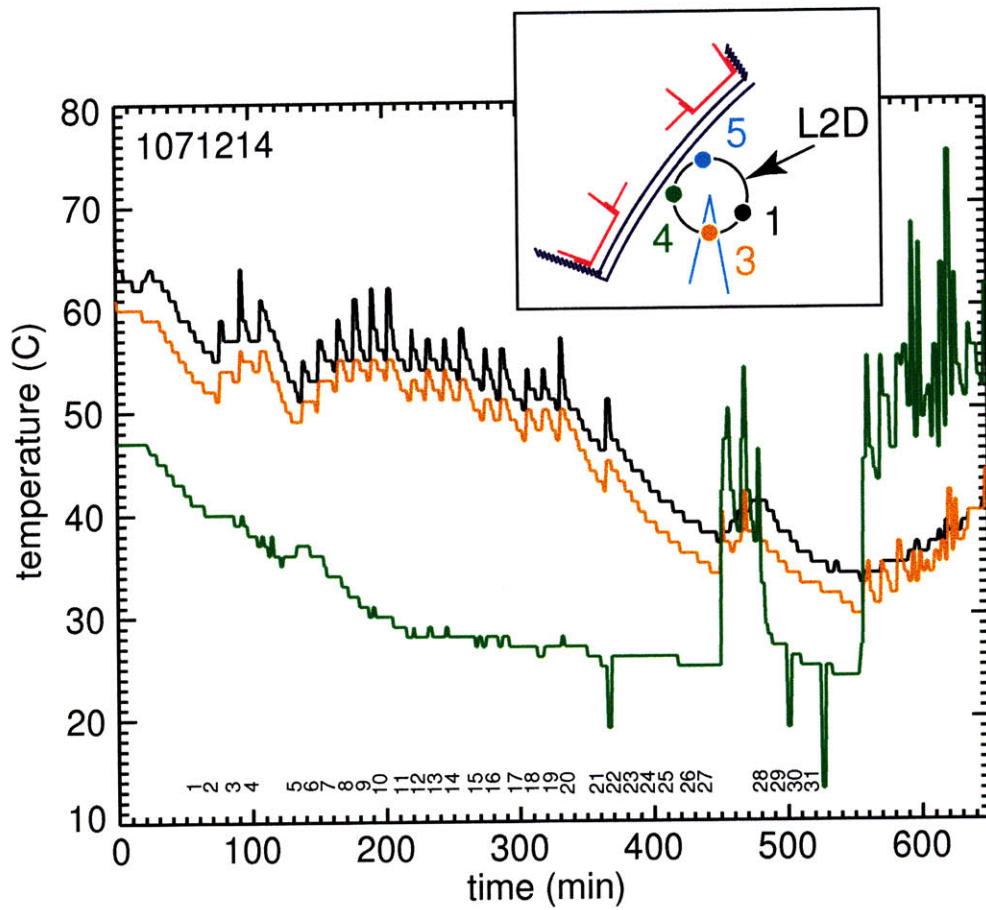
Figure 3-7: The time history of the temperatures on the MSE periscope measured from the thermocouples installed there as shown in Fig 3-6 from the run 1071214. The TC locations are given in the small box and the shot numbers are given at the bottom of the plot box. TC 5 was not recorded at this time.

from TC 1 and 3 monotonically decreased. Between shots 20 and 27, there were a lot of fizzles and therefore, the temperatures from TC 1 and 3 again monotonically decreased because of the lack of any heat from plasmas. After shot 27, the session leader asked for the between-shot ECDC as an effort to overcome these continuous fizzles. During the ECDC, temperatures from TC 1 and 3 increased. It is notable that the TC 4 is very sensitive to the ECDC and it is also true from the observation on the temperature evolution after the run: the temperature from TC 4 increased abruptly while those from TC 1 and 3 started to increase gradually when the ECDC was turned on after the last shot. It is suspected that the TC 4 data is somehow interrupted by the ECDC signals.

Any shot that has the TC measurements can be analyzed this way. The temperature evolution from each thermocouple varies depending on the features of the run such as the level of ICRF power etc. Nevertheless, several common trends can be found and summarized here:

- The MSE invessel periscope experiences several tens of degree variation over the course of a run day.
- The starting temperatures on the plasma-facing side of the MSE periscope are as high as 60°C and sometimes up to 80°C due to the overnight ECDC.
- There is a competition between the plasma (or RF) heating and the liquid nitrogen cooling in determining the overall envelope of the temperature evolution on the plasma-facing side of the periscope.
- The temperature of the outerwall-facing side of the periscope usually stays low (~ 30 °C) due to the active control of the temperature applied for the outer wall of the torus.
- With the preceding two statements, the temperature variation across the L2 lenses is expected to be > 10 °C for most shots.
- Each plasma pulse instantly raises the temperature of the plasma-facing side of the periscope by about $5 \sim 8$ °C right after the shot and the temperature decreases gradually over the between-shot interval. The height of this rise depends

on the RF power applied to the shot.

Beam-into-gas shots with torus temperature control

Based on the temperature measurements, the variation of the temperatures at the MSE optics is correlated with the torus temperature variation. In general, the surface of the MSE periscope is hot (up to 100 ^oC) at the start of a run day (not before shot number 1) due to the overnight ECDC and then rapidly cools down in first few shots by the circulation of the liquid nitrogen. The cooling becomes rather slow as the run goes on since the cooling competes with the heat accumulation due to plasma radiation. This complicated temperature variation can affect the polarization measurement on a shot-to-shot basis in a rather unpredictable manner.

With the temperatures of the invessel MSE periscope measured, it is possible to correlate the shot-to-shot variability in the measured pitch angle with the temperature variability. In the 1080318 beam-into-gas run, a clear indication was obtained that the MSE diagnostic is affected by the thermal stress. The pulse parameters for all shots including B_T, equilibrium field coil currents, and the gas pressure were maintained at constant values during a shot to obtain a single pitch angle profile per shot and to be immune from any possible variability in the pitch angle due to the secondary beam neutral emission discussed in Sec 2.1.4. Four of these identical shots were taken at various times during the run day and their pitch angle profiles are illustrated in the bottom plot of Fig 3-8 (a). The top plot of Fig 3-8 shows the time evolution of the temperatures measured from the MSE thermocouples installed on the invessel periscope during this run and the vertical line with a color indicates the time at which the sample shot, whose profile is shown in the bottom plot with the same color, was taken. As mentioned in the previous subsection, the starting temperatures are high as 70 ^{o}C due to the overnight ECDC and gradually decrease as the run goes on. In these beam-into-gas runs, there was no heat from the plasma and therefore, the temperature time evolution in this case is thought to be dominated only by the magnet cooling and the active outerwall heating control. Note that at the end of the run (around 5pm), the ECDC resumed and the temperatures from all TC's begin to
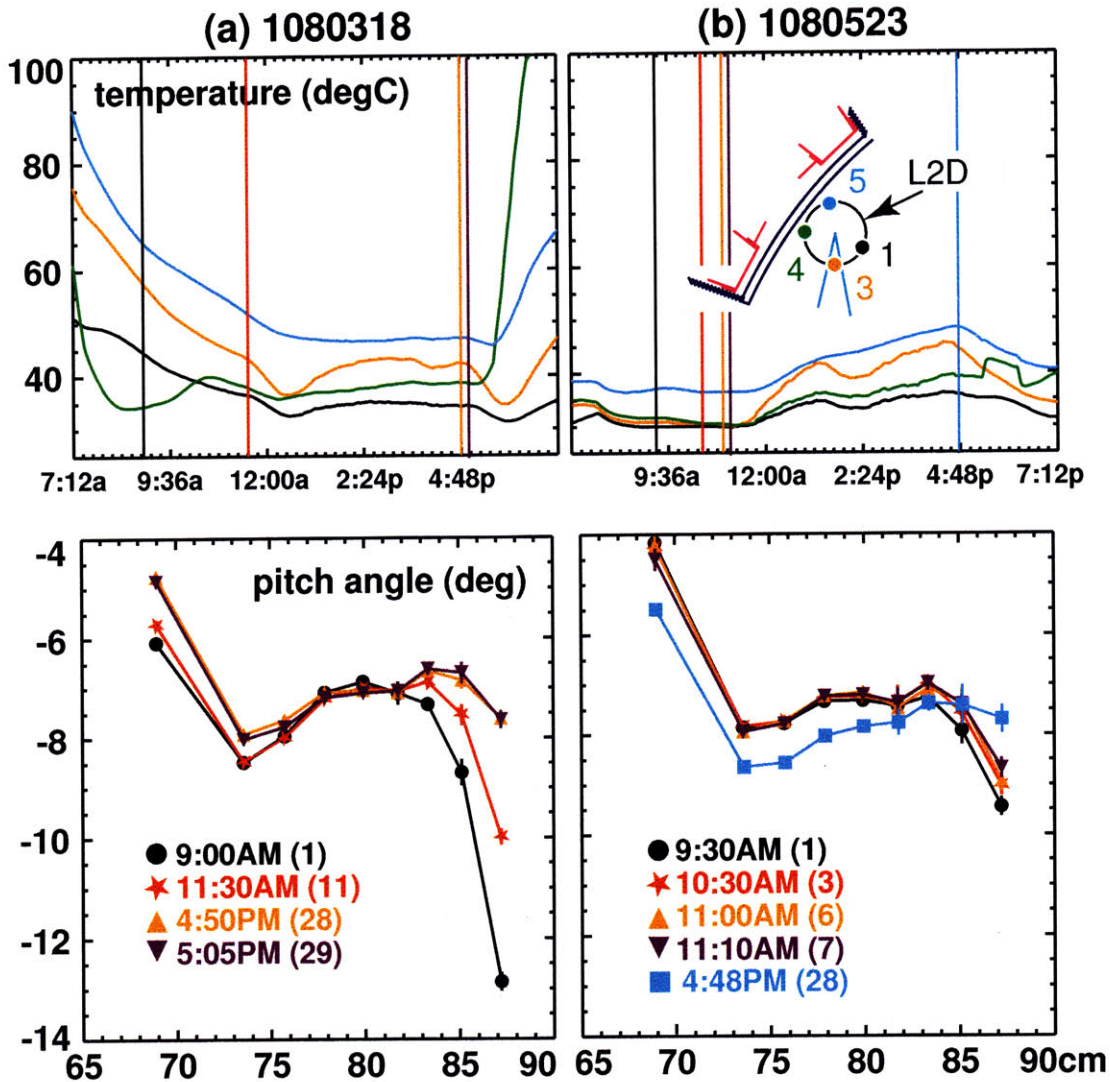
(a) 1080318

(b) 1080523

Figure 3-8: MSE invessel periscope (around L2D) temperature time evolutions (top plots) and the pitch angle profiles selected at several time points (bottom plots) from (a) 1080318 and (b) 1080523 beam-into-gas experiments. The vertical lines with different colors on the top plots indicate the times at which the profiles shown in the bottom plots with corresponding colors are taken. The thermocouple locations are shown here as well. The number in the parentheses after the time in the bottom plot indicates the shot number.

increase.

The temperatures at some locations (TC 3 and 5) of the L2 surrounding of the periscope dropped by more than 10 °C between the first two sample shots and the change in the polarization angle measured by MSE is up to 3° for the edgemost channel between these two shots. It is interesting to see that the periscope temperatures seem to reach their own thermal equilibration by the time the last two samples shots were taken and correspondingly the drift in polarization angle measured by MSE between these two shots became smaller ($< 0.5°$). It should be also noted that the shot-to-shot variability is strongly channel dependent, the edgemost and innermost channels having larger drift and the central channels having smaller drift. This trend is reminiscent of what is observed in Fig 3-4 where the change in the polarization angle is larger for the edge channels when the L2D region is heated. Although not shown in Fig 3-4, the L2D heating test on the bench includes the four more (inner) channels and the profile of the change is almost parabolic, the inner and outer channels having larger drifts than the central channels.

Another beam-into-gas run was conducted on 1080523, but this time, the torus temperature (and thereby the MSE invessel periscope temperature) was maintained as constant as possible ($\Delta \sim 5°$). The two dominant factors in affecting the temperature evolution were appropriately adjusted for this run: (1) No ECDC was done overnight to avoid high temperature at the beginning and; (2) the circulation of the liquid nitrogen was turned on well before the run. The latter was actually accomplished by not turning off the cooling circulation after the run on the previous run day. The temperature control was successful with the variation of the local temperatures maintained under 5 °C for the first 4 sample shots as shown in the top plot of Fig 3-8 (b). After the last sample shot in the morning (Shot 7), several plasma shots were taken in the afternoon for other purposes and the temperature variation became larger again during this period. The pitch angle profiles from five different times are compared in the bottom plot of Fig 3-8 (b). By comparing the drift between the first two sample shots (1 and 11) from 1080318 and that between the shots 1 and 7 from 1080523, it is apparent that the shot-to-shot variability for the edge channel

163

has been decreased by a factor of 3 by improving the temperature uniformity on the MSE invessel periscope. Also note that the profile from the last sample shot of the 1080523 run is somewhat different from the rest of the sample shots on the same run, which may be explained by the fact that the temperature non-uniformity caused by the plasma heat accumulation became larger at this time.

These two sets of beam-into-gas experiments reconfirm that the drift in the measurement is really due to the periscope temperature non-uniformity (thermal stress) and that it can be reduced by keeping the temperature of the system constant. It is also noted that from 1080523 shots, that the temperature uniformity that was achieved on this run is still not enough to completely eliminate the drift. There are still small, but finite, shot-to-shot variability especially at the outer channels over the first 4 samples shots.

3.1.3 Single-waveplate model

The simplest understanding of the physics of birefringence is that it yields different indices of refraction for linearly polarized light in perpendicular directions. The net effect is to shift the phase of one component of the light relative to the other. This is equivalent to what happens when linearly polarized light with polarization angle γ is passed through a waveplate whose effect is only to introduce a phase shift ϵ between two electric field vectors.

The Müeller matrix for a waveplate with its fast axis oriented at an arbitrary angle ϕ with respect to the horizontal axis is

$$
M_w = \begin{bmatrix}
1 & 0 & 0 & 0 \\
0 & \cos^2(2\phi) + \sin^2(2\phi)\cos\epsilon & \sin(2\phi)\cos(2\phi)(1 - \cos\epsilon) & -\sin(2\phi)\sin\epsilon \\
0 & \sin(2\phi)\cos(2\phi)(1 - \cos\epsilon) & \sin^2(2\phi) + \cos^2(2\phi)\cos\epsilon & \cos(2\phi)\sin\epsilon \\
0 & \sin(2\phi)\sin\epsilon & -\cos(2\phi)\sin\epsilon & \cos\epsilon
\end{bmatrix}. \tag{3.6}
$$

Note that this expression becomes Eqn 1.10 with $\phi = 0°$ and $\epsilon = A_1 \cos(\omega_1 t)$ and Eqn 1.11 with $\phi = 45°$ and $\epsilon = A_2 \cos(\omega_2 t)$, the expressions for the two PEMs, since a PEM

is a special case of the waveplate. In order to determine the polarization direction of linearly polarized light with initial polarization angle γ from the horizontal

$$S_{in} = \begin{bmatrix} 1 \\ \cos(2\gamma) \\ \sin(2\gamma) \\ 0 \end{bmatrix}, \tag{3.7}$$

a linear polarizer is used as an 'analyzer', i.e. after the light passes through the waveplate, the light is passed through the linear polarizer, and then its transmission axis at angle θ is determined that gives the maximum intensity. This is the polarization angle of the light as it emerges from the waveplate. The Müeller matrix for a linear polarizer with its transmission axis at angle θ is

$$M_p = \frac{1}{2} \begin{bmatrix} 1 & \cos(2\theta) & \sin(2\theta) & 0 \\ \cos(2\theta) & \cos^2(2\theta) & \sin(2\theta)\cos(2\theta) & 0 \\ \sin(2\theta) & \sin(2\theta)\cos(2\theta) & \sin^2(2\theta) & 0 \\ 0 & 0 & 0 & 0 \end{bmatrix}. \tag{3.8}$$

Again, note that this expression reduces to Eqn 1.12 with $\theta = 22.5^o$. The expression for the output Stokes vector now can be written as

$$S_{out} = M_p \cdot M_w \cdot S_{in} \tag{3.9}$$

and again by taking the total intensity, which is the first element of S_{out}, and then finding the expression for θ that gives the maximum intensity (by setting the derivative of the first element of S_{out} with respect to θ to zero), the expression for the output polarization angle can be obtained as

$$\tan(2\theta) = \frac{\tan(2\gamma)\left[1 - \cos^2(2\phi)(1 - \cos\epsilon)\right] + \sin(2\phi)\cos(2\phi)(1 - \cos\epsilon)}{\cos\epsilon + \cos^2(2\phi)(1 - \cos\epsilon)[1 + \tan(2\phi)\tan(2\gamma)]} \tag{3.10}$$

Since the data acquisition time of the diagnostic (~ 2 sec; one plasma pulse length)

is much shorter than the minimum characteristic time of the thermal diffusion through the periscope ($\sim$ 60 sec), it is possible to characterize the state of the birefringence for each pulse provided that two pairs of known (γ, θ) are obtained right either before or after the pulse. Both pre- and post-pulse calibrations can be used to estimate the uncertainty of the scheme. Once the phase shift, ϵ, and fast axis, ϕ, are determined for the pulse, any measured angle during the pulse can be corrected based on Eqn 3.10.

This model assumes the rest of the optics system is ideal, which as will be described later is not a good assumption in practice. It turns out that the phase shift due to the imperfect mirror property plays an important role and amplifies the change in the polarization angle when combined with a finite phase shift due to the thermal stress-induced birefringence, which is dealt with in Sec 3.3. Nevertheless, the feasibility of this 'in-situ' calibration scheme was experimentally demonstrated when the range of the two reference polarization angles were carefully chosen. Acceptable measurement error can be realized when the range is up to 4° for the incident polarization (i.e. the pitch angle in the MSE frame) outside of the range by up to 2°, providing a total of 8° of pitch angle ranges that can be calibrated. This is about the same range of the pitch angle in the MSE frame that C-Mod plasmas typically experience. The study on the feasibility along with some practical limitations in this calibration scheme are discussed in App E.

3.2 Thermal insulation of the system

Although attractive and feasible in principle, the in-situ calibration method based on the single-waveplate model has some engineering and practical limitations that are hard to overcome. Since the fundamental problem in the thermal stress is the finite temperature gradient across a lens, which is also time-varying, the efforts to remove the temperature variations across the lenses and in time, or minimize those variations to the level of producing acceptable errors, have been made. Based on these studies some thermal insulation means have been designed and proposed. We start with

an analysis of the thermal characteristics of the MSE periscope structure, mainly to provide the design parameters for the thermal insulation. Then we introduce the gold-coated (low-emissivity) heat shielding and the thermal isolation of the lens holder, which is being implemented for the upcoming campaign (FY2009), are introduced.

3.2.1 Characterization of thermal response

Allowable temperature fluctuation on the periscope

The L2 lens doublet (L2D) is more vulnerable to thermal stress-induced birefringence because light from individual MSE channels is nearly in focus there, so a thermal sensitivity test for this doublet was performed. Allowable temporal temperature fluctuations were investigated by applying systematic thermal perturbations to the system and measuring the change in polarization angle. Based on the data, an empirical correlation between the temperature change, ΔT, and the spurious change in polarization angle, $\Delta\theta$, was found. For the input polarization angle of 85°, which is close to a typical pitch angle realized in typical plasma experiments, the sensitivity scales as $\Delta\theta \approx 0.08\Delta T$. This scaling requires $\Delta T \lesssim 0.63$ $^\circ$C to achieve the polarization error $\Delta\theta \lesssim 0.05^\circ$. For the incident polarization of 62.5°, which can be regarded as an upper bound, the scaling becomes $\Delta\theta \approx 0.13\Delta T$, requiring the maximum allowable temperature fluctuation $\Delta T \approx 0.38$ $^\circ$C. The detailed discussion on this test is given in App F.1.

Allowable temperature slew rate

The response of spurious changes in polarization angle measured by MSE to the temperature slew rate has also been evaluated. Polarization change is due to birefringence induced by temperature variation across the lens and therefore, it is important to monitor the temperature distribution on the lens. However, because the lens surface, especially the L2 surface, is physically inaccessible during the normal operation, the direct measurement of the temperature on the L2 surface is impossible. Correlating the polarization drift with the temperature slew rate can provide an indirect

scaling of the drift with the temperature variation across the lens when combined with code simulations.

The acceptable slew rate from this test is estimated to be $0.5 \sim 2$ °C/hour depending on the input polarization angle. When combined with a 3D finite element simulation, the temperature variation across the lens can be scaled as $\Delta T \approx 0.26 \times$ (slew rate in °C/hour). This sets a rather stringent condition in the temperature variability across the lens. For the input angle of $85°$, the maximum allowable temperature variation across the lens is only $0.26 \times 1.5 = 0.39$ °C. The detailed discussion on this test is given in App F.2.

Effect of radiation

The radiative power exchanged between two surfaces 1 and 2 with temperature T_1 and T_2, respectively, facing each other with the same viewing area A is

$$
\begin{aligned}
Q_{12} = Q_1 - Q_2 &= \frac{\sigma A(T_1^4 - T_2^4)}{1/\epsilon_1 + 1/\epsilon_2 - 1} \\
&\approx \frac{4\sigma A T^3 \Delta T}{1/\epsilon_1 + 1/\epsilon_2 - 1},
\end{aligned}
\tag{3.11}
$$

where ϵ is the emissivity of each surface, $\sigma = 5.670 \times 10^{-8}$ W/m²K⁴ is the Stefan-Boltzmann constant, and T is some sort of average temperature between T_1 and T_2. The approximate expression in Eqn 3.12 provides the effective radiative thermal resistance in K/W

$$
R_{rad} = \frac{1/\epsilon_1 + 1/\epsilon_2 - 1}{4\sigma A T^3}.
\tag{3.12}
$$

The thermal resistance in the radiative communication between the L2 lens and the inner wall of the periscope, therefore, becomes 7.2 K/W at T = 300 K and 4.6 K/W at T = 350 K with $\epsilon_1 = \epsilon_2 = 1$ and $A = 2 \times \pi \times (6.5)^2 = 245.4$ cm² where the factor 2 in the area takes into account both the bottom and top surfaces of the lens. One might consider coating the inside of the periscope with a metal (e.g. gold) with low emissivity to increase the thermal resistance. However, this would provide only marginal benefit because the top surface of the L2D faces the M2 mirror and the

bottom surface of the L2D faces the M1 mirror, which, being glass, have $\epsilon = 1$ for wavelengths in the IR.

One of the earlier proposals for minimizing temperature variations across the lens was to maintain its edge temperature at a constant value using a cooling tube, while the temperature elsewhere in the MSE optical housing would be allowed to float freely. The method assumed that temperature gradients generated in the lens due to heat radiation from the optical periscope were acceptable. However, it turns out that the required temperature uniformity on the periscope is more stringent than expected. Suppose the periscope is at temperature T_c and the edge of the lens is maintained as temperature T_o. Considering that heat that starts at the periscope is radiated to the center of the lens, and then conducts to the edge of the lens, the problem can be modeled as a series-resistance problem, yielding the temperature drop across the lens ΔT_{lens} as

$$\Delta T_{lens} = \frac{R_k^{lens}}{R_k^{lens} + R_{rad}}(T_c - T_o), \tag{3.13}$$

where R_k^{lens} is the conductive thermal resistance for a flat disk heated on its flat surface and can be derived as $R_k^{lens} = 1/(2\pi kd) = 18.5$ K/W with $k = 0.01$ W/cm°K and d equal to the average thickness of the lens $((0.41 + 1.3)/2 = 0.86$ cm). Taking ΔT_{lens} $= 0.39$ °C, which is the allowable temperature variation across the lens with the input polarization direction of 85°, Eqn 3.13 gives $(T_c - T_o) = 0.54$ °C at T $= 300$ K and 0.49 °C at T $= 350$ K. This implies that it is necessary to control the temperature of the all surfaces of the periscope that are 'viewed' by the lens, the allowable temperature excursion of these surfaces being ~ 0.5 °C. Note that the temperature of the L2D region of the periscope surface currently drifts at least 30 °C during the course of a day. This would generate temperature variations in the lens of more than 20 °C, about 50 times bigger than what is allowed.

3.2.2   Gold-plated heat shields and periscope

Since the dominant heat transfer mechanism between the MSE invessel periscope and its surroundings at high vacuum (10^{-8} Torr) is radiation, a thermal shield with low

emissivity around the periscope has been proposed to reduce both the heat flux to the periscope and the temperature slew rate at the periscope, which would minimize the temperature variability in time and in space through the periscope. In principle, the radiative heat flux is reduced when both surfaces that face each other have low emissivity. In practice, however, a low-emissivity coating on the plasma-facing surface, i.e., the outer surface of the shield will be degraded rapidly by, for example, boronization, which would result in an emissivity value close to unity. The inner surfaces of the periscope also cannot be shiny since these surfaces should be dark in principle to minimize reflected stray rays. Therefore, the low emissivity coating is possible only on the inner surface of the shield and the outer surface of the periscope.

Two samples (stainless steel 304 and Inconel 625) were polished to about 4-microinch surface roughness and gold-plated by Independence Plating and their emissivities in the IR range of wavelengths were measured by Advanced Fuel Research, Inc. The measured emissivity ranges from 0.02 to 0.04 which is close to the generally known value for 'polished gold'. For the discussions that follow, however, its upper bound, 0.04, is taken as the emissivity for the gold-plated MSE surfaces (either the heat shield or the periscope) for the following conservative reasons: (a) it may be not possible to get good polishing everywhere on the periscope; (b) there will be some scratching of the surface due to handling and (c) there may be some deterioration of the emissivity over time due to coatings by e.g. boron.

Steady-state model

The effect of the thermal shield and periscope with low emissivity can be understood readily with a steady-state model. The MSE periscope and its surroundings are modeled with infinite thin slabs. In this model, the MSE periscope is divided into two surfaces: front (toward plasma) and back (toward outer-wall) surfaces since we are interested in the temperature variation across the two surfaces of the periscope. The detailed description and solution procedures for this model is given in App G.1.

Fig 3-9 illustrates the effect of having low emissivity on the inner surface of the shield and the outer surface of the periscope. Shown in the figure is the ratio of the
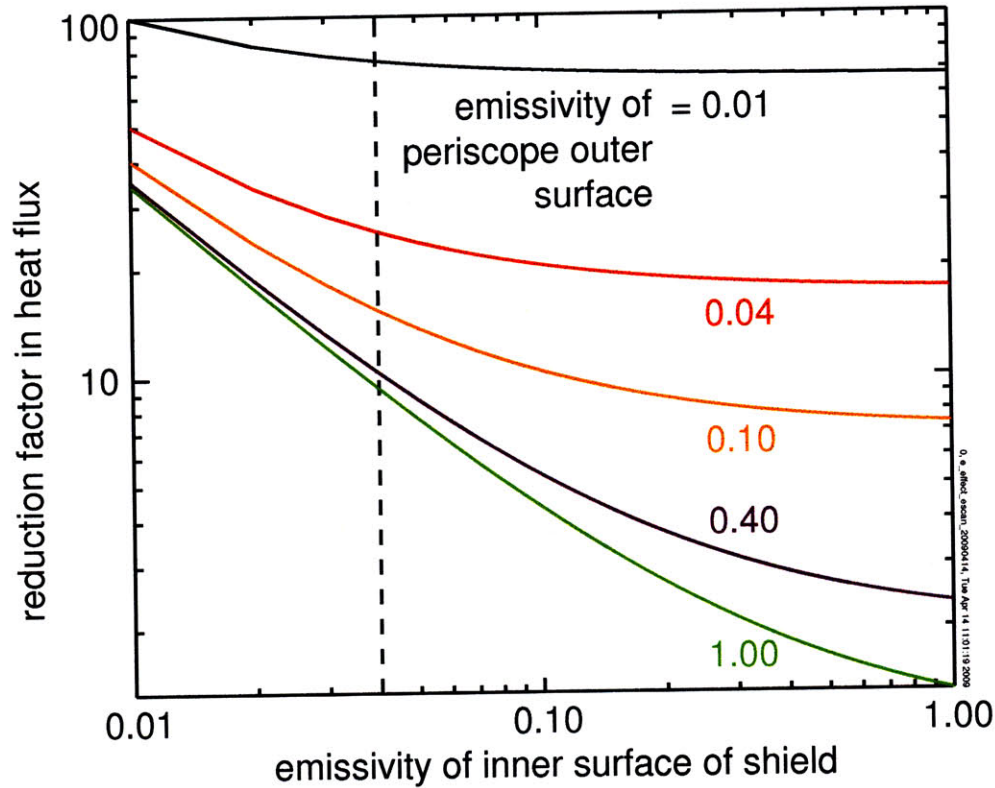
Figure 3-9: Ratio of the heat flux incident on the front side of the periscope without a shield to that with a shield as a function of the emissivity of the inner surface of the shield (ϵ_{2b} in Fig G-1 (a)) calculated by the model in Fig G-1 for 5 different emissivity values at the outer surface of the periscope (ϵ_{3a} in Fig G-1 (b)) with $q_e = 500$ W/m^2. The torus inner and outer wall temperatures are fixed at 27 °C and their emissivities are set to be unity. ϵ_{2a}, the emissivity of the surface directly facing the inner wall and the emissivity of the periscope inside are also assumed to be unity.

net heat flux incident on the front side of the periscope without a shield to that with a shield, representing the power reduction factor by having a shield, as a function of the emissivity of the inner surface of the shield for several different emissivity values of the outer surface of the MSE periscope. The temperatures of the inner and outer walls of the tours is fixed at 27 ^oC and the emissivities of these surfaces are assumed to be unity. The inner surface of the MSE periscope is also assumed to be a black body. For the external heat flux, q_e, 4 MW of power input to the plasma during 1.5 sec is assumed. With assumptions of 50 % radiated power and 7 m^2 of the torus wall area, the average power then becomes about 500 W/m^2 over a 15-minute between-shot interval. Fig 3-9 confirms that having low emissivity values for both surfaces that face each other produces the largest reduction in the heat flux. With the inner surface of the heat shield and the outer surface of the periscope gold-plated ($\epsilon \approx$ 0.04), the reduction factor in the power is expected to be about 25 (vertical dashed line in Fig 3-9).

In the previous subsection, we concluded that the temperature variation on the periscope surface should be kept reasonably small ($\sim$ 0.5 ^oC) to maintain a small temperature variation across the L2 doublet because the periscope and the lenses radiatively communicate each other. Fig 3-10 shows the temperature difference between the front and back sides of the periscope surface for the current configuration (no shield, no gold coating) and the upgraded configuration (shield with gold plating to the inner surface of the shield and to the outer surface of the periscope) as a function of external heat flux, q_e. The current upper bound of q_e is estimated from the following scenario: 6 MW ICRF for 1 sec, 2 MW LHRF for 0.5 sec, and 1 MW Ohmic power for 3 sec with 50 % of the radiation and 7 m^2 of the torus wall area. When averaged over 15 minutes, q_e becomes about 800 W/m^2. The nominal value of q_e (= 500 W/m^2) and this upper bound are indicated as dashed vertical lines in the plot. It is apparent there would be an order of magnitude improvement in the temperature variability across the periscope, which therefore, will reduce the temperature variation across the problematic lens roughly by the same order. However, the improvement is marginal since the temperature variation across the periscope is
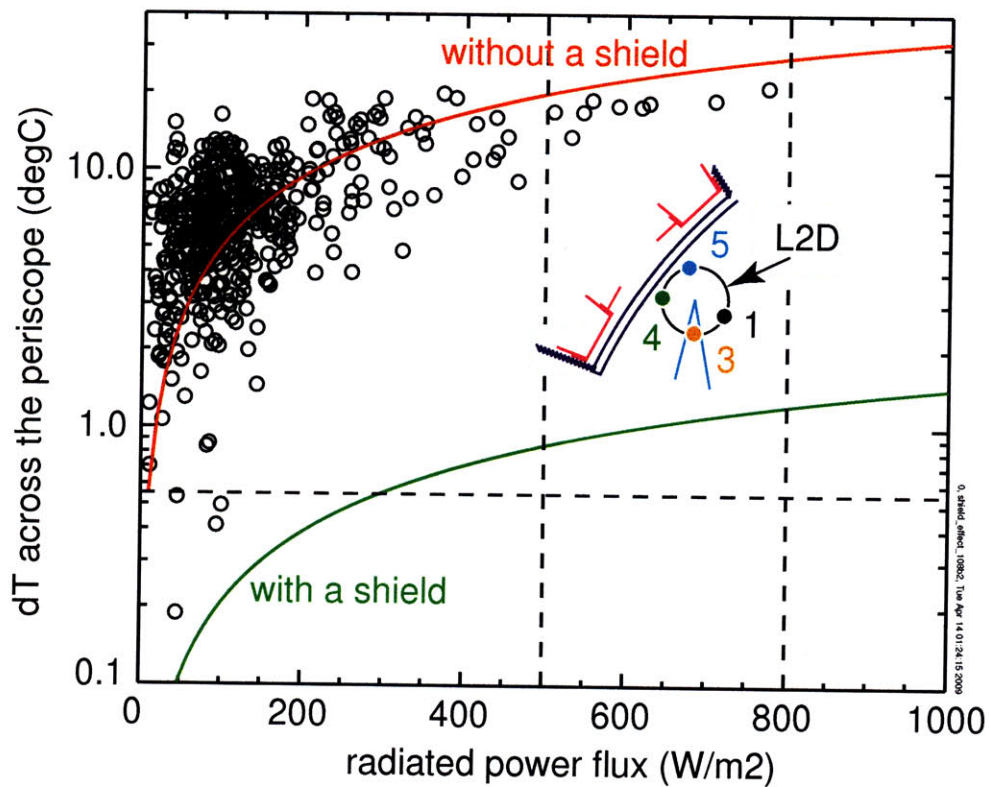
Figure 3-10: Temperature difference between the front and back sides of the periscope as a function of q_e calculated by the model given in Fig G-1 for the configurations with (green) and without (red) heat shielding. The data inferred from the measurements (by MSE thermocouples and 2π diodes) are also plotted (empty circle). Two vertical dashed lines indicate the power flux $q_e = 500$ (nominal) and 800 (upper bound) W/m^2 and the horizontal line at 0.55 °C is the maximum allowable temperature variability across the periscope. The torus wall temperatures are fixed at 27 °C. Emissivities of the torus plasma facing surfaces and the periscope inner surfaces are assumed to be unity.

still greater than 0.55 $^{\circ}C$ which may be required to reduce the temperature variation across the lens down to the point where the thermal stress-induced birefringence is negligible.

Also shown in Fig 3-10 are the equivalent data from the experiments. The radiated power measured by 2π diodes, P_{rad} for 564 shots from 20 run days with ICRF power during FY2008 has been used to infer the radiated heat flux q_e. P_{rad} is integrated over a shot to produce the radiated energy, divided by the torus area, and then divided by the time interval between the shot where the P_{rad} is taken and the next shot to finally obtain q_e. The temperature difference between the front and back sides of the periscope can be inferred based on the MSE invessel thermocouple measurements. The difference has been taken between the TC3 and TC5 (whose positions are also shown in Fig 3-10) where the former is regarded as 'front' and the latter as 'back'. Since these temperatures are measured about every 2 minutes and the temperature from each thermocouple at the beginning of a run vary depending on the conditions prior to the run, the temperatures from each thermocouple are first averaged between shots and normalized with the temperature from the same thermocouple measured before the first shot of each run. It is encouraging to see from Fig 3-10 that the experimental data indeed agree well with those calculated for the 'current' configuration.

Transient model

The model adopted for the steady-state calculations can also be used in the transient calculations. The governing equations are introduced in App G.2. The time history of the temperature difference between the front and back sides of the periscope is plotted in Fig 3-11 for two q_e values, 500 and 800 W/m^2. Again, a comparison is made between the current and the upgraded configurations in the plot and the time period shown in the plot is equivalent to about 10 shots. The temperature differences in both configurations reach their equilibrium value within about 2 shots (half an hour) with different values, again the difference being an order of magnitude larger for the no-shield configuration. Note that the same quantity for the steady state is
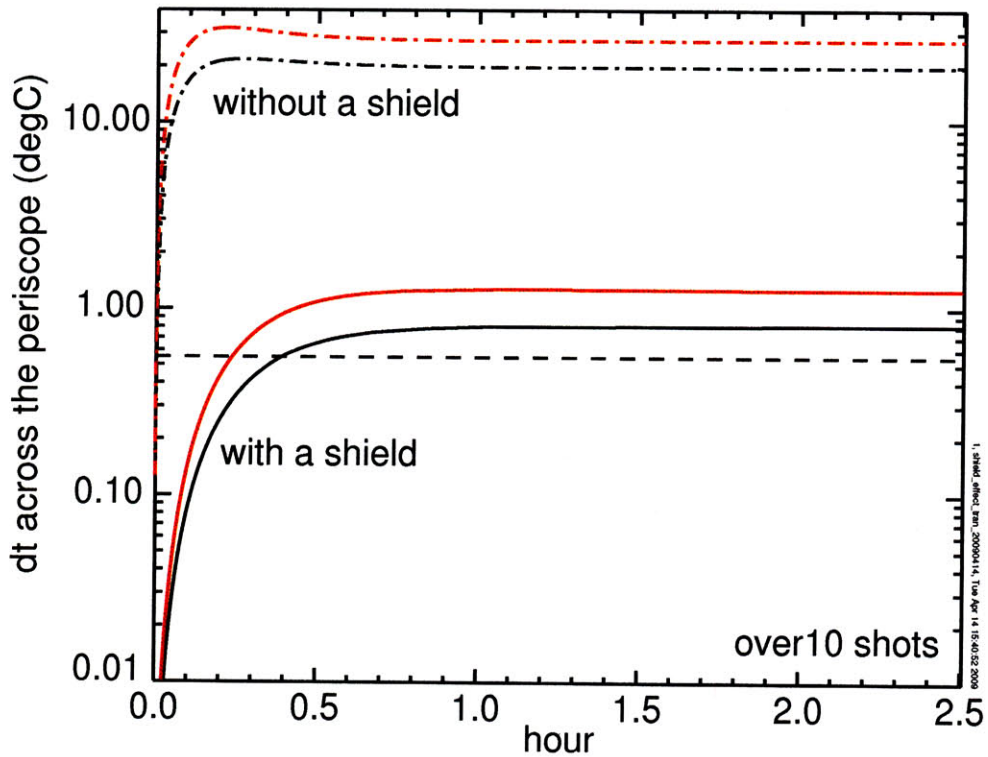
Figure 3-11: Time evolution of the temperature difference between the front and back sides of the periscope calculated by Eqn G.6 with single-shield (solid) and no-shield (dot-dashed) configurations for $q_e = 500$ (black) and 800 (red) W/m^2. Torus wall temperatures are fixed at 27 °C. Emissivities of plasma facing and periscope inner surfaces are assumed to be unity. The horizontal line at 0.55 °C is the maximum allowable temperature variability across the periscope.

Configuration	Solution	q_e (W/m^2)	
		500	800
no shield	steady-state	19.56	27.32
	transient	19.71	27.37
shield	steady-state	0.844	1.215
	transient	0.814	1.263

Table 3.1: The temperature difference (in Kelvin) between the front and back sides of the MSE invessel periscope from both the steady-state (Fig 3-10) and the transient (Fig 3-11) solutions for the no-shield and shield configurations given in Fig G-1.

shown in Fig 3-10 for various q_e values including 500 and 800 W/m^2. It is a good consistency check of the overall calculations to compare the equilibrated values from the transient calculations and the values from the steady-state calculations for the same heat flux. These values are presented in Table 3.1.

By virtue of the transient feature, the external heat flux (q_e) which is assumed to be continuous over a shot-to-shot interval can be treated more realistically, i.e. as a pulsed heat flux only during a plasma shot. Eqn G.6 can be solved with q_e treated in this way. Fig 3-12 compares the pulsed q_e solution with the continuous q_e solution by plotting the time evolution of (a) the temperature of the front side of the periscope and (b) the temperature difference between the front and the back sides of the periscope for the shielded configuration. The calculations are performed for q_e = 220 kW/m^2 and 360 kW/m^2 for 2 seconds every shot which are equivalent to 500 W/m^2 and 800 W/m^2 in the solution with the continuous heat flux, respectively. It is observed from both figures in Fig 3-12 that the solutions with a continuous heat flux provide a base profile for the more realistic profile that has small ripples shot by shot. This observation validates using the solutions with continuous q_e to infer long-time-scale, or between-shot averaged, behavior such as the temperature slew rate which is shown in Fig 3-13. For both heat fluxes, the heat shield can keep the temperature slew rate under 5 °C/hour. Although this is a significant improvement, this value is still larger than the maximum allowable slew rate ($\approx$ 1.5 °C/hour) determined in the bench test discussed in Sec 3.2.1 (See also Fig F-4 in App F.2), implying that the thermal shield with low emissivity (and low-emissivity periscope) alone cannot

176
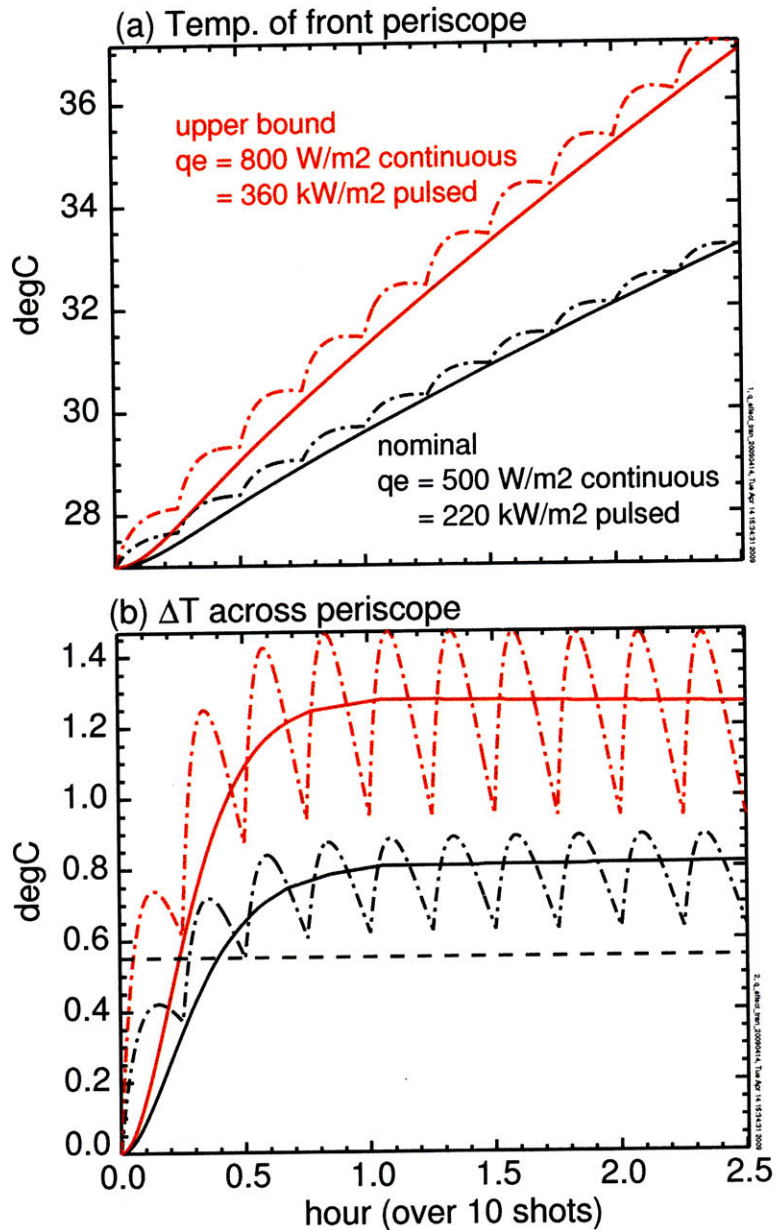
Figure 3-12: Comparison of the time evolutions of (a) periscope front temperature and (b) temperature difference between the front and back sides of the periscope between having continuous (solid) and pulsed (dot-dashed) q_e in solving Eqn G.6 for the single-shield configuration with nominal (black) and upper-bound (red) q_e values. Torus wall temperatures are fixed at 27 °C. Emissivities of plasma facing and periscope inner surfaces are assumed to be unity. The horizontal dashed line at 0.55 ° in (b) is the maximum allowable temperature variability across the periscope.
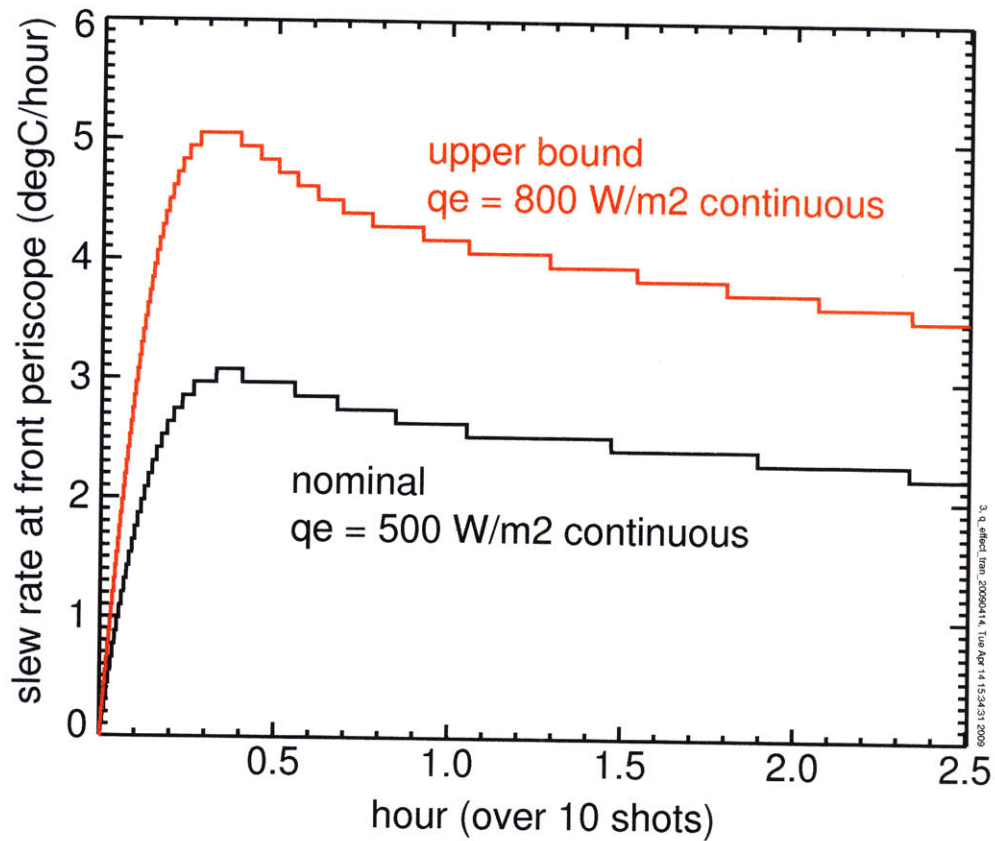
Figure 3-13: Time evolution of the temperature slew rate at the periscope front surface for nominal (black) and upper-bound (red) q_e values. Torus wall temperatures are fixed at 27 °C. Emissivities of plasma facing and periscope inner surfaces are assumed to be unity.

achieve the desired temperature uniformity on the lenses.

Implementation of gold-plated heat shields and periscope

Prior to the FY2009 campaign, design and fabrication of the single-layer thermal shield was carried out performed by the engineering team from the Princeton Plasma Physics Laboratory. The shape of the shield has been determined by several iterations of the invessel test fit and the metrology measurements. The shield is made of annealed Inconel 718 that has the yield strength of about 400 MPa (2/3 yield $\approx$ 266 MPa) which is large enough to withstand the calculated maximum stress during a disruption ($\sim$ 200 MPa).

The inner surface of the shield has been gold coated after polishing to have the emissivity of $\lesssim$ 0.04. In addition, the outer surface of the MSE invessel periscope has been gold coated as well.

3.2.3 Discrete-contact o-ring in lens holder

With a high-performance thermal shield, the dominant factor that affects the temperature variation across the L2 doublet is direct plasma heating of the object lens L1, which is unshielded. Heat energy in L1 is then conducted and radiated upward through the vertical part of the MSE periscope ("turret") into the critical L2 area. To illustrate the effect of the direct radiation from L1, a simple thermal capacitive circuit analysis is discussed. The MSE invessel periscope is simplified to have five temperature 'nodes': at L1, L2 center, L2 edge, the vertical periscope, and the horizontal periscope. The detailed description of the model and solution procedures are discussed in App G.3. The numerical solutions to this model are given in Fig 3-14 (a) for 3 consecutive shots with the nominal pulsed external heat flux to L1 of 220 kW/m^2 for 2 seconds every 15 minutes (500 W/m^2 in the continuous mode) assumed. The wall temperatures are fixed at 300 Kelvin. Overall, the temperature at L1 is decoupled from the rest of the system but it does affect the temperature evolutions at the vertical periscope through the heat conduction and L2 through the radiation.

179
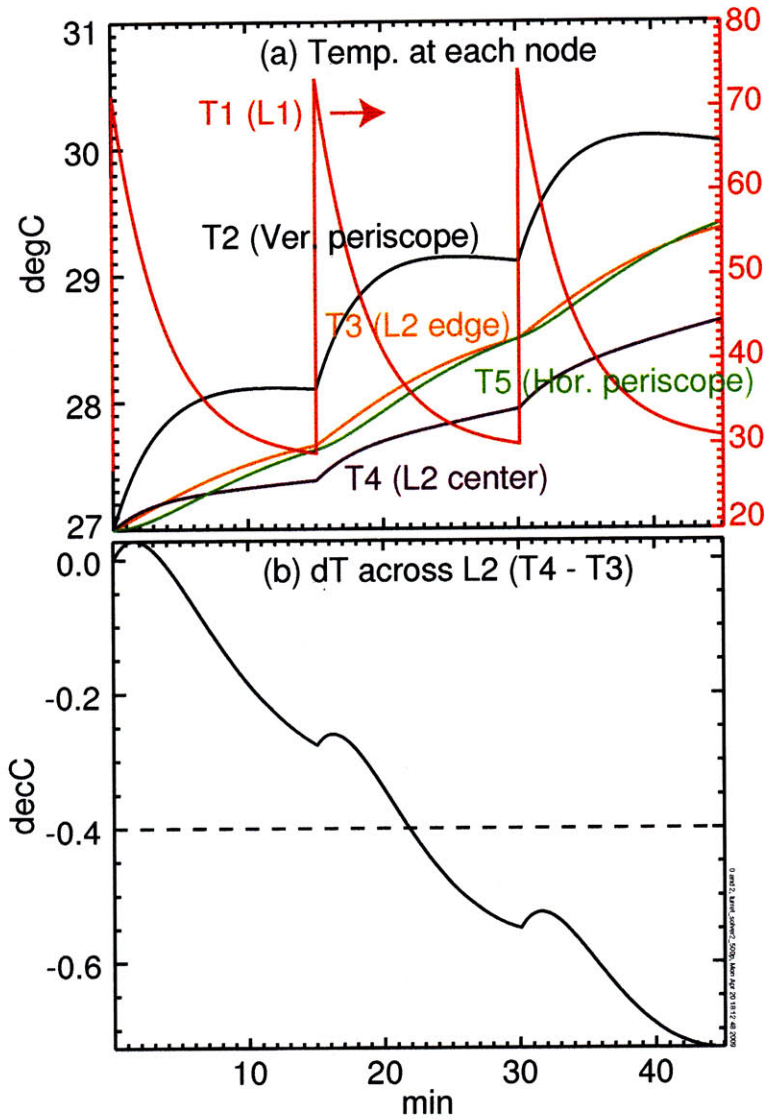
Figure 3-14: Numerical solution to Eqn G.29 with the configuration given in Figs G-2 and G-3 for three consecutive shots with $q_e = 220$ kW/m^2 for 2 seconds every 15 minutes with a fixed wall temperature of 300 Kelvin. (a) shows the temperature time evolution at each node and (b) the temperature difference between the center and the edge of L2 (center - edge).

Since the edge of L2 is coupled not only radiatively to the horizontal part of the periscope but also conductively to the vertical part of the periscope, a temperature variability of order a degree develops between the center and the edge of L2 as shots go along. Note from Table G.3 that R_{L2}^c, the conductive resistance between the central and boundary parts of L2, is much larger than the other conductive resistances in the configuration. Fig 3-14 (b) shows the temperature variability across L2 (center - edge) with the same time frame as (a). The temperature variation exceeds the maximum allowable value ($\sim$ -0.4 °C; dashed horizontal line in the plot) after the first shot and continues to increase. *These observations imply that the temperature variability across the lens L2 can be reduced by minimizing the conduction path between L2 and the surrounding periscope.* This conjecture is tested by solving the problem with several different values of R_{L2o}^c, the conductive resistance across the Viton o-ring between the edge of the lens and the lens holder. Fig 3-15 shows the temperature difference across L2 over 30 consecutive shots for 6 different multiplication factors (f) to the nominal R_{L2o}^c given in Table G.3 with (a) nominal (220 kW/m^2) and (b) upper bound (360 kw/m^2) q_e. The multiplication factors are 0.1, 0.5, 1, 2, 10, and 10^{25}, the last one representing a complete thermal isolation of the lens against conduction through the rest of the system. It is shown that even a factor of 10 reduction in the conduction path is marginal to achieve the temperature variability under 0.4° for the nominal radiative heat flux through L1. A further reduction may be required for the upper-bound radiation. Nevertheless, there seems to be a limit in reducing the temperature variability with this approach since the zero conduction between L2 and the periscope does not produce zero variability, instead, reaching an equilibrium in the rate of change, which is tiny, but finite.

Implementation of lens holder with discrete o-ring contact

Prior to the FY2009 campaign, a thermal isolation mechanism that can minimize the conduction path between the lens L2 and the surrounding material was designed and fabricated. The configuration ultimately adopted was based on an initial proposal to replace the existing, continuous O-ring with a number of small, discrete O-ring
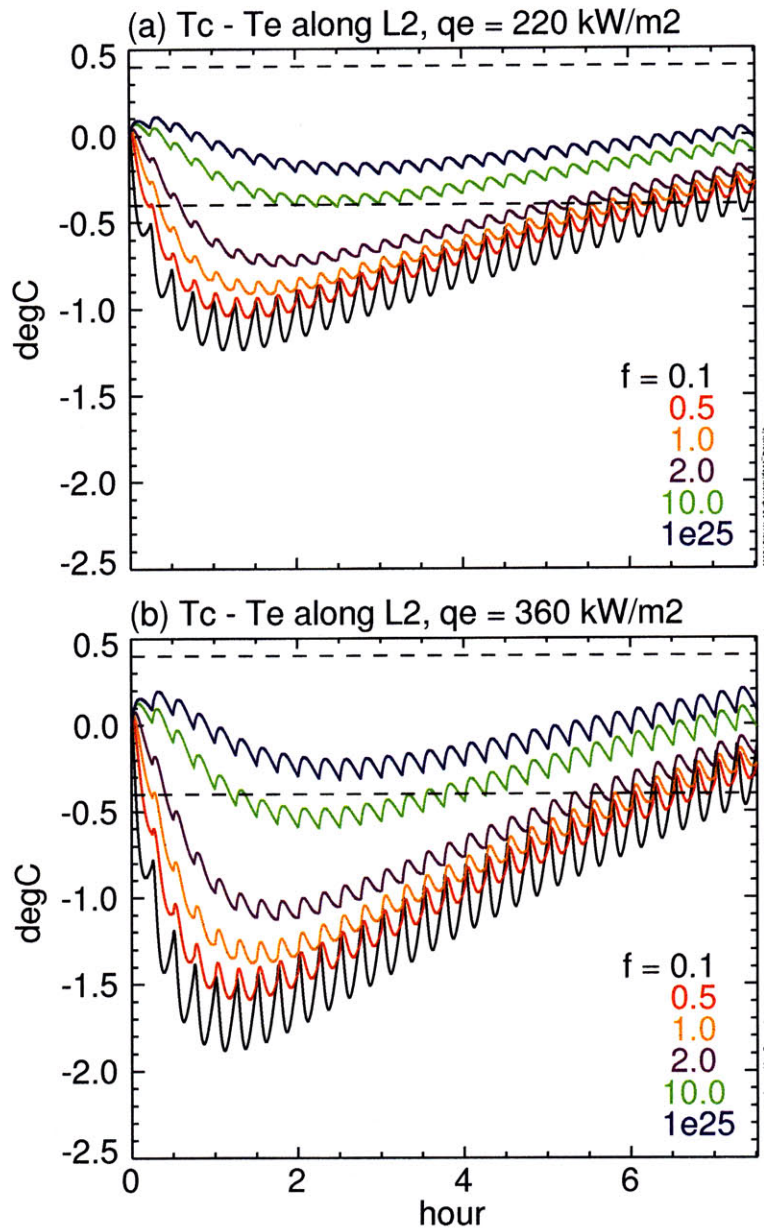
Figure 3-15: Time evolution of temperature difference across L2 from the numerical solution to Eqn G.29 over 30 consecutive shots for 6 different multiplication factors (f) to the nominal R_{L2o}^c, the conductive thermal resistance across the Viton o-ring given in Table G.3 with $q_e =$ (a) 220 kW/m^2 and (b) 360 kW/m^2 for 2 seconds every 15 minutes with a fixed wall temperature of 300 Kelvin.

segments, thereby decreasing the total contact area between the lens and the O-ring. However, this design provided insufficient cushioning of the lenses against the severe vibrations expected during disruptions ($\sim$ 200 G). The design ultimately adopted adds eight raised ridges to the usual rectangular cross section of the O-ring 'gland' (the groove in which the O-ring sits). Effectively, the O-ring contacts the lens only at eight discrete locations along the lens periphery. But in the event of a disruption, the full circumference of the O-ring participates in cushioning the lens.

3.3 Dual-waveplate model of stress birefringence

According to the single-waveplate model (Eqn 3.10) which is the basis of the in-situ calibration scheme presented in Sec 3.1.3, the periodicity is 90° with respect to the direction of an incident polarization, i.e. the magnitude of the change in the polarization angle due to the thermal-stress induced birefringence should have 90°-periodicity as a function of the input polarization with fixed phase shift and fast axis. There is also the same periodicity with respect to the fast axis for fixed phase shift and input polarization angle. These periodicities are the fundamental features with which the argument of the 'averaging' effect is made. The averaging effect, where the thermal stress-induced birefringent effect is averaged out when the incident rays completely fill the lens under a symmetric thermal stress pattern, is believed to be the reason why heating L3 generates a much smaller spurious change in polarization direction compared to heating L2. Several bench experiments were performed to examine this postulate, but no clear periodicity was observed. In this section, the results of such experiments are discussed and a new model, so-called 'dual-waveplate model' is introduced to explain some of the experimental results. Finally, the implications on the effects of the non-thermal phase shifts from, for example, imperfect mirrors are discussed.

3.3.1   L3 heating test with masks

In order to examine the 90° periodicity in the measured polarization angles with respect to the fast axis of the thermal birefringent 'waveplate' suggested in Eqn 3.10, an aperture with a hole whose diameter was 3 cm was installed on the surface of L3 (15.5 cm in diameter) as shown in Fig 3-16. The location of the hole was scanned
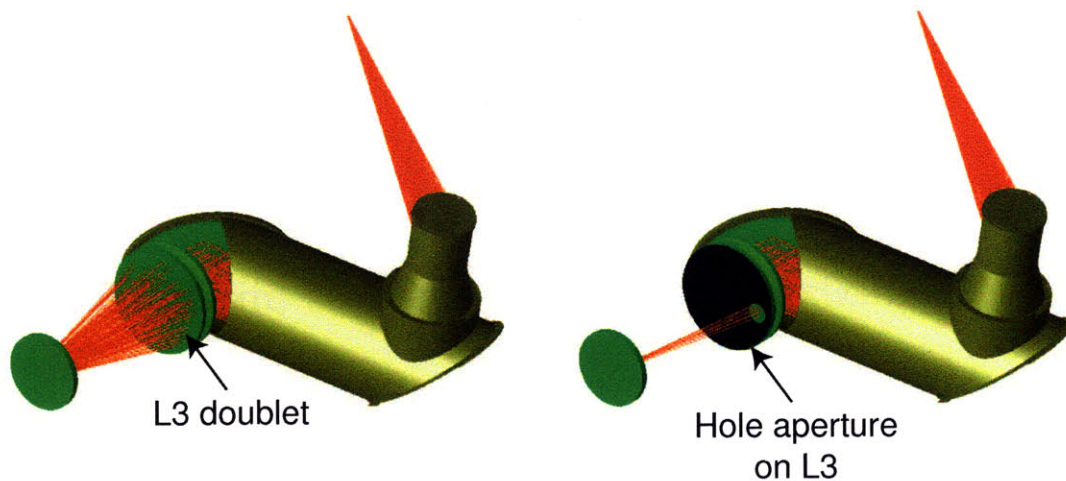
Figure 3-16: L3 heating test setup with a hole-type aperture to localize the thermal stress-induced birefringent effect.

azimuthally every 30° while the periphery of the L3 doublet was being heated and the polarization angles were measured with a fixed input polarization for every location of the hole aperture. By scanning the hole position with a quasi-steady heating, it was expected that only the fast axis of the thermal birefringent waveplate was scanned with a constant phase shift (and a constant input polarization angle, of course). Fig 3-17 shows the experimental results. With a fixed input polarization angle of 50°, the output polarization angle was measured every 30° of the hole aperture position for 6 different MSE channels.

It should be noted that measuring the polarization angle using this kind of small aperture could cause a spurious change in the measured angle even without any heating since the aperture localizes the angles of incidence of the rays and the surface of the PEM where the retardance has a finite spatial distribution. Therefore, the
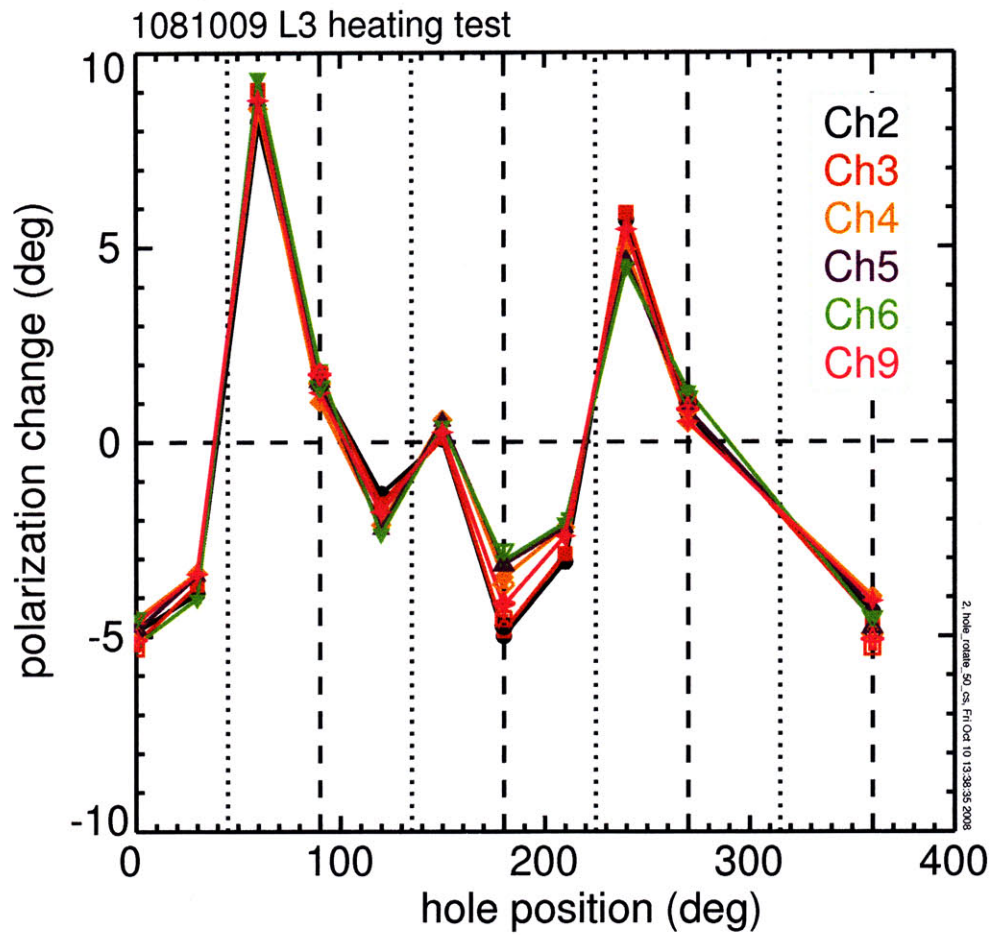
Figure 3-17: Change in the polarization angle from the L3 heating test with the hole-aperture scan for 6 MSE channels. Also shown in the figure are the data points (empty symbols) at some hole positions (180° and 360°) which are taken from a separate test with the same kind of setup, reflecting a good reproducibility.

same hole scan was performed without any heating prior to the scan with heating as a reference. It is the difference between the scan results with and without heating for the same locations of the hole that is plotted in Fig 3-17.

Data were acquired well after the temperature of the system floated sufficiently from the room temperature, which effectively fixed the profile of the temperature near the peripheral region of the lens where the holes were scanned. This way, it was assumed that the fast axis and the phase shift from the thermal stress were fixed during the full scan of the hole position. This assumption can be validated by observing the change in the polarization angles measured at the beginning and at the end of the scan, both having the same position of the hole (0° and 360°), the difference between the two measurements acting as an upper bound of the uncertainty due to the possible change in the thermal condition. As can be seen from the figure, this difference is negligible. The reproducibility of the test can also be checked by looking at a couple of data points (in empty symbols) near the hole locations of 180° and 360° in Fig 3-17. These are the data points obtained from a separate test using the same experimental setup.

It is not immediately apparent from Fig 3-17 that the change in polarization direction has a 90° periodicity with respect to the angular location of the hole position (which is a proxy for the fast-axis direction). The angular resolution (30°) of this initial experiment is somewhat too coarse to make a definitive assessment. Another concern is using hole location as a proxy for the direction of the fast axis; only when the temperature profile is circularly symmetric will the fast-axis direction be in the azimuthal direction (i.e. perpendicular to the radial direction). It is unlikely that the experimental configuration achieved perfect azimuthal symmetry of the temperature distribution because L3 was standing vertically during the experiment, so air convection would create an up-down asymmetry.

To avoid this ambiguity and also to test the 90° periodicity in the polarization angle change with respect to input polarization predicted by the single-waveplate model, the position of the hole was fixed and the input polarization angle was scanned from 0 to 360°. This way, it is possible to ensure that the fast axis and phase shift

are fixed and that only the input polarization changes.

Fig 3-18 shows the spurious change in polarization as a function of input polarization for 6 MSE channels. As before, the same input-polarization scan was performed
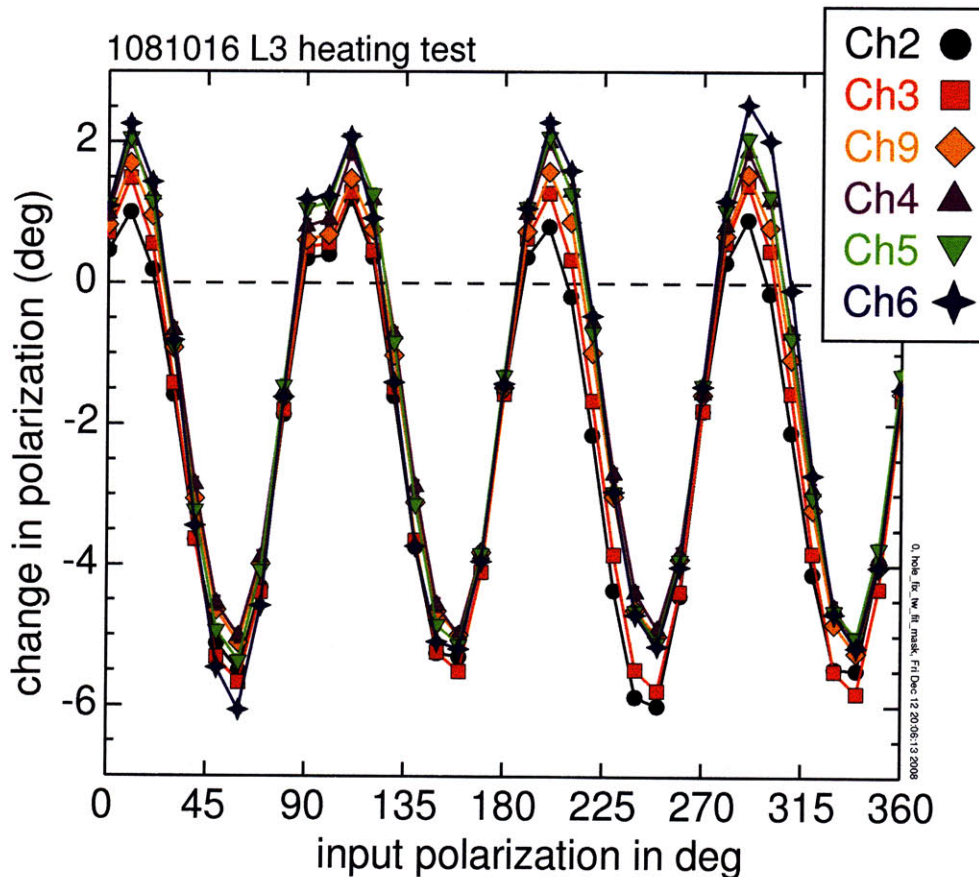
Figure 3-18: Change in the polarization angle from the L3 heating test with the input polarization scan for 6 MSE channels.

in a 'cold' state prior to that with heating and the difference between these two scans are plotted. Now a clear 90° periodicity is evident, but the prominent feature of this result is the up-down asymmetry of the polarization change which is absent from the single-waveplate model. Due to this up-down asymmetry, no cancellation occurs every 45°. This observation motivated a new model - dual-waveplate model - where non-thermal phase shifts that can arise from imperfect mirrors can amplify the phase shift caused by the stress-induced birefringence on the lens. Because the effects of the non-thermal and thermal phase shifts are not linearly related, simple subtraction

Data source	Mirror	Angle of incidence		
(year)		30°	45°	60°
Univ. of	M1	-4°	-9°	1.5^o
Arizona	M2*	$-2^o \sim -1^o$	$-1^o \sim 1^o$	$12^o \sim 14^o$
(2009)	M3	-3°	-2.5^o	9°
RMI	M1	2°	-2.5^o	8°
(2001)	M2	2°	-2.5^o	6°
	M3	2°	-2.5^o	9°

Table 3.2: Mirror retardances measured by University of Arizona and calculated by the original vendor, RMI. *The measurement for M2 by Univ. of Arizona was made multiple times for various portions of M2.

cannot completely eliminate the mirror phase shift.

3.3.2   Model including the non-thermal phase shift

In the 'dual-waveplate' model, the MSE optics system is represented as two waveplates plus an ideal polarimeter. One waveplate represents the fixed phase shift imposed by the MSE elements. For example, it is known that the dielectric mirrors impose a phase shift that is highly dependent on the angle of incidence. The current MSE dielectric mirrors were fabricated to minimize the phase shift through appropriate selection of the dielectric layers, but it is impossible to eliminate the phase shift entirely over a finite range of wavelengths and angles of incidence. Table 3.2 shows the retardances for the current MSE mirrors measured by the Polarization Lab in the University of Arizona near the MSE pass band ($659 \sim 661$ nm) for three typical angles of incidence. Also included in the table are the calculated retardances provided by the original mirror vendor (RMI) at the time of the fabrication (2001). The original mirror dielectric coatings were optimized to have minimum phase shifts over the angles of incidence $45^o \pm 10^o$. However, the angles of incidence for the rays incident on the mirrors range roughly from 30° to 60° depending on channels (more specifically, 32° (core) $\sim 57^o$ (edge) at M1; 34° (core) $\sim 57^o$ (edge) at M2; and 40° (core) $\sim 63^o$ (edge) at M3). The measurements by University of Arizona are somewhat different from the original RMI values, which may be due to either the degradation of the dielectric

coatings or some errors in the original calculations. These measurements indicate some rays could experience multiple degrees of phase shifts when they are reflected onto the mirror surfaces, which will be represented by a waveplate with a fixed fast axis and a phase shift.

The second waveplate represents the additional phase shift due to thermal stress-induced birefringence in the MSE lenses. This effect is caused by non-uniform temperatures in the MSE lenses. This phase shift is variable in time, as the temperature environment of the lenses changes throughout the course of a run day.

In Sec 3.1.3, the Müeller matrix for a waveplate with its fast axis oriented at an arbitrary angle with respect to the horizontal axis was derived (Eqn 3.6). The basic approach is to insert another Müeller matrix for the second waveplate into the matrix equation that gives the output Stokes vector

$$S_{out} = M_{w1} \cdot M_{w2} \cdot S_{in}, \tag{3.14}$$

where S_{in} is the Stokes vector for linearly polarized light with the polarization angle γ which is given in Eqn 3.7. M_{w1} represents the first waveplate whose fast axis and phase shift are ϕ and ϵ and M_{w2} is the Müeller matrix for the second waveplate with its fast axis Φ and phase shift E. The general form of M_{w1} and M_{w2} is given in Eqn 3.6. The polarization direction of the light that passes through both waveplates, θ_{12} can be inferred from $\tan 2\theta_{12} = S_{out}[2]/S_{out}[1]$ where the numerator and the denominator are the third and the second elements of S_{out}, respectively.

In this system, the order of the Müeller Matrices for the two waveplates is such that the incident light passes through the second waveplate W_2 first, and then it passes through the first waveplate W_1. So for example, W_1 can be regarded as being the MSE mirror system, and W_2 as being the effect of the L2 lens doublet. The situation is complicated by the fact that there are three mirrors in the MSE optical chain, and L2 lies between the first and second mirrors. But for simplicity, we will assume that MSE system can be characterized by just a single imperfect mirror, and that this mirror lies 'downstream', i.e. behind the L2 lenses.

189

The quantity of interest is the change in polarization angle measured by MSE due to birefringence in the lenses, which in this model is the polarization-angle change due to the second waveplate W_2. Note that we are not interested in the total change in polarization angle due to *both* waveplates for this quantity, but only in the *additional* change in polarization angle due to W_2. This is because the change in polarization angle due to W_1 becomes part of the MSE calibration and so it is entirely compensated by the calibration procedure. In this analysis, therefore, care must be taken to acknowledge that the invessel MSE calibration compensates for the effect of the imperfect mirrors. Without the thermal effect, the single-waveplate model (Eqn 3.10) can be used to infer the output polarization angle, θ_1, affected by the imperfect mirror only. Then, the change in angle $\Delta\theta_2$ due solely to the second waveplate (i.e. the effect of birefringence in the L2 lenses) is given by

$$\Delta\theta_2 = \theta_{12} - \theta_1, \tag{3.15}$$

$\Delta\theta_2$ being a function of the properties of the two waveplates and the incident polarization direction.

There is a subtle distinction about precisely how the effect of the first waveplate should be accounted for in the analysis. In the discussion above, we simply subtracted the change in polarization angle that would occur if the second waveplate were absent, i.e. if only the first waveplate were present. In principle, the strictly correct procedure is to use Eqn 3.10 to construct a true 'calibration curve' for the MSE optical system, and then use this calibration curve to interpret what polarization angle would be attributed to the final polarization angle θ_{12}. Both approaches yield nearly the same change in angle that is attributed to W_2, so Eqn 3.15 is sufficiently accurate for the purpose of comparing the experimental results.

Fig 3-19 directly addresses the effect of the intrinsic phase shift on the spurious error in polarization in the system under the thermal stress-induced birefringence for four different lens phase shifts, For these calculations, the maximum spurious change in $\Delta\theta_2$ is obtained by computing the change as a function of (a) input polarization
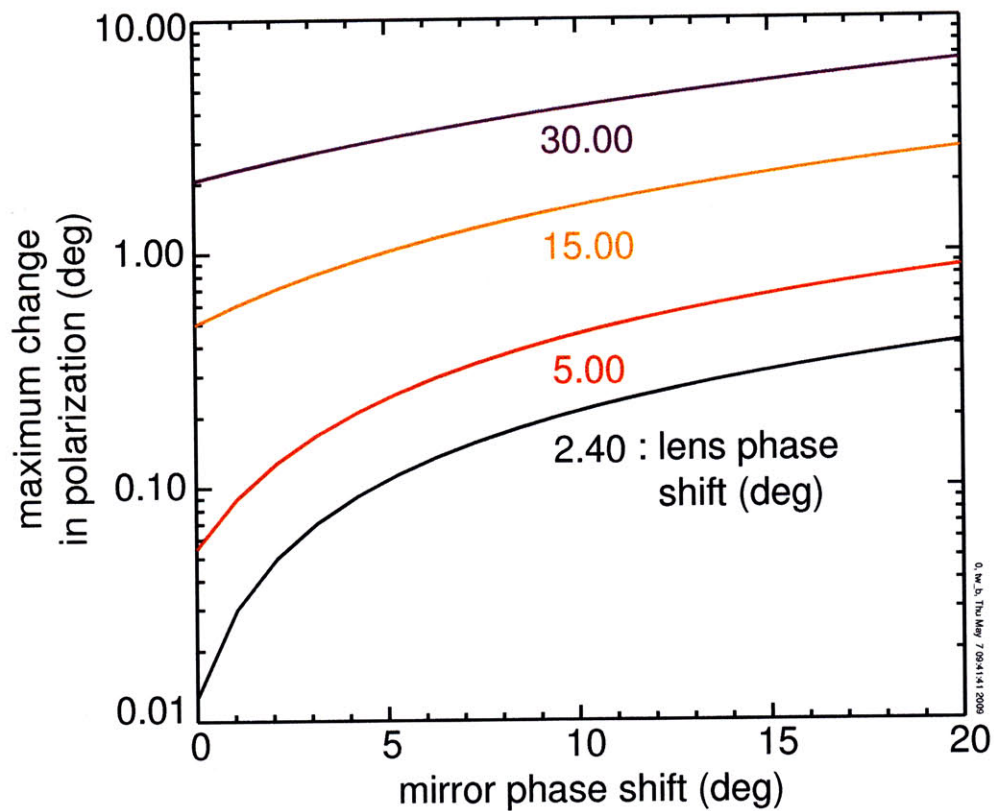
Figure 3-19: Scaling of the maximum change in polarization direction as a function of the magnitude of phase shift of the mirror, ϵ, for four different lens phase shifts, $E's$. The maximum is taken over all input polarization angles and all orientations of the fast axis of the lens. The fast axis of the mirror, ϕ, is assumed to be horizontal.

angle; and (b) fast axis of W_1 (mirror), and taking the maximum over both quantities. The fast axis of the mirror is held constant at 0°. The chosen values for E in this figure correspond to the temperature variation along the L2, $\Delta T = 0.5, 1, 3$, and 6 ^{o}C (using Eqn 3.5). In the absence of a phase shift due to the mirror, i.e. at $\epsilon = 0$, the maximum spurious change in polarization angle is under 0.1^o for the phase shifts imposed by the lens, E, of 2.4 and 5°, which is the result one would obtain in the single-waveplate model as well. However, as illustrated in Fig 3-19, the spurious change in angle grows almost linearly as the phase shift imposed by the mirror increases. For example, if $\epsilon = 10^o$, the spurious change in polarization angle increase to about 0.2^o and 0.4^o for $E = 2.4$ and 5°, respectively - a factor 20 and 8 increase over the error that would be obtained for $\epsilon = 0$. This figure indicates that the phase shifts of the first and second waveplate interact nonlinearly, and therefore the presence of an intrinsic (non-thermal) phase shift in the MSE optics can greatly magnify the change in polarization angle generated by a phase shift induced in the lenses, in a way that is not compensated by the normal MSE calibration. Fig 3-20 is a plot similar to Fig 3-19 but it shows the maximum change as a function of both the temperature variability and the lens phase shift, which are related to each other via Eqn 3.5, for four different mirror phase shifts. Also shown in the figure are the experimental data points which are in better agreement with the cases with mirror phase shifts of $10 \sim 20^o$ rather than zero mirror phase shift which corresponds to the single-waveplate model.

3.3.3 Comparison with the test results

The validity of the dual-waveplate model is compared with the experimental data from the hole-apertured L3 heating test with the input-polarization scan introduced in Sec 3.3.1. The experimental configuration with a hole-apertured mask onto L3 with heating corresponds to having fixed fast axis E and phase shift Φ in the thermal waveplate (W_2). In addition, the fast axis ϵ and phase shift ϕ of W_1 (imperfect mirror) are independent of the thermal stress and stationary during the test. Fig 3-21 shows the same experimental data shown in Fig 3-18 but with the fit using Eqn
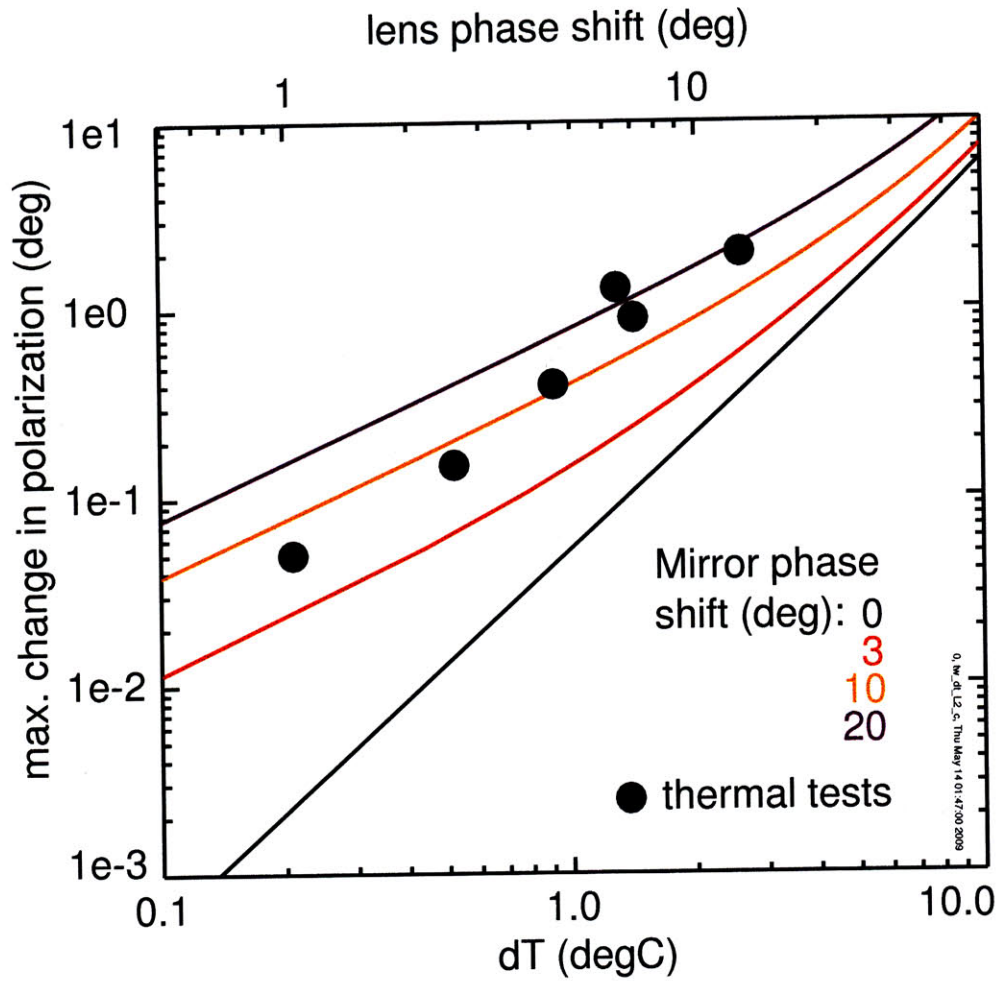
Figure 3-20: Scaling of the maximum change in polarization direction as a function of the magnitude of phase shift of the lens, E, and the temperature variability across the lens for four different mirror phase shifts, ϵ. The maximum is taken over all input polarization angles and all orientations of the fast axis of the lens. The fast axis of the mirror, ϕ, is assumed to be horizontal. The points are from thermal bench tests.

3.15 overplotted and indicates that the up-down asymmetry can be well modeled using the dual-waveplate model.
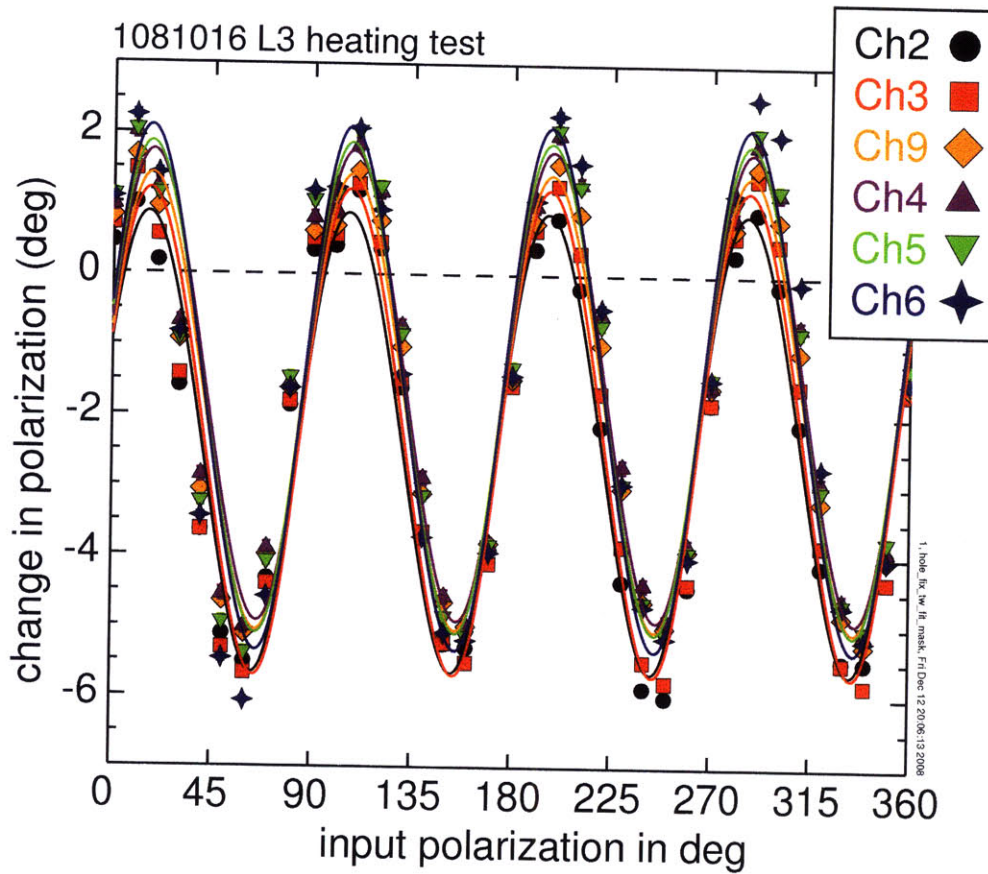
Figure 3-21: Data shown in Fig 3-18 with the fit using the dual-waveplate model: Change in the polarization angle from the L3 heating test with the input polarization scan for 6 MSE channels (Ch2:edge → Ch6:core).

By fitting the experimental data, complete information on the waveplate parameters both for the imperfect mirror and the birefringent lens is obtained, which enables one to characterize the dependence of the spurious change in polarization on the birefringence state of the lens and to compare it with the dual-waveplate model. Table 3.3 summarizes the coefficients of the fit shown in Fig 3-21. Note that the mirror phase shift, ϵ, obtained from this fit corresponds to the fixed phase shift imposed by the mirrors whose measured values are given in Table 3.2. The mirror phase shifts from both tables are near $10 \sim 20^{\circ}$. This presents good qualitative agreement be-

Part	Ch	fast axis (^{o})	phase shift (^{o})
Mirror		ϕ	ϵ
	2	10.9 ± 1.58^o	19.0 ± 0.99^o
	3	12.2 ± 1.73^o	17.0 ± 0.92^o
	9	14.6 ± 3.42^o	14.5 ± 1.62^o
	4	13.2 ± 8.00^o	11.5 ± 2.45^o
	5	7.49 ± 7.78^o	10.4 ± 1.38^o
	6	4.36 ± 3.91^o	9.64 ± 0.47^o
Lens		Φ	E
	2	50.2 ± 0.14^o	27.4 ± 1.18^o
	3	49.4 ± 0.12^o	29.3 ± 1.15^o
	9	48.9 ± 0.14^o	29.0 ± 1.96^o
	4	47.9 ± 0.17^o	31.6 ± 3.55^o
	5	47.1 ± 0.14^o	34.4 ± 2.94^o
	6	46.6 ± 0.07^o	36.8 ± 1.34^o

Table 3.3: Coefficients of the fit shown in Fig 3-21 with the dual-waveplate model for 6 MSE channels (Ch2:edge $\rightarrow$ Ch6:core).

tween the data fit and the dual-waveplate model. Also, it should be noted that all the coefficients shown in Table 3.3 smoothly vary with channel number, which is another consistency check in this approach since the lens stress state and mirror phase shift should vary smoothly, as one moves smoothly across the surface of the mirror and lens. Recalling Eqn 3.5 which relates the temperature variation from the center to the edge of the lens to the thermal-stress induced phase shift, yet another consistency check is possible. Eqn 3.5 can be re-written as

$$\Delta T = \frac{\epsilon}{26} \left(\frac{b}{r} \right)^m \left(\frac{m+2}{m} \right) \tag{3.16}$$

for L3. Using the phase shift imposed by the lens (i.e. thermally induced phase shift) given in Table 3.3 ($\approx 30^o$), ΔT becomes 3.1 ^{o}C, 3.4 ^{o}C, and 3.0 ^{o}C for $m = 2$, 1.5, and 2.5, respectively. The temperatures were measured at three peripheral locations around L3 during this test and the temperature differences range from 1 ^{o}C to $\gtrsim$ 3 ^{o}C. Although these temperature differences are not the temperature variation from the center to the edge of the lens, they should not be much different from the real ΔT of the lens, implying that the lens phase shifts obtained from the fit are reasonable.

The top plot in Fig 3-22 shows the maximum polarization change versus the phase shift of the lens using the dual-waveplate model where the waveplate parameters Φ, ϕ, and ϵ are from the fit shown in Fig 3-21. Also shown in the plot are the data points directly obtainable from the experiment, i.e. the maximum change in the polarization during the input scan, whose position on the horizontal axis is determined by the fit coefficient for the lens phase shift (E). The corresponding plot purely from the model using Eqn 3.14 is given at the bottom in Fig 3-22 where the maximum polarization change is taken over the input polarization (γ) and the fast axis of the lens (Φ) with the fast axis (ϕ) and phase shift (ϵ) of the mirror fixed at 0° and 9°, respectively.

The average polarization change can also be compared in a similar way. The top plot in Fig 3-23 shows the average change in polarization over the full 360° scan as a function of the fast axis of the lens (Φ) using the dual-waveplate model with the other parameters from the fit. The data points directly obtainable from the experiment are also shown in this plot, this time, their positions on the horizontal axis determined by the fit coefficient for the lens fast axis (Φ). The corresponding scaling purely from the model using Eqn 3.14 is given at the bottom in Fig 3-23 where the average polarization change is taken over the input polarization (γ) with the phase shift of the lens (E) held at 16° and the fast axis (ϕ) and phase shift (ϵ) of the mirror fixed at 0° and 9°, respectively. Note from both the top and bottom plots that except at special fast-axis angles of the lens, the change in polarization angle does not vanish, i.e. the spurious change in polarization due to the thermal stress-induced birefringence is not 'averaged out' all the time even if the input polarization rotate by 360°. This is the observation the single-waveplate model would never predict.

Retrospectively, we might have been scanning not only the fast axis on the heated lens but also effectively the fast axis (and phase shift) of the mirror by changing the angles of incidence of the rays in the L3 heating test with the hole aperture position scan. This might have complicated (and probably made almost impossible) the correct interpretation of the data (shown in Fig 3-17). Fixing the position of the hole and scanning the input polarization instead, therefore, seems to be a more reasonable approach to test the model.
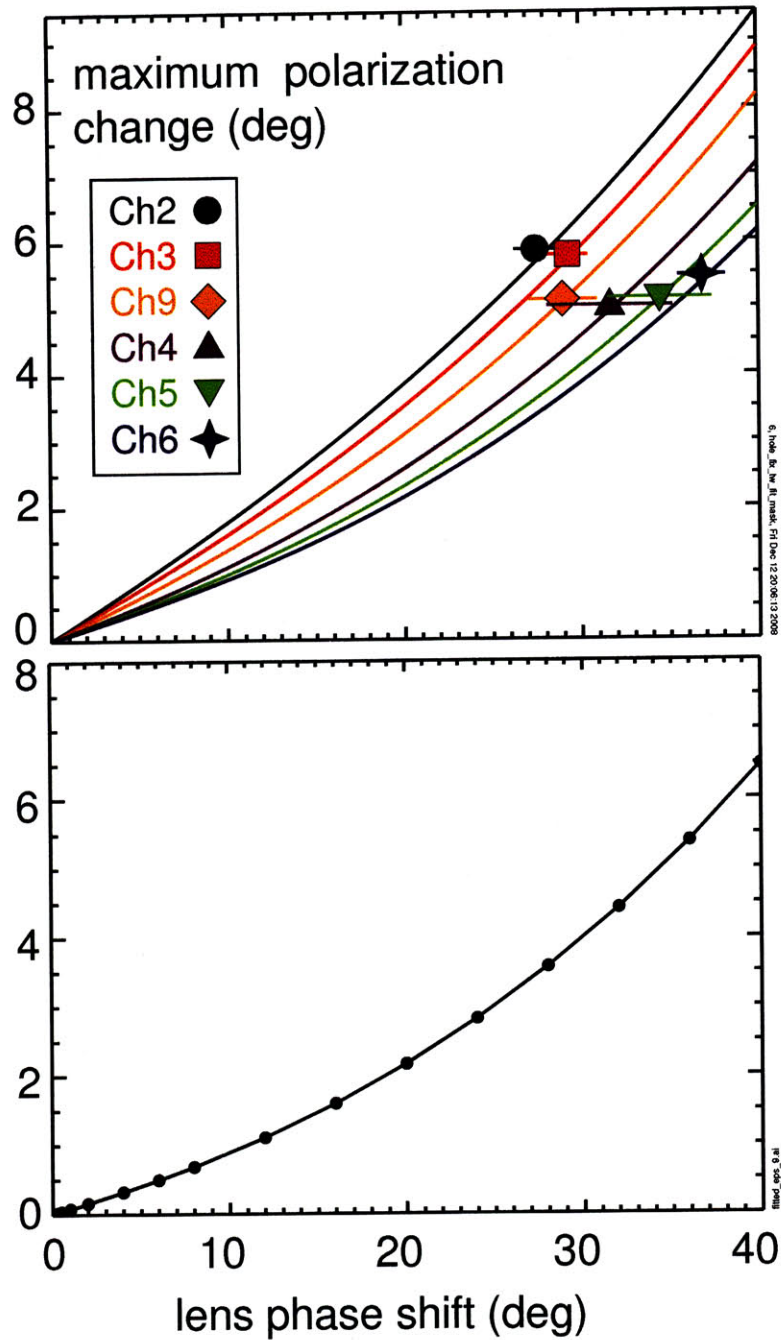
Figure 3-22: Maximum polarization change versus the phase shift of the lens calculated by the dual-waveplate model with the remaining variables determined from the fit of the experimental data (top) and purely computed by the model using Eqn 3.14 (bottom). The symbols on the top plot are directly from the experimental data
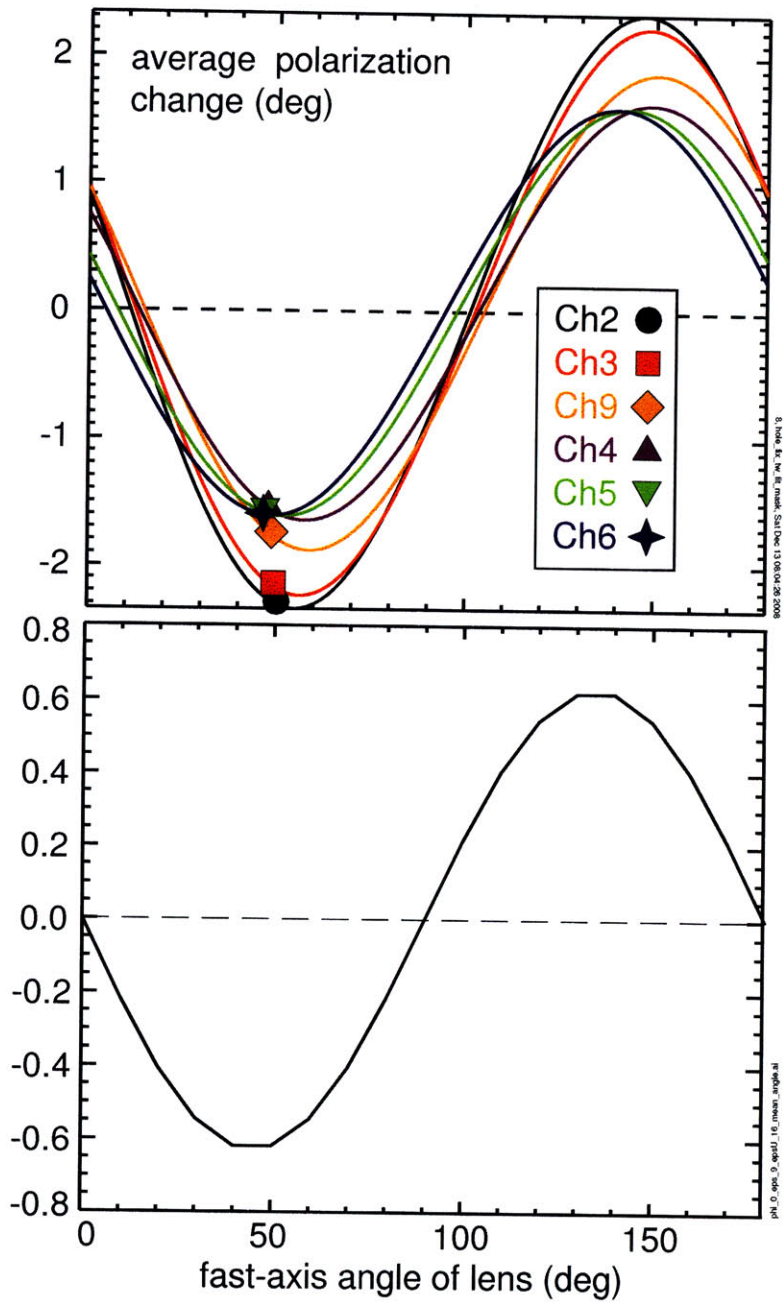
Figure 3-23: Average polarization change versus the fast axis of the lens calculated by the dual-waveplate model with the remaining variables determined from the fit of the experimental data (top) and purely computed by the model using Eqn 3.14 (bottom). The symbols on the top plot are directly from the experimental data

3.3.4 Implications on mirrors

The dual-waveplate model and its comparison with the experiments imply:

- The existence of 'intrinsic' (i.e. fixed) phase shift in the MSE optics can greatly magnify the change in polarization direction that is caused by thermal stress-induced birefringence in the lenses.

- The change in polarization angle due to the second (thermal stress) waveplate should be periodic in 4γ, where γ is the input polarization direction, with a finite vertical offset.

- The average change in polarization angle due to the second waveplate should be periodic in 2Φ, where Φ is the fast-axis angle of the second waveplate. It is not averaged to zero all the time.

- It may be possible to reduce the spurious changes in polarization angle that are caused by stress-induced birefringence in the lenses by reducing the fixed, intrinsic phase shift that is caused by other optical elements.

Regarding the last point, the phase shifts imposed by the current MSE optical elements were measured by the Polarization Lab in the University of Arizona prior to the FY2009 campaign to identify which element was the dominant source of fixed phase shift. The measurements indicate the lenses impose negligible intrinsic phase shifts (less than $1.2°$). However, as already shown in Table 3.2, it turns out that the retardances from the mirrors are significantly different and larger than the predictions by RMI, the manufacturer of the current MSE dielectric mirrors, the biggest discrepancy being about $8°$ at M2 with $60°$ of angle of incidence ($14°$ vs. $6°$).

Based on the dual-waveplate model, its good agreement with the experimental results, and the evidence for the degradation of the performance in the current MSE mirrors, all the old dielectric mirrors have been replaced by new ones fabricated by the MLD technologies prior to the FY2009 campaign in addition to the thermal shield and the new lens mount. The phase shifts imposed by these new mirrors are expected to be $\lesssim 3°$ for the angles of incidence of $30° \sim 60°$ over the wavelength range of 658 $\sim$ 664 nm.

199

Chapter 4

Measurement of current density profile modification in LHCD experiments

Despite the thermal drift issue on the C-Mod MSE diagnostic, several efforts have been made to infer the current density profiles in the Lower Hybrid Current Drive experiments using a 'within-shot' calibration technique. Following a brief introduction to the LHCD experiments, this chapter evaluates the accuracy of the within-shot calibration technique and then applies the technique to infer the current density in LHCD experiments. The measured current density profiles successfully demonstrate some straightforward predictions of LHCD theory.

4.1   Introduction to LHCD experiments

The LHCD experiments were carried out on the Alcator C-Mod tokamak using a radio-frequency system at 4.6 GHz to assist in achieving advanced non-inductive plasma regimes [76, 77, 78, 79]. The C-Mod tokamak is an ideal device for this study with the internal poloidal field coils to provide the strong shaping for high β_n operation [80] with high-power (up to 6 MW) ICRF heating. The current relaxation time under these conditions can be approximated as $\tau_{CR} = 1.4a^2 \kappa T_e^{1.5}(keV)/Z_{eff} \approx 0.2 - 1.44$

seconds for $Z_{eff} = 1.5, \kappa \approx 1.7$, and $T_e \approx 2 - 7.5$ keV [78]. This time is considerably shorter than the maximum pulse duration (up to 5 seconds) the machine can achieve with a toroidal field of 5 T, which makes it possible to observe the improved energy confinement with the fully relaxed current, or q, profile in advanced tokamak regimes.

RF power is generated by 12 klystrons operating at up to 250 kW with a maximum duration of 5 seconds. Recently, up to 1 MW of LH power with various parallel refractive indices, $n_\parallel$, $(1.6 \sim 4.0)$ has been coupled to the plasma to produce nearly full current drive in 1 MA plasma at $\bar{n}_e \approx 0.5 - 1 \times 10^{20}$ m^{-3}. Fig 4-1 shows the LH power, loop voltage, and internal inductance, l_i, from one of the LHCD shots along with an Ohmic discharge with the same plasma current, density, and magnetic field for comparison. Also shown at the bottom of this figure is the time evolution of the magnetic pitch angle directly measured by MSE at $r/a = 0.44$. Note that a zero loop voltage was transiently achieved at around 0.75 sec. The pitch angle change measured by MSE between non-LHCD and LHCD shots is up to 25 %.

We have observed suppression of sawtooth instabilities in some plasmas with high power LHCD, implying that the safety factor at the magnetic axis, q_0, was raised above unity. Fig 4-2 shows the time evolution of the sawtooth inversion radius (SIR) inferred from Electron Cyclotron Emission measurements (ECE) [81] for electron temperature from four LHCD shots with the power of $0.8 \sim 1$ MW and $n_\parallel = 1.56$ (60° phasing). Note that there is a delay of roughly $200 \sim 300$ msec between the start of LHCD and the suppression of sawteeth, which is qualitatively consistent with typical τ_{CR} with these plasma conditions ($T_e \approx 3$ keV). Inferring the SIR from the ECE data is performed semi-automatically based on the electron temperature time evolutions from available ECE spatial channels. The slopes of individual 'teeth' within about 80 msec time bin are observed and averaged. The inversion radius is determined by fitting the change of the averaged slope as a function of major radius and picking up the radius where the sign of the slop changes. In the following section, the SIR data inferred from the ECE are used to constrain the EFIT magnetic reconstruction for quiescent Ohmic phases preceding and/or following the LHCD period, which in turn, participates in the within-shot MSE calibration procedures. Throughout this chapter, a series of
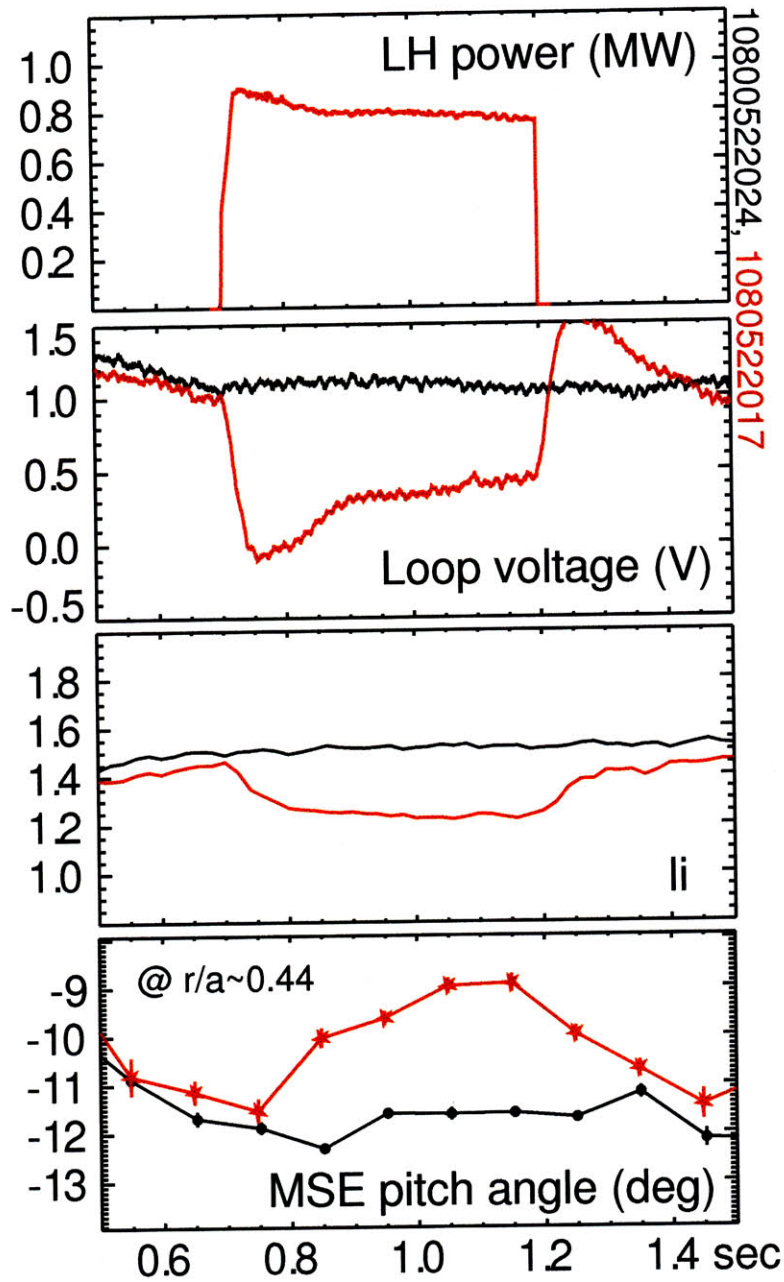
Figure 4-1: Time evolutions of Lower Hybrid power, loop voltage, internal inductance, and MSE pitch angle at $r/a \approx 0.44$ (from top to bottom) from Shots 1080522017 (red; with LHCD) and 1080522024 (black; without LHCD).
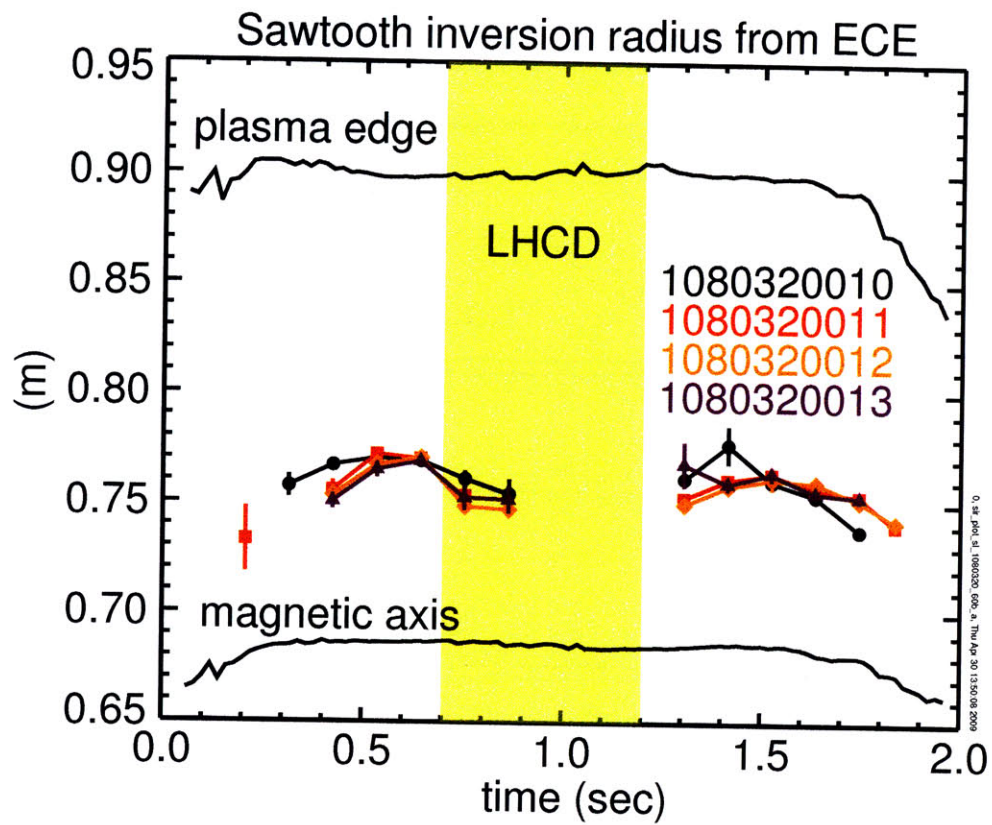
Figure 4-2: Time evolution of sawtooth inversion radius inferred from ECE data for four LHCD shots. Each data point is the average over 80 msec.

Shot	nl_{04} $(10^{19}$ m$^{-2})$*	P_{LH} (MW)	$n_{\parallel}$ (Phase)
1080320010	2.7 ~ 3.2	0.8 ~ 0.9	1.56 (60°)
1080320011	2.6 ~ 3.3	0.8 ~ 0.9	1.56 (60°)
1080320012	2.9 ~ 3.6	0.8 ~ 0.9	1.56 (60°)
1080320013	2.8 ~ 3.3	0.9 ~ 1.0	1.56 (60°)
1080320017	2.3 ~ 3.0	0.8 ~ 0.9	1.95 (75°)
1080320018	2.4 ~ 3.2	0.9 ~ 1.0	1.95 (75°)
1080320019	2.6 ~ 3.3	0.8 ~ 0.9	1.95 (75°)
1080320023	2.7 ~ 3.5	0.8 ~ 0.9	2.33 (90°)
1080320025	2.8 ~ 3.5	0.8 ~ 0.9	2.72 (105°)
1080320029	3.3 ~ 4.3	0.9 ~ 1.0	1.95 (75°)

Table 4.1: List of shots that are mainly used in this chapter for applying the within-shot calibration procedures and inferring current density profiles along with the plasma density (nl_{04}), lower hybrid power (P_{LH}), and parallel refractive index, $n_{\parallel}$. *The plasma density is from the I_p and B_T flattop (0.5 ~ 1.5 sec). During the flattop, $I_p = 0.8$ MA and $B_T = 6.2$T. The lower hybrid power is applied from 0.7 to 1.2 sec.

shots from a particular LHCD experiment (1080320) are mainly used in applying the within-shot calibration technique and deducing the current density profiles. Table 4.1 summarizes the plasma conditions for these shots. The run 1080320 is one of the best LHCD experiments during FY2008 where the LHCD power is close to 1 MW with the DNB current close to its maximum performance ($\lesssim$ 7A). The shots are reproducible with low density. As a result, the MSE data have reasonably high signal-to-background ratios, and correspondingly, reasonably low statistical errors. Fig 4-3 superimposes the statistical error in measured pitch angle for the shots in the 1080320 experiment (red) on the larger database of error as a function of signal-to-noise that was presented earlier in Figs 2-48 and 2-49. Except the edge channel (Ch1), the other channels have marginally acceptable measurement errors, typically less than 10 % of the change in pitch angle due to the LHCD pulse.

4.2 Within-shot calibration scheme

Due to the shot-to-shot drift caused by thermal stress-induced birefringence on the invessel optics discussed in Chapter 3, a separate absolute calibration, such as an
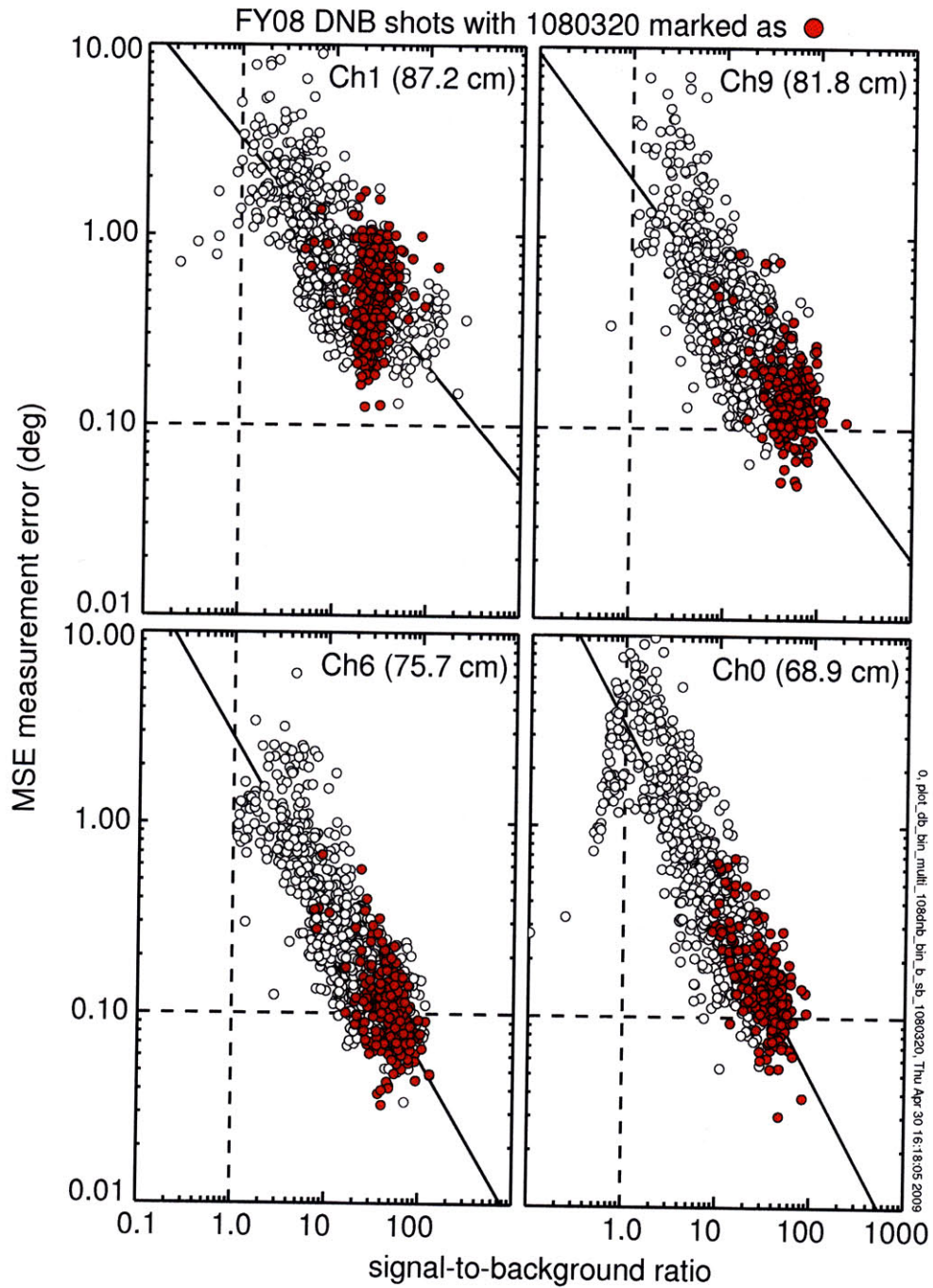
Figure 4-3: Macro-bin pitch angle error in degree vs signal-to-background ratio for four MSE channels from the same database used in Figs 2-48 and 2-49 in Sec 2.3 with the shots from 1080320 marked in red. The solid line is the linear fit of the data and the horizontal dashed line indicates the target accuracy (0.1°) [19].

invessel calibration, is not guaranteed to provide accurate information. Fig 4-4 shows the time evolutions of (a) the temperatures around the MSE invessel periscope (L2 region) and (b) the deviation in pitch angle measured by MSE from the EFIT-predicted pitch angle at a flattop Ohmic time point (around 0.65 sec) from the shots given in Table 4.1. Without high heating power, the periscope temperatures gradually decrease throughout a run day, as discussed in Sec 3.1.2. By the time the shots given in Table 4.1 were taken (from 0.49 days $\approx$ 11:45 AM), the temperature variations across the L2 lens roughly remained the same. The small and smooth change in temperature results in relatively small shot-to-shot drifts in pitch angle shown in Fig 4-4 (b). For the edgemost channel (Ch1), however, the shot-to-shot scattering is rather large with large error bars, but the variability becomes less severe after Shot 18 (around 0.56 day). The shot-to-shot variations from the next two outer channels (Chs 2 and 3) are smoother and seem to reach their thermal equilibration at around 0.52 days. The inner channels show small ($\lesssim 1°$) shot-to-shot drifts, as usual. Note that the EFIT pitch angles at inner channels may not be 'true' pitch angles but they are assumed to be invariant during the same Ohmic phases shot by shot, so it should be reasonable to regard the deviation from the EFIT-predicted pitch angle as an indicator for a shot-to-shot drift.

The shot-to-shot drift necessitates a scheme that calibrates the system shot by shot. The basic approach is the following:

1. Infer a 'baseline' pitch angle, γ_0, from a magnetic reconstruction code, such as EFIT, at a quiescent Ohmic phase of the shot ($t = t_0$); and

2. Obtain the change in pitch angle, $\Delta\gamma(t)$, from MSE relative to the baseline pitch angle at the quiescent Ohmic phase.

Then the new pitch angle $\gamma(t) = \gamma_0 + \Delta\gamma(t)$ is used either to directly calculate the current density using analytic expressions or to constrain a magnetic reconstruction procedure. The baseline pitch angle, γ_0, is calculated by EFIT. The 'normal' EFIT calculations routinely performed on a shot-to-shot basis in C-Mod (stored in the ANALYSIS tree in the MDSPlus database) either have a fixed safety factor value
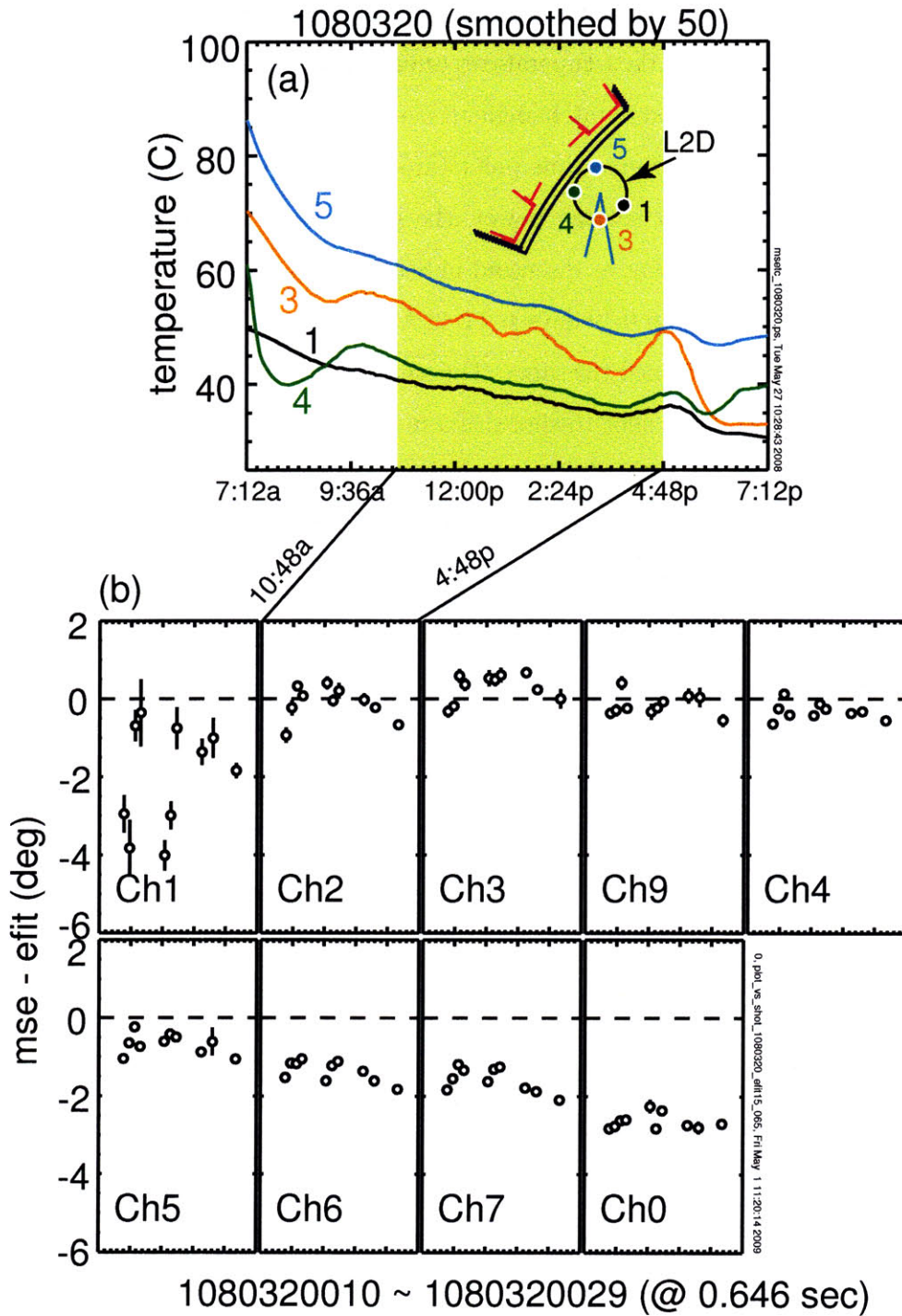
Figure 4-4: Time evolutions of (a) the temperatures around the MSE invessel periscope (L2 region) and (b) the deviation in pitch angle measured by MSE from the EFIT-predicted pitch angle at a flattop Ohmic time point (where $I_p = 0.8$ MA, $B_T = 6.2$ T, and $nl_{04} = 3 \sim 4 \times 10^{19}$ m^{-2}) from the shots given in Table 4.1. The yellow shaded region in plot (a) is the horizontal range of the individual plots in (b) which are arranged in the major radius order (edge → core).

(~ 0.9) at the magnetic axis or allow only a small deviation from that value, which may not be correct in general. The present scheme utilizes the SIR data obtained from ECE measurements as a correction method; the safety factor at the magnetic axis is left as a free parameter and determined such that $q = 1$ surface coincides with the SIR following the classical Kadomtsev sawtooth model [2]. The schematic diagram of this 'within-shot' calibration procedure is illustrated in Fig 4-5. The equilibrium reconstruction constrained by the SIR is performed and stored in the EFIT15 tree in the MDSPlus database. This provides the baseline pitch angle $\gamma_{15}(t_0)$ at $t = t_0$ where t_0 is a time (or times) during the Ohmic flattop phase in a shot. When multiple t_0's are chosen, the average value over the time points is used for $\gamma_{15}(t_0)$. The complete pitch angle, $\gamma(t)$, which is the summation of $\gamma_{15}(t_0)$ and the change in pitch angle from that at $t = t_0$ measured by MSE, or $\Delta\gamma_m(t) = \gamma_m(t) - \gamma_m(t_0)$, is used to constrain a new equilibrium reconstruction procedure whose results are stored in the EFIT17 tree in the MDSPlus database. From EFIT17, all the equilibrium quantities, both global and local, can be read including current density, safety factor etc. The following subsections discuss the validity of this approach.

4.2.1 Verification using plasma-current ramp shots

The linear relation between the true pitch angle and the pitch angle measured by MSE, which is assumed in the within-shot calibration scheme, can be tested in several plasma-current (I_p) ramp shots from experimental run 1070615. The original purpose of these shots was to check the feasibility of calibrating edge MSE channels with known pitch angles obtained by EFIT near the edge, as discussed in Sec 2.2.1. The waveforms for several plasma parameters for these shots are given in Fig 2-30. Regarding the within-shot calibration scheme, these shots are a good opportunity to test this scheme since they provide large ranges of pitch angle within a shot (-10 to -1° for the edge channel) with an environment relatively benign compared to the usual plasma current ramp-up phases.

Table 4.2 shows the coefficients of the linear fit, $\gamma_{MSE} = a + b \times \gamma_{EFIT}$, where γ_{MSE} and γ_{EFIT} are the pitch angles from MSE and normal EFIT (from ANALYSIS),
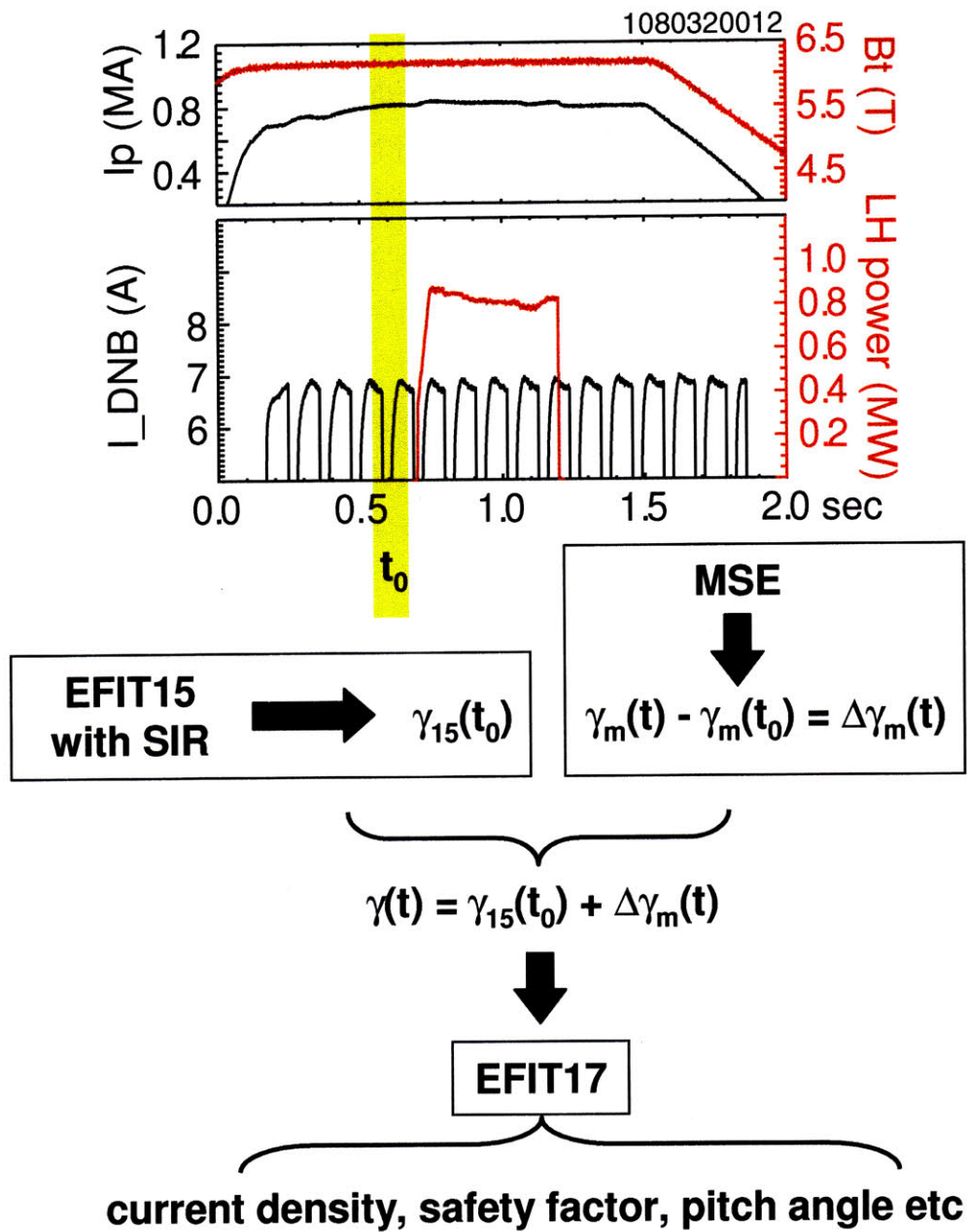
Figure 4-5: Schematic diagram for the within-shot calibration procedure.

respectively, from for three outer MSE channels from three I_p ramp shots.

channel	shot	a	δa	b	δb
0 (85.74 cm)	19	1.69	0.17	1.03	0.02
	20	1.81	0.22	1.02	0.02
	24	2.56	0.22	1.05	0.03
1 (84.06 cm)	19	1.80	0.15	1.09	0.02
	20	1.20	0.13	0.98	0.02
	24	2.13	0.20	1.03	0.03
2 (85.13 cm)	19	1.97	0.15	1.19	0.02
	20	1.71	0.12	1.15	0.01
	24	2.21	0.20	1.15	0.03

Table 4.2: Coefficients of the linear fit $\gamma_{MSE} = a + b \times \gamma_{EFIT}$. The shot number is 10706150XX. δ denotes the 1-σ error of the fit coefficient.

As also discussed in Sec 2.2.1, the strong linear relation is implied between the pitch angle measured by MSE and that from EFIT, the linear coefficients close to unity, with a certain constant offset which varies shot by shot. The variability in the constant offset is regarded as the finite shot-to-shot drift due to the thermal-stress induced birefringence. It should also be noted that the linear relation becomes weaker, i.e. the deviation in the linear coefficient from unity becomes larger as we go inward. More rigorous scheme would be one that includes these non-unity linear coefficients and constant offsets (mainly, for inner channels) to correct the MSE pitch angles which are then used to constrain a magnetic reconstruction. However, this fine correction would be meaningful only if there is not much smoothing in the equilibrium reconstruction process, combined with finer internal constraints (i.e. more MSE channels with smaller channel-to-channel distances). Later in this chapter, it will be shown that the linear assumption which bases the within-shot calibration demonstrates its validity in investigating the general LHCD effects.

4.2.2   Sawtooth behavior and plasma stored energy

Although the cross check using the I_p ramp shots examines the linear nature in the relation between the MSE-measured and the reconstructed pitch angles, it does not tell much about the validity on the baseline pitch angle itself, which is constructed (in

EFIT15) with the SIR data for flattop Ohmic phases as the first step in the within-shot calibration procedure. Here, the validity of the baseline pitch angle is examined by comparing the following two magnetic reconstructions:

1. EFIT17 constrained by $\gamma(t) = \gamma_{15}(t_0) + \Delta\gamma_m(t)$ where $\gamma_{15}(t_0)$ is the pitch angle from EFIT15 which is constructed based on the SIR data. This is basically the magnetic reconstruction based on the within-shot calibration scheme discussed so far.

2. EFIT16 constrained by $\gamma(t) = \gamma_{AN}(t_0) + \Delta\gamma_m(t)$ where γ_{AN} is the pitch angle from ANALYSIS which is the 'normal' magnetic reconstruction without any constraints for the internal plasma parameters.

Effectively, this comparison examines whether or not the constrained baseline improves the performance.

Figs 4-6 $\sim$ 4-9 illustrate the comparison between EFIT16 and EFIT17 in terms of sawtooth activities and central safety factor, q_0, for four shots with $n_{||} = 1.56$ from Table 4.1. Each figure contains the time evolutions of q_0 (TOP) and sawtooth inversion radius (BOTTOM) calculated by EFIT16 and EFIT17. Also contained on these plots is the result from the ANALYSIS equilibrium reconstruction. The raw sawtooth inversion radius data, which are used to constrain EFIT15, are also shown on the bottom plot. In addition, the time evolutions of electron temperature from the ECE Channel 17 whose major radius ($\sim$ 66 cm) is close to the magnetic axis are added for the two shaded (in yellow and cyan) time durations marked on the plots for q_0 and SIR on the left column. These time durations are determined such that the suppression and reappearance of the sawtooth activities can be roughly included in each time duration. The following observations can be made:

1. The main effect from constraining the baseline pitch angle is to shift down q_0 from the value obtained with the baseline unconstrained. This may also be directly inferred from the observation that the SIR inferred directly from the ECE data is always larger than that from the unconstrained EFIT (ANALYSIS) by a few centimeters.

212
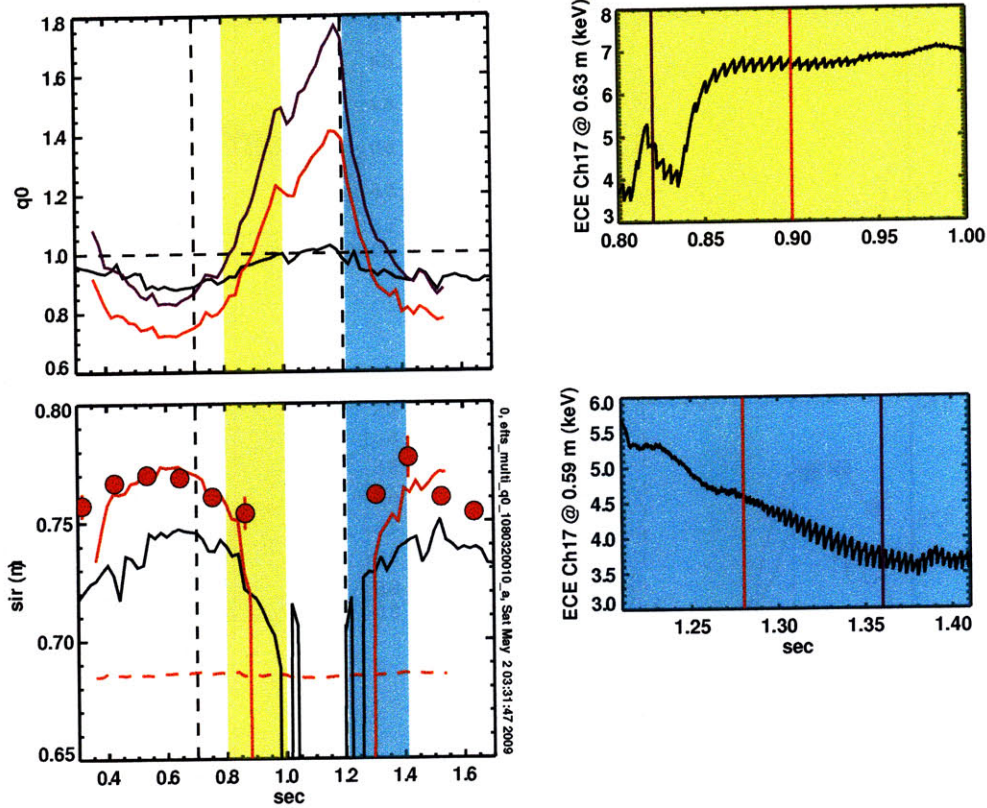
Figure 4-6: Time evolutions of q_0 (TOP LEFT) and SIR (BOTTOM LEFT) calculated by the ANALYSIS (black), EFIT16 (purple), and EFIT17 (red) equilibrium reconstructions for 1080320010. The LHCD pulse duration is marked as two vertical lines. In the bottom plot, the raw SIR data from ECE is included and the magnetic axis is marked with a red dashed line. Time evolutions of electron temperature from two shaded (in yellow and cyan) areas are separately plotted on the right column. In each plot on the right column, the vertical lines indicate the time when q_0 crosses 1 (becoming either larger or smaller than 1) in a color which corresponds to either EFIT16 or EFIT17.

Figure 4-7: Time evolutions of q_0 (TOP LEFT) and SIR (BOTTOM LEFT) calculated by the ANALYSIS (black), EFIT16 (purple), and EFIT17 (red) equilibrium reconstructions for 1080320011. The LHCD pulse duration is marked as two vertical lines. In the bottom plot, the raw SIR data from ECE is included and the magnetic axis is marked with a red dashed line. Time evolutions of electron temperature from two shaded (in yellow and cyan) areas are separately plotted on the right column. In each plot on the right column, the vertical lines indicate the time when q_0 crosses 1 (becoming either larger or smaller than 1) in a color which corresponds to either EFIT16 or EFIT17.

1080320012 (analysis, efit16, efit17)
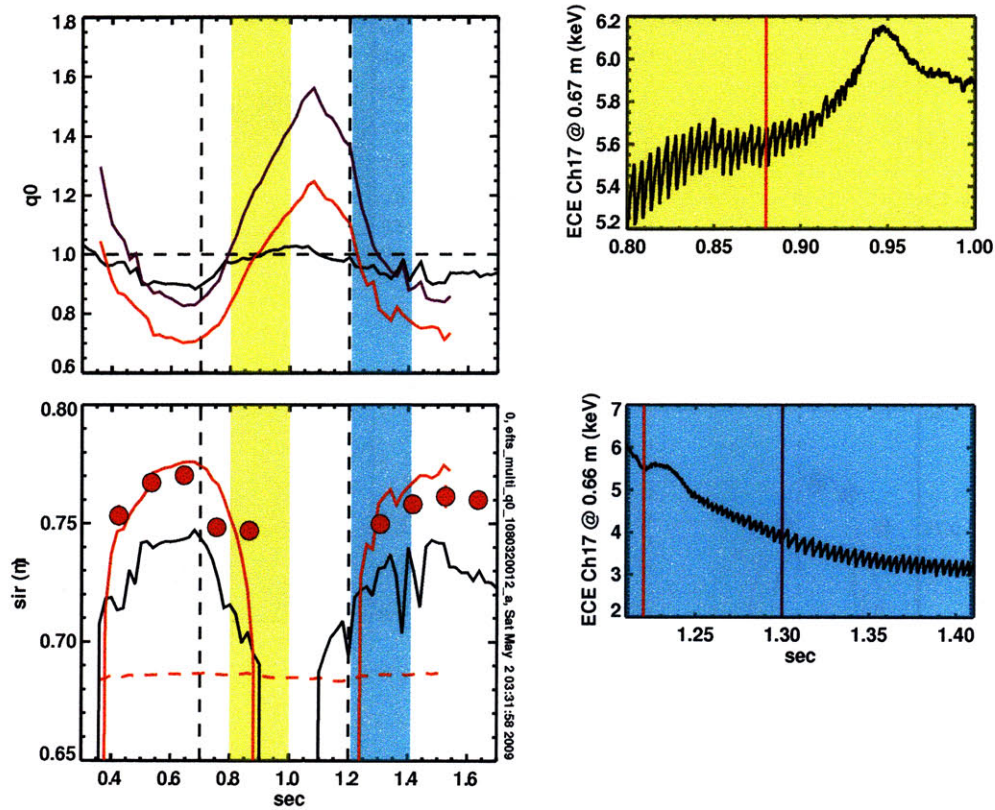
Figure 4-8: Time evolutions of q_0 (TOP LEFT) and SIR (BOTTOM LEFT) calculated by the ANALYSIS (black), EFIT16 (purple), and EFIT17 (red) equilibrium reconstructions for 1080320012. The LHCD pulse duration is marked as two vertical lines. In the bottom plot, the raw SIR data from ECE is included and the magnetic axis is marked with a red dashed line. Time evolutions of electron temperature from two shaded (in yellow and cyan) areas are separately plotted on the right column. In each plot on the right column, the vertical lines indicate the time when q_0 crosses 1 (becoming either larger or smaller than 1) in a color which corresponds to either EFIT16 or EFIT17.

Figure 4-9: Time evolutions of q_0 (TOP LEFT) and SIR (BOTTOM LEFT) calculated by the ANALYSIS (black), EFIT16 (purple), and EFIT17 (red) equilibrium reconstructions for 1080320013. The LHCD pulse duration is marked as two vertical lines. In the bottom plot, the raw SIR data from ECE is included and the magnetic axis is marked with a red dashed line. Time evolutions of electron temperature from two shaded (in yellow and cyan) areas are separately plotted on the right column. In each plot on the right column, the vertical lines indicate the time when q_0 crosses 1 (becoming either larger or smaller than 1) in a color which corresponds to either EFIT16 or EFIT17.

216

2. During the LHCD pulses, q_0 from both EFIT16 and EFIT17, both of which are constrained by the MSE data, exceeds unity. This is consistent with the suppression of the sawtooth activities during this interval.

3. However, there is a difference in timing when the sawtooth is suppressed during the LHCD pulse and when it appears again after the LHCD pulse. The moment when q_0 (both from EFIT16 and EFIT17) crosses unity, becoming either larger or smaller than unity, is indicated on the separate plots on the right column which show the electron temperature time evolution with a higher resolution. It is apparent that the q_0 time evolution from EFIT17 is more consistent with the real sawtooth crashing moment and with its reappearance moment than that from EFIT16.

Fig 4-10 illustrates another way to check the validity of EFIT17 (against EFIT16 and ANALYSIS) where the plasma stored energies, W_p, obtained by various EFIT calculations are compared with W_p^{kin}, the plasma stored energy inferred based on kinetics. Two shots with $n_{||} = 1.56$ (TOP) and 1.95 (BOTTOM) are tested. W_p^{kin} is inferred from the kinetic energies of electrons and ions. The electron kinetic energy is obtained from Thomson scattering measurements. For the ion temperature, the ion temperature at the plasma center is inferred from neutron rates and its profile is assumed to be the same as that of the electrons. The ion density is measured from the effective ion charge, Z_{eff}, assuming the ratio of electron to ion densities is constant across the profiles. Both EFIT16 and EFIT17, being constrained by MSE, show more stable stored energy compared with that from the unconstrained EFIT (ANALYSIS). However, the absolute value of W_p from EFIT17 is more close to the W_p^{kin} than that from EFIT16, implying that constraining a baseline equilibrium by the realistic SIR as in the within-shot calibration is important in obtaining reasonable magnitudes of equilibrium properties.
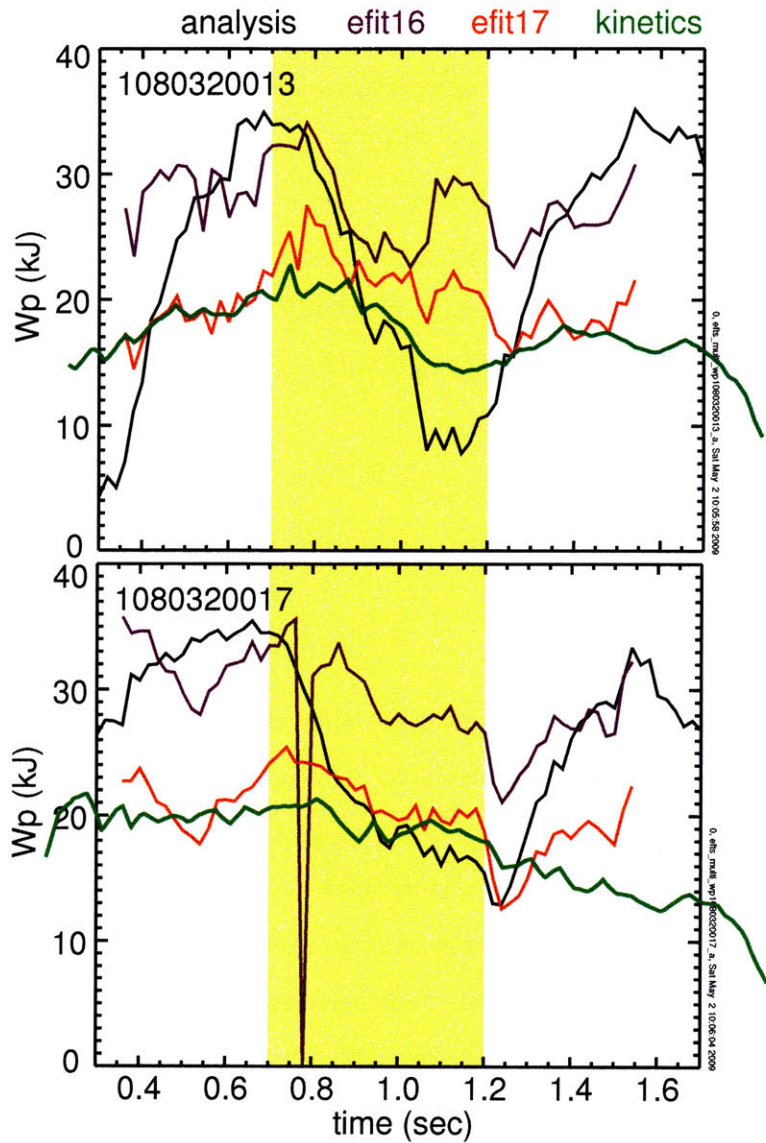
Figure 4-10: Comparison of plasma stored energy obtained from ANALYSIS (black), EFIT16 (purple) and EFIT17 (red) with W_p^{kin} (green), the plasma stored energy inferred from kinetics for 1080320013 (TOP) and 1080320017 (BOTTOM). The LHCD phase is marked in yellow

4.3 Applications to LHCD experiments

One additional constraint made during the procedure is to deselect the pitch angles measured by two MSE channels - innermost and outermost. Although within-shot calibrated, the edgemost MSE channel usually suffers from the thermal-stress induced birefringence the most and has the highest measurement uncertainties as shown in Fig 4-3. The pitch angle data from the ANALYSIS equilibrium reconstruction at the plasma boundary is used instead. The main reason that the innermost channel (68.94 cm), which is near the magnetic axis ($\sim$ 68.5 cm), is deselected is its poor radial resolution ($\sim$ 9 cm). In addition, the vertical size of the MSE footprint (3 cm) may be comparable to the size of the flux surface around this region. Therefore, a more reasonable constraint has been used instead: the pitch angle is forced to be zero at the magnetic axis the location of which is determined by the ANALYSIS equilibrium.

4.3.1 Change in total current density profiles

The shots from Table 4.1 are divided into four groups based on four different $n_{\parallel}$'s and analyzed using the within-shot calibration procedure. Fig 4-11 shows the radial profiles of change in poloidal field from an Ohmic baseline value, ΔB_v, (TOP), toroidal current density, J_ϕ, (MIDDLE), and the safety factor, q, (BOTTOM) at the midplane for these four groups of shots, the plots on the left column from an Ohmic phase (t = 0.65 sec) and those on the right column from an LHCD duration (t = 1.025 sec). The profiles for $n_{\parallel}$ = 1.56 and $n_{\parallel}$ = 1.95 are from averaging the shots with the same $n_{\parallel}$, i.e. the shots from 1080320010 to 1080320013 are averaged for $n_{\parallel}$ = 1.56 and the shots 1080320017, 1080320018, and 1080320029 are averaged for $n_{\parallel}$ = 1.95. The reference baseline Ohmic phase (for EFIT15) is taken from 0.55 to 0.65 seconds. The plots on the left column show not only the profiles during the Ohmic phases but also how reproducible the plasma conditions, and therefore the profiles, are. The plots on the right column clearly show the effect of LHCD and qualitatively demonstrate the $n_{\parallel}$ dependence in the LHCD efficiency and the off-axis current drive[78].

The magnetic equilibrium reconstruction procedures tend to smooth out the pro-

219
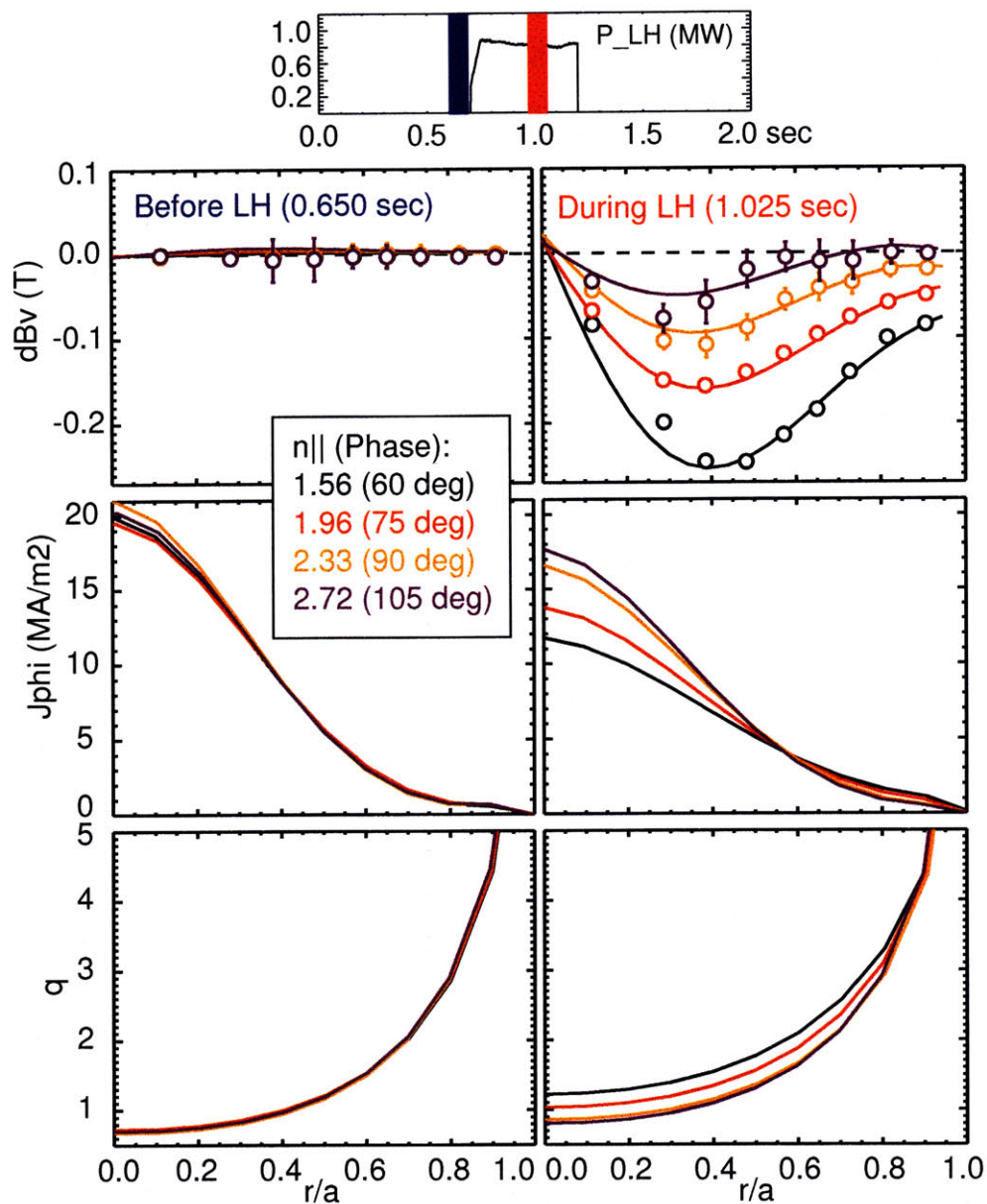
Figure 4-11: Radial profiles of change in poloidal field from an Ohmic baseline value, ΔB_v, (TOP), toroidal current density, J_ϕ, (MIDDLE), and the safety factor, q, (BOTTOM) at the midplane for four groups of shots with different $n_\|$'s. The top plot also shows the value from the raw MSE data as symbols. The plots on the left column are from a pre-LHCD phase (Ohmic flattop at $t = 0.65$ sec) and the plots on the right column are from a time during the LHCD pulse ($t = 1.025$ sec). These two durations are shown in the plot on the top right.

duced quantities due to their approximations made for the source terms (P' and FF') in the Grad-Shafranov equation. Typically, in c-Mod, 1st and 2nd-order polynomials are used for P' and FF', respectively. A direct measurement of J_ϕ has been obtained directly from the MSE data using an analytic relation between J_ϕ and B_v based on a magnetic topology modeled using shifted D-shaped flux surfaces, where the local toroidal current density on the midplane is expressed as [16]

$$J_\phi = -\frac{1}{\mu_0}\frac{B_v}{\kappa^2 A}\left(1 + \frac{2\delta A}{a}\right) - \frac{1}{\mu_0}\frac{\partial B_v}{\partial R}, \tag{4.1}$$

where μ_0 is the permeability of free space, κ is the vertical elongation, δ is the triangularity, R is the major radius, and $A = R - R_{axis} - \Delta$, where R_{axis} is R for the magnetic axis and Δ is the Shafranov shift and expressed as

$$\Delta = -\frac{a^2}{4(R_{axis} - R_0)}\left\{1 - \left(1 - \frac{4(R_{axis} - R_0)}{a^2}(R - R_{axis})\right)^{1/2}\right\}^2, \tag{4.2}$$

where a is the horizontal minor radius and R_0 is the major radius of the geometric center of the plasma. The accuracy of J_ϕ inferred from Eqn 4.1 is examined in Ref [16] with various ranges of equilibrium quantities which are somewhat similar to those in C-Mod and estimated to be within 5 % except the edge. In Eqn 4.1, B_v and $\partial B_v/\partial R$ are directly obtained from the MSE data which are corrected by EFIT15 as in the within-shot calibration scheme. When first these formulas were applied, the current density near the magnetic axis was unacceptably large. Later it turns out that the first term in Eqn 4.1 has a singularity when combined with Eqn 4.2. This problem can be overcome by applying l'Hôpital's rule and then Eqn 4.1 becomes

$$J_\phi = -\frac{1}{\mu_0}\frac{\partial B_v/\partial R}{\kappa^2}\left(1 + \frac{2\delta A}{a}\right) - \frac{1}{\mu_0}\frac{\partial B_v}{\partial R}. \tag{4.3}$$

When the distance $R - R_{axis}$ is less than half the MSE channel-to-channel separation, Eqn 4.3 is used; otherwise Eqn 4.1 is used. The quantity $\partial B_v/\partial R$ is directly obtained from the MSE data and the major radii of two adjacent MSE channels. The poloidal field B_v on the same spatial grid is linearly interpolated from the same pair of MSE

channels. All other global equilibrium quantities are from the ANALYSIS magnetic reconstruction data. Due to the high sensitivity of J_ϕ on the radial gradient of B_v, this analytic method has been applied only to two $n_{||}$ cases where multiple shots with the same $n_{||}$ are available to have better statistics (4 shots for $n_{||} = 1.56$ and 3 shots for $n_{||} = 1.95$). Fig 4-12 shows the same radial profiles similar to those shown in Fig 4-11 but only for $n_{||} = 1.56$ and 1.95 cases and the plots for J_ϕ now have the results obtained from the analytic formulas described above. Both J_ϕ profiles based on the non-iterative analytic model and the iterative within-shot calibration scheme (EFIT17) are in good agreement but for $n_{||} = 1.56$, the direct method implies two local structures which were 'hidden' in the profile based on the iterative method. This kind of smoothing is one of the main issues in the iterative magnetic equilibrium reconstructions and efforts are being made to overcome this by improving the fit algorithms [82, 83]. It is noted that the local structures that appear in J_ϕ profiles from the direct method (MIDDLE) are directly implied by the local structures of the raw MSE pitch angle data in the top plot.

More evidence of off-axis current drive is the time evolution of 'regional' plasma currents which can be calculated by integrating the current densities for a certain range of major radii. Fig 4-13 shows, for two $n_{||}$'s, these regional I_p's obtained by integrating the current density over the major radii less than (solid line) and larger than (dashed line) $r/a = 0.44$. The former can be regarded as 'central I_p' and the latter as 'off-axis I_p'. Also overplotted are the values from the direct method using Eqns 4.1 $\sim$ 4.3. The error bar for a value from the analytic model is applicable to the rest of the values and mainly due to the uncertainties in the process of integrating the current density obtained from the direct method. The figure clearly shows redistribution of current from central to off-axis during LHCD.

4.3.2 Lower hybrid contribution to current drive

By subtracting the part of the current density which can be attributed to purely Ohmic induction from the total current density measured by MSE, it is possible to infer the component that arises from Lower Hybrid. The total parallel current density
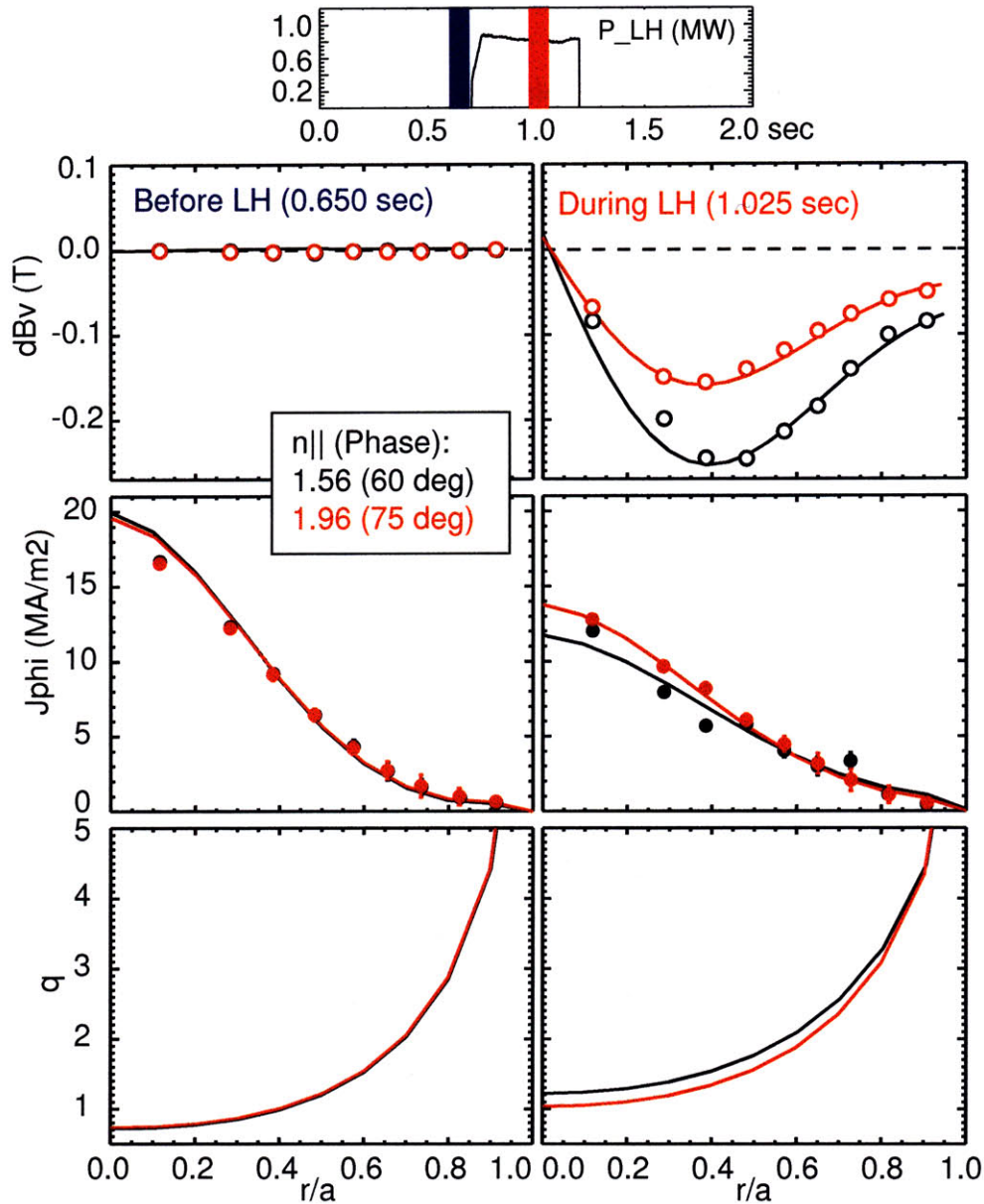
Figure 4-12: Radial profiles of change in poloidal field from an Ohmic baseline value, ΔB_v, (TOP), toroidal current density, J_ϕ, (MIDDLE), and the safety factor, q, (BOTTOM) at the midplane for two groups of shots with different $n_\parallel$'s. The top plot also shows the value from the raw MSE data as symbols and the middle plot includes the values inferred from the analytic expression as symbols. The plots on the left column are from a pre-LHCD phase (Ohmic flattop at $t = 0.65$ sec) and the plots on the right column are from a time during the LHCD pulse ($t = 1.025$ sec). These two durations are shown in the plot on the top right.
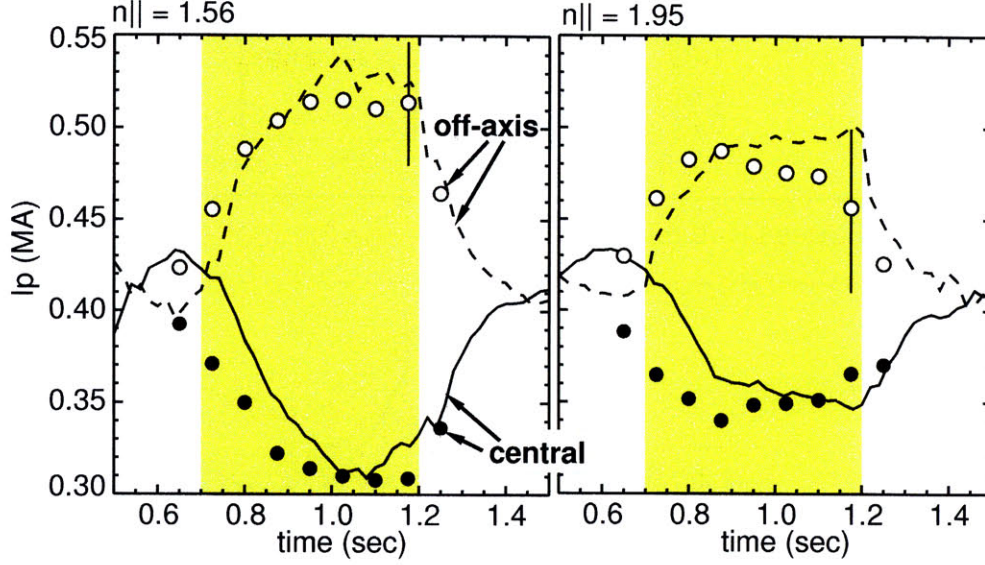
Figure 4-13: Time evolutions of central and off-axis I_p's for $n_{||} = 1.56$ (LEFT) and 1.95 (RIGHT). Lines are from EFIT17 and symbols from the analytic model. The LHCD duration is marked in yellow.

in general can be written as

$$
\begin{aligned}
J_{||} &= J_{OH} + J_{LH} + J_{BS} \\
&= \sigma_{neo} E_{||} + J_{LH} + J_{BS},
\end{aligned}
\tag{4.4}
$$

where J_{OH} is the Ohmic inductive current density, J_{LH} is the current density from LHCD, and J_{BS} is the bootstrap current, $E_{||}$ is the parallel electric field, and σ_{neo} is the conductivity which can be scaled as [86, 1]

$$
\sigma_{neo} \approx \sigma_0 \frac{T_e^{3/2}}{Z N(Z) \ln \Lambda_e},
\tag{4.5}
$$

where σ_0 is a proportionality constant to be determined, T_e is the electron density and Z is the average ion charge, Λ_e is the Coulomb logarithm, and $N(Z)$ is the correction for the resistive anomaly and a function of Z:

$$
N(Z) = 0.58 + \frac{0.74}{0.76 + Z}.
\tag{4.6}
$$

224

A technique similar to the within-shot calibration was used to deduce σ_0. Assuming negligible bootstrap current density, the total current density during non-LHCD phases in a plasma discharge should be entirely from the inductive Ohmic contribution, in principle. Therefore, Eqn 4.5 at a certain Ohmic time, t_0 and at an arbitrary time, t, can be written as, when combined with Eqn 4.5,

$$J_{||}(t_0) = 0 + \sigma_0 \frac{T_e(t_0)^{3/2} E_{||}(t_0)}{Z(t_0) N(Z(t_0)) \ln \Lambda_e(t_0)} \tag{4.7}$$

$$J_{||}(t) = J_{LH}(t) + \sigma_0 \frac{T_e(t)^{3/2} E_{||}(t)}{Z(t) N(Z(t)) \ln \Lambda_e(t)}. \tag{4.8}$$

$$\tag{4.9}$$

Combining these two equations give an expression for $J_{LH}(t)$,

$$J_{LH}(t) = J_{||}(t) - J_{||}(t_0) \left(\frac{T_e(t)}{T_e(t_0)} \right)^{3/2} \left(\frac{E_{||}(t)}{E_{||}(t_0)} \right) \left(\frac{Z(t_0) N(Z(t_0))}{Z(t) N(Z(t))} \right) \left(\frac{\ln \Lambda_e(t_0)}{\ln \Lambda_e t} \right) \tag{4.10}$$

which does not require the knowledge of σ_0. Shot 1080320010 ($n_{||} = 1.56$) was analyzed with this method and the results are shown in Figs 4-14 where the time evolution of the loop voltages, obtained by the MSE within-shot calibrated EFIT (EFIT17), at several radial locations are given at the top and the profiles of T_e, $E_{||}$, loop voltage, and the current densities at the bottom. A manual inspection on the time evolution of loop voltage was required to pick up the appropriate time points over which an averaged profile was obtained. As illustrated in the top plot in Fig 4-14, it is apparent the loop voltage evolution is strongly dependent of the LH power. It is also encouraging to observe that the drop in the loop voltage follows the physical intuition: it takes place at the outer radii first when the LH power is turned on, penetrates inward as time proceeds, and finally converges, making the loop voltage constant across the plasma. This trend is obvious except at the moments when the LH power temporarily faults (This trend is more obvious in more plots of loop voltage time evolution for other shots that follow later in this section). The profiles are taken and averaged over relatively quiescent time points during the LH phase.

In the profile calculations using Eqn 4.10, no radial variation is assumed for Z,
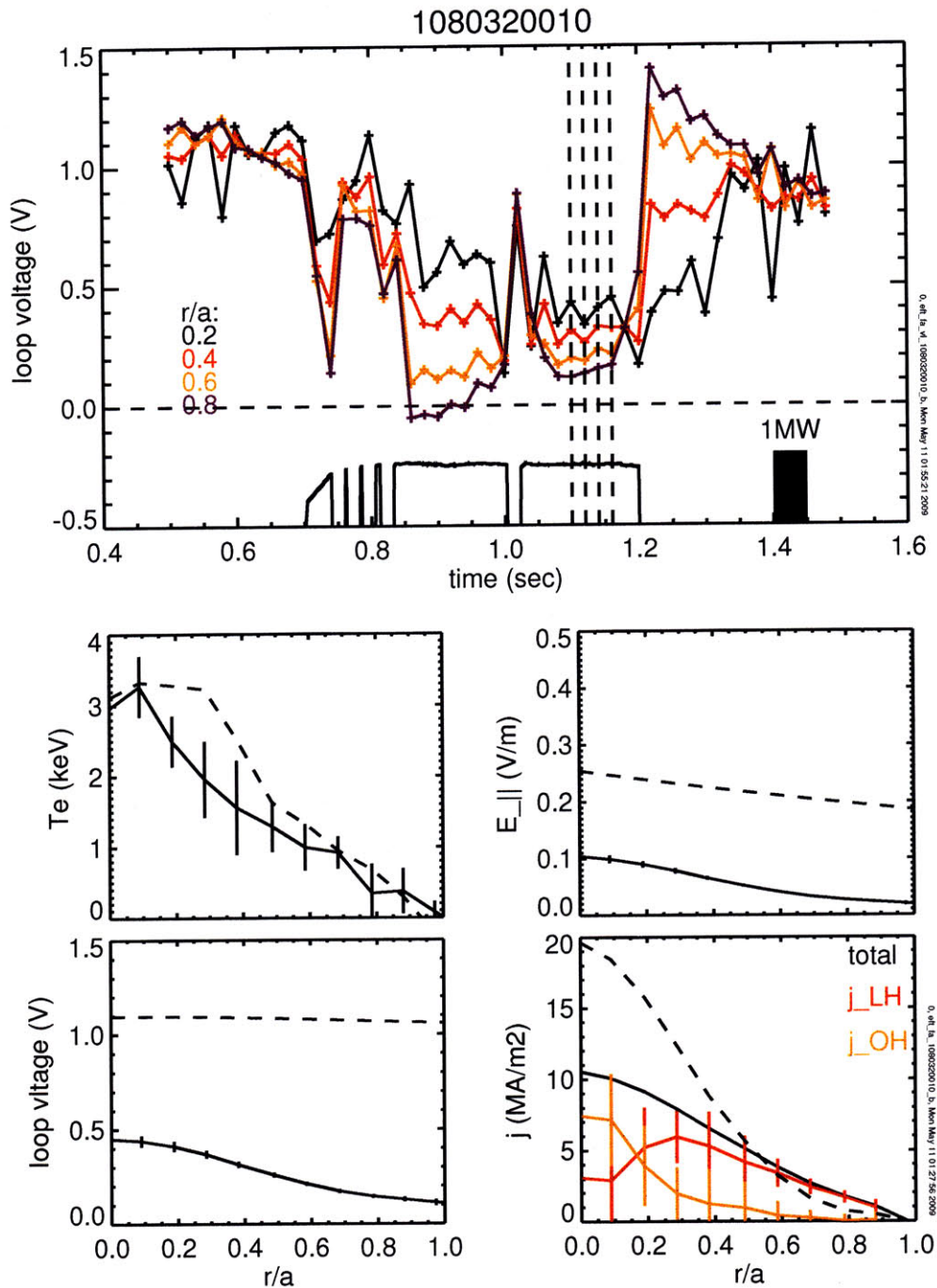
Figure 4-14: Time evolution of loop voltages at four radial locations (TOP) from 1080320010. The radial profiles of T_e, $E_{||}$, loop voltage, and three current densities (total, LH-driven, and Ohmic) averaged over the time points marked as vertical lines on the top plot are shown at the four plots at the bottom. The dashed curves on these profile plots are the profiles at 't_0' (averaged over $0.6 \sim 0.65$ sec). The waveform of the LH power applied to this shot is also illustrated at the top plot.

226

and the time history of Z during the LH pulse was linearly interpolated the values before and after the LHCD pulse. The electron temperatures are taken from Thomson scattering measurements and $\ln \Lambda_e(t_0)/\ln \Lambda_e(t)$ is assumed to be unity. $E_{\parallel}$ is the flux-surface-averaged loop voltage obtained from EFIT17 divided by the toroidal circumference of each major radius. The current densities obtained from the within-shot calibration are used for $J_{\parallel}(t_0)$ and $J_{\parallel}(t)$. Note that these current densities are *local* whereas the current densities in Eqn 4.10 are *flux-surface-averaged*. Therefore, this analysis is only zeroth-order, probably overestimating the magnitudes due to the inclusion of neoclassical Pfirsch-Schlüter current, and the uncertainty in the inferred J_{LH} and J_{OH}, mainly due to the fluctuation in the loop voltage, is rather large. Nevertheless, the results qualitatively demonstrate the off-axis contribution of the LHCD to the current drive. Also note that J_{LH} includes the *inductive* part of the current density which is driven by LH-induced fast electrons accelerated by $E_{\parallel}$. Two more shots (1080320011 and 1080320012) with the same $n_{\parallel}$ ($= 1.56$) were analyzed and the results are given in Figs 4-15 and 4-16, respectively. The overall trend from these two shots is the same as the first one. In addition, the convergence in the loop voltages at four radii is more clearly observed from the top plots in each figure since there is no fault in the LH power. The time constant for the convergence (i.e. $\approx$ current relaxation) is roughly 200 msec.

$n_{\parallel}$ dependence was investigated again this time only on J_{LH}. Fig 4-17 (a) shows the J_{LH} profiles inferred from Eqn 4.10 for four different $n_{\parallel}$ (Four shots from Table 4.1 were chosen). The dependence is rather weak, although the overall magnitude of the profile slightly decreases with increasing $n_{\parallel}$ except for the largest $n_{\parallel}$ (2.72), the reason for which will be discussed shortly. Fig 4-17 (b) illustrates that the uncertainty in inferred $J_{LH}(r)$ is considerable due predominantly to the fluctuation of the loop voltage. This implies that this approach (Eqn 4.10) will not yield precise measurements of $J_{LH}(r)$ and its $n_{\parallel}$ dependence unless uncertainties in the loop voltage can be reduced although it qualitatively distinguishes J_{LH} from the total current. Fig 4-18 shows the time evolution of loop voltage for the shots given in Fig 4-17. Shot 1080320019 exhibits an almost complete current relaxation by virtue of the stable LH
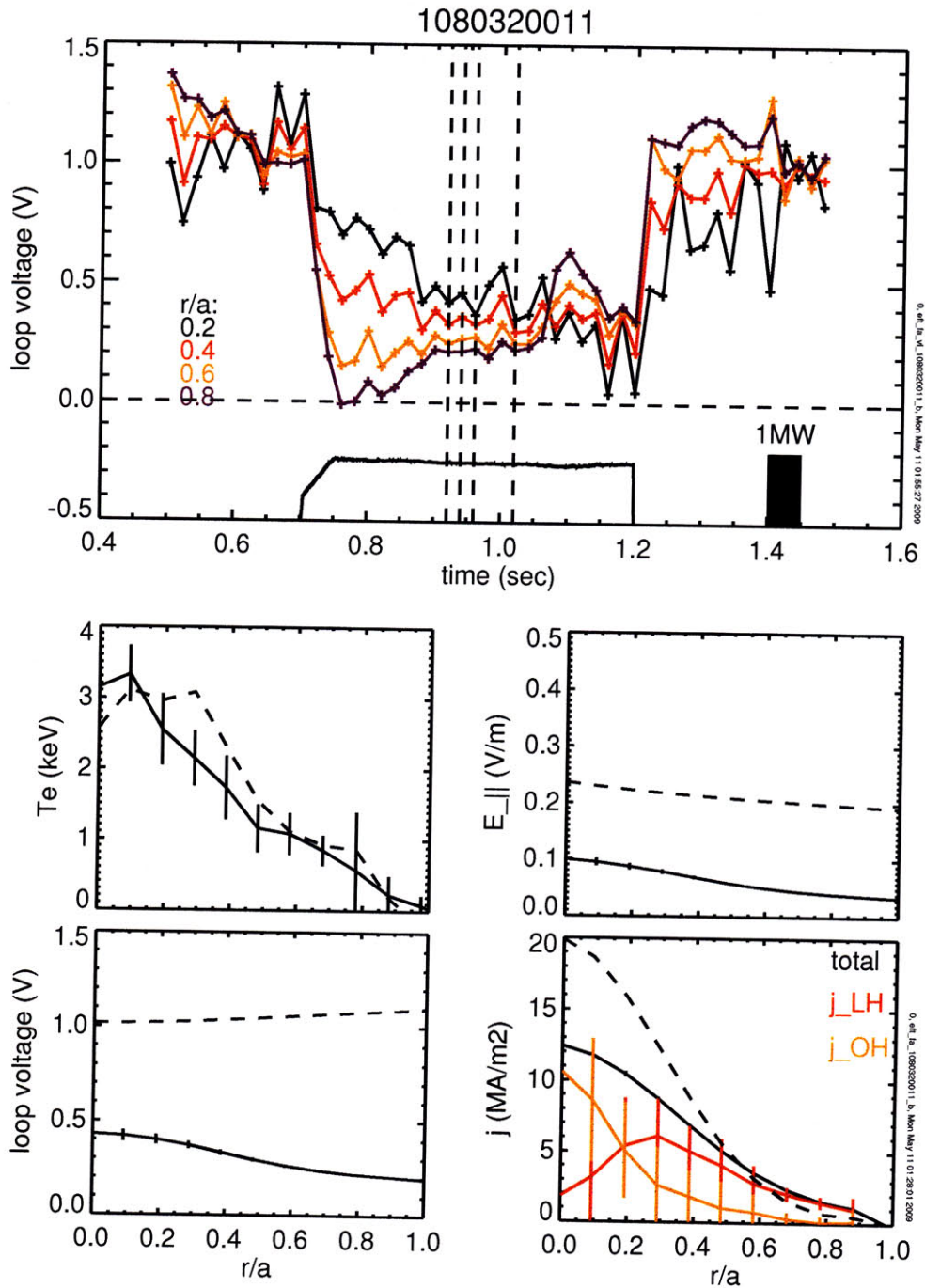
Figure 4-15: Time evolution of loop voltages at four radial locations (TOP) from 1080320011. The radial profiles of T_e, $E_{||}$, loop voltage, and three current densities (total, LH-driven, and Ohmic) averaged over the time points marked as vertical lines on the top plot are shown at the four plots at the bottom. The dashed curves on these profile plots are the profiles at 't_0' (averaged over $0.6 \sim 0.65$ sec). The waveform of the LH power applied to this shot is also illustrated at the top plot.
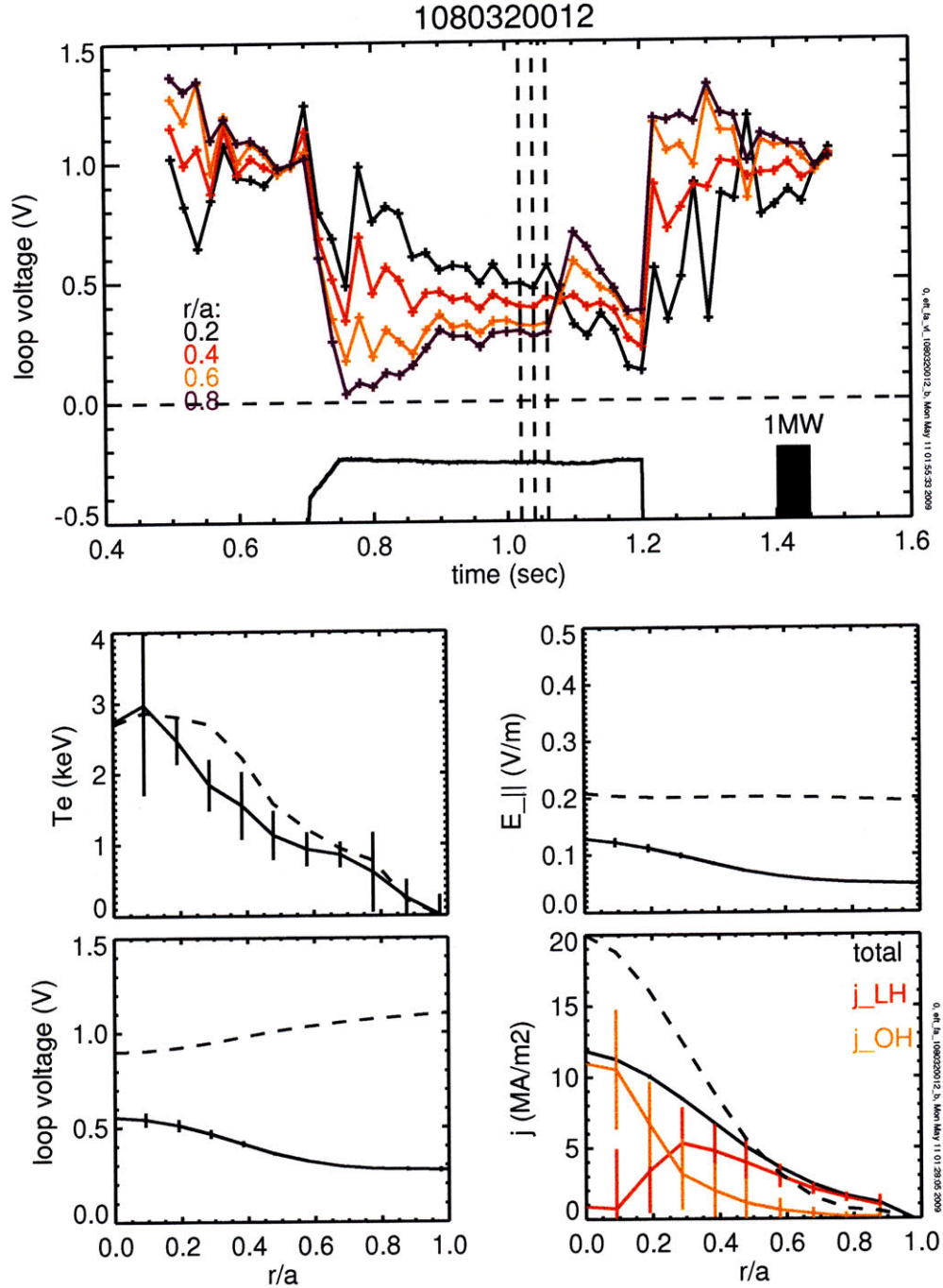
Figure 4-16: Time evolution of loop voltages at four radial locations (TOP) from 1080320012. The radial profiles of T_e, $E_{||}$, loop voltage, and three current densities (total, LH-driven, and Ohmic) averaged over the time points marked as vertical lines on the top plot are shown at the four plots at the bottom. The dashed curves on these profile plots are the profiles at 't_0' (averaged over $0.6 \sim 0.65$ sec). The waveform of the LH power applied to this shot is also illustrated at the top plot.
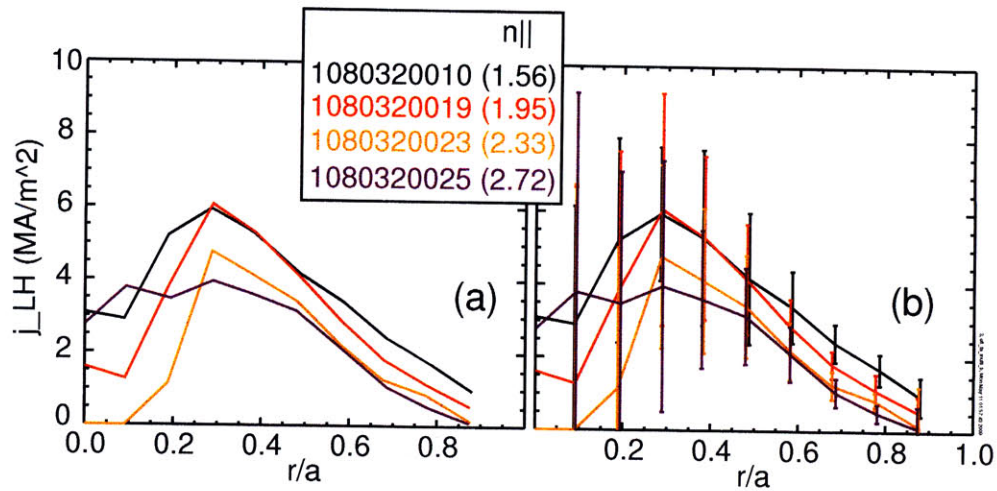
Figure 4-17: Radial profile of J_{LH} for four different $n_{\parallel}$ (a) without and (b) with the uncertainties.
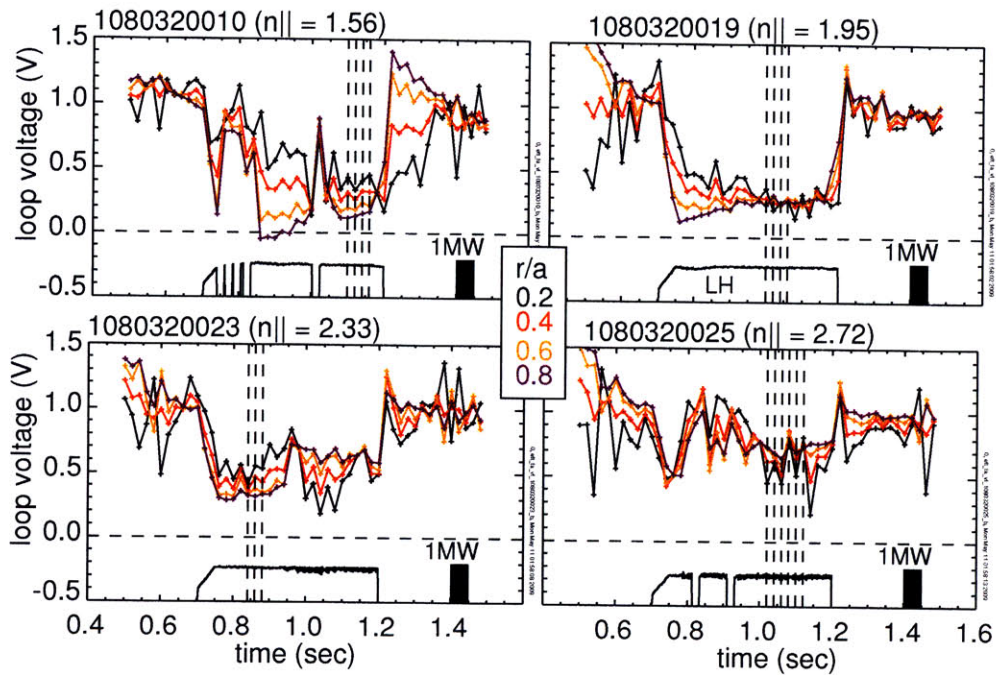
Figure 4-18: Time evolutions of loop voltage at four radial locations for the shots shown in Fig 4-17. The vertical dashed lines indicate the time slices over which the profile shown in Fig 4-17 is averaged. The waveform of the LH power is also illustrated in each plot.

pulse in this shot. The time points which are used in averaging the profiles shown in Fig 4-17 are also indicated by vertical dashed lines. It should be noted that there are some instabilities during the half way of the LH pulse in shot 1080320023 and during the entire LH pulse in shot 1080320025. Therefore, some quiescent time points can be obtained in shot 1080320023, but the profiles from 1080320025 must unfortunately averaged over the times with the instabilities. This may be the reason that the averaged profile for this shot shown in Fig 4-17 shows some anomalous behavior.

The agreement of the current drive location obtained this way with the expectations from modeling is rather unclear at this stage. Fig 4-19 shows the radial profiles of the total, LH-driven, and Ohmic current densities from EFIT17 for shot 1080320017 for which the CQL3D modeling was performed. Also shown in the plot is the lower hybrid power deposition calculated from CQL3D for this shot at 1 sec. Due to the smoothing by the EFIT magnetic reconstruction, it is hard to tell how well J_{LH} follows the power deposition. The LHCD modeling using full-wave analyses as well as CQL3D is still evolving. In addition, more elaborate fit algorithms are required in the equilibrium reconstruction, supported by MSE data with smaller radial resolutions.
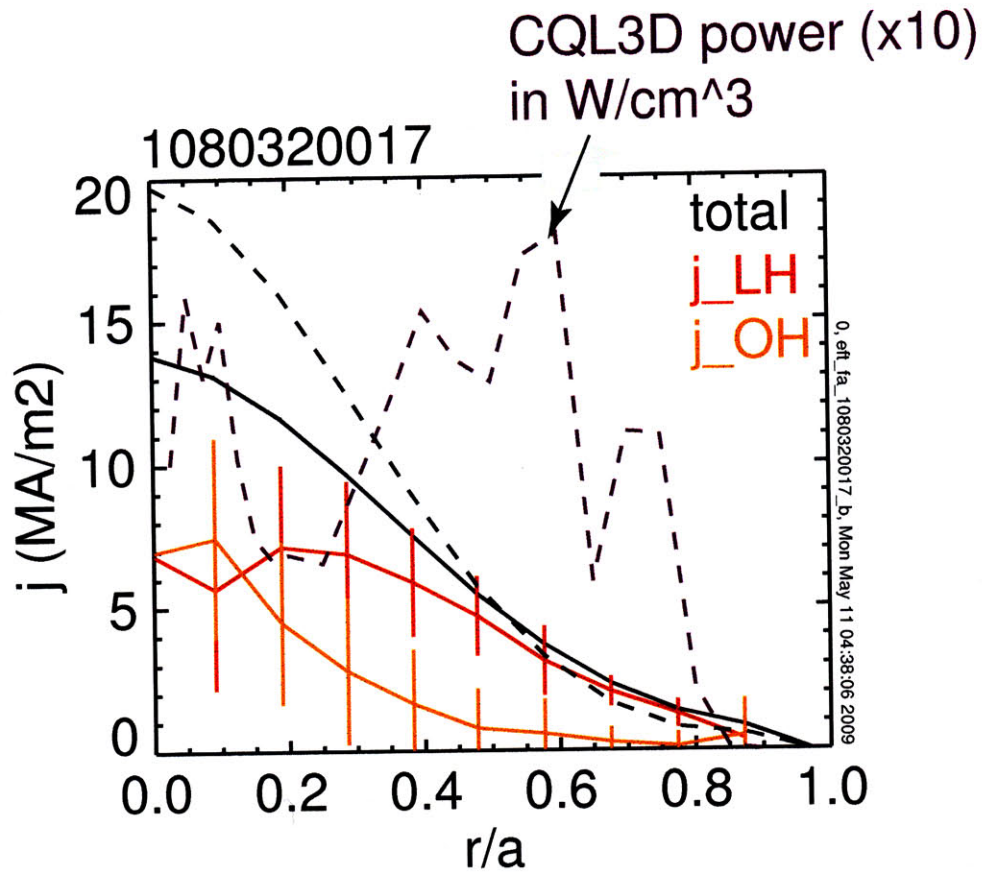
Figure 4-19: Radial profiles of total, LH-driven, and Ohmic current densities during the LHCD pulse (at 1 sec) for 1080320017. Also overplotted on the plot is the lower hybrid power deposition profile calculated by CQL3D (blue dashed line) and the current during the Ohmic reference phase (0.6 ∼ 0.65 sec).

Chapter 5

Summary and future work

This chapter reviews: (1) the current status of the C-Mod MSE diagnostic including major upgrades in the hardware and calibration techniques; (2) the spurious drift in the polarization measurements due to thermal-stress induced birefringence; and (3) the measurement of current density profiles in LHCD experiments using a within-shot calibration technique. Each activity is summarized and future work is proposed in several areas.

5.1 Current status of the diagnostic

Avalanche photodiodes (APD) replaced the original photomultiplier tubes (PMT) during the FY2006 campaign. The sensitivity on the intensity of the ratio of 40 and 44 kHz (drive frequencies of the two Photoelastic Modulators) signals was examined and the effect on the polarization angle is approximately $0.011°$ for an order of magnitude change in the light intensity. The APD quantum efficiency was experimentally verified to be an order of magnitude higher than that of the existing PMTs, which is consistent with the advertised values.

A Wire Grid Polarizer (WGP) was installed on the rotational MSE shutter to provide a source of linearly polarized light with fixed polarization direction. The shutter can now be positioned in three orientations: open, closed, and WGP. The invessel WGP can be used to detect possible Faraday rotation and shot-to-shot drift

in the diagnostic on a routine basis. For a correct interpretation on the measured polarization angle, the effect of arbitrary angles of incidence on a linear polarizer was mathematically derived and was shown to be in good agreement with the bench test results. During the FY2005 campaign, the measurement of possible Faraday rotation was performed using the WGP during a series of plasma discharges with either plasma current (I_p) or toroidal field (B_T) ramping to provide the MSE lenses with systematic changes in the amount of Faraday rotation. The results show the change in measured polarization angle has negligible correlations with the changes both in I_p and B_T, i.e.,

$$
\begin{aligned}
\Delta\gamma_{avg} &= -0.002 \pm 0.021^o/B_T(Tesla) \\
\Delta\gamma_{avg} &= -0.047 \pm 0.104^o/I_p(MA)
\end{aligned}
\tag{5.1}
$$

where $\Delta\gamma_{avg}$ is the MSE channel-averaged polarization change. This indicates that Faraday rotation is not a significant source of systematic error in the C-Mod MSE system.

After a strong correlation of the MSE background signals with the thermal H_α signals was observed during the FY2007 campaign, steep edge filters that would reduce the radiation at wavelengths less than 656.9 nm by two orders of magnitude was added onto the existing the bandpass filters. Subsequent measurements indicated, however, that the edge filters have absolutely no effect on the magnitude of the MSE background nor on its correlation with the H_α intensity. **FUTURE WORK:** The conclusion made from these observations is that the background source is not the H_α radiation itself but something that is correlated with the H_α signal such as impurity line radiation from charge exchanges with neutrals or D_2 molecular line radiation. More than half the FY2008 campaign were performed without the diagnostic neutral beam (DNB). Data mining for these 'background' runs including a dedicated run for the MSE background study at the end of the campaign (1080523) would be worthwhile performing. Since the ICRF antennas are the viewing dump of the MSE lines of sight, the investigation on the geometrical effects should be considered as well. For example, swapping the bandpass filters for a pair of MSE channels was performed during the

1080523 run 1080523025 and 1080523026). The result implied the effect is more spectrum-related rather than spatial, but more statistics are required to draw a firm conclusion.

The DNB orientation was modified from radial to $7°$-tangential injection prior to the FY2007 campaign based on the conjecture that the 'secondary' beam neutrals - the neutrals that ionize following collisions with the torus gas and then re-charge exchange at a random gyro angle - caused the anomalous behavior in the beam-into-gas calibrations. A significant improvement has been observed in the pitch angle measurements with this modification and the dedicated beam-into-gas experiments verified the conjecture by demonstrating the gas-pressure dependence on the pitch angle deviation.

The feasibility of two plasma calibration techniques - I_p ramp and plasma sweep - was studied. In the 1070615 run, it was possible to obtain the edge pitch angle range from $-10°$ to $-1°$ by ramping down the I_p from 0.8 to 0.1 MA within a shot. The total range of the pitch angle that can be calibrated from combined shots is $-13°$ to $-1°$. A strong linear relation between the pitch angle measured by MSE and that from EFIT was observed for the edge channel, implying the edge channel can be correctly calibrated simply by adding or subtracting the constant offset from the EFIT value. The plasma-sweeping shots taken on the 1070629 run successfully demonstrate their applicability to the MSE calibrations. The edge major radius was stably reduced from 89 to 76 cm within a shot and up to 7 MSE channels (out of 10) were swept by the edge of the plasma. **FUTURE WORK:** These techniques should certainly be re-visited after the MSE system is upgraded to reduce the thermal shot-to-shot drift. A quantitative approach to estimate, and include, the uncertainty in the pitch angles inferred from EFIT (although small at the plasma boundary) should be included. Both calibration techniques can be combined with the one-point inner-channel calibration method using the sawtooth inversion radius (SIR) data.

Two more calibrations that were performed for the first time are the absolute intensity calibration and the intensity-weighting position calibration. The absolute intensity calibration was able to estimate the light-gathering power of the current MSE

system. This was possible by performing two separate absolute intensity calibrations (one with the full MSE system and the other with the fiber-only MSE system) and a series of tests where the transmission (for lenses and windows) and the reflectivity (for mirrors) of individual optical elements were examined. The result indicates that the étendue of the current system is smaller by a factor of $3 \sim 4$ than that based on either the first lens (L1) or the fiber entrance, implying that the system étendue is determined by somewhere else in the optical train. The reduced étendue is also consistent with the aperture broadening smaller than expected based on the size of L1. **FUTURE WORK:** A group from the polarization lab in the University of Arizona visited MIT in 2009 prior to the FY2009 campaign and made several suggestions to test the real étendue of a system. This includes observing the shape of the image, backlit from the fiber end, right in front of the first lens, L1. If it does not have the round shape as L1, the L1 is not the real 'aperture'. They also suggest a 'front-lighting' test where the light source located at the DNB trajectory should be observed at the region of the fiber entrance.

Finally, a database study was performed for the DNB-runs from the FY2008 campaign (326 shots) to examine the MSE measurement error and its correlation with the signal-to-background ratio. The correlation study shows that the signal-to-background ratio $\gtrsim 100$ is required to have measurement errors $\lesssim 0.1^o$ for most of the channels. The signal-to-background ratio itself has a strong correlation with the plasma density and the beam energy; lower density and higher beam provides higher signal-to-background ratio. The database also correlates the measurement error with the plasma density with various plasma conditions (L and H modes and L-H transitions). For a given density, the statistical errors are larger if the measurement interval includes an L-to-H transition than if the plasma remains in L-mode or H-mode throughout the measurement interval. The effect of the individual ICRF antennas was also examined using this database but no noticeable trend was observed. Measurement errors are larger for the innermost and outermost channels than for the channels near the optical axis. **FUTURE WORK:** The correlation between the measurement error and the individual ICRF antenna requires more data points.

The currently available data with appropriate environment (such as reasonable beam currents in L-mode plasmas) is not large enough to draw a firm conclusion. Since this requires an exclusive control on the RF antennas, a dedicated run may be desirable where the effect of the viewing dump on the MSE background intensity can be performed simultaneously.

5.2 Thermal drift

A shot-to-shot drift due to the temperature excursion on the in-vessel optics was identified in several ways. This included a series of Ohmic plasmas with identical conditions (FY2007) and a series of heating and stressing tests for the invessel periscope (during the manned access after FY2007). A subsequent series of tests verify that the spurious change in polarization angle is larger by an order of magnitude at the L2 doublet than at the L3 doublet and that it is strongly channel-dependent at the L2 doublet. This can be explained by light pattern incident on each doublet: light from the DNB is completely out of focus at the L3 doublet whereas it is nearly in focus at L2, the rays from the edgemost channel being focused at the periphery of the L2 doublet. This difference makes their respective responses to the thermal stress-induced birefringence completely different: the effect on L2 is locally concentrated and channel-dependent while that on L3 is averaged out. During the FY2008 campaign, newly installed thermocouples provided the measurements of temperature variations around the problematic region of the periscope on a 24/7 basis. The effect of the customary daily temperature variation in the C-Mod vacuum vessel was evaluated by comparing the spurious shot-to-shot drift in polarization angle during beam-into-gas shots in a standard run day (1080318) versus a run day in which special care was taken to minimize the temperature decrease that normally occurs at the start of the day. This exercise confirmed that temperature variations are the cause of the spurious drift and that reducing the temperature variations can reduce the drift.

By modeling the thermal stress-induced birefringence phenomenon as an arbitrarily oriented waveplate imposing a certain amount of phase shift onto linearly

polarized light, a reasonable calibration concept was developed where a pair of two known reference polarization angles are measured before and/or after each plasma pulse to characterize the system's thermal birefringent conditions for that moment. The feasibility of this in-situ scheme was demonstrated through a series of bench tests. Acceptable measurement errors were obtained when the range of the two reference polarization angles was up to 4° for the pitch angles that were outside of the reference range by up to 2°. This implies that the total of 8° in the MSE frame can be calibrated in this method. This is about the same range of the pitch angle in the MSE frame that C-Mod plasmas typically experience. Practical limitations on this scheme were also discussed.

A series of bench experiments were performed to characterize the thermal responses of the MSE system, mainly in order to provide the design parameters for the thermal insulation mechanisms. The upper bound of the maximum allowable temperature variation around the L2 lens was determined to be $\sim 0.38\ ^oC$ for the input polarization angle of 62.5^o in the MSE frame. It increases to $\sim 0.63\ ^oC$ for the input polarization of 85° which is closer to the polarization angles typically realized in plasma experiments. The allowable temperature slew rate at the periscope surface near the L2 doublet was also determined to be $0.5 \sim 2^oC/\text{hour}$ depending on input polarization angles. The maximum tolerable slew rate increases as the input polarization angle approaches a vertical orientation. For the input of 85°, the acceptable slew rate is about $1.5\ ^oC/\text{hour}$. A combination of these experimental results with a full 3D finite element calculation implies that the maximum allowable temperature variation across the lens (from the center to the edge) is $0.4\ ^oC$. A simple 1D calculation that includes the radiative communication between the lens surface and the inner wall of the periscope implies that the variability of the temperature throughout the periscope surface should be kept under $\sim 0.5\ ^oC$.

With these design parameters, two main thermal insulation mechanisms were developed and implemented:

1. A single-layer thermal shield whose inner (MSE periscope-facing) surface was polished and gold-plated with the emissivity of $0.02 \sim 0.04$ was installed onto the

plasma-facing side of the periscope to reduce both the heat flux to the periscope and the temperature slew rate at the periscope. At the same time, the outer surface of the MSE invessel periscope was gold-plated as well to minimize the the radiative communication between the periscope and the surroundings (both the plasma and the outer wall of the torus). Both the steady-state and the transient calculations for a simplified 1D shield model gave consistent values in the reduction of heat flux (by a factor of 25) and the expected temperature variability across the front- and back-sides of the periscope of $0.8 \sim 1.2$ °C for the between-shot averaged radiated powers from the plasma of $500 \sim 800$ W/m^2.

2. The effective area of the contact between the lens and the O-ring that cushioned the lens against the vibration inside the lens holder was reduced by about a factor of 10 by adding eight raised ridges to the existing rectangular cross section of the O-ring gland (the groove in which the O-ring shits). Effectively, the O-ring contacts the lens only at eight discrete locations along the lens periphery except at the moment of a disruption. A thermal capacitive circuit analysis was performed that included the heat transfer effects from the direct heating of the first lens, L1, which can not be protected by the gold-plated thermal shield. The analysis showed that the temperature variation across the lens L2 can be reduced to be $\lesssim 0.5$ °C by reducing the conductive resistance between the lens and the lens holder by a factor of 10.

Finally, the thermal-stress induced birefringence model was enhanced by adding the effect of the 'static' (non-thermal) phase shift, for example, induced by the imperfect dielectric coatings on the MSE mirrors, in addition to the thermally induced phase shift from the lenses. This dual-waveplate model explains why there was no perfect averaging effect in the L3 heating tests, which the single-waveplate model failed to explain. The dual-waveplate model also suggested that the static phase shift can significantly magnify the change in polarization direction that is caused by thermal stress-induced birefringence in the lenses. Based on the dual-waveplate model, its good agreement with the experiments, and the evidence for the degra-

dation of the performance in the current MSE mirrors, the three existing dielectric mirrors were replaced by new ones with smaller phase shifts ($\pm$ 3° over the angles of incidence of 30° $\sim$ 60°). **FUTURE WORK:** The dual-waveplate model should be verified by additional tests using controllable waveplates. The experiments done to date involve heating the lenses where finite non-uniform heating and convection may complicate precise interpretations. With controllable waveplates, both the fast axes and the phase shifts can be quantitatively imposed and the test can provide direct comparisons with the model.

5.3   Measurement of current density profiles

The feasibility of the within-shot calibration scheme was examined. In the within-shot calibration, the baseline pitch angle from a quiescent Ohmic flattop phase was obtained from a separate equilibrium reconstruction corrected by the sawtooth inversion radius data (EFIT15) and a complete pitch angle data for constraining the second, and final, equilibrium reconstruction (EFIT17) was obtained by summing the baseline pitch angle and the change in pitch angle from the value at the baseline time inferred from MSE. The cross check using the I_p ramp shots implied that this linear approach could be applicable to the cases where there were multiple degrees of pitch angle changes such as the LHCD plasmas.

The validity of the baseline magnetic reconstruction based on the sawtooth inversion radius data from the ECE diagnostics was checked by comparing the magnetic equilibria with and without the within-shot calibration procedure. The sawtooth crash and its reappearance during and after the LHCD pulse, respectively, are more consistent with the within-shot calibrated equilibrium data. The comparison of the plasma stored energy inferred from the equilibrium based on the within-shot calibration with that obtained from independent measurements on the plasma temperature and density also showed reasonable agreement with each other while there was nearly a factor 2 difference for the equilibrium data without the within-shot calibration.

FUTURE WORK (for the preceding two paragraphs): Currently, both

240

equilibrium reconstruction procedures that participate in the within-shot calibration scheme (i.e. EFIT15 and EFIT17) assume 1st and 2nd-order polynomials for the fit functions of P' and FF', which is the default setting for the normal EFIT that is automatically run after each shot in C-Mod. This tends to smooth out the spatial variations on calculated quantities such as current density and safety factor as well as pitch angle itself. No detailed sensitivity study has been done for the fit parameters and therefore, no quantitative uncertainties for the EFIT data are available. The EFIT uncertainties should be included for more complete analyses. The effect of the finite radial resolution of the MSE views has not been taken into account when constraining the EFIT. Although the innermost MSE channel was deselected in the calibration procedure due to its large radial resolution (~ 9 cm), the next innermost channel still has a significant radial resolution (~ 7 cm) for the 13-cm diameter DNB. This is indeed a fundamental MSE problem that was appreciated at the incipient stage of installing the MSE system in C-Mod and expected to be resolved by having a neutral beam with a reduced size. Although the installation of the DNB aperture was in progress at the time of this dissertation work (prior to the FY2009 campaign), having a systematic approach to deal with a finite radial resolution in the analysis procedure, such as weighted averaging, is desirable.

Finally, the within-shot calibration scheme was applied to deduce the toroidal current density profiles. The results directly demonstrated, for the first time in the Alcator history, several standard predictions of LHCD theory such as the parallel refractive index ($n_{\parallel}$) dependence in its efficiency and the off-axis current drive. A non-iterative method using an analytic expression that directly relates the local toroidal current density with the poloidal magnetic fields measured by MSE was also incorporated with the within-shot calibration. The results from this direct method were in good agreement with those from the iterative method, additionally providing small local structures in the profile which the iterative method had smoothed out. **FUTURE WORK:** More physics can be derived by further analyzing the LHCD data. For example: (1) by adding the measured pressure profiles in the analysis procedure for P' and using neoclassical Spitzer conductivity to subtract out the inductive part

of the current density, the realistic contribution from the bootstrap current can be reasonably estimated [84]; (2) Ref [85] suggests a parametric method to estimate the RF enhanced ('hot') electrical conductivity by fitting the loop voltage drop and the LHCD power. A similar approach can be attempted in C-Mod as well and the result can be compared with that from the approach with the neoclassical conductivity; and (3) the radial profile of the neoclassical Pfirsch-Schlüter current, J_{PS}, can be calculated directly from the MSE data using the analytic formulas given in Ref [16]. The obtained J_{PS} can be used to calculate P' which, in turn, can produce the bootstrap current density. The bootstrap contribution from this direct method can be compared with that obtained from the method given in (1).

Appendix A

The relation between the pitch angle and the polarization in MSE optics

A general formula to relate the linear polarization angle seen by the MSE optics (γ) to the local magnetic pitch angle in the tokamak (γ_m) is derived in this section. The formula derived here is independent of DNB trajectory and viewing geometry and can be applied to any tokamak. The formula is applied for C-Mod geometry and the conversion between two kinds of angles and the uncertainties of γ_m, $\delta\gamma_m$, are investigated for given uncertainties from other factors.

A.1 Derivation

All geometry is considered in spherical coordinates. Fig A-1 shows (a) the DNB beam velocity vector and (b) the MSE line-of-sight vector expressed in two spherical coordinate systems. The general Cartesian coordinated system (x, y, z) is replaced by (R, T, V), where R is in the major radius direction, T is in the toroidal direction, and V is in the vertical direction. Also, shown in Fig A-1 (b) is the 2D rectangular coordinate systme (y', z') for the MSE view plane. The polarization angle viewed by the MSE optics, γ, is indicated. Note that these coordinate systems are local, that
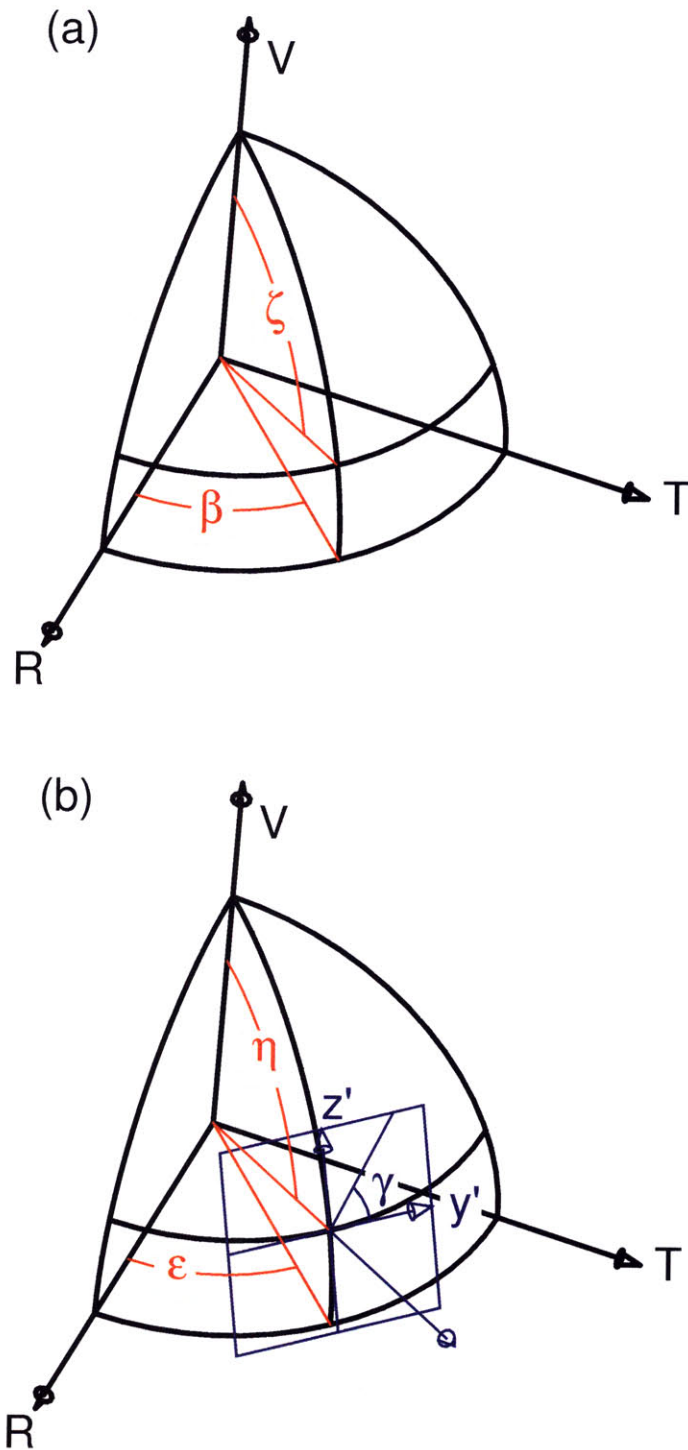
Figure A-1: Local spherical coordinate systems representing (a) the DNB vector and (b) the MSE line-of-sight vector

is, channel-dependent; The origin of the coordinate systmes is at the intersection of the DNB trajectory and the MSE viewing sightline for a given MSE channel.

The Cartesian components of the DNB vector $\mathbf{v}$ are expressed as follows in the spherical coordinate system

$$
\begin{aligned}
v_R &= v \sin \zeta \cos \beta, \\
v_T &= v \sin \zeta \sin \beta, \\
v_V &= v \cos \zeta.
\end{aligned}
\tag{A.1}
$$

Therefore, the induced Stark electric field $\mathbf{E} = \mathbf{v} \times \mathbf{B}$ is

$$
\begin{aligned}
\mathbf{E} = \mathbf{v} \times \mathbf{B} &= v(B_V \sin \zeta \sin \beta - B_T \cos \zeta)\mathbf{e_R} \\
&\quad -v(B_V \sin \zeta \cos \beta - B_R \cos \zeta)\mathbf{e_T} \\
&\quad +v(B_T \sin \zeta \cos \beta - B_R \sin \zeta \sin \beta)\mathbf{e_V},
\end{aligned}
\tag{A.2}
$$

where $\mathbf{e_R}$, $\mathbf{e_T}$, and $\mathbf{e_V}$ are the unit vectors in R, T, and V directions, respectively. From Fig A-1 (b), it is inferred that the unit vectors that represent the horizontal and the vertical directions on the MSE view plane ($\mathbf{e_{y'}}$ and $\mathbf{e_{z'}}$, respectively) are such that

$$
\begin{aligned}
\mathbf{e_{y'}} = \mathbf{e}_\epsilon &= (\mathbf{e_R} \cdot \mathbf{e}_\epsilon)\mathbf{e_R} + (\mathbf{e_T} \cdot \mathbf{e}_\epsilon)\mathbf{e_T} + (\mathbf{e_V} \cdot \mathbf{e}_\epsilon)\mathbf{e_V} \\
&= -\sin \epsilon \mathbf{e_R} + \cos \epsilon \mathbf{e_T},
\end{aligned}
\tag{A.3}
$$

$$
\begin{aligned}
\mathbf{e_{z'}} = -\mathbf{e}_\eta &= -(\mathbf{e_R} \cdot \mathbf{e}_\eta)\mathbf{e_R} - (\mathbf{e_T} \cdot \mathbf{e}_\eta)\mathbf{e_T} - (\mathbf{e_V} \cdot \mathbf{e}_\eta)\mathbf{e_V} \\
&= -\cos \eta \cos \epsilon \mathbf{e_R} - \cos \eta \sin \epsilon \mathbf{e_T} + \sin \eta \mathbf{e_V}.
\end{aligned}
\tag{A.4}
$$

Therefore, the polarization angle seen by the invessel MSE optics, γ, is expressed as

$$
\tan \gamma = \frac{\mathbf{E} \cdot \mathbf{e_{z'}}}{\mathbf{E} \cdot \mathbf{e_{y'}}} = \frac{B_V \sin \zeta \cos \eta \sin(\epsilon - \beta) + C_\epsilon + S_\beta}{-B_V \sin \zeta \cos(\epsilon - \beta) + \cos \zeta (B_R \cos \epsilon + B_T \sin \epsilon)}.
\tag{A.5}
$$
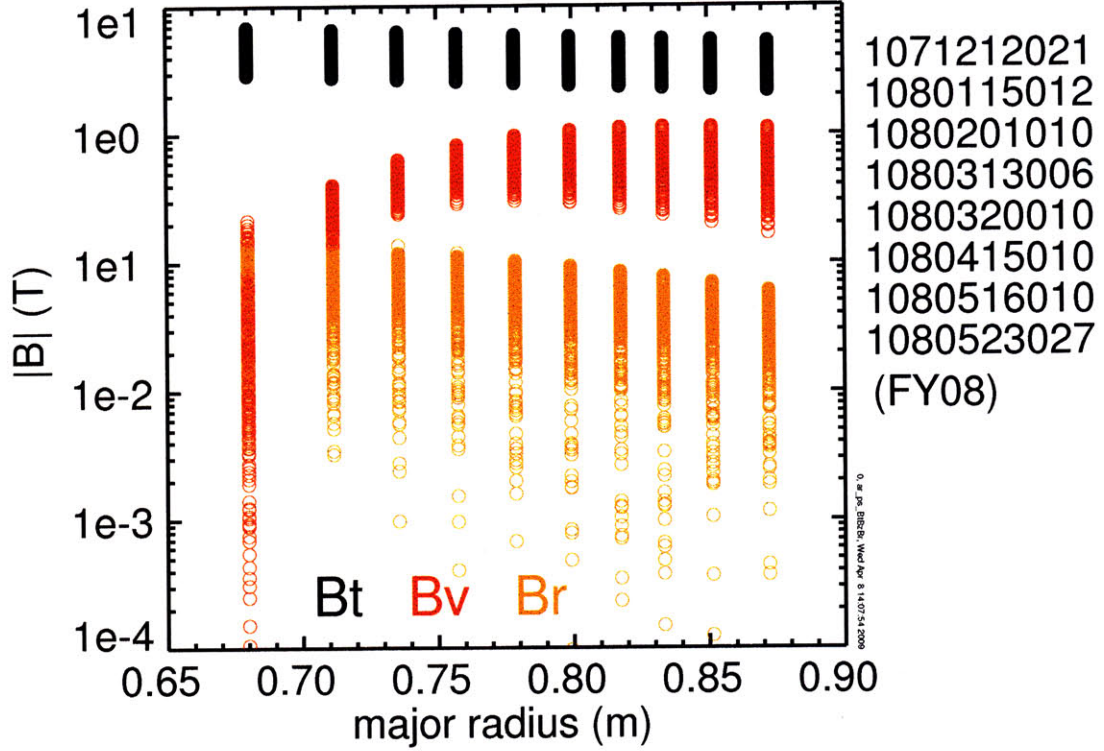
Figure A-2: Comparison of the magnitudes of B_T, B_V, and B_R at the MSE channel locations from some typical shots during the FY08 campaign.

where

$$C_\epsilon = \cos\eta\cos\zeta(B_T\cos\epsilon - B_R\sin\epsilon)$$

$$S_\beta = \sin\eta\sin\zeta(B_T\cos\beta - B_R\sin\beta).$$

A.2 Applications to C-Mod

The terms that contain B_R in Eqn A.5 is smaller at least by two orders of magnitude than those having B_T. Fig A-2 compares the magnitudes of B_T, B_V, and B_R at the locations of the MSE channels from some typical shots during the FY08 campaign. As shown in the figure, B_T is larger typically by two orders of magnitude than B_v. In addition, $\cos\epsilon$ is in the same order as $\sin\epsilon$ for the MSE channels (ϵ ranging $-70 \sim -46°$) and $\cos\beta$ is larger by an order of magnitude than $\sin\beta$ for $\beta \approx -10°$ with a

7°-tilted DNB. Therefore, ignoring the B_R terms and taking $\zeta = 90^o$, Eqn A.5 reduces to

$$\tan\gamma = \frac{\tan\gamma_m \cos\eta \sin(\epsilon - \beta) + \sin\eta \cos\beta}{-\tan\gamma_m \cos(\epsilon - \beta)},\tag{A.6}$$

where $\tan\gamma_m$ is defined as $\frac{B_V}{B_T}$. Straightforwardly, we have

$$\tan\gamma_m = -\frac{\sin\eta \cos\beta}{\tan\gamma \cos(\epsilon - \beta) + \cos\eta \sin(\epsilon - \beta)}.\tag{A.7}$$

Fig A-3 shows the plot of the real tokamak pitch angle (γ_m) versus the MSE polarization angle (γ) for the channel 0. The overplotted star symbols are from the
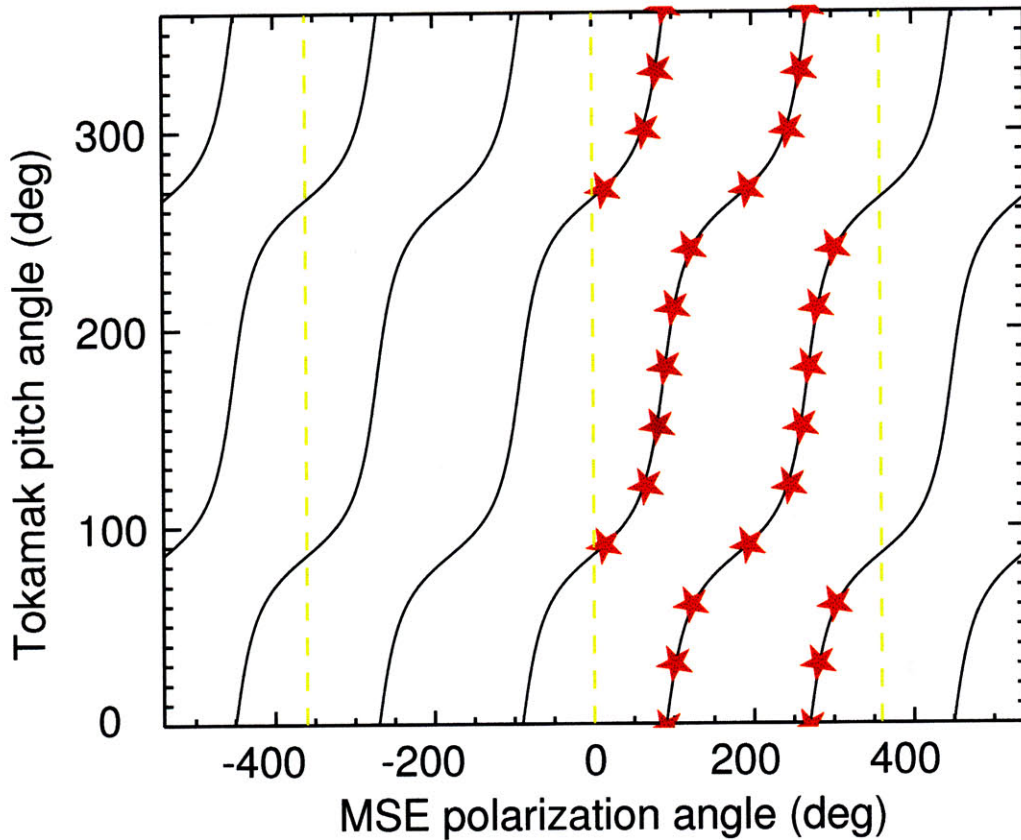
Figure A-3: Real tokamak pitch angle versus MSE polarization angle. Lines from Eqn A.7 and the star symbols from 3D CAD drawing

3D CAD drawing that gives the angle of the π component of the Stark electric field projected on to the MSE frame. Note here that the MSE polarization angle cannot

distinguish the real magnetic pitch angles, say, $170°$ and $170 + 180 = 350°$ (that is, the same angle, but opposite magnetic field vector). Here, this pitch angle can be coventionally (or conveniently) read as $170 - \pi = 350 - 2\pi = -10°$.

A plot similar to Fig A-3 is shown in Fig A-4 where the mapping to real tokamak pitch angle for the MSE polarization angles from $0° \sim 180°$ is shown for all 10 MSE channels. The box near the center of the plot indicates the range of MSE polarization
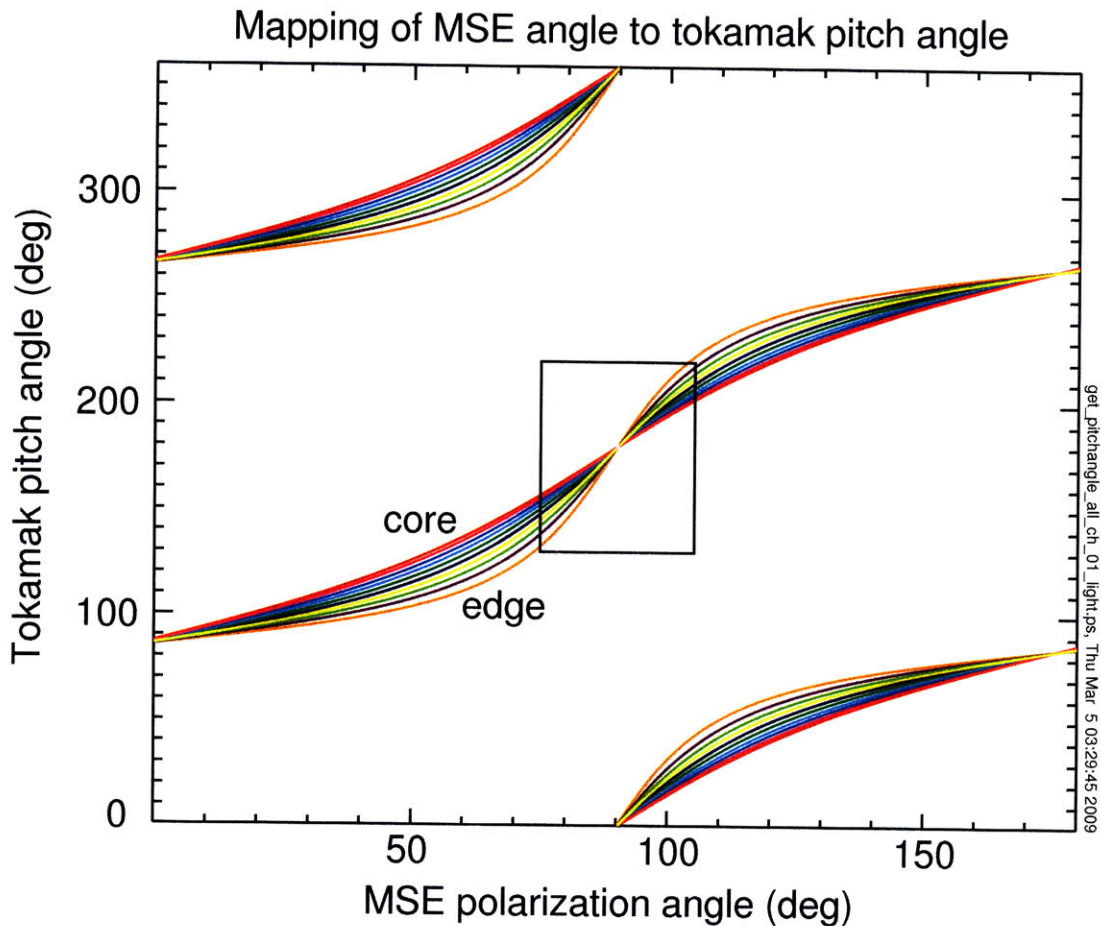
Figure A-4: Real tokamak pitch angle versus MSE polarization angle for ten MSE channels.

angles typically measured. This shows that although the mapping looks linear in the typical region of MSE angles (in the box), the real mapping is not in general. The magnified plot of this box region is in Fig A-5 (top).

From Eqn A.7, the propagation of the uncertainty in γ can be estimated by

$$\delta\gamma_m = \sqrt{\left(\frac{\partial\gamma_m}{\partial\gamma}\right)^2 (\delta\gamma)^2} \qquad (\text{A.8})$$

$$= \sqrt{\frac{\cos^2\beta \cos^2(\beta-\epsilon) \sec^4\gamma \sin^2\eta}{D}(\delta\gamma)^2},$$

where $\delta\gamma$ is the uncertainty in γ and

$$D = (\cos^2\eta \sin^2(\beta-\epsilon) + \cos^2\beta \sin^2\eta - \cos\eta \sin(2(\beta-\epsilon))\tan\gamma + \cos^2(\beta-\epsilon)\tan^2\gamma)^2.$$

$$(\text{A.9})$$

Eqn A.9 simply has the form of $\delta\gamma_m = f_{em}\delta\gamma$ and defines a very important factor, f_{em}, so called the *error multiplication factor*. This factor is the number that should be multiplied the error in the MSE polarization angle (γ) by in order to evaluate the error in the real tokamak pitch angle (γ_m). The propagation of the uncertainties in β, ϵ, and η comes into play as systematic errors. The invessel measurements give the DNB tilting angle as $6.64^o \pm 0.58^o$ and the L1 location as $(x, y, z) = (92.40 \pm 0.07, -31.48 \pm 0.10, 2.72 \pm 0.03)$ cm where x, z, and y are the radial (toward F port), vertical, and the $z \times x$ coordinates in the tokamak. Based on these measurements and their uncertainties, the errors in β, ϵ, and η range $0.65 \sim 0.67^o$, $0.38 \sim 0.41^o$, and $0.42 \sim 0.51^o$, respectively, with a slight channel dependence. The bottom of Fig A-5 shows the error multiplication factor for the same range of MSE polarization angle as that of the top plot for 4 selected MSE channels including the innermost and outermost channels. The error bars are from the systematic errors in the measurements of β, ϵ, and η. It is essential to include these factors whenever the pitch angle unceratinties are estimated from the uncertainties in the polarization angle measured in the MSE frame.
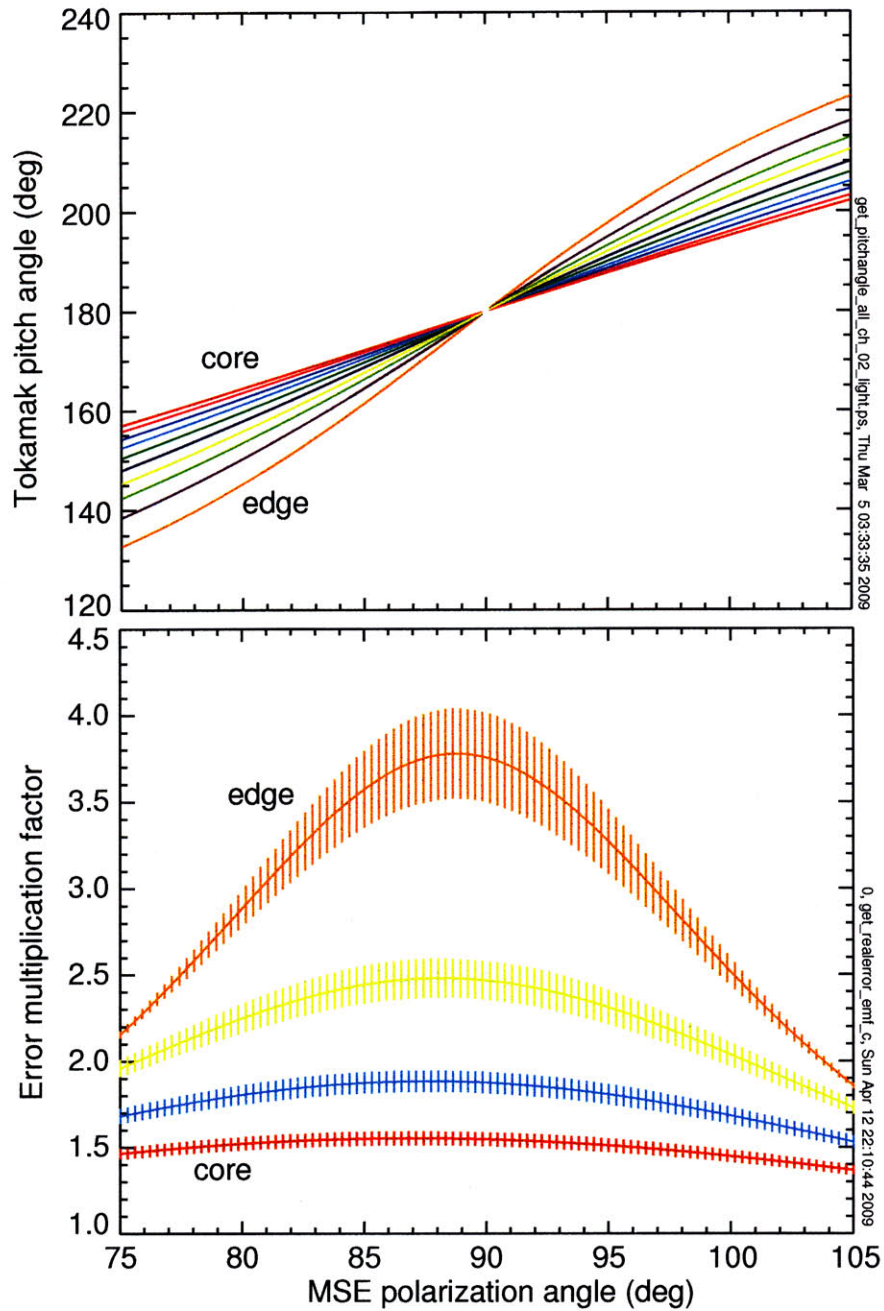
Figure A-5: Boxed region magnified from Fig A-4 (top). The error multiplication factor for this range at the MSE channels 1 (orange:outermost), 9 (yellow), 6 (blue), and 0 (red:innermost) with the systematic errors from the measurements of β, ϵ, and η included (bottom).

Appendix B

Study on the aperture broadening

As a part of the activities to investigate the fast ion effect on beam-into-gas MSE measurement during FY06, which is discussed in Sec 2.1.4, a spectrum measurement in the He-filled torus without toroidal field was performed to identify the 'blue feature'. During this test, a measurement of aperture broadening was also attempted. The lens shutter was used to change the size of the aperture. The results of this spectrum measurement for the MSE channel 7 is given in Fig B-1 along with the aperture configuration created by the shutter rotation. As illustrated in the figure, the instrumental broadening seems to be insensitive to the size of the aperture up to about 50 % reduction in the aperture size. A multi-Gaussian fit was performed for these spectra. The finite continua between individual beam energy components are believed to be emission from beam ions that are neutralized after partially accelerated in the acceleration grids in the beam system. The best fit was obtained by adding 'daughter' Gaussians for these partially accelerated beam components. Fig B-2 shows the normalized FWHM, normalized peak intensity, and the shift of the centroid from that with the full aperture as a function of the fraction in the closed part of the aperture for four beam energy components. No significant reduction in FWHM up to $\sim$ 60 % closed is observed. Note that the FWHMs for small aperture sizes have large uncertainties due to low signal intensity. The peak intensity and shift do not show change significantly until the reduction in aperture size exceeds 50 %.

The expected aperture broadening was modeled numerically, mimicking the aper-
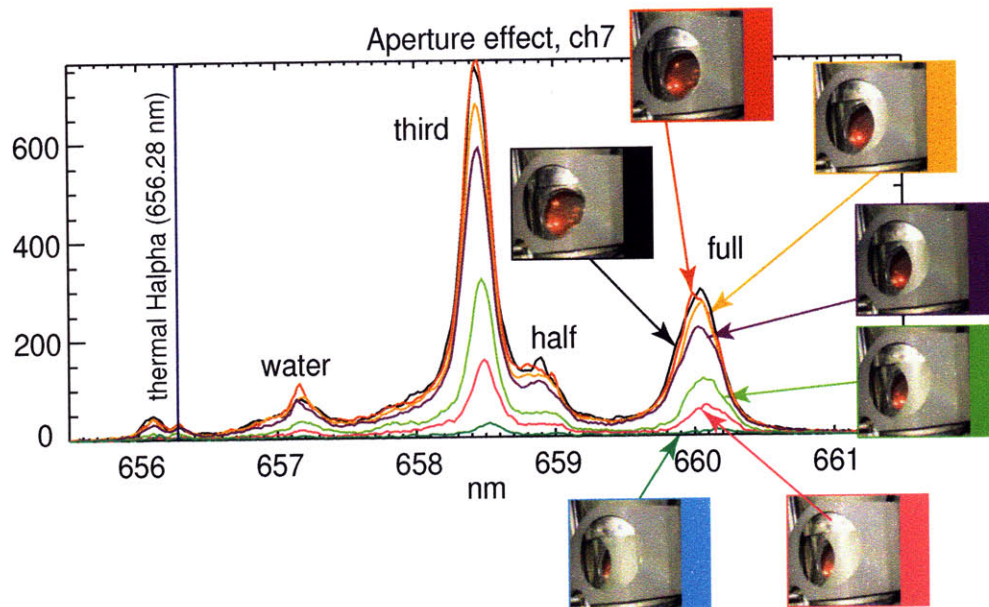
Figure B-1: MSE spectra from 1060724 beam-into-He gas shots with no fields for MSE Ch7. The corresponding shutter configuration is indicated.

ture configurations used in the spectrum measurements in Fig B-1. Fig B-3 shows the pictures of the aperture shape seen from Ch7 and their images numerically mapped for the 2D modeling and Fig B-4 compares the measured and modeled spectra for four aperture configurations. As expected, the measured broadening is smaller than predicted by the model for the full energy component. This is consistent with the observation shown in Fig 2-28 in Sec 2.1.4.

Prior to the FY2007 campaign, custom apertures were fabricated to investigate this issue further. The plasma-facing MSE lens L1 was apertured by one of a set of paper apertures illustrated in Fig B-5. The system was then illuminated with a light source positioned at the nominal location of the DNB and the corresponding images at the end of the MSE optical train outside the vacuum vessel (at the location of the linear polarizer) were recorded. Subsequently, metal aperture plates were fabricated whose apertures match the recorded images, as shown in Fig B-6. Thus, positioning a metal plate at the same location along the MSE optical train during plasma operation yields the same reduction in viewing area as would the original L1 lens apertures. Fig B-7 shows the measured spectra with these air-side apertures. This spectrum
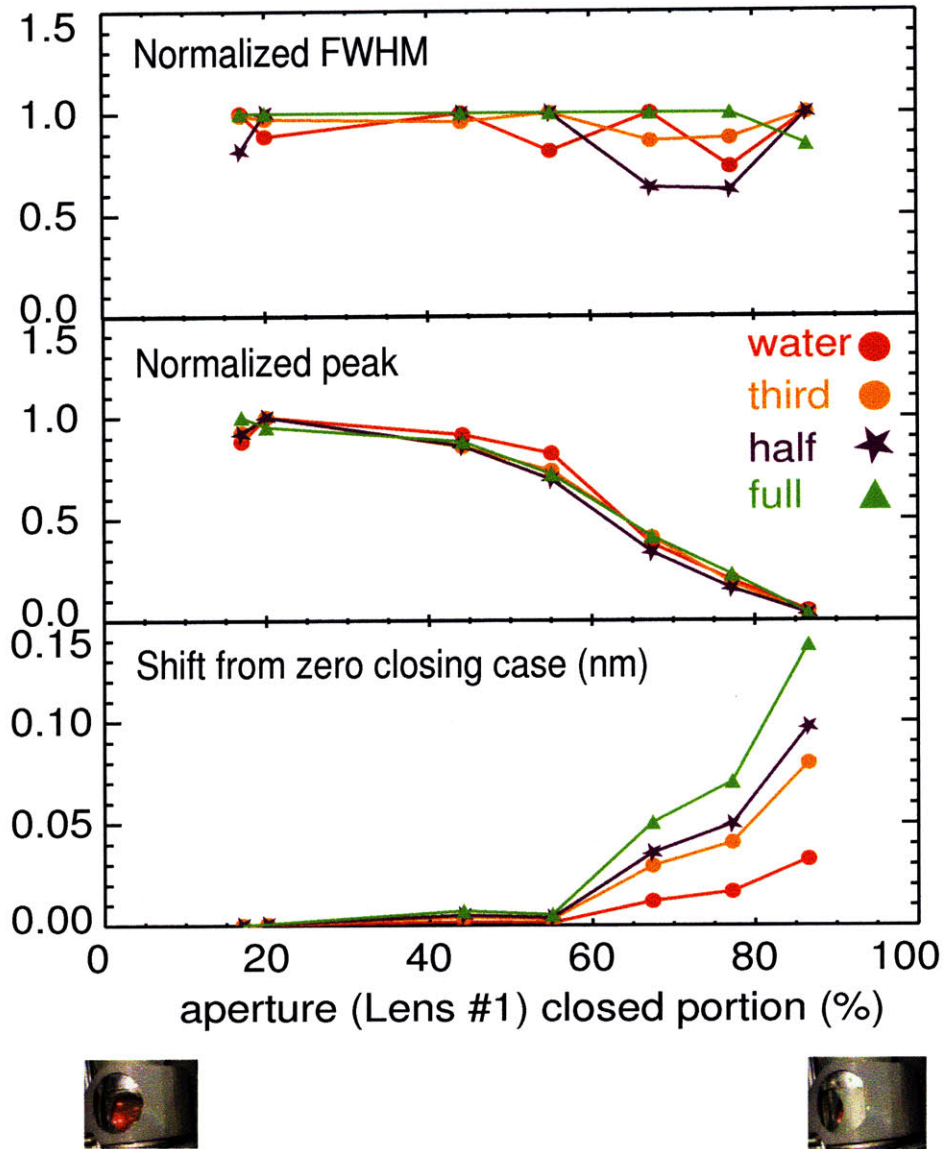
Figure B-2: Normalized FWHM (TOP), normalized peak (MIDDLE), and shift of the centroid from that with the full aperture (BOTTOM) as a function of the aperture closed portion (i.e. the size of the aperture decreases from left to right) for four beam energy components.
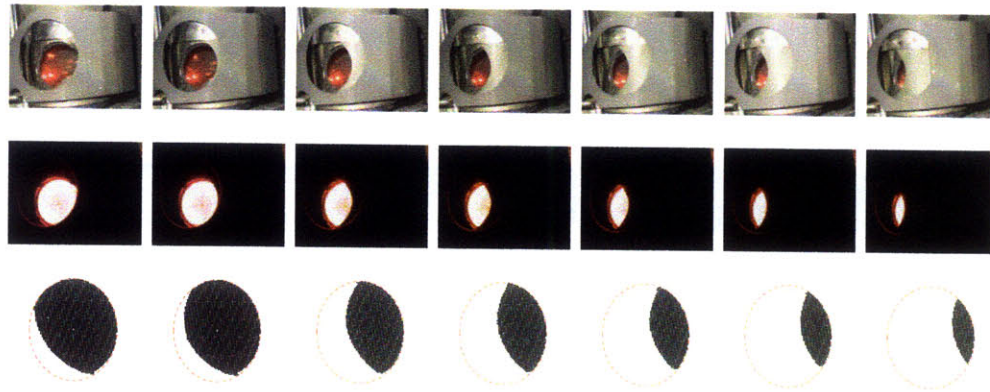
Figure B-3: Pictures of the aperture shape seen from Ch7 on the DNB trajectory (First two rows) and their numerical mapping for the modeling (Bottom row)

measurement also shows that no reduction in the broadening takes place until the L1 surface is masked by about 50 %. In Sec 2.2.2, it is discussed that the étendue of the MSE system is smaller by a factor of $3 \sim 4$ than the étendue based on L1. This corresponds to the reduction in the size of the L1 (radius) by a factor of 1.7 to 2. This reduction is consistent with the observed aperture broadening which is smaller by about $50 \sim 60$ % than that estimated from the real size of L1 (5 cm in radius).
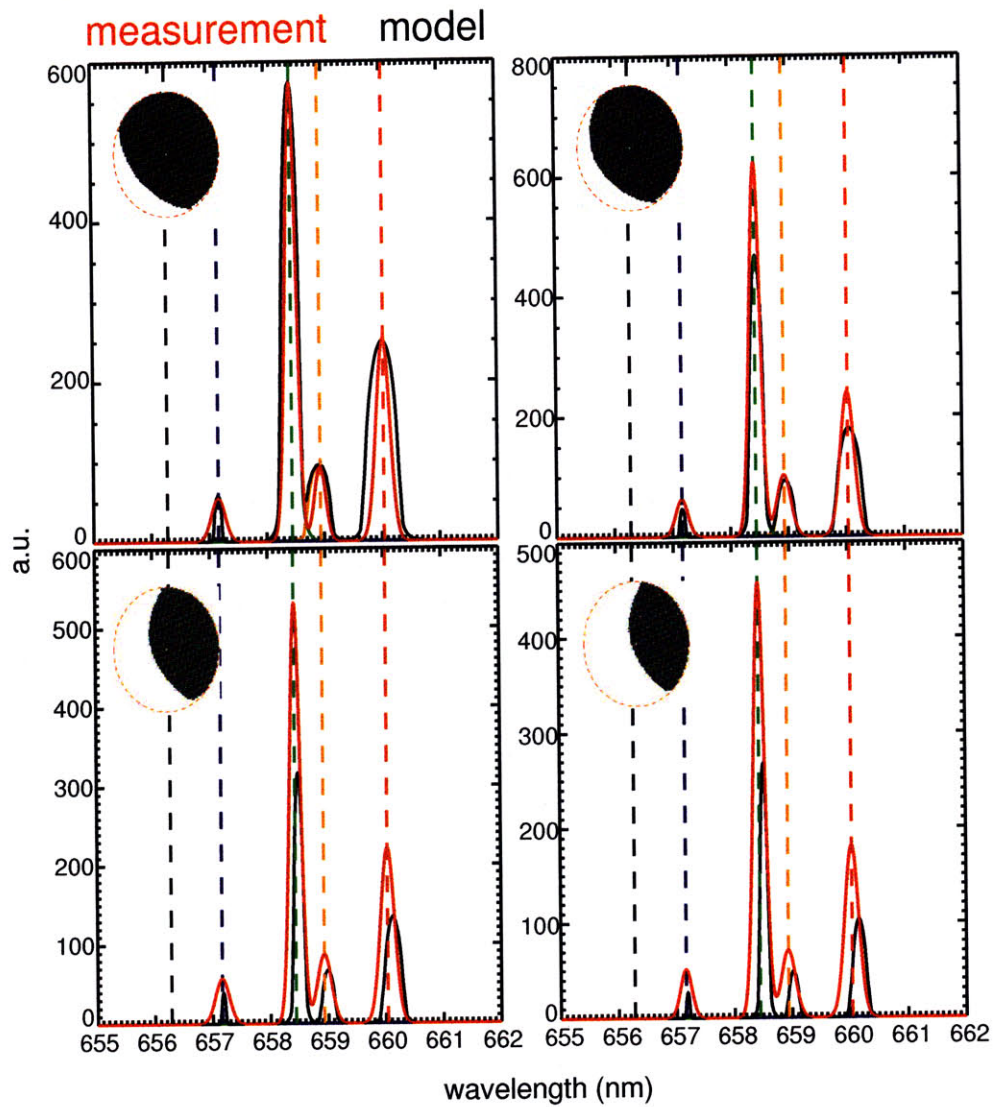
Figure B-4: Comparison of measured (red) and calculated (black) spectra for four different aperture sizes.
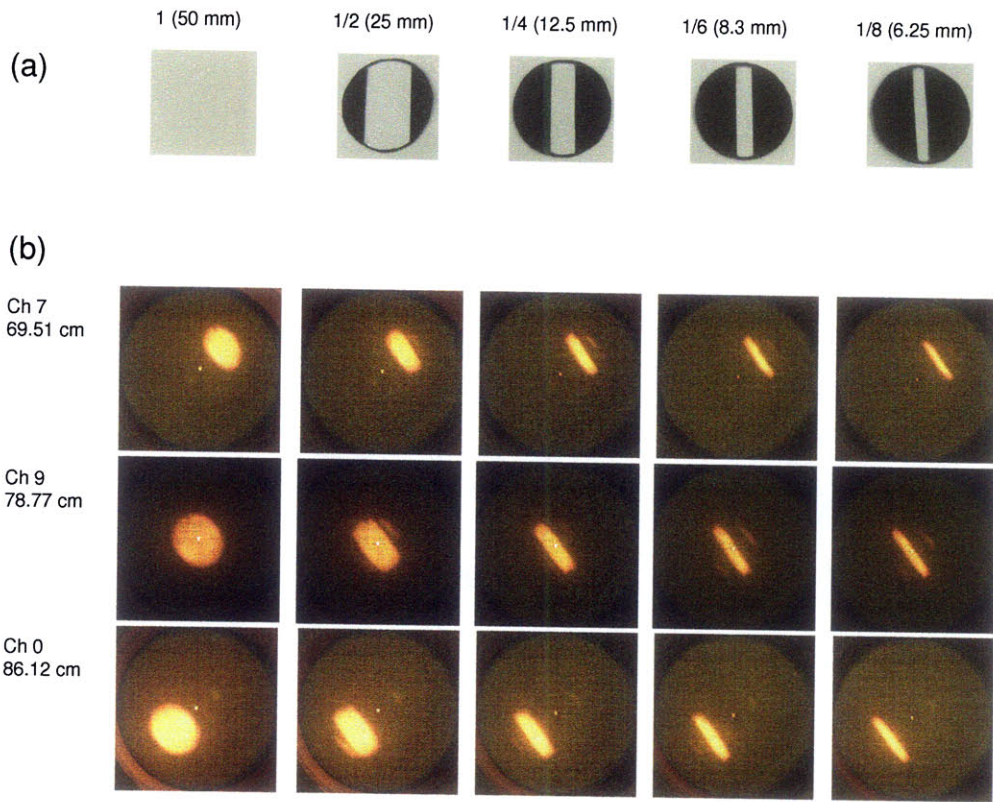
Figure B-5: (a) Aperture paper installed on L1 and (b) their images at the end of the optical train outside the F port for three MSE channels.

Figure B-6: Aperture plates fabricated based on the images shown in Fig B-5 (b) and used to mimic the L1 aperture shown in Fig B-5 (a) during the FY2007 campaign.
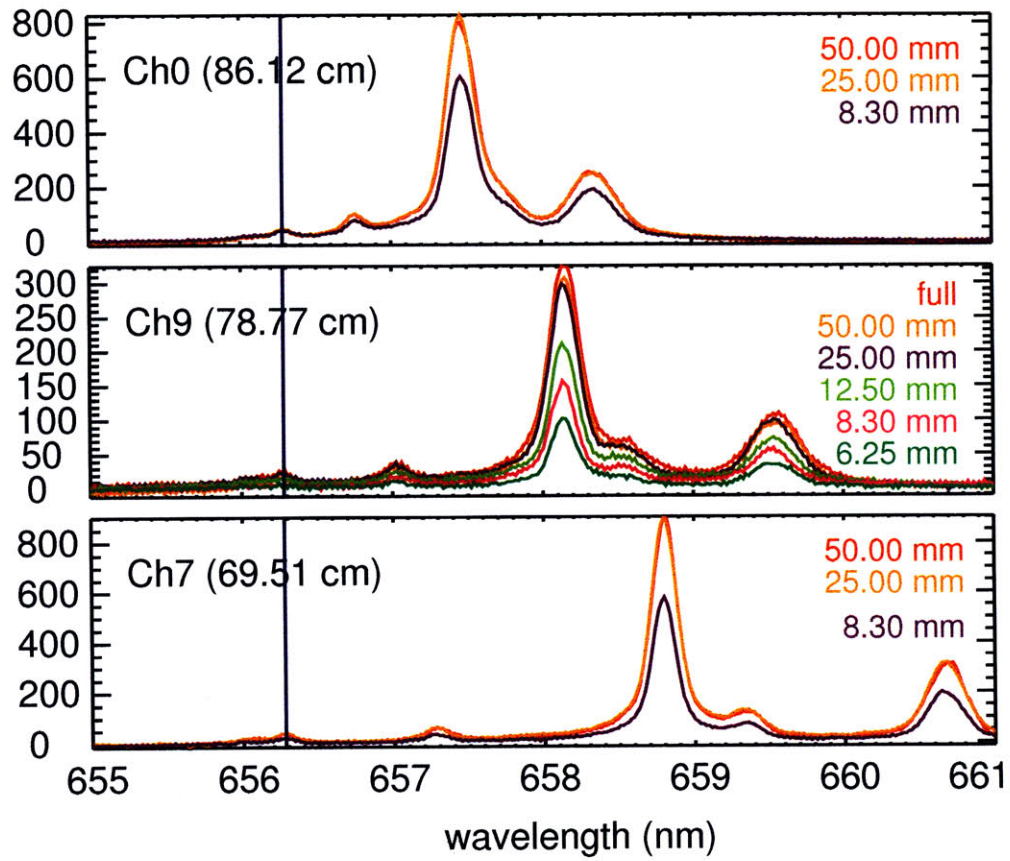
Figure B-7: Measured spectra from 1070402 beam-into-He gas shots with no fields for three MSE channels. The numbers on the plots indicate the size of the aperture given in Fig B-5 (a). The thermal H_α line (656.28 nm) is indicated by a blue vertical line.

Appendix C

Additional evidence for thermal drift

C.1   Invessel periscope bulk heating

The first heating test was performed in the C-Mod vessel with the MSE periscope installed. A large heating pad was applied to most of the plasma-facing surface of the periscope and a fixed polarized light source was positioned in front of the object lens, L1. The experimental setup is shown in Fig C-1. The invessel heating pad was powered by a variac outside the vacuum vessel. Four hundred shots each 0.5 seconds in duration were taken for 5 hours as the temperature at several locations on the periscope surface was monitored with thermocouples every 5 shots. The variac power was gradually increased over the course of the scan such that the maximum temperature reached 80 °C and was off about 2 hours 30 minutes. The measurements were continued for another 2 hours 30 minutes after the variac was off to observe the effect of temperature decrease. This test provided the first direct evidence that the MSE diagnostic is affected by the temperature variation on the periscope. Fig C-2 shows the time variations of the temperatures at the heated region of the canister and the opposite (outer wall-facing) region (top plot) and the measured polarization angle (bottom plot). The variation in the polarization is several tenths of degrees in most channels and almost a degree for the outermost channel. The variation well
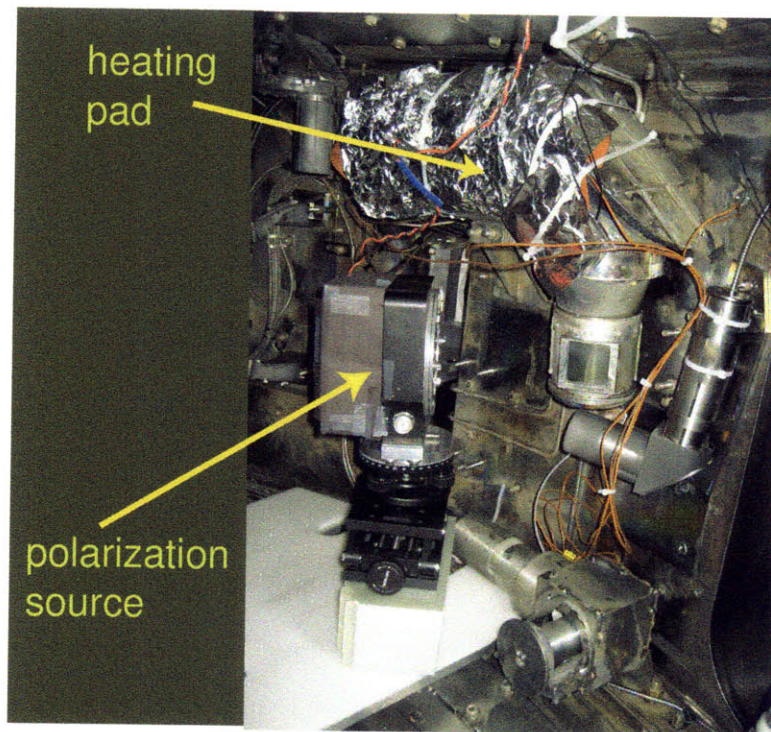
Figure C-1: MSE invessel periscope heating test setup. The heating pad is applied to most of the plasma-facing part of the periscope.
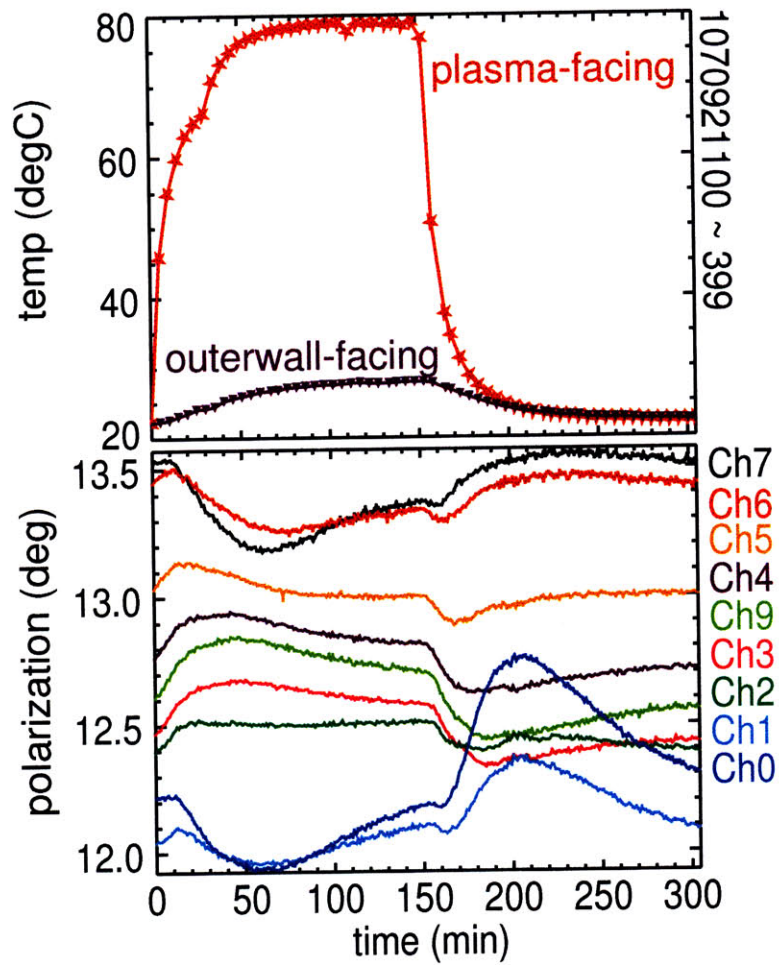
Figure C-2: MSE invessel periscope heating test result: Time evolution of the temperatures from the heated (plasma-facing) region and the cold (outerwall-facing) region of the periscope (top) and the measured polarization angle from 9 MSE channels (bottom). Channel numbers have been written in order of core (Ch7) to edge (Ch0).

follows the temperature variation with a certain time delay. For example, the temperature changes dramatically between 150 and 165 minutes, while the polarization angle changes only a little. By contrast, the change in temperature between 165 and 200 minutes is considerably smaller than the change between 150 and 165 minutes, but the change in polarization angle is large. This suggests that the underlying problem, which is clearly thermal related, also has a time constant measured in minutes. A more designated thermal test on the MSE periscope, which will be presented in Sec 3.2.1, estimates the response time of about 10 minutes.

Fig C-2 also shows that the magnitude of polarization drift is channel-dependent, the outermost and innermost channels having relatively larger changes than the central channels. It is also noted that the sign of the change in angle for 'edge' channels (0, 1, 6, and 7) differs from that for the 'core' channels (2, 3, 4, 5, and 9). However, a careful observation on the polarization change during the initial heating phase and the cooling phase around 150 minutes would imply that the time response is actually shorter for the core channels than for the edge channel. This seems to be counter-intuitive for the following reason: one of the MSE invessel optical elements (the L2 doublet in Fig 1-3) has a focusing property that is channel-dependent, i.e., the rays from an edge channel are conversed at a small 'edge' region of the lens L2 while those from a core channel conversed at its small 'core' region. Then, one might think that the heat would diffuse into the lens from the surface of the periscope, thereby, the edge channels response to the thermal perturbation first before the core channels do.

However, the in-vessel bulk heating tests effectively heated both the lenses and the mirrors, and so the results from these tests are less definitive about whether the underlying problem is caused by the mirrors or lenses. Indeed, some features from the in-vessel bulk heating test support a conjecture involving the lenses, while other features of the data do not. This strongly motivated subsequent bench tests to identify the individual contributions from the invessel optics elements.

C.2 Mirror heating

The first mirror heating test performed on the bench, where the mirror was completely isolated from the rest of the optical elements, used a sheet of plastic polarizer to generate the polarized light source, while the MSE mirror M3 was heated by an electric heat gun up to 80 °C. The change in the polarization angle in this test was small, about 0.1 °, and showed a small correlation with the temperature change. In this test, it was suspected that the sheet polarizer might have been distorted by the heat which was located nearby, which might be responsible for the 0.1° change. An improved setup was implemented using a heating pad to apply more controllable heat over the surface of the mirror and to allow more stable temperature measurements not only on the mirror but also on the polarizer. In this experiment, the correlation of the measured polarization angle and the temperature became even weaker and the temperature on the polarizer remained unchanged throughout the test while the temperature on the mirror front surface went up to 60 °C. In order to achieve higher temperature on the mirror surface without thermally affecting the polarized light, a third setup employed a wire-grid polarizer to generate the polarization. A wire-grid polarizer is effectively a set of fine electrically-conducting wires deposited on a glass substrate, and is much less subject to thermal distortion than plastic polarizers. In this final setup, the mirror surface temperature reached about 80°C and the polarizer surface remained under 30°C. The change in the polarization angle during this 2-hour heating experiment was less than 0.1°. The result with this final heating test setup is shown in Fig C-3 where the time evolutions of the temperatures at several locations in the setup (top plot) and the polarization angle from 6 MSE channels (bottom plot) are given. It can be concluded that mirrors by themselves have negligible thermal effects on the drift in the polarization measurements.

263
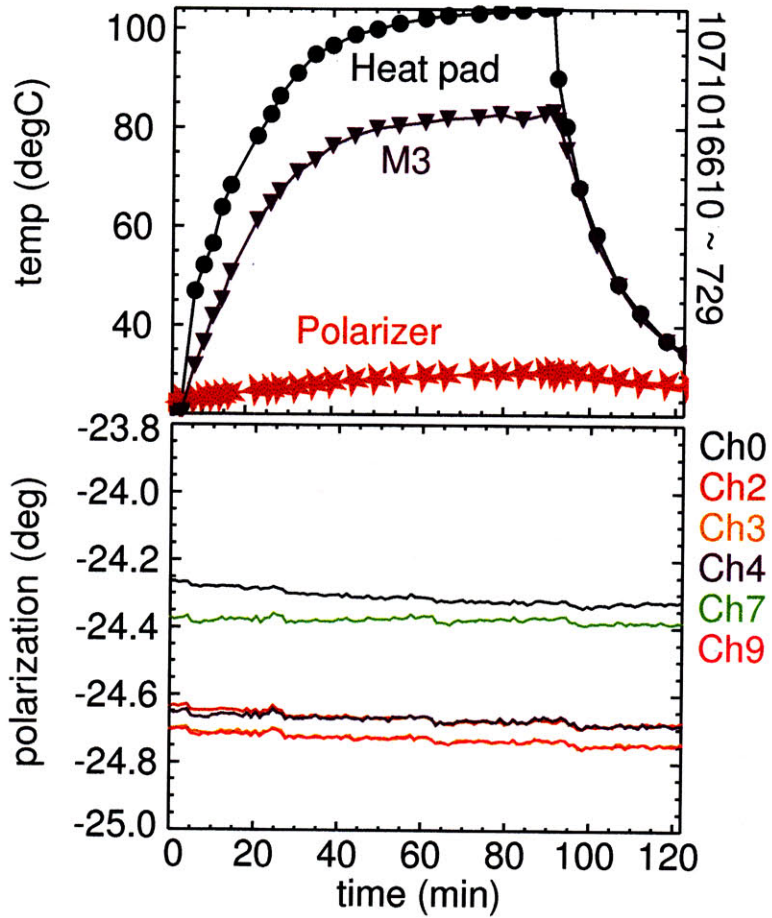
Figure C-3: MSE M3 bench heating test result: Time evolutions of the temperatures from heating pad, M3 surface, and the polarizer (top) and the measured polarization angle from 6 MSE channels (bottom).

C.3 Lens stressing: L2

Having established that a lens can be more subject to significant thermal stress-induced birefringence when illuminated locally, a direct mechanical stress test was performed on the L2D. A hose clamp surrounded the L2 peripheral region of the periscope and by squeezing the clamp, radial stress was generated on the L2. The amount of stress was calibrated in terms of the amount of reduction in the clamp diameter as squeezed, prior to the main invessel test, giving 3.7-mm reduction per 0.34 MPa.

Fig C-4 shows the invessel stress test result on the L2 region using this setup. In this figure, the change in the measured polarization angle from 8 MSE channels is plotted as a function of the 'deviation' which is the amount of reduction in diameter of the clamp, i.e., the amount of radial stress. There are two sets of data in each plot: one before a modification of the L2 lens mount, discussed below, (black) and the other after the modification (red). Apparent correlation between the amount of stress and the change in the polarization was detected with the original L2 lens mount and again, it is channel-dependent, with the outer channels showing larger effects. In the subsequent test with the modified L2 holder (red), the effect of the mechanical stress effectively disappears for all channels.

This is indeed one reason that the L2 holder was modified. At the time of these activities, it was believed that the thermal stress might be caused by the differential thermal expansion between the stainless-steel holder and the lens and that the Teflon cushioning was not 'soft' enough to compensate the resultant strain. Another major design change between the original L2/L3 lens mounts and the new ones: the new ones are factor ~ 100 stronger. Not only do the new lens mounts have a much thicker radial build, but also they do not have the "cut" in them that the original ones did. The motivation for this change was to ensure that thermal warping of the periscope could not transmit mechanical stresses into the lenses. After the series of heating and stressing tests on the lenses, the new Inconel L2 and L3 holder replaced the old stainless-steel counterpart and the cushioning, which had been provided by a Teflon
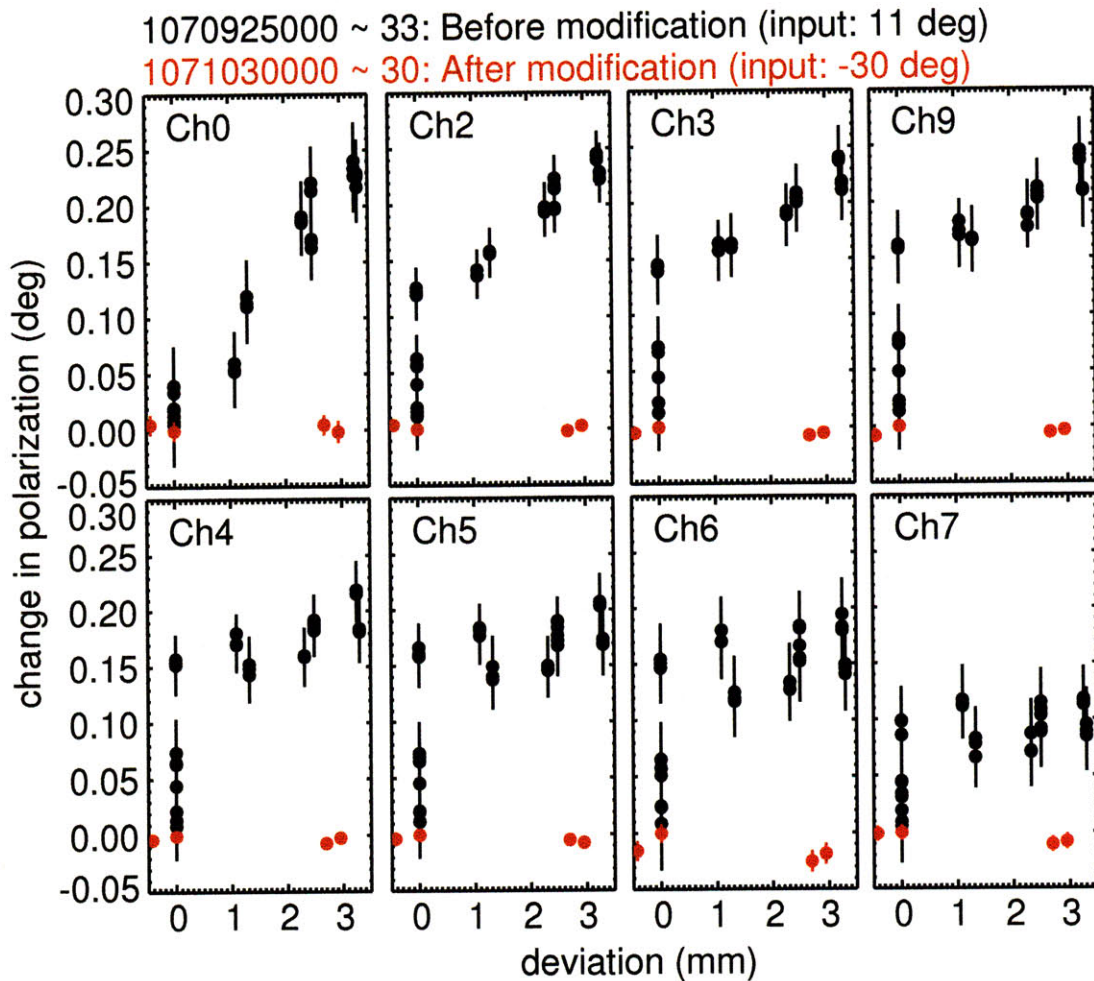
Figure C-4: Comparison of the stress effect on the L2D before and after the L2D holder modification. The change in the polarization angle has been plotted as a function of 'deviation' of the hose clamp diameter from the non-stress value, which is proportional to the amount of stress applied. The plots are arranged in the channel order.

sheet inserted between the holder and the lens, was provided by three Viton o-rings, each of them supporting the side, top, and bottom of the lens, respectively. With the new Inconel lens holders with Viton o-rings, the holder became mechanically more robust (as shown in Fig C-4) and that the Viton o-rings provided enough cushioning to compensate the differential thermal expansion. Although the new lens mounts effectively eliminated thermal stresses that might be communicated from the MSE optics periscope to the lenses, as well as greatly reducing the thermal stress due to differential thermal expansion between the lens and the lens mount, they did not meaningfully reduced the spurious changes in polarization angle during plasma operation or during bench tests This suggests that temperature gradients within the lenses themselves are responsible for the stress that ultimately generates the birefringence. What counts, therefore, is how effectively one can eliminate various heat transfer mechanisms such as conduction and radiation between the lenses and the surrounding structures. Note that the large excursion in the pitch angle observed in Figs 3-3 and 3-4 (but not those in Fig C-2, which were measured with the old lens holder) are indeed all from the configurations with these new Inconel lens holders. Another recent iteration of the holder upgrade, and many other efforts, to overcome this drift is introduced in Sec 3.2

Appendix D

Counter evidence on other possible effects on shot-to-shot drift

D.1 Rotation of external optics

One possible explanation on the shot-to-shot drift is that the external optics periscope might be rotating shot by shot. In this case, a degree rotation of the periscope would generate a degree change in the polarization angle in the MSE frame. A laser was installed onto the PEMs which are located outside the port as shown in Fig D-1. The laser spot on the target attached to the igloo was monitored via a real-time camera. Observations on the laser spot movements for more than 7 run days with more than 100 shots (1070617 ~ 1070717) indicate the motion of the PEMs during a plasma pulse is less than 1 mm. This corresponds to 0.1 degree rotation of the PEM body, or the external optics periscope, based on the geometry given in Fig D-1. This is far less than 1 degree in the MSE frame and too small to explain the shot-to-shot variation (a few degrees).

During this activity, it was found that the fused silica supporting structure in one of the PEMs had been broken and so the PEM system was shipped to and repaired by the manufacturer. This repair did not eliminate the spurious shot-to-shot drift.
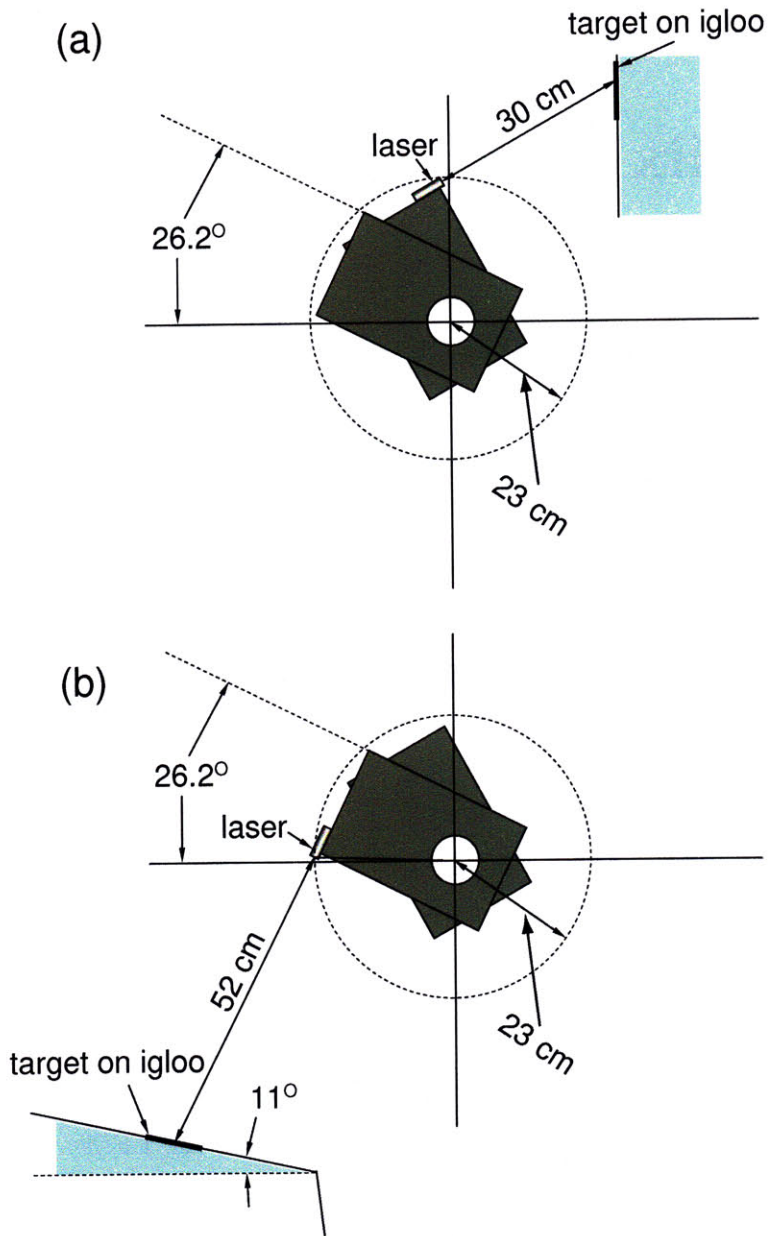
Figure D-1: Two configurations to check any possible external optics movement with a laser installed on the PEM top and the laser spot on the target which is attached on the igloo wall is monitored shot by shot in real time. Based on this geometry, the movement of the spot is converted into the rotation of the air-side optics periscope.

D.2 Rotation of internal optics

If the spatial positions viewed by MSE drifted over time due to vibration or thermal
distortion of the optics periscope, then the amount of Doppler shift in the MSE spec-
trum would change. This idea was motivated from the comparison of the 1070402 and
1070409 MSE spectra measured by a 1-m McPherson 2051 Czerny-Turner monochro-
mator during the beam-into-He tests with zero fields (with neither toroidal nor equi-
librium field coils on), which implies a shift of the MSE spectrum shown in bottom
plots in Fig D-2 both for (a) an edge channel and (b) a core channel. The absence of
such a shift in the beam spectra measured in multiple times in each shot by another
spectrometer installed in the DNB system and shown in top plots implies the beam
voltage is not the cause of the MSE spectrum shift. The observed shift in the MSE
spectrum corresponds to $1 \sim 2^o$ rotation of the MSE vertical periscope ('turret').
A simple geometry calculation involving the mirror orientations shows the horizon-
tal rotation of the MSE turret by a degree can cause about a degree change in the
polarization angle.

Over six run days (1070731, 1070801, 1070803, 1070807, 1070816, and 1070820),
several beam-into-He gas shots were taken at the end of the experimental run day
without any field to measure the Doppler shift of the MSE spectrum for a single MSE
channel (Channel 9) and any shot-to-shot change in it (more appropriately speaking in
this case, a run-to-run change). From the measured spectra, the following parameters
were inferred:

1. Wavelength of the Doppler-shifted full energy peak in the MSE spectrum: this
   was found by Gaussian-fitting the full energy portion of the spectrum. A sep-
   arate Gaussian fit was performed for the unshifted D_α line and a small offset
   between its true wavelength (656.11 nm) and the wavelength inferred from the
   fit was used to correct the wavelength of the Doppler-shifted full energy peak.
   When multiple shots were taken on a run day, the average value was used. The
   uncertainty of the final peak wavelength was chosen whichever was the largest,
   the 1-σ errors in the fit or the standard deviation of the mean. When there was
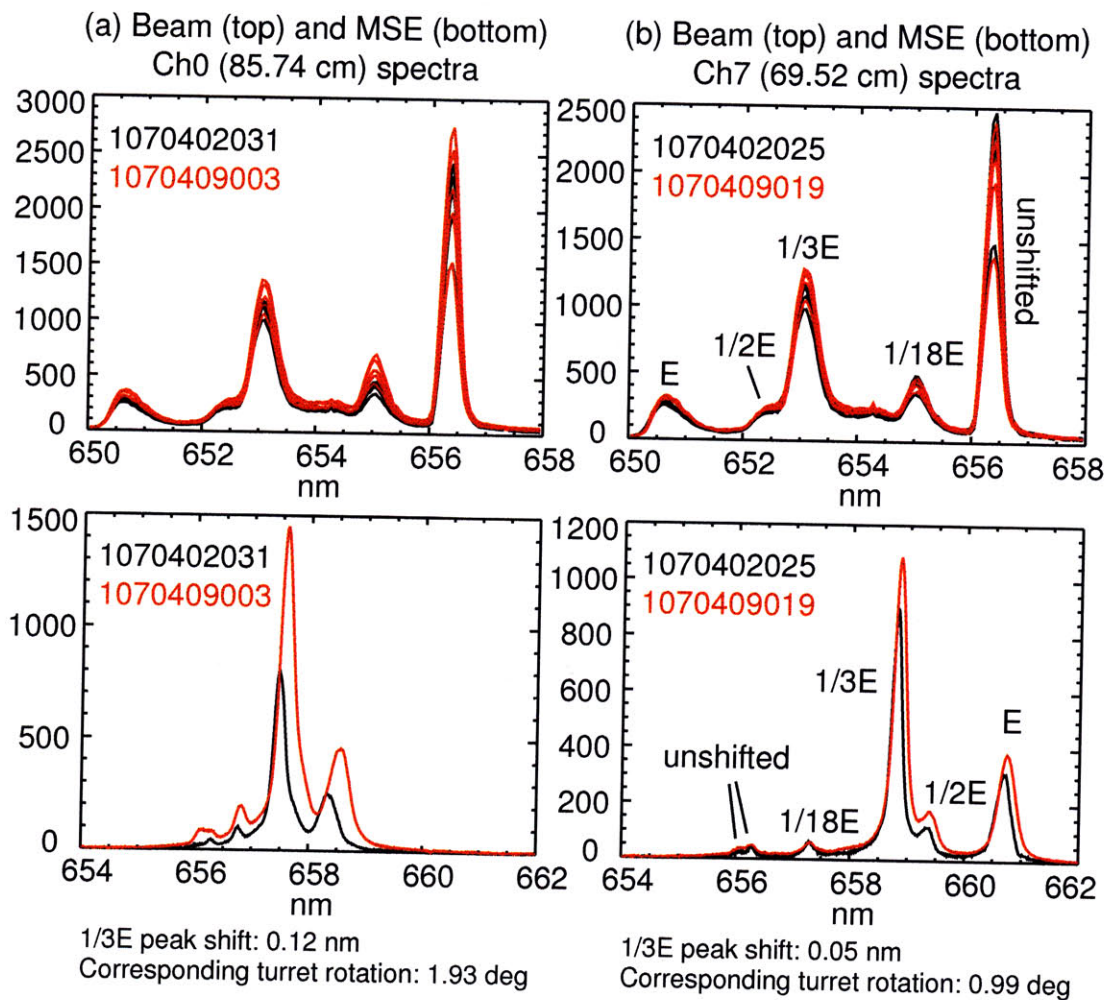
Figure D-2: Beam (top) and MSE (bottom) spectra from two beam-into-He gas runs with zero field (1070402 and 1070409) for (a) Channel 0 (edge) and (b) Channel 7 (core). Beam spectra have taken multiple times within a shot, showing multiple spectra for each shot. The shift in a third energy component peak between two spectrum runs in each channel is shown at the bottom along with the estimated MSE turret rotation that can give this much of the shift.

only a single shot on a run day, the 1-σ error was used.

2. DNB energy: although the beam energy was routinely measured at the electrical circuit level for each shot, it was suspected that the signal from this measurement was being saturated. Therefore, the beam energy was also independently obtained based on the wavelength of the Doppler-shifted full energy peak from the beam spectrum fit with a known viewing angle of the beam spectrometer. The uncertainty in the wavelength of the Doppler-shifted full energy peak in the beam spectrum was obtained in a similar way mentioned in #1. From the fact that the beam energy is a function of its Doppler shift and its viewing angle, the uncertainty of the beam energy was analytically calculated based on the uncertainties in the Doppler shift.

3. MSE viewing angle: With the known Doppler shift in the full energy peak of the MSE spectrum and beam energy, this value was calculated. Note that if the turret remains motionless, this value should remain constant at all times. Again, since the MSE viewing angle is a function of its Doppler shift and the beam energy, the uncertainty in the viewing angle was analytically calculated based on the uncertainties in the Doppler shift (from #1) and the beam energy (from #2).

These three parameters are shown in Fig D-3 from the top to the bottom as a function of 'run day index' which is defined as follows:

- 0 and 1: 1070402, 1070409 spectrum measurements, respectively. A large shift (shown in Fig D-2) in spectrum between these two runs was first observed.

- 2, 3, 4, 5, and 6: 1070731, 1070801, 1070803, 1070807, 1070816 spectrum measurements, respectively.

- 6 and 7: 1070816 and 1070820 spectrum measurements, respectively. Between these two runs, nothing was changed in the spectrometer setup but there were about 19 plasmas shots in-between. Note that during the previous measurements, the spectrometer setup such as fibers' connection was always reset between measurements.

and the run day indices after 7 (inclusive) are all from 1070820 but the following manipulations were made between shots:

- 7 and 8: Nothing was changed in the setup. No plasma shots in-between.

- 8 to 10: The fiber-spectrometer connection was disassembled and re-assembled between shots (but a reasonable effort was made to retrieve the original position).

- 10 to 13: The fiber-spectrometer connection was disassembled and re-assembled between shots, but in this case, the connection was deliberately distorted by a small amount between shots.

Returning to Fig D-3, it is apparent that the largest shift actually took place between the first two runs, which motivated the subsequent multi-run spectrum measurements. Based on the large error bar on the full energy peak on the run day index = 0 (from the top plot), it is suspected the spectrum measurement from this run was somehow erratic. The more important point can be made by comparing the change in the full energy peak (top plot) between 6 and 7 with those after 7. The fact that the change between 6 and 7 is larger than the changes in the following shots implies that this change might be due to the motion of the internal optics which might be affected by multiple plasma 'loads' since any possible systematic error can be excluded between 6 and 7 and since the variation is larger than those from possible systematic errors which were artificially made after 7. With relatively small run-to-run variations in the beam energy (middle plot), this trend is preserved in the calculated MSE viewing angle (bottom plot). Recall that if the turret does not move, the correct estimates on the MSE Doppler shift and the beam energy should give a constant viewing angle along the run day index, but it has a variation of about $0.5°$ between 6 and 7.

This exercise does show the internal optics might be moving by a small amount, but overall, this is still too weak to explain the several degrees of observed variability. In addition, the change in Doppler shift between the run day indices 6 and 7, which is regarded as 'real', is only 3 % the bandwidth of the MSE bandpass filter. This amount of change in the MSE spectrum with respect to the fixed bandpass filter is
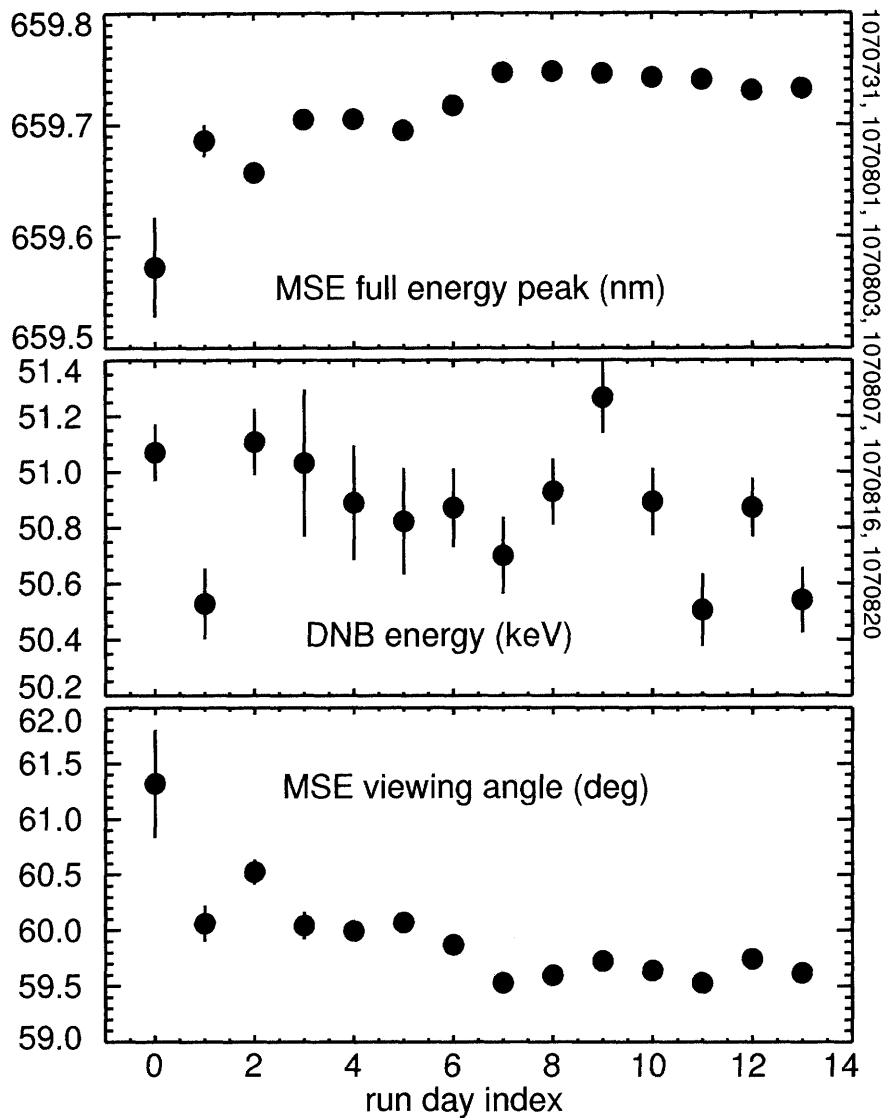
Figure D-3: Run-to-run variations of MSE full energy peak (top), DNB energy (middle), and MSE viewing angle (bottom) inferred from the zero-field beam-into-He gas spectrum measurements over 6 run days (1070731 ~ 1070820). The details on the horizontal axis ('run day index') are described in the text.

negligible in changing the measured polarization angle.

D.3   Thermal distortion of the periscope

One of the conjectures regarding the MSE shot-to-shot drift is that thermal expansion might cause the invessel periscope to warp slightly, which would change the direction of the periscope, and thereby induce spurious changes in the measured polarization angle. This possibility was taken seriously and tested by backlighting while simultaneously heating the invessel periscope.

The back-end of the fiber bundle was illuminated with a bright light source, and then the photons were allowed to proceed backwards through the MSE optics. Then the image of the fibers was observed at a target mounted along the trajectory of the DNB. The size, shape, and position of the backlit footprint were observed under normal temperature conditions (room temperature, everything at thermal equilibrium) as well as under a 'heated' condition where a heating pad was affixed to the front, plasma-facing surface of the invessel MSE periscope and the temperature went up to 80 °C.

During the heated condition, a picture of the footprint image was taken every 15 minutes over 3 hours. If the heating were to cause the optics periscope to warp, this would in turn cause the orientation of the mirrors to change, and in turn this would cause the observed image at the DNB location to move. A finite element simulation done by the MIT engineering team on the MSE invessel periscope with 2-second heat pulse of 22 W/cm^2 for an hour shows that shows that the periscope should warp about 0.2° for a 120 °C change of temperature. In this test, the temperature change $\Delta T \sim$ 77 - 27 = 50 °C and the distance between the image and the object lens is about 32 cm. Therefore, the expected distortion in the periscope would be 50 °C × 0.2° / 120 °C = 0.08° and the resultant shift of the image is expected to be tan(0.08°)× 32 cm = 0.04 cm. The inspection on the pictures for such a movement implies that to the resolution of the pictures (about 0.04 cm) there is no motion at all, i.e. the periscope warping is negligible.

Appendix E

In-situ calibration scheme

By modeling the thermal stress-induced birefringence phenomenon as an arbitrarily oriented waveplate imposing a certain amount of phase shift onto linearly polarized light, as discussed in Sec 3.1.3, a reasonable calibration concept can be developed. In this appendix, the study on the feasibility and limitations with this 'in-situ' calibration scheme is discussed.

E.1 Feasibility test

The overall design objective is to provide a calibration that is accurate to better than 0.1^o in pitch angle, which requires an accuracy of better than 0.05^o in the MSE frame of reference. Due to the simplicity of the single-waveplate model, it is necessary to evaluate whether the accuracy of this calibration scheme meets this requirement under the typical thermal environment that the system experiences. A dedicated series of bench tests was performed to check its feasibility by heating the periphery of the invessel optical periscope with the maximum slew rate of 10 ^{o}C per hour which is roughly the same as the periscope experiences in the real experiments. Four different input polarization angles (79°, 82°, 85°, and 91°) were evaluated to provide multiple combinations of one 'tested' angle and two 'reference' angles because identifying the optimum range and values of the two reference polarizations is another important purpose of the test. The input polarization angles were chosen such that they are

277

close to what is typically obtained in the real tokamak experiments (near vertical in the MSE frame).

The top plot in Fig E-1 is the time evolution of the peripheral temperature of the L2D area during the test. The positions of the thermocouples around this region
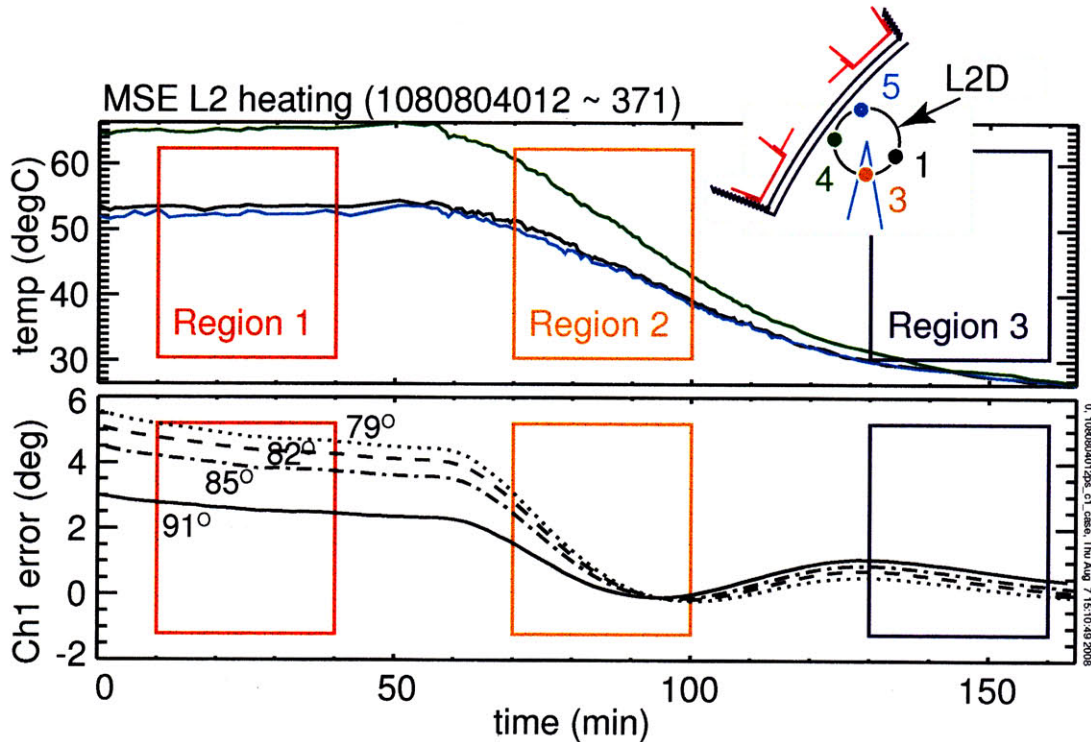
Figure E-1: Time evolution of three peripheral temperatures of the L2D area (Top) and the polarization drift from the true reference value for four different reference polarization angles ($79°$, $82°$, $85°$, and $91°$) from the MSE channel 1 (Bottom) during 1080804 L2 region heating bench test. The experimental region is divided into three regions depending on the temperature evolution condition: steady high-temperature (red), transient (orange), and steady low-temperature (blue) regions.

are illustrated in the cartoon at the top again and the positions for the temperature measurements in this test correspond to 1 (black), 4 (green), and 5 (cyan) in the TC location cartoon. The bottom plot in Fig E-1 shows the polarization drift from the true reference value for the four different reference polarization angles from the MSE channel 1 (the worst channel). The test period is divided into three regions depending on the shape of the temperature evolution for the further local analysis which is given later in this section and marked by three boxes with different colors: Region 1 is the

steady high-temperature region, Region 2 is the transient region, and Region 3 is the steady low-temperature region. According to the top plot of Fig 3-8 (a) where the temperature evolution for the 1080318 beam-into-gas run is shown, the temperature slew rates for the TC 1, 4, and 5 are about 3.3, 10, and 10.3 $°C/h$, respectively, over 5 hours (7:12AM $\sim$ 12:00AM). The pitch angle drift for the channel 1 between Shots 1 and 11 is about $3°$ (in the tokamak frame) under this thermal drift of the system and the angle drift would have been larger by more than a factor of 2 if the first shot had been taken at around 7:00AM. In the bench test shown in E-1, the temperature slew rates for the same TCs (1, 4, and 5) are about 11, 30, 11 $°C/h$, respectively, over the region 2 and the minimum drift in the measured polarization angle over this period is about $3°$, which is about $10°$ in the tokamak frame. Therefore, the thermal drift in this bench test is expected to provide the upper bound higher than what the system would experience practically.

Besides the calibration scheme using Eqn 3.10 where two reference angles are sufficient to calibrate another angle, there can be two more calibration schemes if there are four different angles at a single time point. The first possible calibration scheme is to fit two reference angles linearly and calibrate a third using this linear function and the second possible calibration scheme is to fit three reference angles with a parabolic function and use it to calibrate a fourth angle. In summary, the calibration cases that can be investigated from this 4-input thermal test are

1. Single-waveplate scheme: $_4C_2 \times 2 = 12$ cases,

2. Linear-fit scheme: $_4C_2 \times 2 = 12$ cases; and

3. Parabolic-fit scheme: $_4C_3 = 4$ cases.

Fig E-2 shows the polarization drift error corrected by (a) single-waveplate scheme, (b) linear-fit scheme, and (c) parabolic-fit scheme. These errors can be compared with those shown in the bottom plot of Fig E-1. Note that to the first order, all the calibration schemes reduce the drift by an order of magnitude. However, the calibration errors from all the schemes strongly depend both on cases and regions, making quantitative analyses rather complicated. To be more quantitative and to make more
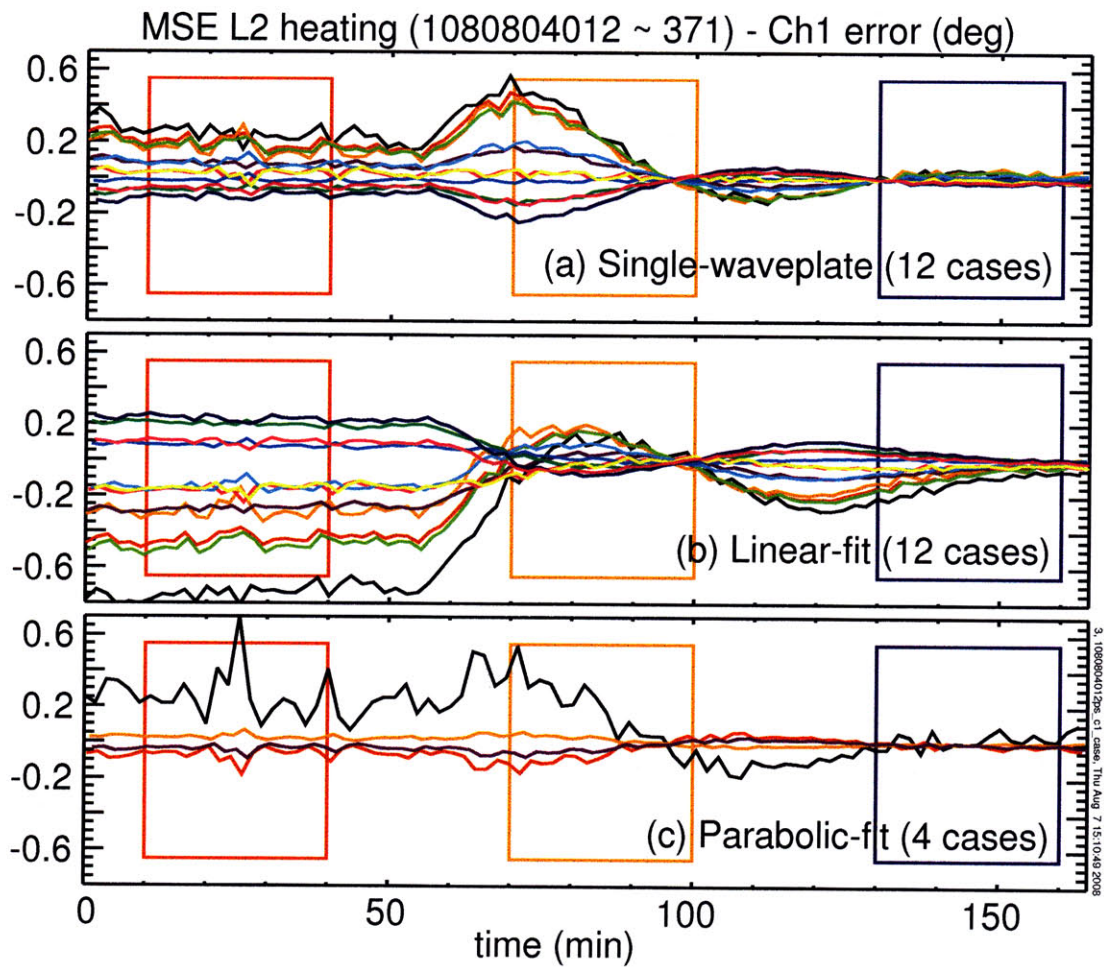
Figure E-2: Time evolution of the polarization drift from the true reference value for the MSE channel 1, originally shown in the bottom plot of Fig E-1, corrected by (a) single-waveplate scheme, (b) linear-fit scheme, and (c) parabolic-fit scheme.

'case-resolved' arguments, the following three parameters have been established for the single-waveplate and linear-fit calibration schemes, which characterize a case in different ways:

- Maximum angle difference: maximum angle difference among all three participating angles (two references + one tested angle). This parameter basically represents the total range of the angles.

- Total reference range: maximum angle difference between two reference angles; and

- Minimum reference difference: minimum distance between the tested angle and one of the references.

and the following two parameters for the parabolic-fit calibration scheme:

- Total reference range: maximum angle difference between three reference angles; and

- Maximum reference difference: maximum distance between the tested angle and one of the references.

The average calibration error in each region for each case can be found from Fig E-2 for each calibration scheme and this local average error can be plotted as a function of each case characteristic parameter. The following three mini sections summarize the correlation of the calibration error with cases for each calibration scheme.

E.1.1   Single-waveplate scheme

Fig E-3 shows the local calibration error as a function of (a) maximum angle difference, (b) total reference range, and (c) minimum reference distance. The errors taken from a different region are marked in a different color and with a different symbol. When a tested angle is between the references, the errors are marked with filled symbols and otherwise, with empty ones. Also shown in the figure is the acceptable range of the polarization angle in the MSE frame ($\pm 0.05^{\circ}$). The first thing to note is that all the errors from Region 3 (steady low-temperature region) are within the acceptable error
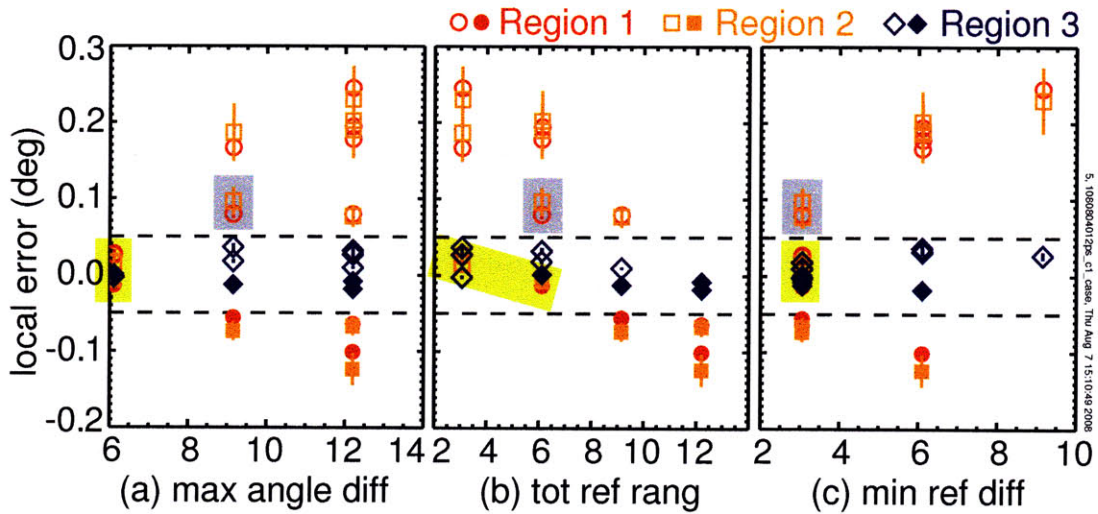
Figure E-3: Correlations between the local calibration error from each region and the three case parameters, (a) maximum angle difference, (b) total reference range, and (c) minimum reference distance all in degree using the single-waveplate scheme. Different colors and symbols denote the errors from different regions shown in Fig E-1. Filled symbols indicate the tested angle is between two references and empty symbols indicate otherwise. The acceptable range of the error ($\pm0.05°$) is marked as two horizontal dashed lines.

range independent of the case characteristics. Unfortunately, however, this region is not a region of interest since the real experimental situations hardly come across the thermal environment like Region 3. More relevant are Region 1, a uniform high-temperature situation, and Region 2, a situation with a high temperature slew rate. A careful observation on the errors from these two regions reveals that acceptable errors can be obtainable when the total range is small ($\lesssim 8°$) with a tested angle reasonably near the reference angles ($\lesssim 4°$). The yellow-boxed regions on Fig E-3 denote this observation and the blue-boxed regions illustrate that satisfying only one condition (either small total range or proximity to the reference) is not enough to achieve acceptable errors. It should also be noted that a tested angle can reside outside the reference range, which has a very important implication in implementing the single-waveplate calibration technique to the instrument, combined with the first two criteria.
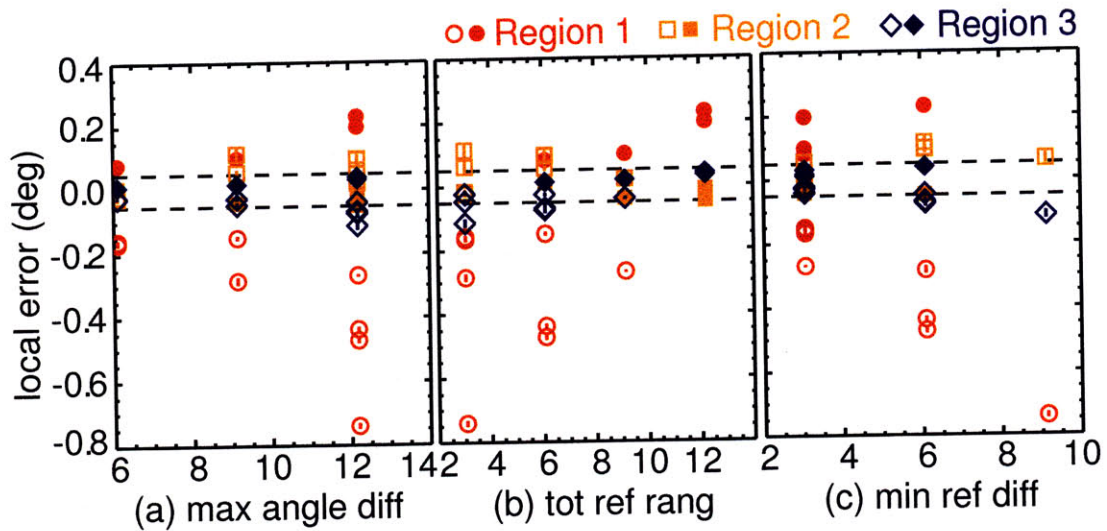
Figure E-4: Correlations between the local calibration error from each region and the three case parameters, (a) maximum angle difference, (b) total reference range, and (c) minimum reference distance all in degree using the linear-fit scheme. Different colors and symbols denote the errors from different regions shown in Fig E-1. Filled symbols indicate the tested angle is between two references and empty symbols indicate otherwise. The acceptable range of the error (±0.05°) is marked as two horizontal dashed lines.

E.1.2 Linear-fit scheme

Fig E-4 shows the local calibration error as a function of (a) maximum angle difference, (b) total reference range, and (c) minimum reference distance. Unlike the correlation shown in the single-waveplate scheme (Fig E-3), there is no clear knob to turn to reduce errors in the linear-fit model except there is one clear trend that whenever the tested angle is outside the two reference angles (empty symbols in the figure), the errors become large. This means when the tested angle is extrapolated, the two-point linear scheme works rather poorly regardless the region. For Region 1, even the linear interpolation does not produce acceptable errors.

E.1.3 Parabolic-fit scheme

Finally, Fig E-5 shows the local calibration error as a function of (a) total reference range and (b) maximum reference distance. Overall, the performance is similar to
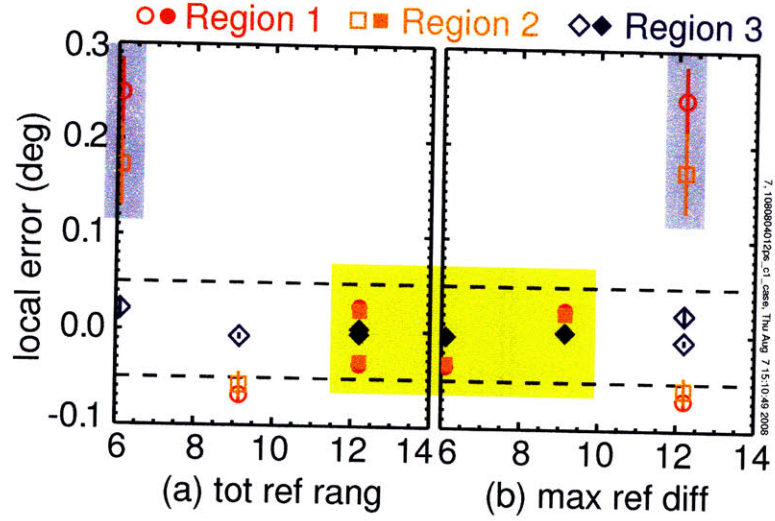
Figure E-5: Correlations between the local calibration error from each region and the two case parameters, (a) total reference range and (b) maximum reference distance all in degree using the parabolic-fit scheme. Different colors and symbols denote the errors from different regions shown in Fig E-1. Filled symbols indicate the tested angle is between any two of the three references and empty symbols indicate otherwise. The acceptable range of the error ($\pm 0.05°$) is marked as two horizontal dashed lines.

that of the single-waveplate technique. As in the single-waveplate scheme, the errors in Region 3 are within the acceptable error range independent of the case characteristics. However, the noticeable difference is that the errors are acceptable when interpolated (yellow-boxed regions) and become large when extrapolated (blue-boxed regions) regardless the size of the total reference range and the proximity of the tested angle to the references. This is a similar nature to that of the linear-fit technique although in this case, this trend is also true for the errors from Region 1 whereas the errors in this Region is outside of the acceptable range even when the tested angle is interpolated in the linear-fit method.

E.1.4   Summary on the in-situ calibration schemes

The single-waveplate model and the parabolic-fit model can produce acceptable calibration errors, under the thermal environment that the MSE diagnostic typically experiences, when the reference angles and the tested angles are carefully chosen. For

these two calibration models, the correlation between the error and the case charac-
teristics is clear enough to define 'knobs' to turn to optimize the angle configurations.
For the single-waveplate scheme,

1. Small total range + proximity to the reference; and

2. Having a tested angle outside the reference range is allowed.

and for the parabolic-fit scheme,

1. Having a tested angle within the reference range (interpolation) is essential; and

2. Total range and proximity to the reference do not affect the calibration perfor-
   mance.

Practically, the single-waveplate model is more preferable because this requires
only two reference polarization sources inside the torus while the parabolic-fit scheme
requires three. One of the possible configurations that can produce acceptable errors
is illustrated in Fig E-6 (a). Here, the two references are separated by only 4° from one
another. However, the total range of angles that can be calibrated is 8° because each
reference allows the tested angle to stay outside it by about 2°. This is encouraging
because the typical range of the pitch angles in the MSE frame during many plasma
experiments is about this much at most (at some outer channels), as shown in Fig E-6
(b) where the EFIT-calculated pitch angle data at the major radii where the MSE
channels are have been converted into the polarization angle in the MSE frame and
plotted. The sample shots include those having toroidal magnetic field as high as 7
T.

E.2 Limitations

Despite the theoretical feasibility for the in-situ calibration method based on the
single-waveplate model, there are some practical challenges from an engineering point
of view. As mentioned in Sec E.1, the overall design objective is to provide a cali-
bration that is accurate to better than 0.05^o in the MSE frame of reference. If the
calibration (reference) polarized light source were to wobble about its axis by some

(a)

Reference 1

2

4   Reference 2

2

Total range of angles that
can be calibrated: 8

(b)

Typical polarization angle
in mse frame (08 campagin)

1071212021
1080115012
1080201010
1080313006
1080320010
1080415010
1080516010

(deg)

95

90

85

80

major radius (m)

0.65   0.70   0.75   0.80   0.85   0.90
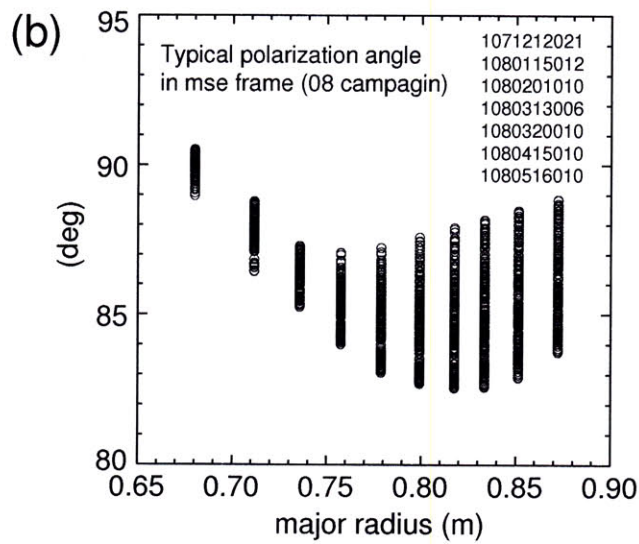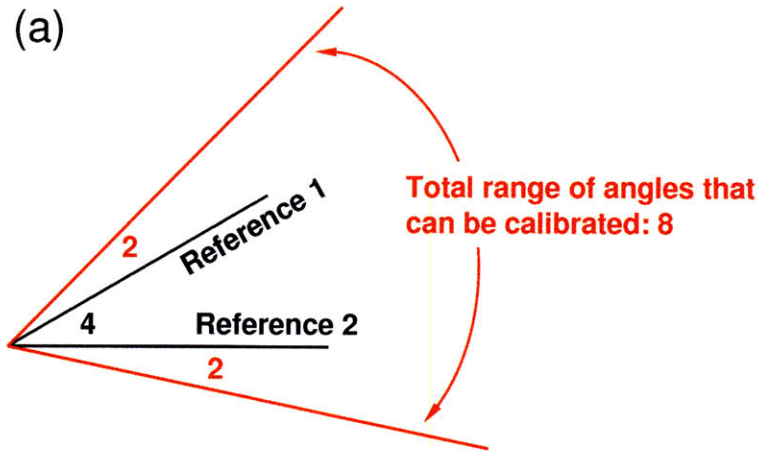
Figure E-6: (a) An example configuration for the in-situ single-waveplate calibration scheme that is capable of calibrating an 8°-range of angles. (b) EFIT-calculated pitch angle converted into the polarization angle in the MSE frame as a function of MSE major radius. The shots are from the FY08 campaign and include some high-field ($\sim$ 7 T) shots.

angle, the polarization angle of is light changes by the same amount. This places a very demanding requirement on the mechanical design of the translatable light source: it must retain its orientation, over a period of months, to approximately 0.05^o. The following two mini sections introduce the mechanisms to overcome this difficulty and discuss their limitations.

E.2.1 Retractable mirror with fixed polarization source

This difficult requirement may be avoided in an alternative scheme that uses a fixed (nonmoving) polarized light source which is mounted on the MSE optics periscope. The polarized light source then is reflected by a mirror that is translated into the MSE field of view before or after each shot. This scheme still requires that the polarized light source retain its orientation to better than 0.05^o over a period of months, but this should not be difficult to achieve because the light source is firmly attached to the rugged MSE optics periscope. Ray tracing calculations, shown in Fig E-7 have identified an optimized mirror shape that can provide the full field of view from all the MSE channels with full angles by having the horizontally extended polarized light source on the both sides of the lens.

One difficulty in this concept is the effect on the polarization angle from reflection off the mirror at non-normal incidence, since there will be unavoidable errors in orienting the mirror. Fig E-8 illustrates ray tracing calculations that examine this effect for ideal dielectric mirrors, showing the change in polarization angle upon reflection from the mirror as a function of mirror vertical tilt for three different horizontal tilting cases of the mirror. The rate of change in the polarization angle before and after the reflection is about $2 \sim 5^o$ per a degree of mirror vertical tilting depending on the mirror horizontal tilting. It is also observed that the rate of change is independent of the incident polarization angle by comparing Fig E-8 (a) and (b). Further calculations show that the rate decreases as the angle of incidence increases. However, as shown in Fig E-7, there are bound to be the rays whose angles of incidence more than 30° in some extreme (either outermost or innermost) channels.

Analytic formulas based on Ref [72] have been derived for the case where there is
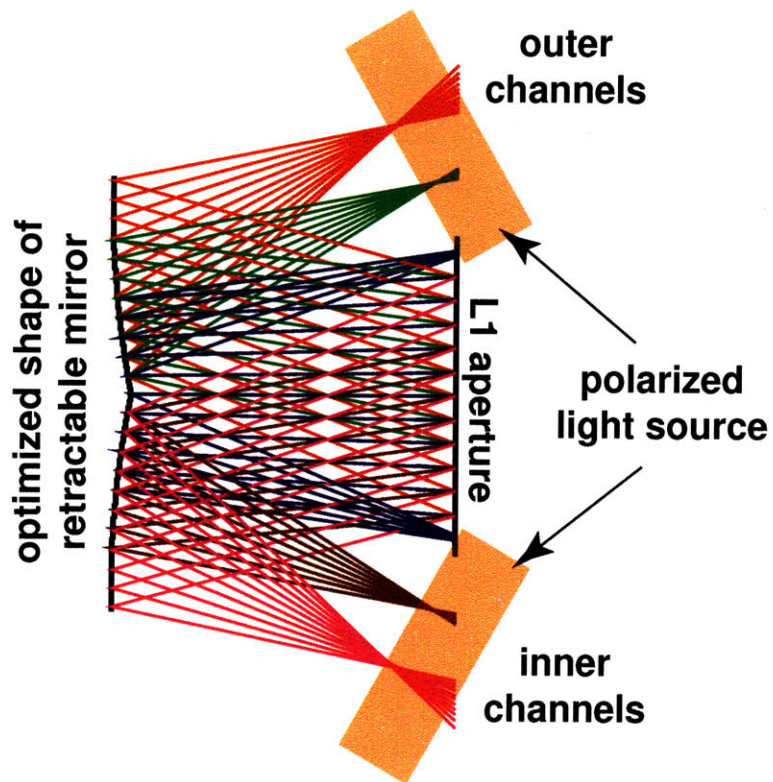
Figure E-7: Ray tracing calculations to optimize the retractable mirror shape to provide the full MSE field of view at all angles. The rays with different colors simulate those from the real light source at the different locations along the DNB trajectory.

polarization change before and after the reflection (after - before; deg)
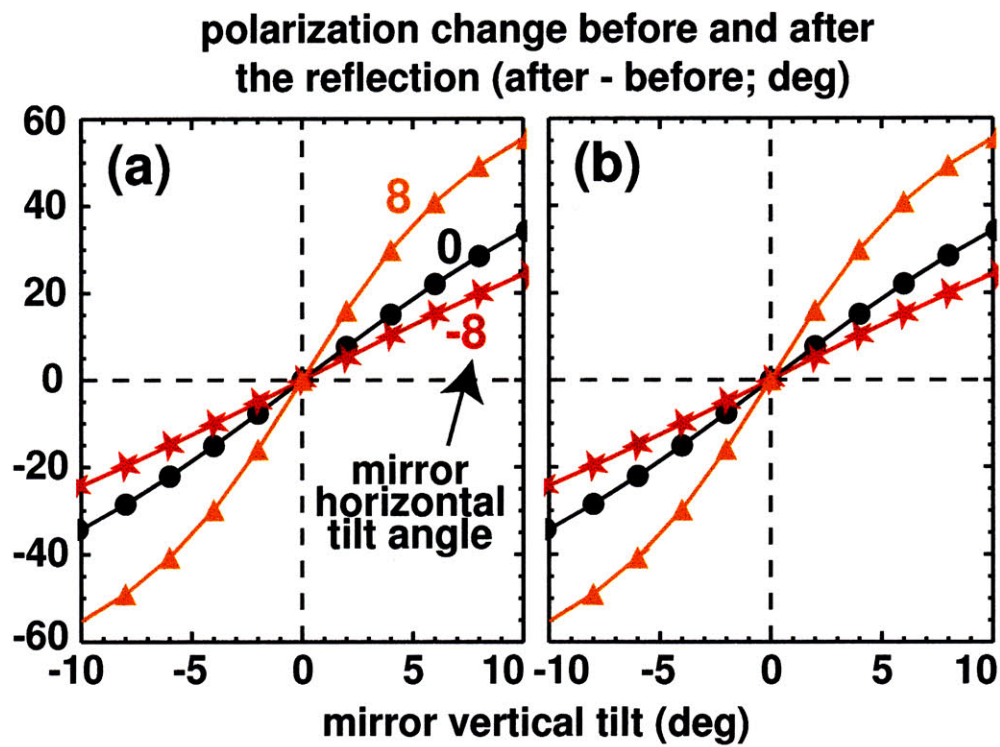
Figure E-8: Ray tracing calculation results for mirror tilting effect on the reflected polarization, which shows the difference between the incident and the reflected polarizations with the polarization of the incident light of (a) $80°$ and (b) $105°$ as a function of mirror vertical tilting angle for 3 different mirror horizontal tilting angles. The angle of incidence is $15°$ in both cases.

only vertical tilting of a mirror:

$$\tan \Delta\phi_p = \frac{\sin\theta \sin(2\epsilon) \cos^2\epsilon}{\tan^2\theta - \cos(2\epsilon) \sin^2\epsilon} \qquad (E.1)$$

for ideal dielectric mirrors and

$$\Delta\phi_p = \pi - 2\phi_p + \tan^{-1}\left(\frac{\sin\theta \tan\epsilon[1 + \sin^2\theta - \cos^2\theta \cos(2\epsilon)]}{\tan^2\epsilon[\sin^2\theta - \cos^2\theta \cos(2\epsilon)] - \sin^2\theta}\right), \qquad (E.2)$$

for ideal metallic mirrors, where $\Delta\phi_p$ is the change in the polarization angle before and after the reflection, ϕ_p is the incident polarization, θ is the angle of incidence, and ϵ is the vertical tilting angle of the mirror. The analytic expression for ideal dielectric mirrors yields the same result as the rays tracing calculations shown in E-8. In addition, the analytic calculations show that the rate of change in the polarization is somewhat less for an ideal metallic mirror than for the dielectric mirror and that the dependence on the angle of incidence is reversed: the change in polarization angle vanishes for small angles of incidence on metal mirrors. However, the maximum angle of incidence that gives allowable tolerance in polarization change is about 14° for a metal mirror, which is far smaller than the practical maximum value ($\gtrsim 30^o$). Overall, this variation of polarization angle on reflection from a mirror significantly can complicate the optical design of the in-site calibration system using a fixed polarized light source and a translated mirror.

E.2.2   Fixed annular polarization light source around L1

Another effort to overcome the stringent mechanical tolerance in the calibrator structure is to have a fixed and direct polarization source. In order not to obstruct the real view from the DNB trajectory to the object lens (L1), the polarized light source can be installed only across a small portion of the peripheral area of L1, forming an annular polarized light source. The disadvantage of this approach is that the amount of real signals from the plasma is reduced by as much as blocked by this annulus. The strong advantage, however, is that there are no moving parts.

A question that arises with this configuration is whether rays from the annular light source correctly mimic the real rays from the beam, and thereby experience the same amount of thermal stress-induced phase shift as the real rays when they pass through the lens. The straightforward way to check this concern is to measure and compare the thermal drifts in the polarization angle with and without a mask that provides the annular aperture when installed on L1. This test has been performed for both local-focusing lenses (L2D) and diffusing lenses (L3D). Fig E-9 plots the difference in the thermal drift in the polarization angle measured with and without the annular-aperture mask on L1 as a function of MSE radius when heating is applied on (a) the L2D and (b) the L3D for 3 different fixed input polarization angles. Both heating tests have a slew rate of about 6 °C/h and the data shown were taken 40 minutes after the test started. As can be seen from the figure, there is a noticeable difference between heating the local focusing lens (L2) and heating the diffusing lens (L3). The difference in the polarization drift between the annular and the full apertures is within the allowable uncertainties when the heating is applied to the local-focusing lenses (L2D) as shown in Fig E-9 (a) but the differences become larger than the acceptable accuracy when the heating is applied to the filling, or diffusing lenses (L3D) shown in Fig E-9 (b). This result seems counter-intuitive but can be reasonable from the following argument. The rays from each channel are concentrated at a small portion ($\sim$ 1 cm) of the L2 surface and whether the rays are from the periphery from the L1 or from the full L1 does not make a big difference in this case because the effect is already local. On the other hand, the rays from the periphery from the L1 are also expected to reach the peripheral region of the L3 where the effect of the thermal stress-induced birefringence is somewhat different from the average value over the L3 surface which the rays passing through the full L1 surface would experience.

It is weird in a sense that the averaging effect which has saved the L3 from the thermal stress-induced birefringence in most cases is actually the culprit which makes the usage of the annular reference polarization source impractical. The same weirdness exists in that the local effect of the birefringence at L2D which is the very cause of the shot-to-shot drift in the diagnostic might have made possible the in-situ
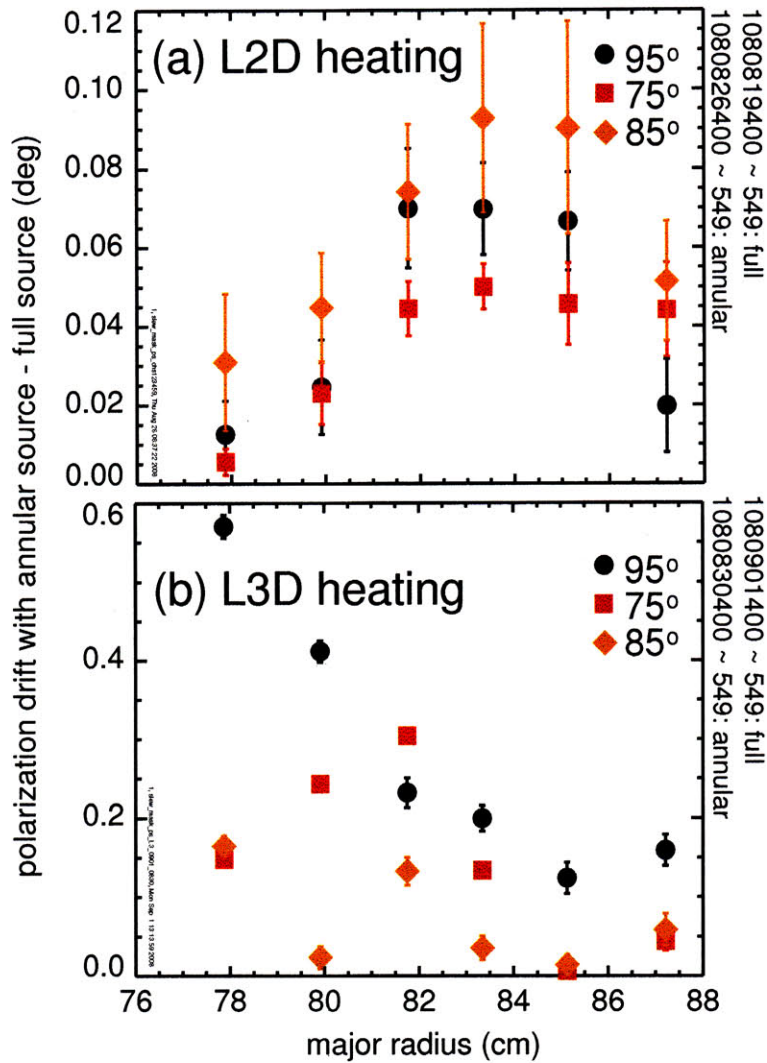
Figure E-9: The difference in the polarization drift between annular and full apertures on L1 as a function of MSE major radii from (a) L2D heating and (b) L3D heating bench tests. Both heating tests have 6 °C/h slew rate.

calibration method using the annular light source.

Appendix F

Tests to characterize thermal responses

F.1   Allowable temperature fluctuation on the periscope

The L2 lens doublet (L2D) is more vulnerable to thermal stress-induced birefringence because light from individual MSE channels is nearly in focus there, so a thermal sensitivity test for this doublet was performed. Two fixed input polarizations ($85°$ and $85°$ - $22.5° = 62.5°$) were examined while an artificial thermal perturbation was applied to the periphery of the L2D. Fig F-1 shows the time history of the temperature around the L2D (top) and the change in polarization (bottom) for the channel 1. The repetition rate for the heating cycles in this bench test was deliberately chosen to be 15 minutes to match the typical C-Mod shot cycle. However, it should be noted that this setup is not a perfect mockup of the in-vessel configuration, because there is heat convection in the bench test but none during routine plasma operation. Three thermocouples have been used to measure the temperatures and their average value is marked as a boldface dashed line on the plot. As illustrated in the plots, the evolution of the change in polarization angle is correlated with the temperature evolution, with a time offset that corresponds to a characteristic time constant for the thermal stress-induced birefringence in this configuration.

Based on this data, we would like to develop a semi-quantitative correlation be-
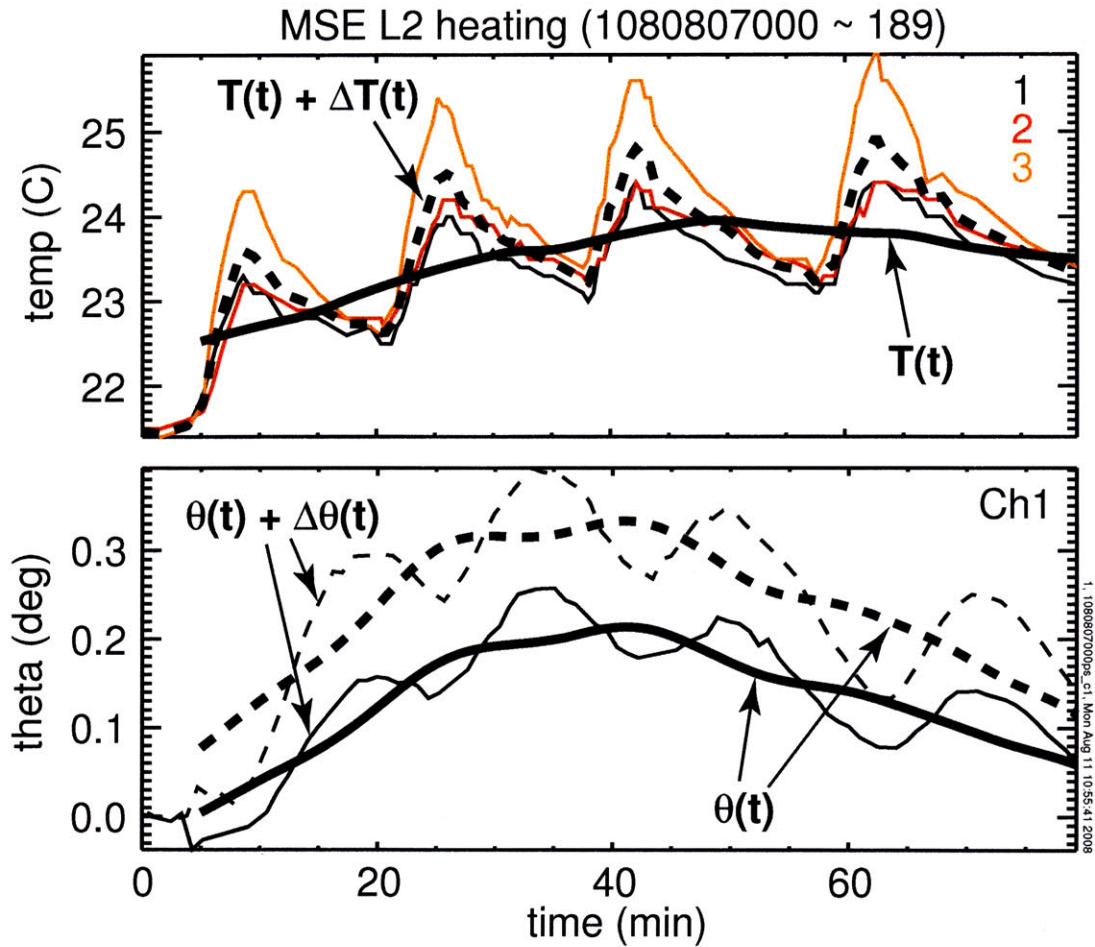
Figure F-1: Thermal fluctuation test results: The time evolutions of the temperatures around the L2D from three thermocouples with their average marked in a boldface dashed line (Top) and the polarization change for the input polarizations of 85° (solid) and 62.5^o (dashed). The base evolution curves, $T(t)$ and $\theta(t)$, are marked as a boldface solid line for the temperature (Top) and solid and dashed boldface lines for the two input polarization angles. The raw data are expressed as the sum of these base evolutions and the fluctuation terms, $\Delta T(t)$ and $\Delta\theta(t)$.

tween temperature change and the spurious change in polarization angle. A small complication is that, as shown in Fig F-1, the temperature time history has a long-term secular variation in addition to the repeated heating/cooling cycles, and the change in polarization angle correspondingly varies in time on both short and long time scales. We therefore time-smooth the temperature time history and the time history of the change in polarization angle to generate 'base' evolutions $T(t)$ and $\theta(t + \alpha)$, which are indicated as bold lines in Fig F-1. The residual difference between the actual temperature and the time-smoothed temperature, $\Delta T(t)$, and the corresponding difference between the actual change in polarization angle and its time-smoothed version, $\theta(t + \alpha)$ represent the effect of the short-term heating cycles. Here, α is an empirically-determined time delay between the temperature (measured at the surface of the lens holder of L2D) and the change in polarization angle.

Correlations between $\Delta T(t)$ and $\Delta\theta(t + \alpha)$ have been examined with several different α's and the result is shown in Fig F-2 where $\alpha = 8$ minute has been used. Both
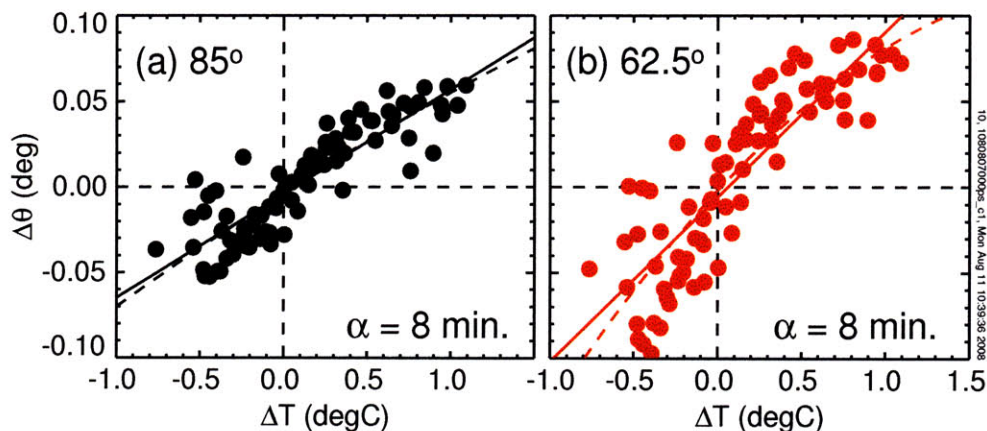
Figure F-2: The correlation between $\Delta T(t)$ and $\Delta\theta(t + \alpha)$ in the thermal fluctuation test shown in Fig F-1 for the input polarizations of (a) 85° and (b) 62.5^o with the time offset in the polarization change $\alpha = 8$ minutes. Also shown in the figure are linear (solid) and quadratic (dashed) fits for the relations.

the linear and quadratic fits have been applied and the linear coefficients from the both fits are comparable and give 0.06 ± 0.004 ^{o}/Celsius and 0.09 ± 0.008 ^{o}/Celsius for the input polarization of 85° and 62.5^o, respectively, and these quantities can be

regarded as a thermal error multiplication factor, τ. Then, the change in the polarization angle due to the temperature fluctuation on the periscope can roughly be related as $\Delta\theta \approx \tau\Delta T \approx 0.06\Delta T$. This relation implies that one needs stringent temperature control of $\Delta T \lesssim 0.83$ ^{o}C to achieve the polarization error $\Delta\theta \lesssim 0.05^{o}$ when the input polarization angle is 85° and $\Delta T \lesssim 0.50$ ^{o}C for the input polarization angle of 62.5^{o}.

Finding the optimized α (the offset time, or the time delay, in the polarization change with respect to the temperature change) might be subjective unless the subsequent α-scan showed somewhat consistent behavior. Fig F-3 (a) plots the thermal error multiplication factor, τ, as a function of the offset time, α from both linear (circle) and quadratic (star) fits of the $\Delta\theta$-ΔT relation for two input polarization angles (85° and 62.5^{O}) given in Fig F-1. With the offset time around $8 \sim 9$ minutes, the linear coefficients (i.e. τ) from both linear and quadratic fits become almost identical for both input polarization angles, implying that the linear scaling between the temperature change and the polarization change is most dominant with this time offset. The quality of the fit is also a function of α. This can be noticed by the change in size of the error bar. The goodness-of-fit (χ^2) indeed smoothly changes with α and becomes minimized at around 8 minutes for both fits, indicating the best fit is achieved with this time offset.

Note that Fig F-3 (a) has the initial temperature $T(0) = 22$ ^{o}C as can be observed in Fig F-1. Another set of data has been obtained with a different initial temperature, $T(0) = 35$ ^{o}C. Similar analysis has been performed for this data set and is plotted in Fig F-3 (b). Again, with the time offset, α, at around 9 minutes, the two linear coefficients coincide with each other. It is also noted, however, that the thermal error multiplication factors themselves are slightly larger than those from the test with $T(0) = 22$ ^{o}C. Since the typical input angle in the MSE frame is near vertical, and the temperature of the MSE invessel periscope is around 30 ^{o}C when there is no large effect from the plasma radiation, it is appropriate to take the value of τ for the input polarization angle 85° with $T(0) = 35$ ^{o}C from Fig F-3 (b) as a nominal thermal error multiplication factor, that is, $\tau \approx 0.08^{o}/^{o}C$ ($\pm 0.0075^{o}/^{o}C$). This means the change in the polarization angle can be scaled as $\Delta\theta \approx 0.08\Delta T$, requiring $\Delta T \lesssim 0.63$ ^{o}C for
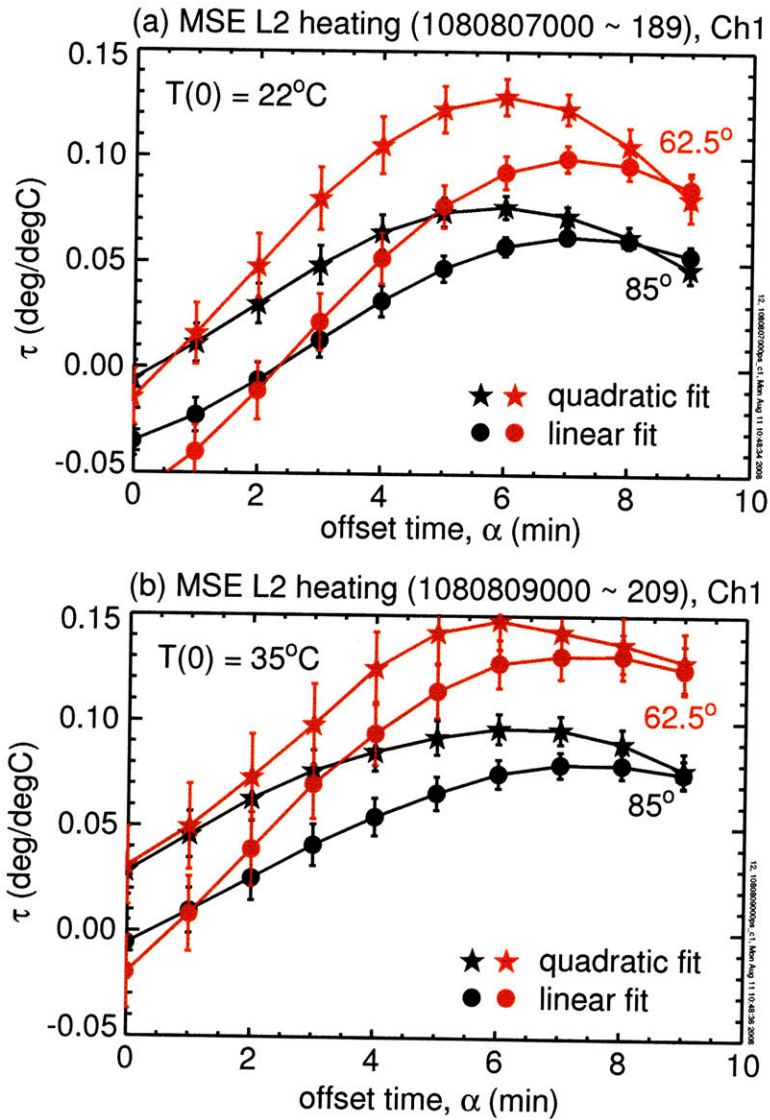
Figure F-3: Thermal error multiplication factor, τ, both from linear and quadratic fits as a function of offset time, α, for two different input polarization angles from the data set with the initial temperature of (a) 22 °C (shown in Fig F-1) and (b) 35 °C.

$\Delta\theta \lesssim 0.05^{\circ}$. One can regard τ at $\alpha = 9$ minutes for the input polarization angle 62.5° with $T(0) = 35$ °C as an upper bound, giving the scaling of $\Delta\theta \approx 0.13\Delta T$. In this case, the maximum allowable temperature fluctuation becomes $\Delta T \approx 0.38$ °C.

F.2 Allowable temperature slew rate

The outputs polarization angles with three fixed input values (95°, 75°, and 85°) was measured while the periphery of the L2D region in the periscope was heated on the bench with four different temperature slew rates (0.8, 2.1, 3.5, and 5.5 °C/hr). Fig F-4 (a) plots the maximum drift (output angle - input angle) in the polarization angle, which usually took place about 40 minutes after the heating started, as a function of temperature slew rate from MSE channel 1. Fig F-4 (b) is simply the absolute value of the maximum drift. To the first order, the drift is quadratically increasing with the slew rate and is also a strong function of input polarization angle. Also shown in the figure is a parabolic fit of the data with a constraint of zero change at zero slew rate for each input polarization angle. The acceptable slew rate that produces the drift of 0.05° also depends on the input polarization directions and ranges from 0.5 to 2 °C/hour as denoted in the yellow box on the plot. A finite element simulation using COMSOL on this bench heating scales the temperature variation across the lens as $\Delta T \approx 0.26\times$ (slew rate in °C/hour). This implies, for example, that the maximum allowable temperature variation across the lens is only $0.26 \times 1.5 = 0.39$ °C for the input angle of 85°. However, the COMSOL simulation only includes conduction and radiation but not convection which exists in the bench test, so this comparison should be regarded only as approximate.

The thermal conduction resistance of the cylindrical shell [73],

$$R_k = \frac{\ln(R_2/R_1)}{2\pi L k} \ [^{\circ}K/W], \tag{F.1}$$

where R_1 and R_2 are inner and outer diameter of the shell, L is the length, and k is the thermal conductivity, can be multiplied by the specific heat capacity, C_p, the
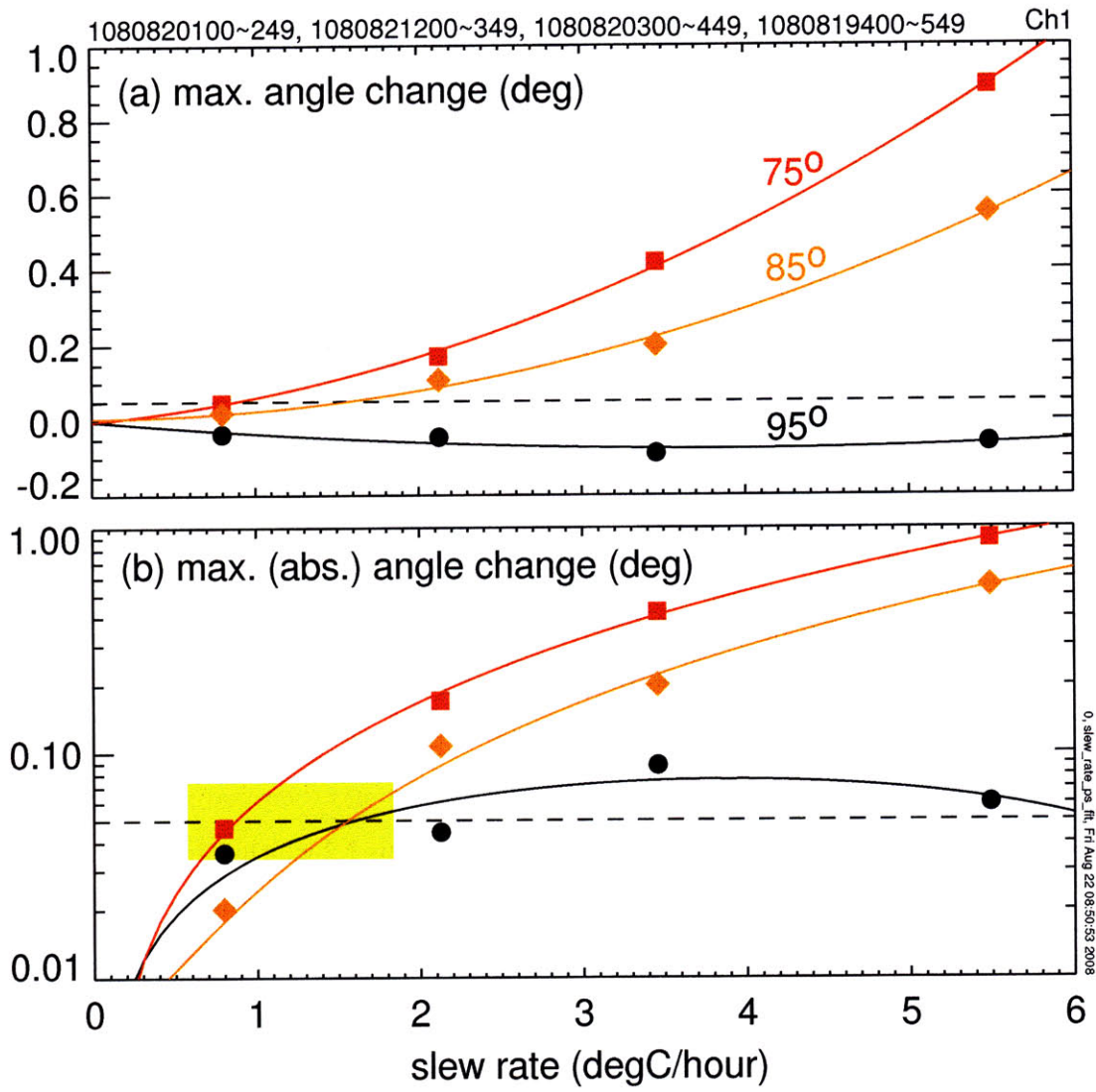
Figure F-4: (a) Maximum drift in the polarization angle and (b) its absolute value as a function of temperature slew rate for three different input polarization directions from MSE channel 1. A measurement with each slew rate takes 50 shots and the shot numbers are written at the top in the order of increasing slew rate. The lines are the quadratic fit of the data. The 0.05° in the drift is marked as a horizontal dashed line.

Layer	τ_k sec	Material	ρ g/cm^3	C_p J/g$^\circ$K	k W/cm$^\circ$K	d cm
Periscope	0.64	Stainless Steel 304	8.0	0.50	0.16	0.16
Lens holder	32	Inconel 625	8.2	0.43	0.11	1.0
O-ring	35	Viton	1.2	2.0	0.002	0.17
Lens L2	$23 \sim 46$ min	SFL6	3.4	0.6	0.01	6.5*

Table F.1: Characteristic conductive thermal time constants for the L2 lens surrounding layers and the L2 lens itself. The dimension d for the lens is the radius of the lens.

density, ρ, and the volume of the shell, $V = \pi L(R_2^2 - R_1^2)$, to yield the characteristic conductive thermal time constant

$$\tau_k = \frac{\ln(R_2/R_1)}{2k} C_p \rho (R_2^2 - R_1^2) \approx \frac{d^2 C_p \rho}{k}, \qquad (F.2)$$

where $R_2 = R_1 + d$ with $d/R_1 \ll 1$ is used for the final approximated form. The L2D is supported by an Inconel lens holder with a Viton O-ring in-between and the holder is inside the 1.6-mm-thick stainless steel periscope. Table F.1 summarizes the conductive time constant estimated by Eqn F.2 for these layers and their material properties along with the conductive characteristic time for the lens L2 which is estimated later in this paragraph. The characteristic conductive thermal time constant for the L2 lens, which is a plano-convex lens with the radius of curvature of 22.5 cm, is not straightforward to estimate because the thickness varies along the radial direction. The conductive time constant for a disk of constant thickness is $\tau_k^{disk} = 0.173 a^2/\alpha$ where a is the radius of the disk and α is the thermal diffusivity and defined as $\alpha = k/(\rho C_p)$ [74]. For the L2 lens (SFL6 glass), $k = 0.01$ W/cm$^\circ$K, $\rho = 3.4$ g/cm^3, $C_p = 0.6$ J/g$^\circ$K, and $a = 6.5$ cm, yielding $\tau_k^{disk} \approx 1380$ sec $= 23$ min. Designating the thickness at a particular radius as $h(r)$, the heat flow equation becomes

$$\frac{1}{\alpha}\frac{\partial T}{\partial t} = \frac{1}{hr}\frac{\partial}{\partial r}\left(hr\frac{\partial T}{\partial r}\right) = T'' + \frac{1}{r}\left(1 + \frac{h'}{h}\right)T'. \qquad (F.3)$$

For a plano-convex lens with a radius of curvature r_c and the central thickness h_o, h

is explicitly, $h(r) = \sqrt{r_c^2 - r^2} + (h_o - r_c)$ and therefore,

$$\frac{h'}{h} = \frac{-r}{r_c^2 - r^2 + (h_o - r_c)\sqrt{r_c^2 - r^2}}. \tag{F.4}$$

With $r_c = 22.5$ cm and $h_o = 1.3$ cm, this is a monotonically decreasing function of r from 0 to 6.25 cm, ranging 0 to -0.7. Therefore, the effect of having the additional term h'/h is to decrease the temperature time derivative somewhat, which will increase the characteristic thermal conductive time constant. A very simple scaling from Eqn F.3 gives

$$\tau \sim \frac{a^2}{\alpha\left(2 + \frac{h'}{h}\right)} \tag{F.5}$$

and this implies that the characteristic time would be increased by a factor of $2/(2 + h'/h)$, which is a factor of 2 at its maximum, from its flat disk version.

By comparing the time constants between the lens and its surrounding structures, it can be argued that the dominant temperature variability would occur across the lens throughout the heating test although the heat was applied to the outermost layer (i.e. the outer surface of the periscope). The time constant for the heating experiment is one hour which is 1.3 $\sim$ 2.6 times larger than the time constant for heat to be conducted into the center of the lens (23 $\sim$ 46 minutes). Only if the lens's time constant is much greater than an hour would one expect that the temperature at its center would remain unperturbed after an hour of heating, i.e. we could get $\Delta T = 10$ °C after one hour of heating at 10 °C/hour only if $\tau_k^{lens} \gg 3600$ seconds. On this basis, it seems quite reasonable that the maximum ΔT is only 26% of the temperature slew rate.

Appendix G

Modeling of thermal isolation mechanisms

G.1 Steady-state model for thermal shield

The MSE periscope and its surroundings are modeled with infinite thin slabs as shown in Fig G-1 for (a) a single layer of thermal shield configuration and (b) a no-shield (current) configuration. In this model, the MSE periscope is divided into two surfaces: front (toward plasma) and back (toward outer-wall) surfaces since we are interested in the temperature variation across the two surfaces of the periscope, that is, $T_3 - T_4$ in Fig G-1 (a) and $T_2 - T_3$ in (b). The thermal conduction along the length of the canister is ignored in this model since it is very slow due to the poor thermal conductivity of stainless steel and the long path length (~ 40 cm). The temperatures of the thermal shield and the periscope surfaces are allowed to float between two fixed temperatures of inner and outer walls of the vacuum vessel. 'a' denotes the surfaces that face outward (away from the torus center) and 'b' for the surfaces that face inward (toward the torus center). The power flux leaving each surface is the sum of the intrinsic thermal emission plus the fraction of power that is reflected from the adjacent surface. Assuming the grey body radiation, the power flux at each surface

torus inner wall — heat shield — periscope front side — periscope back side — torus outer wall

q1b → q2b → q3b → q4b →

← q2a ← q3a ← q4a ← q5a

b | a b | a b | a b | a

T1   T2   T3   T4   T5

(a) Single-shield configuration

torus inner wall — periscope front side — periscope back side — torus outer wall

q1b →

q2b → q3b →

← q2a ← q3a ← q4a

b | a b | a b | a

T1   T2   T3   T4
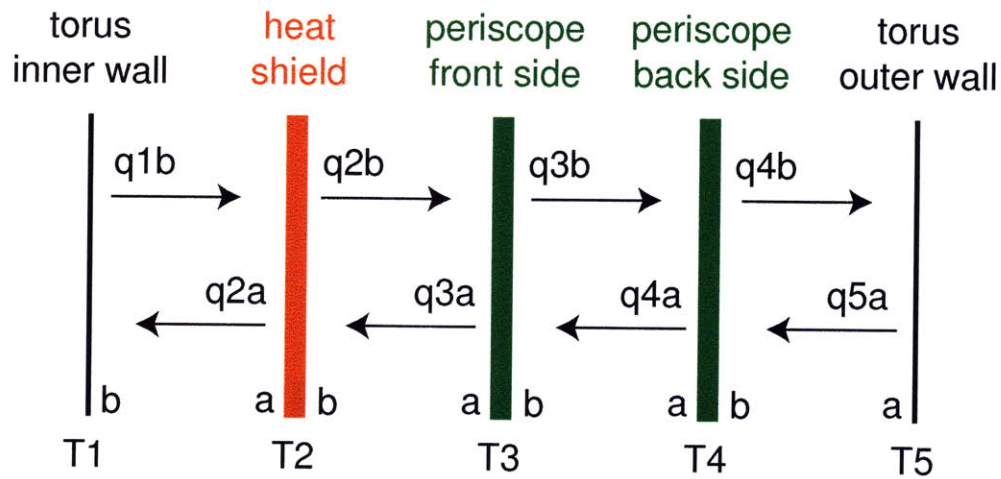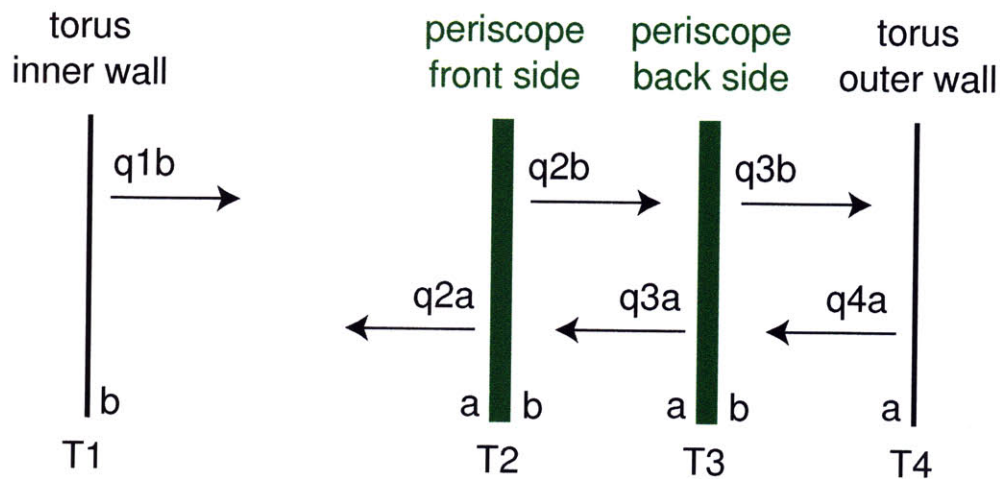
(b) No-shield configuration

Figure G-1: Infinite thin slab model of the MSE invessel periscope and its surroundings to compute heat flows and temperatures for (a) single-layer thermal shield and (b) no-shield configurations. 'a' denotes a surface facing the torus inner wall and 'b' for a surface facing the torus outer wall. Radiative heat flows from surfaces are also shown as $q1b$, $q2a$ etc. An external heat flow, for example from the plasma is included in $q1b$.

can be written as

$$q_{1b} = \epsilon_{1b}\sigma T_1^4 + (1 - \epsilon_{1b})q_{2a} + q_e \tag{G.1}$$

$$q_{2a} = \epsilon_{2a}\sigma T_2^4 + (1 - \epsilon_{2a})q_{1b}$$

$$q_{2b} = \epsilon_{2b}\sigma T_2^4 + (1 - \epsilon_{2b})q_{3a}$$

$$q_{3a} = \epsilon_{3a}\sigma T_3^4 + (1 - \epsilon_{3a})q_{2b}$$

$$q_{3b} = \epsilon_{3b}\sigma T_3^4 + (1 - \epsilon_{3b})q_{4a}$$

$$q_{4a} = \epsilon_{4a}\sigma T_4^4 + (1 - \epsilon_{4a})q_{3b}$$

$$q_{4b} = \epsilon_{4b}\sigma T_4^4 + (1 - \epsilon_{4b})q_{5a}$$

$$q_{5a} = \epsilon_{5a}\sigma T_5^4 + (1 - \epsilon_{5a})q_{4b}.$$

for the single-shield configuration (Fig G-1 (a)). Note the first equation that describes the heat flux incident on the outer shield surface has an additional term q_e, which denotes the external heat flux from a plasma. At steady state, the power incident on each surface must equal the power leaving:

$$q_{1b} + q_{3a} = q_{2a} + q_{2b} \tag{G.2}$$

$$q_{2b} + q_{4a} = q_{3a} + q_{3b}$$

$$q_{3b} + q_{5a} = q_{4a} + q_{4b}.$$

Note that in 11 equations in Eqns G.2 and G.3, T_1, T_5, q_e, and all the emissivity values are assumed to be known and the rest 11 variables are unknown. Then Eqns G.2 and G.3 constitute a set of linear simultaneous equations that can be easily solved:

$$
\begin{bmatrix}
1 & \epsilon_{1b}-1 & 0 & 0 & 0 & 0 & 0 & 0 & 0 & 0 & 0 \\
\epsilon_{2a}-1 & 1 & 0 & 0 & 0 & 0 & 0 & 0 & -\sigma\epsilon_{2a} & 0 & 0 \\
0 & 0 & 1 & \epsilon_{2b}-1 & 0 & 0 & 0 & 0 & -\sigma\epsilon_{2b} & 0 & 0 \\
0 & 0 & \epsilon_{3a}-1 & 1 & 0 & 0 & 0 & 0 & 0 & -\sigma\epsilon_{3a} & 0 \\
0 & 0 & 0 & 0 & 1 & \epsilon_{3b}-1 & 0 & 0 & 0 & -\sigma\epsilon_{3b} & 0 \\
0 & 0 & 0 & 0 & \epsilon_{4a}-1 & 1 & 0 & 0 & 0 & 0 & -\sigma\epsilon_{4a} \\
0 & 0 & 0 & 0 & 0 & 0 & 1 & \epsilon_{4b}-1 & 0 & 0 & -\sigma\epsilon_{4b} \\
0 & 0 & 0 & 0 & 0 & 0 & \epsilon_{5a}-1 & 1 & 0 & 0 & 0 \\
-1 & 1 & 1 & -1 & 0 & 0 & 0 & 0 & 0 & 0 & 0 \\
0 & 0 & -1 & 1 & 1 & -1 & 0 & 0 & 0 & 0 & 0 \\
0 & 0 & 0 & 0 & -1 & 1 & 1 & -1 & 0 & 0 & 0
\end{bmatrix}
\cdot
\begin{bmatrix}
q_{1b} \\ q_{2a} \\ q_{2b} \\ q_{3a} \\ q_{3b} \\ q_{4a} \\ q_{4b} \\ q_{5a} \\ T_2^4 \\ T_3^4 \\ T_4^4
\end{bmatrix}
=
\begin{bmatrix}
q + \sigma\epsilon_{1b}T1^4 \\ 0 \\ 0 \\ 0 \\ 0 \\ 0 \\ 0 \\ \sigma\epsilon_{5a}T5^4 \\ 0 \\ 0 \\ 0
\end{bmatrix}
\tag{G.3}
$$

A similar set of linear simultaneous equations can be constructed and solved for the configuration without a heat shield (Fig G-1 (b)).

G.2 Transient model for thermal shield

The model shown in Fig G-1 can also be used in the transient calculations. Eqn G.2 is still valid, but one cannot use Eqn G.3 because the net heat flux is not the same surface to surface. Recalling the general form of the radiated power exchanged between two surfaces facing each other with the same viewing area given in Eqn 3.12, the net heat flux through each surface in the single-shield model given in Fig G-1 (a) can be written

$$
\begin{aligned}
q_2^{net} &= \frac{\sigma(T_1^4 - T_2^4)}{1/\epsilon_{1b} + 1/\epsilon_{2a} - 1} - \frac{\sigma(T_2^4 - T_3^4)}{1/\epsilon_{2b} + 1/\epsilon_{3a} - 1} + q_e \\
q_3^{net} &= \frac{\sigma(T_2^4 - T_3^4)}{1/\epsilon_{2b} + 1/\epsilon_{3a} - 1} - \frac{\sigma(T_3^4 - T_4^4)}{1/\epsilon_{3b} + 1/\epsilon_{4a} - 1} \\
q_4^{net} &= \frac{\sigma(T_3^4 - T_4^4)}{1/\epsilon_{3b} + 1/\epsilon_{4a} - 1} - \frac{\sigma(T_4^4 - T_5^4)}{1/\epsilon_{4b} + 1/\epsilon_{5a} - 1}
\end{aligned}
\tag{G.4}
$$

and then the following heat flow equations can be constructed:

$$
\begin{aligned}
\rho_2 C_{p2} w_2 \frac{dT_2}{dt} &= q_2^{net} \\
\rho_3 C_{p3} w_3 \frac{dT_3}{dt} &= q_3^{net} \\
\rho_4 C_{p4} w_4 \frac{dT_4}{dt} &= q_4^{net}
\end{aligned}
\tag{G.5}
$$

where ρ_i, C_{pi}, and w_i are the density, specific heat capacity, and the thickness of the surface material i, respectively. These quantities for the participating surface materials are summarized in Table G.1. (This table is almost identical to Table F.1 in App F.2 It is straightforward to solve Eqn G.6 numerically with appropriate initial conditions.

Surface	Material	ρ g/cm^3	C_p J/g°K	w cm
Periscope	Stainless Steel 304	8.0	0.50	0.16
Shield	Inconel 718	8.2	0.43	0.16

Table G.1: Material properties of the periscope and shield surfaces.

G.3 Thermal capacitive circuit model for bottom part of the periscope

Fig G-2 illustrates the 2D cross-sectional view of the simplified geometry for the lower part of the periscope that has L1 and the L2 doublet with the five temperature nodes denoted as $\bigotimes_i$ where i is the node number. Note that the L2 doublet is divided into a cylinder surrounded by an annular ring with a smaller thickness, the former representing the thick 'central' part of the L2 lens and the latter its thin 'edge' part. The periscope is also divided into two: one that surrounds the L2 holder and extends vertically, conductively communicating with the L2 holder; and the other is positioned above L2 horizontally, radiatively communicating with the L2 lens surfaces. Both periscope parts conduct heat to each other and radiate heat to the wall with a fixed temperature. The dimensions and material properties shown in Fig G-2 are summarized in Table G.2.

Fig G-3 illustrates a circuit network of the heat transfer mechanism among nodes for the geometry shown in Fig G-2 where conductive and radiative thermal 'resistance-equivalents' are denoted as C and D, respectively. Also shown in the figure are the directions of the heat flow rate in Watt between two nodes either via conduction (denoted as 'i') or radiation (denoted as 'j'), including j_0 which represents the power flow incident on L1 directly from the plasma, and then the individual heat flow rates can be written as

$$i_{12} = \frac{T_1 - T_2}{C_{12}} = \frac{T_1 - T_2}{R^c_{L1h} + R^c_{tur}} \tag{G.6}$$

$$i_{32} = \frac{T_3 - T_2}{C_{32}} = \frac{T_3 - T_2}{R^c_{L2o} + R^c_{L2h}} \tag{G.7}$$
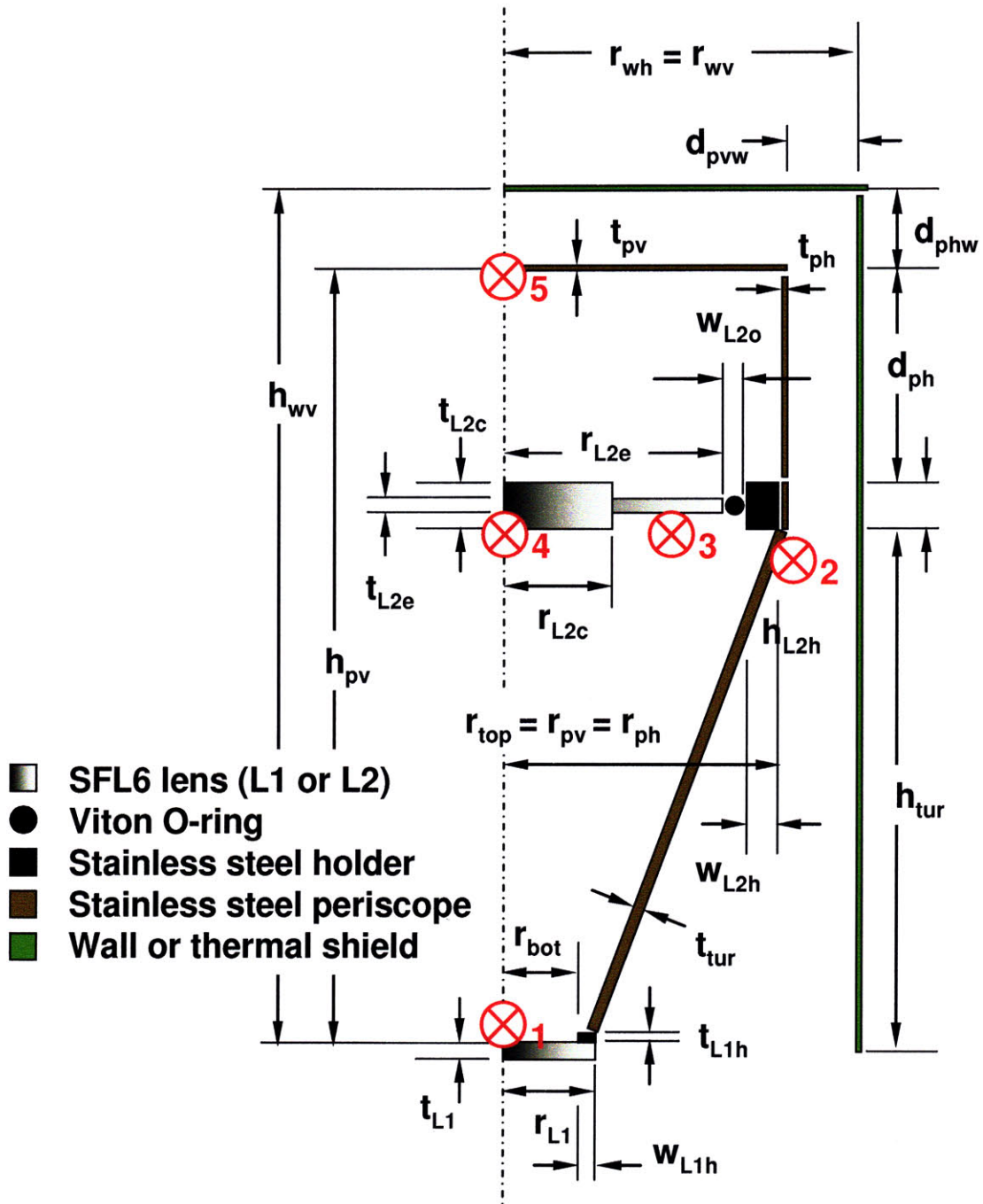
Figure G-2: 2D cross-sectional view of the simplified geometry for the lower part of the periscope. The temperature nodes at which temperatures are calculated are denoted as $\bigotimes_i$ in red where $i = 1$ for L1, 2 for the vertical part of the periscope adjacent to the L2 lens holder, 3 for the edge of L2, 4 for the center of L2, and 5 for the upper part of the periscope. The dimensions and the material properties are given in Table G.2.

Variable	Material	Dimension (mm)	Density ρ (g/cm^3)	Specific heat C_p (J/gK)	Heat conductivity k (W/cmK)
r_{L1}	SFL6	26.5	3.37	0.6	0.00945
t_{L1}	SFL6	5	3.37	0.6	0.00945
t_{L1h}	SS	1	8	0.5	0.16
w_{L1h}	SS	1.2	8	0.5	0.16
r_{L2c}	SFL6	31.25	3.37	0.6	0.00945
t_{L2e}	SFL6	62.5	3.37	0.6	0.00945
t_{L2c}	SFL6	13	3.37	0.6	0.00945
t_{L2e}	SFL6	4.1	3.37	0.6	0.00945
w_{L1o}	Viton	1.84	1.2	2	0.0022
w_{L2h}	Inconel	9.2	8.2	0.43	0.098
h_{L2h}	Inconel	13.43	8.2	0.43	0.098
t_{tur}	SS	3.27	8	0.5	0.16
t_{ph}	SS	1.6	8	0.5	0.16
t_{pv}	SS	1.6	8	0.5	0.16
h_{tur}		151			
d_{ph}		66			
d_{pvw}		20			
d_{phw}		20			
r_{bot}	$r_{L1} - w_{L1h}$				
r_{top}	$r_{L2e} + w_{L2o} + w_{L2h}$				
r_{ph}	r_{top}				
r_{pv}	r_{top}				
h_{pv}	$h_{L2h} + h_{tur} + d_{ph}$				
h_{wv}	$h_{L2h} + h_{tur} + d_{ph} + d_{phw}$				
r_{wv}	$r_{pv} + d_{pvw}$				
r_{wh}	r_{wv}				

Table G.2: Dimension and material properties shown in Fig G-2. *SS* stands for Stainless steel

311
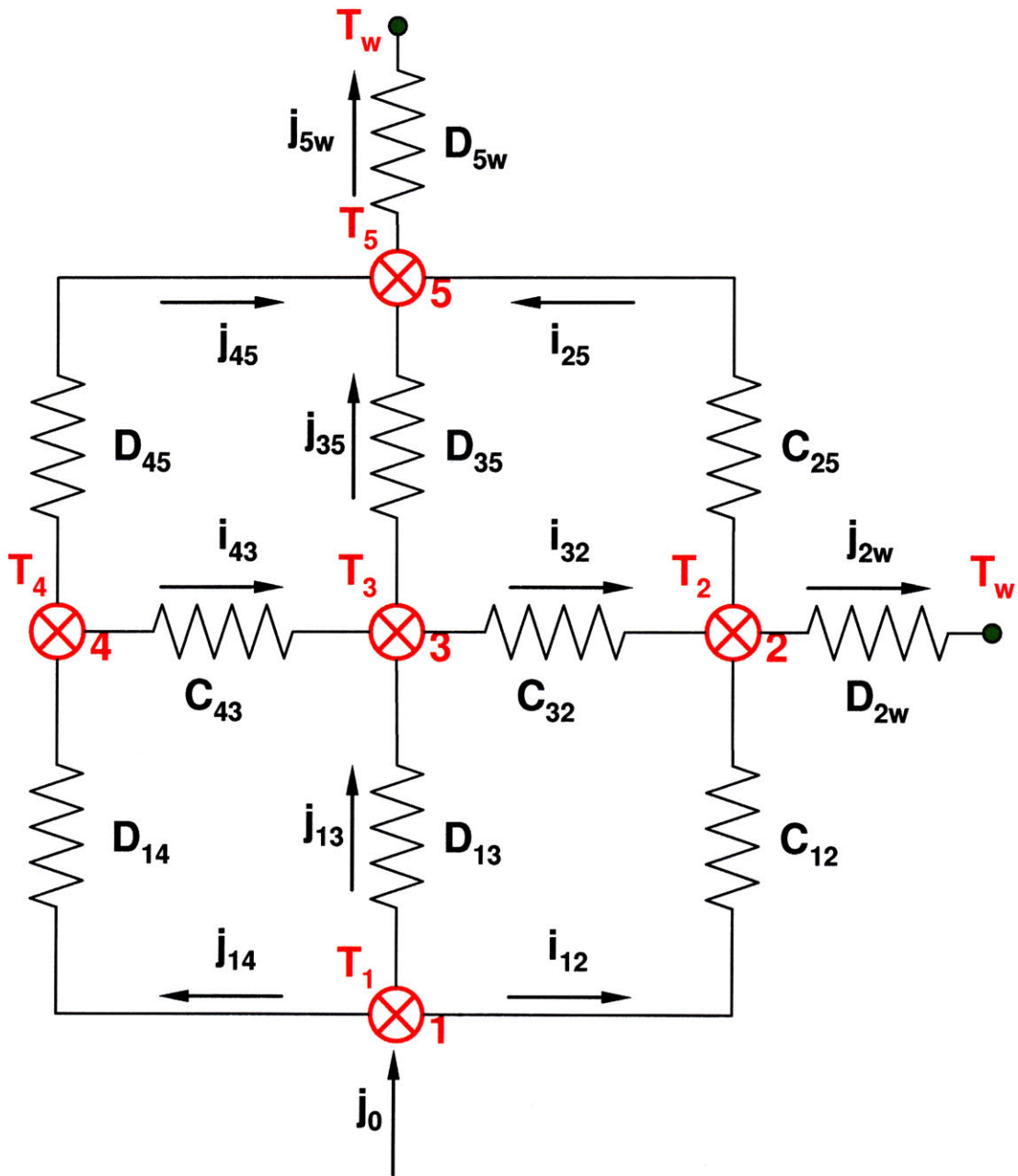
Figure G-3: Circuit diagram for the geometry shown in Fig G-2. C_{mn} and D_{mn} denotes the conductive and radiative thermal 'resistance-equivalents', respectively, between nodes m and n. i_{mn} and j_{mn} denotes the power flow (in Watt) via conduction and radiation, respectively, from node m to node n. j_0 is the radiative power incident on L1 (node 1) directly from the plasma. T_m is the temperature at node m.

$$i_{43} = \frac{T_4 - T_3}{C_{43}} = \frac{T_4 - T_3}{R_{L2}^c} \tag{G.8}$$

$$i_{25} = \frac{T_2 - T_5}{C_{25}} = \frac{T_2 - T_5}{R_{phv}^c} \tag{G.9}$$

$$j_{13} = \frac{\sigma(T_1^4 - T_3^4)}{D_{13}} = \sigma(T_1^4 - T_3^4)A_{L1}F_{L1-L2e} \tag{G.10}$$

$$j_{14} = \frac{\sigma(T_1^4 - T_4^4)}{D_{14}} = \sigma(T_1^4 - T_4^4)A_{L1}F_{L1-L2c} \tag{G.11}$$

$$j_{35} = \frac{\sigma(T_3^4 - T_5^4)}{D_{35}} = \sigma(T_3^4 - T_5^4)A_{L2e}F_{L2e-ph} \tag{G.12}$$

$$j_{45} = \frac{\sigma(T_4^4 - T_5^4)}{D_{45}} = \sigma(T_4^4 - T_5^4)A_{L2c}F_{L2c-ph} \tag{G.13}$$

$$j_{2w} = \frac{\sigma(T_2^4 - T_w^4)}{D_{2w}} = \frac{\sigma(T_2^4 - T_w^4)}{\frac{1-\epsilon_2}{\epsilon_2 A_{pv}} + \frac{1}{A_{pv}F_{pv-wv}} + \frac{1-\epsilon_w}{\epsilon_w A_{wv}}} \tag{G.14}$$

$$j_{5w} = \frac{\sigma(T_5^4 - T_w^4)}{D_{5w}} = \frac{\sigma(T_5^4 - T_w^4)}{\frac{1-\epsilon_5}{\epsilon_5 A_{ph}} + \frac{1}{A_{ph}F_{ph-wh}} + \frac{1-\epsilon_w}{\epsilon_w A_{wh}}} \tag{G.15}$$

where R_m^c represents the usual thermal conductive resistance which is the path length divided by area and thermal conductivity of the material m: R_{L1h}^c for the resistance across the L1 stainless steel holder; R_{tur}^c for the resistance across the 'turret' which is a part of the periscope between the L1 and the L2 regions; R_{L2o}^c for the resistance across the Viton o-ring between the L2 lens and its holder; R_{L2h}^c for the resistance across the Inconel lens holder; R_{L2}^c for the resistance across the L2 lens itself from the 'central' to 'edge' regions of the lens; and finally, R_{phv}^c is the resistance between the vertical and the horizontal periscopes. Thermal contact resistances between the materials are ignored in this analysis although it may increase the conductive resistances further. Therefore, the result from this analysis may put the upper bound for the temperature variation across the lens L2. The thermal resistances in Eqns G.6 $\sim$ G.9 are calculated by

$$R_{L1h}^c = \frac{t_{L1h}}{2\pi r_{L1}w_{L1h}k_{L1h}} \tag{G.16}$$

$$R_{tur}^c = \frac{\ln(r_o/r_i)}{2\pi t_{tur}k_{tur}}\frac{r_i}{r_{bot}} \tag{G.17}$$

$$R_{L2o}^c = \frac{w_{L2o}}{2\pi r_{L2e}w_{L2o}k_o} \tag{G.18}$$

$$R^c_{L2h} = \frac{\ln(r_{top}/(r_{L2e} + w_{L2o}))}{2\pi k_{L2h} h_{L2h}} \tag{G.19}$$

$$R^c_{L2} = \frac{\ln(r_{L2e}/r_{L2c})}{2\pi k_{L2} t_{L2e}} \tag{G.20}$$

$$R^c_{phv} = \frac{d_{ph}}{2\pi r_{pv} t_{pv} k_{pv}} \tag{G.21}$$

where $r_o = \sqrt{(x + h_{tur})^2 + r^2_{top}}$ and $r_i = \sqrt{x^2 + r^2_{bot}}$ with $x = r_{bot} h_{tur}/(r_{top} - r_{bot})$. A_m in Eqns G.10 $\sim$ G.15 is the area of the node m viewed by the other node in the radiative communication, and F_{m-n} in the same equations denotes the radiative view factor that is the fraction of the radiated power leaving the node m, that arrives at node n [73]. All the radiating surfaces in the first four radiation heat flow rates (Eqns G.10 $\sim$ G.13) which are taking place *inside* the periscope are assumed to be black-body and therefore, the thermal radiative resistance, D_{mn}, only depends on the *view-factor resistance*, $A_m F_{m-n}$. On the other hand, the last two power flows (Eqns G.14 and G.15) involve the radiation that occur outside the periscope. Therefore, the full expression for the radiative resistance is used, which is the sum of the view-factor resistance and the surface-grayness resistances from the two surfaces involved. In reality, about half the periscope will be surrounded by the heat shield whose inner surface is gold-plated ($\epsilon \sim 0.04$) and the other half by the outer wall of the torus ($\epsilon \sim 1$). Therefore, ϵ_w is reasonably assumed to be 0.1. ϵ_2 and ϵ_5, the emissivities of the gold-coated outer surfaces of the periscope, are assumed to 0.04. Note that the conductive and radiative resistances are not in the same unit, the former in K/W and the latter in $1/m^2$.

Recalling the geometry shown in Fig G-2, it is observed that the view factors from L1 to L2c, F_{L1-L2c}, and from L1 to L2e, F_{L1-L2e}, in Eqns G.11 and G.10, respectively, correspond to "Disk to parallel coaxial disk of unequal radius" (C-41 in Ref [75]) and "Disk to coaxial annular ring on parallel disk" (C-47 in Ref [75]), respectively. These are expressed as, therefore,

$$F_{L1-L2c} = \frac{1}{2} \left\{ X - \left[X^2 - 4 \left(\frac{R_2}{R_1} \right)^2 \right]^{\frac{1}{2}} \right\}, \tag{G.22}$$

314

where $R_1 = r_{L1}/h_{tur}$, $R_2 = r_{L2c}/h_{tur}$, and $X = 1 + (1 + R_2^2)/R_1^2$ and

$$F_{L1-L2e} = \frac{1}{2}\left\{ R_3^2 - R_2^2 - \left[(1 + R_3^2 + H^2)^2 - 4R_3^2\right]^{\frac{1}{2}} + \left[(1 + R_2^2 + H^2)^2 - 4R_2^2\right]^{\frac{1}{2}} \right\},$$

$$(G.23)$$

where $H = h_{tur}/r_{L1}$, $R_2 = r_{L2c}/r_{L1}$, and $R_3 = r_{L2e}/r_{L1}$. Since view-factor resistances are reciprocal, i.e., $A_m F_{m-n} = A_n F_{n-m}$, the view-factor resistances from L2c to the horizontal periscope, which is assumed to have a disk shape with a radius r_{ph} as shown in Fig G-2, and from L2e to the horizontal periscope can be re-written as

$$A_{L2c} F_{L2c-ph} = A_{ph} F_{ph-L2c} \qquad (G.24)$$

$$A_{L2e} F_{L2e-ph} = A_{ph} F_{ph-L2e} \qquad (G.25)$$

and the expressions in Eqns G.22 and G.23 can be used for F_{ph-L2c} and F_{ph-L2e}, respectively. The assumption of having disks parallel to the L2 lens as the radiation source (from L1) and sink (to the bulk periscope) is reasonable since the radiated power passing through L1 will be reflected to the L2 lenses via the mirror M1 in-between and the most of the radiated power from L2 will reach the M2 mirror above it. The view-factor from the horizontal periscope to the wall, F_{ph-wh} in Eqn G.15 is also obtained using the same formula for F_{L1-L2c} (Eqn G.22). The view-factor from the vertical periscope to the wall, F_{pv-wv} in Eqn G.14 is approximated to "Inner coaxial cylinder to outer coaxial cylinder; inner cylinder entirely within outer" (C-95 in Ref [75]) which is

$$F_{pv-wv} = 1 + \frac{X}{Z}F_X + \frac{Z}{L}F_Z - \left(\frac{L+X}{L}\right)F_{L+X} - \frac{L+Z}{L}F_{L+Z}, \qquad (G.26)$$

with the following definitions:

$$A_\xi = \xi^2 + R^2 - 1 \qquad (G.27)$$

$$B_\xi = \xi^2 - R^2 + 1$$

Resistance per flow	Individual resistance	value
C_{12}	R^c_{L1h}	0.309 K/W
	R^c_{tur}	10.5 K/W
C_{32}	R^c_{L2o}	11.6 K/W
	R^c_{L2h}	0.162 K/W
C_{43}	R^c_{L2}	28.5 K/W
C_{25}	R^c_{phv}	5.51 K/W
D_{13}	$1/(A_{L1}F_{L1-L2e})$	4810 /m^2
D_{14}	$1/(A_{L1}F_{L1-L2c})$	2640 /m^2
D_{35}	$1/(A_{L2e}F_{L2e-ph})$	253 /m^2
D_{45}	$1/(A_{L1c}F_{L2c-ph})$	616 /m^2
D_{2w}	$(1-\epsilon_2)/(\epsilon_2 A_{pv})$	225 /m^2
	$(1-\epsilon_w)/(\epsilon_w A_{wv})$	61.0 /m^2
	$1/(A_{pv}F_{pv-wv})$	9.8 /m^2
D_{5w}	$(1-\epsilon_5)/(\epsilon_5 A_{ph})$	1413 /m^2
	$(1-\epsilon_w)/(\epsilon_w A_{wh})$	327 /m^2
	$1/(A_{ph}F_{ph-wh})$	65 /m^2

Table G.3: The thermal conductive and radiative resistances for the model given in Figs G-2 and G-3.

$$F_\xi = \frac{B_\xi}{8R\xi} + \frac{1}{2\pi}\left\{\cos^{-1}\frac{A_\xi}{B_\xi} - \frac{1}{2\xi}\left(\frac{(A_\xi+2)^2}{R^2}-4\right)^{1/2}\cos^{-1}\frac{A_\xi R}{B_\xi} - \frac{A_\xi}{2\xi R}\sin^{-1}R\right\},$$

where $X \approx 0$, $Z = d_{phw}/r_{wv}$, $L = h_{pv}/r_{wv}$, and $R = r_{pv}/r_{wv}$. Table G.3 summarizes the thermal conductive and radiative resistances obtained using Eqns G.16 $\sim$ G.28. Also note that the radiative communications involving the vertical inner wall of the periscope is ignored in this model for simplicity. The view-factor resistances for these are larger than, or at best, comparable to those between the lens and the horizontal part of the periscope and as shown in Table G.3, all the view-factor resistances inside the periscope are an order of magnitude or two larger than the conductive heat transfer, making this assumption reasonable.

Now with the help of Fig G-3, the capacitive (i.e. time-dependent) heat flow equations for individual nodes can be written as

$$\rho_1 C_{p1} V_1 \frac{dT_1}{dt} = j_0 - i_{12} - j_{13} - j_{14} \tag{G.28}$$

$$\rho_2 C_{p2} V_2 \frac{dT_2}{dt} = i_{12} + i_{32} - i_{25} - j_{2w}$$

$$\rho_3 C_{p3} V_3 \frac{dT_3}{dt} = j_{13} + i_{43} - i_{32} - j_{35}$$

$$\rho_4 C_{p4} V_4 \frac{dT_4}{dt} = j_{14} - i_{43} - j_{45}$$

$$\rho_5 C_{p5} V_5 \frac{dT_5}{dt} = j_{45} + j_{35} + i_{25} - j_{5w}$$

where ρ_m, C_{pm}, and V_m are the density, specific heat capacity, and the volume of node m and j_0 again is the heat flow rate incident on L1 which is the external heat flux q_e multiplied by the area of L1.

Bibliography

[1] I. Hutchinson, *Principles of Plasma Diagnostics, 2nd Edition*, Cambridge University Press (2002)

[2] J. Wesson, *Tokamaks, 2nd Edition*, Clarendon Press, Oxford (1997)

[3] T.S. Taylor *et al.*, "Optimized profiles for improved confinement and stability in the DIII-D tokamak", Plasma Phys. Control. Fusion 36 (1994) B229-B239

[4] J. Manickam *et al.*, "The prospects for magnetohydrodynamic stability in advanced tokamak regimes", Phys. Plasmas 1 (1994) 1601

[5] T.S. Taylor "Physics of advanced tokamaks", Plasma Phys. Control. Fusion 39 (1997) B47-B73

[6] Yu.F. Baranov *et al.*, "On the link between the q-profile and internal transport barriers", Plasma Phys. Control. Fusion, 46 (2004) 1181-1196

[7] M. Yamada *et al.*, "Investigation of magnetic reconnection during a sawtooth crash in a high-temperature tokamak plasma", Phys. Plasmas, 1:10 (1994), 3269-3276

[8] Jeffrey Freidberg, *Plasma Physics and Fusion Energy*, Cambridge University Press (2007)

[9] Charles Kessel, "Advanced tokamak plasmas and the fusion ignition research experiment", Bulletin of APS Spring Meeting (2003)

[10] K.H. Burrell, "Diagnostics for advanced tokamak research", Rev. Sci. Instrum. 72:1 (2001) 906-914

[11] L.L. Lao *et al.*, "Separation of $\bar{\beta}_p$ and l_i in tokamaks of non-circular cross-section", Nuclear Fusion 25 (1985) 1421

[12] L.L. Lao *et al.*, "Reconstruction of current profile parameters and plasma shapes in tokamaks", Nuclear Fusion 25 (1985) 1611

[13] L. L. Lao *et al.*, "Equilibrium analysis of current profiles in tokamaks", Nuclear Fusion 30 (1990) 1035

[14] R. Giannella, "Point-to-point analysis of MSE data for plasma diagnostics and control", Rev. Sci. Instrum. 75 (2004) 4247

[15] C.C. Petty *et al.*, "Analysis of current drive using MSE polarimetry without equilibrium reconstruction", Nuclear Fusion 42 (2002) 1124-1133

[16] C.C. Petty *et al.*, "Direct measurement of neoclassical currents using motional Stark effect polarimetry", Plasma Phys. Control. Fusion 47 (2005) 1077-1100

[17] H. Soltwisch, "Current density measurements in tokamak devices", Plasma Phys. Control. Fusion 34:12 (1992) 1669-1698

[18] W.P. West *et al.*, "Diagnostic instrument for the measurement of poloidal magnetic fields in tokamaks", Rev. Sci. Instrum. 57:8 (1986) 1552-1556

[19] F.M. Levinton *et al.*, "Magnetic field pitch-angle measurements in the PBX-M tokamak using the motional Stark effect", Phys. Rev. Lett. 63 (1989) 2060-2063

[20] F.M. Levinton *et al.*, "Magnetic field pitch angle diagnostic using the motional Stark effect", Rev. Sci. instrum. 61:10 (1990) 2914-2919

[21] D. Wroblewski *et al.*, "Motional Stark effect polarimetry for a current profile diagnostic in DIII-D", Rev. Sci. Instrum. 61 (1990) 3552-3556

[22] D. Wroblewski *et al.*, "Polarimetry of motional Stark effect and determination of current profiles in DIII-D", Rev. Sci. Instrum. 63 (1992) 5140-5147

[23] F.M. Levinton *et al.*, "Improved confinement with reversed magnetic shear in TFTR", Phys. Rev. Lett. 75 (1995) 4417-4420

[24] B.W. Rice *et al.*, "Motional Stark effect upgrades on DIII-D", Rev. Sci. Instrum. 66 (1995) 373-375

[25] B.W. Rice *et al.*, "Effect of plasma radial electric field on motional Stark effect measurements and equilibrium reconstruction", Nuclear Fusion 37 (1997) 517-522

[26] N.C. Hawkes "Design study of a motional Stark effect diagnostic for JET", JET-R(96)10 (1997)

[27] J. Hobirk *et al.*, "Measurements of the poloidal magnetic and radial electric field profiles in ASDEX Upgrade and JET", International Conference on Advanced Diagnostics for Magnetic and Inertial Fusion, Varenna (2001)

[28] R.D. Cowan, *The Theory of Atomic Structure and Spectra*, University of California Press (1981)

[29] A. Beiser, *Concepts of Modern Physics, 4th Edition*, McGraw-Hill Book Company (1987)

[30] N.A. Pablant *et al.*, "Measurements of the internal magnetic field on DIII-D using intensity and spacing of the motional Stark multiplet", Rev. Sci. Instrum. 79 (2008) 10F517

[31] E.L. Foley *et al.*, "The motional Stark effect diagnostic for ITER using a line-shift approach", Rev. Sci. Instrum. 79 (2008) 10F521

[32] J.C. Kemp, "Polarized light and its interaction with modulating devices: a methodology review", Hinds Instruments (1987)

[33] J.C. Kemp *et al.*, "The optical polarization of the sun measured at a sensitivity of parts of 10 million", Nature 326:6110 (1987) 270-273

[34] B. Wang *et al.*, "Evaluation of a dual PEM Stokes polarimeter using different signal processing methods", Proc. of SPIE 5888 (2005)

[35] E. Hecht, *Optics, 4th Edition*, Addison Wesley (2002)

[36] H.Y. Yuh, "The motional Stark effect diagnostic on Alcator C-Mod", PhD Thesis (2005)

[37] G. Arfken, *Mathematical Methods for Physicists*, Academic Press, Inc. (1985)

[38] J. Ko *et al.*, "Spectroscopic investigation on the beam fast ion effects on Alcator C-Mod MSE diagnostic", Bulletion of APS DPP Fall Meeting (2006)

[39] S. Scott *et al.*, "Effect of secondary beam neutrals on MSE: Theory", Bulletin of APS DPP Fall Meeting (2007)

[40] J. Ko *et al.*, "Effect of secondary beam neutrals on MSE: Experiment", Bulletin of APS DPP Fall Meeting (2007)

[41] H.Y. Yuh *et al.*, "Simulation of the motional Stark effect diagnostic gas-filled torus calibration", Rev. Sci. Instrum. 79 (2008) 10F523

[42] I.H. Hutchinson *et al.*, "First results from Alcator C-Mod", Phys. Plasmas 1:5 (1994) 1511-1518

[43] S. Scott *et al.*, "Overview of the Alcator C-Mod research programme", Nuclear Fusion 47 (2007) 598-607

[44] R. Bravenec *et al.*, "Characterization of the new diagnostic neutral beam on Alcator C-Mod", Bulletin of APS DPP Fall Meeting (2005)

[45] M.B. Sampsell *et al.*, "Comparisons of measurements and gyrokinetic simulations of turbulence and transport in Alcator C-Mod EDA H-mode discharges", Bulletin of APS DPP Fall Meeting (2004)

[46] R.M. McDermott *et al.*, "Edge radial electric field structure and connection to H-mode confinement in Alcator C-Mod plasmas", Bulletin of APS DPP Fall Meeting (2008)

[47] I.O. Bespamyatnov *et al.*, "Light impurity transport studies in Alcator C-Mod", Bulletin of APS DPP Fall Meeting (2008)

[48] HAMAMATSU, "Characteristics and use of Si APD (Avalanche Photodiode)", Technical Information SD-28

[49] PerkinElmer, "Avalanche photodiode: A User Guide", Application Note

[50] R.J. McIntyre, "Multiplication noise in uniform avalanche diodes", IEEE Trans. on Electron Devices ED-13:1 (1966) 164-168

[51] M.C. Teich, "Excess noise factors for conventional and superlattice avalance photodiodes and photomultiplier tubes", IEEE J. Quantum Electron. QE-22:8 (1986) 1184-1193

[52] N.Z. Hakim, "Generalized excess noise factor for avalanche photodiodes of arbitrary structure", IEEE Trans. on Electron Devices 37:3 (1990) 599-610

[53] M. Akiyama, "Excess noise characteristics of hydrogenated amorphous silicon p-i-n photodiode films", Jpn. J. Appl. Phys. 41 (2002) 2552-2555

[54] N. Bertone *et al.*, "Noise and stability in PIN detectors", PerkinElmer Note

[55] Y. Fainman *et al.*, "Polarization of nonplanar wave fronts", App. Optics 23:18 (1984) 3188-3195

[56] B. Gimeno *et al.*, "A polarized rotator system for three-dimensional oblique incidence", IEEE Trans. Antennas Propagat. 42:7 (1994) 912-919

[57] X.J. Yu *et al.*, "Optical wire-grid polarizers at oblique angles of incidence", J. Appl. Phys. 93:8 (2003) 4407-4412

[58] D. Kim, "Polarization characteristics of a wire-grid polarizer in a rotating platform", App. Optics 44:8 (2005) 1366-1371

[59] M. Xu *et al.* "Wire-grid diffraction gratings used as polarizing beam splitter for visible light and applied in liquied crystal on silicon", Optics Express 13:7 (2005) 2303-2320

[60] K. Bhattacharya *et al.*, "Simulation of effects of phase and amplitude coatings on the lens aperture with polarization masks", J. Opt. Soc. Am. A 11:2 (1994) 586-592

[61] T. Manabe *et al.*, "Transmission and reflection characteristics of slightly irregular wire-grids with finite conductivity for arbitrary angles of incidence and grid rotation", IEEE Trans. Antennas Propagat. 53:1 (2005) 250-259

[62] S.D. Scott *et al.*, "Invessel Calibration of the Alcator C-Mod MSE Diagnostic", Bulletin of APS DPP Fall Meeting (2004)

[63] H.A. Bethe, *Quantum mechanics of one- and two-electron atoms*, Plenum Pub. Corp., New York (1977)

[64] S.L. Allen, *et al.*, "In-situ calibration of the DIII-D MSE diagnostic system with magnetic fields", Bulletin of APS DPP Fall Meeting (2003)

[65] N.C. Hawkes *et al.*, "Calibration and operational experience with the JET motional Stark effect diagnostic", Rev. Sci. Instrum. 77 (2006) 10E509

[66] F.M. Levinton *et al.*, "q-profile measurements in the Tokamak Fusion Test Reactor", Rhys. Fluids B 5:7 (1993) 2554-2561

[67] W.M. Solomon *et al.*, "Cross-calibrating spatial positions of light-viewing diagnostics using plasma edge sweeps in DIII-D", Rev. Sci. Instrum., 74:12 (2003) 5084-5089

[68] B.C. Stratton *et al.*, "Instrumentation for the joint European torus motional Stark effect diagnostic", Rev. Sci. Instrum., 70:1 (1999) 898-901

[69] F.W. Perkins *et al.*, "ITER physics basics: Chatper 1. Overview and summary", Nuclear Fusion, 39:12 (1999) 2137-2174

[70] B.A. Boley and J.H. Weiner, *Theory of Thermal Stresses*, Dover Publications (1997)

[71] A. Khalilollahi, "Finite element evaluation of thermal stresses in a composite circuit board cooled by mixed convection", International ANSYS conference Proceedings (2002)

[72] N.M. Elias II, "Optical interferometric polarimetry. I. Foundation", Astrophys. J. 549 (2001) 647-668

[73] M. Kaviany, *Principles of Heat Transfer*, John Wiley & Sons, Inc. (2002)

[74] H.S. Carslaw and I.C. Jaeger, *Conduction of Heat in Solids*, Clarendon Press (1986)

[75] J.R. Howell, *A Catalog of Radiation Heat Transfer Configuration Factors, 2nd Edition*, www.me.utexas.edu/˜howell/

[76] S. Bernabei *et al.*, "Design of a compact lower hybrid coupler for Alcator C-Mod", Fusion Sci. Technol. 43:2 (2003) 145-152

[77] P.T. Bonoli *et al.*, "Wave-particle studies in the ion cyclotron and lower hybrid ranges of frequencies in Alcator C-Mod", Fusion Sci. Technol. 51:3 (2007) 401-436

[78] P.T. Bonoli *et al.*, "Lower hybrid current drive experiments on Alcator C-Mod: Comparison with theory and simulation", Phys. Plasmas 15:056117 (2008)

[79] J.R. Wilson *et al.*, "Overview of LHCD experiments on Alcator C-Mod", Bulletin of APS DPP Fall Meeting (2008)

[80] P.T. Bonoli *et al.*, "Negative magnetic shear modes of operation in the Alcator C-Mod tokamak near the beta limit", Plasma Phys. Control. Fusion 39 (1997) 223-236

[81] P. Phillips *et al.*, "ECE high resolution electron temperature profiles on Alcator C-Mod", Bulletin of APS DPP Fall Meeting (2002)

[82] C.C. Petty *et al.*, "Detailed measurements of the electron cyclotron current drive efficiency on DIII-D", Nucl. Fusion 42 (2002) 1366-1375

[83] M. Brix *et al.*, "Accuracy of EFIT equilibrium reconstruction with internal diagnostic information at JET", Rev. Sci. Instrum. 79 (2008)

[84] C.C. Petty, *Private communication*

[85] G. Giruzzi *et al*,, "Measurement of the hot electrical conductivity in the PBX-M tokamak", Nucl. Fusion 37:5 (1997) 673-680

[86] O. Sauter *et al*,, "Neoclassical conductivity and bootstrap current formulas for general axisymmetric equilibria and arbitrary collisionality regime", Phys. Plasmas 6:7 (1999) 2834-2839